



Planetary Mission Concept Study for the 2023-2032 Decadal Survey

Enceladus Orbilander

A Flagship Mission Concept for Astrobiology

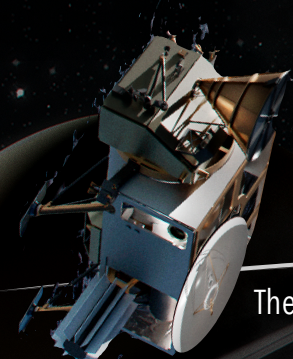
Shannon M. MacKenzie

Principal Investigator
Johns Hopkins University Applied Physics Laboratory
shannon.mackenzie@jhuapl.edu

Karen W. Kirby and Peter J. Greenauer

Design Study Leads
Johns Hopkins University Applied Physics Laboratory
karen.kirby@jhuapl.edu
peter.greenauer@jhuapl.edu





ENCELADUS ORBILANDER



A FLAGSHIP MISSION CONCEPT TO SEARCH FOR LIFE

The Orbilander can detect life from orbit at levels ~500x scarcer than in Earth's oceans, and from the surface at levels ~500,000x scarcer than in Earth's oceans.

Life at these detection levels can be sustained by Enceladus' supply of energy and CHNOPS measured by *Cassini*.

Whether or not Enceladus is found to be inhabited, the Orbilander measurements will tell us why.

Science Objectives

Determine whether or not Enceladus is *inhabited* and why

- In plume materials:

- 1. characterize the bulk organic fraction** (distribution, pathway complexity, component-level isotopic composition)

- 2. characterize amino acids** (relative abundances, handedness)

- 3. characterize lipids** (commonalities among long-chain hydrocarbons)

- 4. search for a polyelectrolyte** capable of storing genetic information

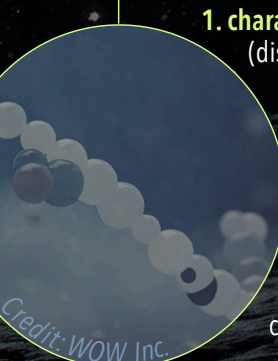
- 5. search for any cell-like morphologies**

- To **constrain the biomass** that Enceladus could support and determine **how ascent and ejection affect plume material**, **obtain** geochemical and geophysical **context for life detection**:

- 6. the physicochemical conditions** in the **ocean**

- 7. the structure and dynamics** of the **interior**

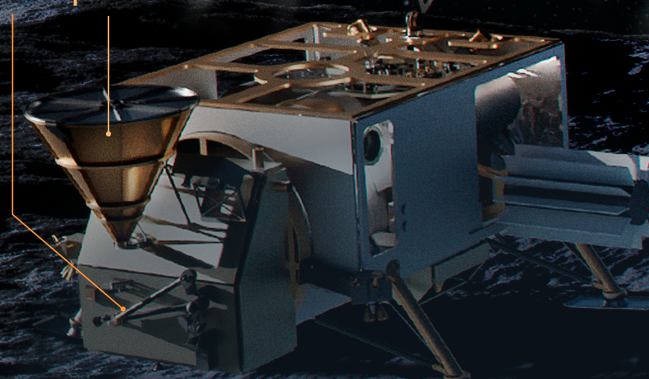
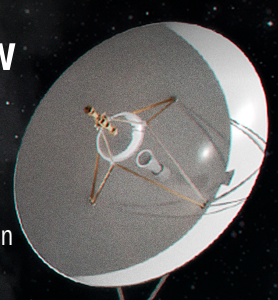
- 8. the structure** of the **jet vents**



Credit: WOW Inc.

Mission Overview

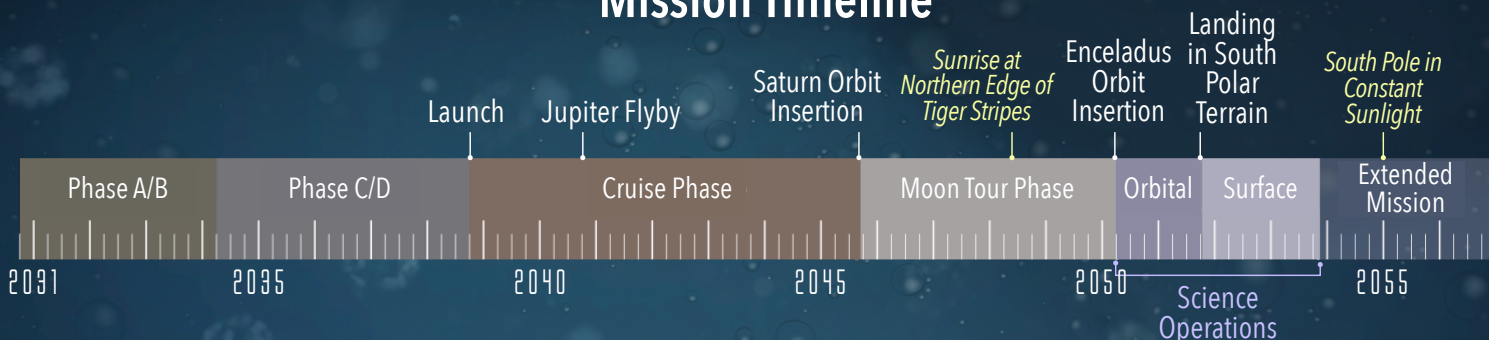
- 13 instruments
- Science Phase 2050 - 2054
- 1.5 Earth-year orbit science; **passive** plume sample collection
- 2 Earth-year surface science; **active & passive** collection



6610 kg launch wet mass | 2690 kg landed | 142 kg science payload

- Powered with 2 Next-Generation RTGs
- Chemical propulsion: $\Delta V > 2400 \text{ m s}^{-1}$
- Enceladus L1/L2 south polar **halo orbit** with autonomous station-keeping
- Deorbit & landing with on-board terrain-relative navigation
- **Ka-band direct-to-Earth** telecom for science (~1 Tb data return capability)
- Cost: \$FY25 2.5B excluding launch vehicle

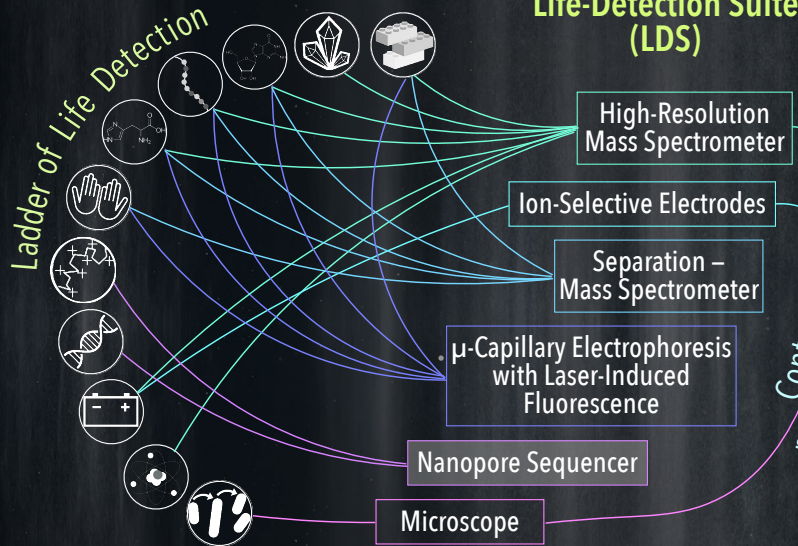
Mission Timeline



Payload

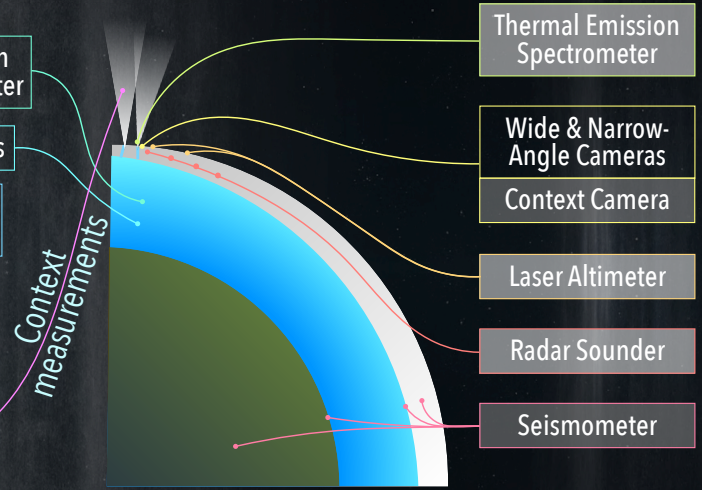
Orbit only | Surface only | Both

Ladder of Life Detection



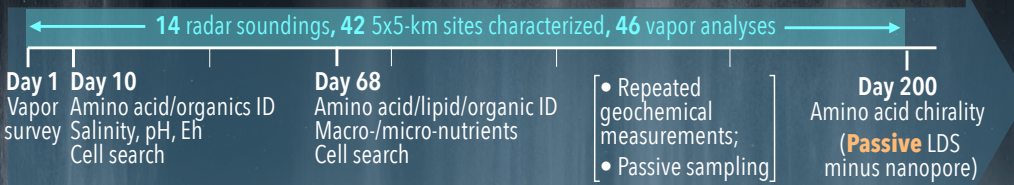
Life-Detection Suite (LDS)

Context Instruments

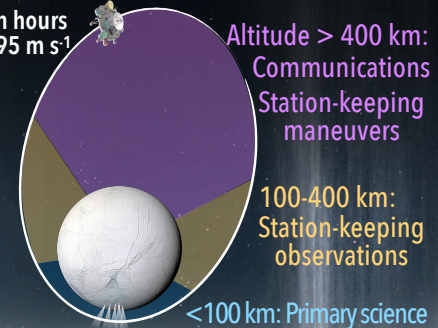


Concept of Operations

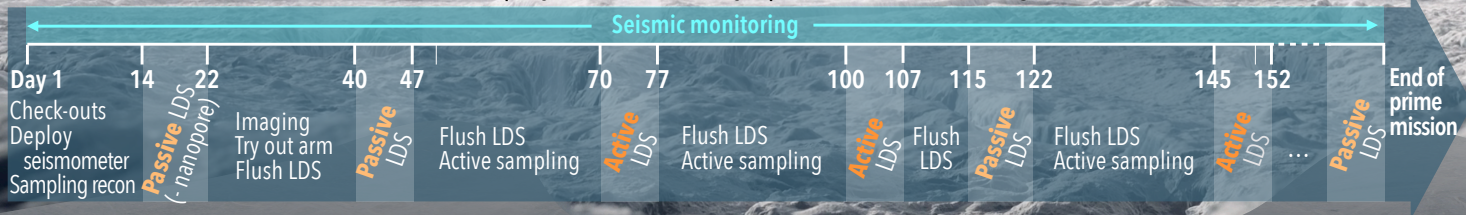
In Enceladus orbit | 1.5 Earth years \approx 550 Earth days | 2.5x schedule margin



Orbital period: 12 Earth hours
Periapsis: 20-70 km, 195 m s⁻¹



On the South Polar Terrain surface | 2 years \approx 730 days | 4.1x schedule margin



Study Team

Science Team

APL Concurrent Engineering Team

PI Shannon MacKenzie | Applied Physics Laboratory

Karen Kirby & Pete Greenauer | Study Leads

Dep. PI Marc Neveu | NASA Goddard Space Flight Center

Helmut Seifert | Project Management

Project Scientist Rob Gold | Applied Physics Laboratory

Ryan Hacala | Payload Systems Engineering

Theme Leads Alfonso Davila | NASA Ames Research Center

Grace Colonell | Systems Engineering

Jonathan Lunine | Cornell University

Amanda Haapala Chalk | Mission Design

Morgan Cable | Jet Propulsion Laboratory

Seth Kijewski, Stewart Bushman | Propulsion

Kate Craft | Applied Physics Laboratory

Rob Coker | Thermal Design

Jennifer Eigenbrode | NASA Goddard Space Flight Center

Erich Schulze | Mechanical Design

Science Co-Is Christopher Glein | Southwest Research Institute

Spencer Brock | Mechanical Configuration Design

Jason Hofgartner | Jet Propulsion Laboratory

Matt Shannon | Telecom & Radiofrequency Design

Christopher McKay | NASA Ames Research Center

Dan Gallagher | Power

Charity Phillips-Lander | Southwest Research Institute

Jeff Boye | Command & Data Handling

Hunter Waite | Southwest Research Institute

John Wirzburger | Guidance, Navigation, & Control

Michelle Chen, Tom Criss, Steve Jenkins, Ryan Mitch, Carolyn Sawyer | Autonomous & Terrain-Relative Navigation

Shyam Bhaskaran (JPL), Ralph Roncoli (JPL) | Navigation

Kim Ord | Mission Operations

Kathy Kha | Cost Evaluation

Stephen Price | Schedule Evaluation

DATA RELEASE, DISTRIBUTION & COST INTERPRETATION STATEMENTS

This document is intended to support the 2023–2032 Planetary Science and Astrobiology Decadal Survey.

The data contained in this document may not be modified in any way.

Cost estimates described or summarized in this document were generated as part of a preliminary concept study, are model-based, assume an APL in-house build, and do not constitute a commitment on the part of APL.

Cost reserves for development and operations were included as prescribed by the NASA ground rules for the Planetary Mission Concept Studies program. Unadjusted estimate totals and cost reserve allocations would be revised as needed in future more-detailed studies as appropriate for the specific cost-risks for a given mission concept.

ACKNOWLEDGMENTS

The Johns Hopkins Applied Physics Laboratory would like to extend a special thank you to all of the team members and to NASA for the opportunity to investigate this mission concept.

The Enceladus Astrobiology Mission Study Team

Science Team					
Shannon MacKenzie	<i>APL</i>	Alex Pathoff	<i>Planetary Science Institute</i>	Hajime Yano	<i>JAXA</i>
Mark Neveu	<i>NASA GSFC</i>	Wes Patterson	<i>APL</i>	Alison Murray	<i>Desert Research Institute</i>
Alfonso Davila	<i>NASA Ames</i>	Frank Postberg	<i>Freie Universität Berlin</i>	Jorge Nunez	<i>APL</i>
Jonathon Lunine	<i>Cornell University</i>	Richard Quinn	<i>NASA Ames</i>	Ariel Anbar	<i>Arizona State University</i>
Rob Gold	<i>APL</i>	Anthony Ricco	<i>NASA Ames</i>	Doug Archer	<i>NASA JSC</i>
Kate Craft	<i>APL</i>	Paul Schenk	<i>Planetary Science Institute</i>	Laurie Barge	<i>JPL Caltech</i>
Morgan Cable	<i>JPL Caltech</i>	Britney Schmidt	<i>Georgia Institute of Technology</i>	John Brucato	<i>National Institute for Astrophysics</i>
Jennifer Eigenbrode	<i>NASA GSFC</i>				
Chris Glein	<i>SwRI</i>	Steve Vance	<i>JPL Caltech</i>	Anna Butterworth	<i>UC Berkley</i>
Jason Hofgartner	<i>JPL Caltech</i>	Steve Vance	<i>JPL Caltech</i>	Ben Clark	<i>Space Science Institute</i>
Chris McKay	<i>NASA Ames</i>	Peter Willis	<i>JPL Caltech</i>	Max Coleman	<i>JPL Caltech</i>
Charity Phillips-Lander	<i>SwRI</i>	Kathryn Bywaters	<i>SETI Institute</i>	Kosuke Fujishima	<i>Tokyo Tech</i>
Hunter Waite	<i>SwRI</i>	Matt Hedman	<i>University of Idaho</i>	Kevin Hand	<i>JPL Caltech</i>
Dana Burton	<i>George Washington University</i>	Jean-Pierre de Vera	<i>DLR</i>	Joern Helbert	<i>DLR</i>
		Chris German	<i>WHOI</i>	Tori Hoehler	<i>NASA Ames</i>
Chris Bradburne	<i>APL</i>	Jen Heldman	<i>NASA Ames</i>	Terry Hurford	<i>NASA GSFC</i>
Will Brinckerhoff	<i>NASA GSFC</i>	Julie Huber	<i>WHOI</i>	Susan Lang	<i>University of South Carolina</i>
Caroline Frissinet	<i>LATMOS</i>	Dana Hurley	<i>APL</i>		
Rob Hodyss	<i>JPL Caltech</i>	Michael Malaska	<i>JPL Caltech</i>	William McKinnon	<i>Washington University, Saint Louis</i>
Sean Hsu	<i>CU Boulder</i>	Michael Manga	<i>UC Berkley</i>		
Sam Kounaves	<i>Tufts University</i>	Alfred McEwan	<i>University of Arizona</i>	Jurgen Schmidt	<i>University of Oulu</i>
Ralph Lorenz	<i>APL</i>	Aaron Noell	<i>JPL Caltech</i>	Yasuhito Sekine	<i>University of Tokyo</i>
Emily Martin	<i>National Air and Space Museum</i>	Mark Perry	<i>APL</i>	Takazo Shibuya	<i>JAMSTEC</i>
		Carolyn Porco	<i>UC Berkley</i>	Tom Spilker	<i>JPL Caltech</i>
Richard Mathies	<i>UC Berkley</i>	Danielle Simkus	<i>NASA GSFC</i>	Ben Teolis	<i>SwRI</i>
Jay Nadeau	<i>Portland State University</i>	Krista Soderlund	<i>University of Texas</i>	Elizabeth Turtle	<i>APL</i>
Mark Panning	<i>JPL Caltech</i>	Linda Spilker	<i>JPL Caltech</i>	Peter Wurz	<i>Universität Bern</i>
Engineering Team					
Pete Greenauer	<i>APL</i>	Dan Gallagher	<i>APL</i>	Carolyn Sawyer	<i>APL</i>
Karen Kirby	<i>APL</i>	Amanda Haapala-Chalk	<i>APL</i>	Erich Schulze	<i>APL</i>
Helmut Seifert	<i>APL</i>	Ryan Hacala	<i>APL</i>	Christopher Scott	<i>APL</i>
Jeff Boye	<i>APL</i>	Steve Jenkins	<i>APL</i>	Matt Shannon	<i>APL</i>
Spencer Brock	<i>APL</i>	Kathy Kha	<i>APL</i>	John Wirzburger	<i>APL</i>
Michelle Chen	<i>APL</i>	Seth Kijewski	<i>APL</i>	Ike Witte	<i>APL</i>
Rob Coker	<i>APL</i>	Ryan Mitch	<i>APL</i>	Shyam Bhaskaran	<i>JPL Caltech</i>
Grace Colonel	<i>APL</i>	Kim Ord	<i>APL</i>	Ralph Roncoli	<i>JPL Caltech</i>
Tom Criss	<i>APL</i>	Stephen Price	<i>APL</i>	Juan Arrieta	<i>Nabla Zero Labs</i>
Doug Crowley	<i>APL</i>				

TABLE OF CONTENTS

1. SCIENTIFIC OBJECTIVES AND TRACEABILITY	1
2. HIGH-LEVEL MISSION CONCEPT	4
2.1. Overview	4
2.2. Summary of Environments	5
2.2.1. Contamination Control and Planetary Protection	5
2.3. Architecture Assessment	5
2.4. Technology Maturity	6
2.5. Key Trades	7
3. TECHNICAL OVERVIEW	8
3.1. Instrument Payload Description	8
3.1.1. Instrument Operations in Orbit	8
3.1.2. Instrument Operations on the Surface	10
3.2. Flight System	11
3.3. Mechanical	12
3.4. Electrical Power	13
3.5. Propulsion	15
3.6. Guidance, Navigation, and Control	15
3.7. Descent and Landing	16
3.8. Avionics	17
3.9. Flight Software	18
3.10. Telecommunications	18
3.11. Thermal	18
3.12. Mission Design and Navigation	19
3.12.1. Launch and Interplanetary Cruise	19
3.12.2. System Capture and Pump-Down	19
3.12.3. Science Orbit	20
3.13. Navigation and Orbital Maintenance	21
3.13.1. Navigating Interplanetary Cruise and Moon Tour	21
3.13.2. Maintaining the Science Orbit	21
3.13.3. Landing	22
3.13.4. Mission Design Parameters and ΔV Budget	22
3.14. Concept of Operations	22
3.15. Risk List	24
4. DEVELOPMENT SCHEDULE AND SCHEDULE CONSTRAINTS	25
4.1. Mission Schedule	25
4.2. Technology Development Plan	25
5. MISSION LIFE-CYCLE COST	26
5.1. Mission Ground Rules and Assumptions	26

5.2.	Cost Benchmarking.....	28
5.3.	Costing Methodology and Basis of Estimate.....	28
5.4.	Confidence and Cost Reserves	29
APPENDIX A. ACRONYMS.....		A-1
APPENDIX B. DESIGN TEAM REPORT		B-1
B.1.	Science Motivation and Detailed Implementation.....	B-1
B.1.1.	Science Questions and Objectives	B-1
B.1.2.	Traceability to Science Payload	B-6
B.1.3.	Sample Collection Strategies.....	B-11
B.1.4.	Concept of Operations.....	B-14
B.2.	Mission Design and Navigation Study Report.....	B-21
B.2.1.	Interplanetary Cruise	B-21
B.2.2.	Pump-Down.....	B-25
B.2.3.	Science Orbit.....	B-25
B.3.	CML 3 Study	B-30
B.3.1.	Architectures and Payloads.....	B-30
B.3.2.	Mission Design and Subsystems.....	B-31
B.3.3.	Selection of Point Design	B-31
B.4.	Costing Methodology and Basis of Estimate.....	B-97
B.4.1.	WBS 1, 2, 3 Project Management, Systems Engineering, Mission Assurance (PM/SE/MA).....	B-97
B.4.2.	WBS 4 Science.....	B-98
B.4.3.	WBS 5 Payload.....	B-98
B.4.4.	WBS 6 Spacecraft.....	B-99
B.4.5.	WBS 7 and 9 Mission Operations (MOps) and Ground Data Systems (GDS)..	B-99
B.4.6.	WBS 8 Launch Vehicle and Services.....	B-100
B.4.7.	WBS 10 Systems Integration and Testing.....	B-100
B.4.8.	Deep Space Network (DSN) Charges	B-100
APPENDIX C. SPECIAL TECHNICAL ANALYSES.....		C-1
C.1.	Autonomous Optical Navigation.....	C-1
C.1.1.	Use of Autonomous Optical Navigation for Stationkeeping.....	C-1
C.2.	Descent and Landing Analysis	C-6
C.2.1.	Use of Terrain Relative Navigation for Descent.....	C-6
C.2.2.	Use of LIDAR for Hazard Detection and Avoidance During Landing.....	C-7
C.3.	Planetary Protection and RTGs	C-10
C.3.1.	Ice Sublimation Rates Due to RTG Heat in Conductive Coupling Cases.....	C-11
C.3.2.	Ice Sublimation Rates Due to RTG Heat, Radiative Coupling Case.....	C-16
C.3.3.	Ensuring planetary protection compliance	C-18
C.4.	Landing Site Contamination During Descent.....	C-18
C.4.1.	Scoop Arm Length.....	C-19
C.4.2.	High cutoff altitude	C-19
C.4.3.	Mobility	C-20
C.4.4.	Descent Maneuver to Land Away from Thruster-Affected Surface.....	C-21

APPENDIX D. ADDITIONAL INFORMATION ON TECHNOLOGIES AND TECHNIQUES.....	D-1
D.1. Instrument Calibration and Data Products.....	D-1
D.1.1. Life Detection Suite	D-1
D.1.2. Reconnaissance and Remote Sensing Suite.....	D-2
D.1.3. In Situ Suite.....	D-2
D.2. Power	D-2
D.3. Thermal Alternatives	D-3
D.4. Risk evaluation definitions	D-3
D.5. Organizational chart.....	D-4
APPENDIX E. REFERENCES	E-1

TABLE OF EXHIBITS

Exhibit 1-1. Science Traceability Matrix (STM).....	3
Exhibit 2-1. Mission phases from launch to end of mission (EOM).....	4
Exhibit 2-2. Summary of lowest TRL items, the assignment rationale, and some examples of development efforts currently underway. Continued support for technological developments like these is encouraged.....	6
Exhibit 2-3. The Enceladus team conducted a number of system-level trades during concept development.....	7
Exhibit 3-1. Modes of the LDS. Passive sample collection drives the cadence of analyses in both orbital and surface phases of the mission. In orbit, it takes longer to build up enough sample, so intermittently conducting a subset of the LDS measurements ensures science return at a reasonable pace. The sample required for each instrument is derived from analogies with terrestrial ocean abundances and described in detail in §B.1.3.1.....	8
Exhibit 3-2. Concept of science operations for the first 200 days of Orbilander’s orbital phase.....	9
Exhibit 3-3. Payload mass, power, and data table. For a detailed description of the data derivation, see §B.1.4.4. The minimum total data shown here represents only the data collected in the first 200 days in orbit and 176 days on the surface.....	10
Exhibit 3-4. Orbitlander configuration, with deployed antenna after landing on Enceladus.....	11
Exhibit 3-5. Enceladus Orbilander block diagram.....	12
Exhibit 3-6. Orbilander mass budget by subsystem.....	13
Exhibit 3-7. Orbilander has sufficient power margins with two NGRTGs.....	13
Exhibit 3-8. Flight system element characteristics table.....	14
Exhibit 3-9. Orbilander mechanical system.....	15
Exhibit 3-10. Orbilander descent and landing strategy. By translating 25 m vertically, Orbilander lands clear of thruster-contaminated surface (§C.4).....	17
Exhibit 3-11. Interplanetary cruise, direct transfer + JGA 2038 launch open trajectory.....	19
Exhibit 3-12. Launch periods for direct transfer with JGA, patched conic analysis. (Other viable interplanetary options exist).....	19
Exhibit 3-13. Period-3 halo orbits about Enceladus. (a) Sample members from L1-family (blue-green) and L2-family (cyan-magenta), where each orbit is plotted with a unique color; (b) L1-family ground-tracks near the south pole, with tiger stripes highlighted in cyan and potential landing target areas (based on high rates of plume fallout) in blue circles. The study team selected a period-3 halo L1 orbit for the Orbilander mission.....	20
Exhibit 3-15. ΔV budget by mission event.....	22
Exhibit 3-14. Mission design table.....	22
Exhibit 3-16. Mission operations and ground data systems table. Enceladus has five major mission phases.....	23
Exhibit 3-17. Enceladus top risks. Risk and consequence likelihoods scale as 1 (very low), 2 (low), 3 (moderate), 4 (high), and 5 (very high). See §D.4 for more detailed definition.....	24

Exhibit 3-18. Enceladus risk matrix. High risks are red; medium risks are yellow; and low risks are green. Full definition of these categories is given in §D.4.....	25
Exhibit 4-1. Orbilander schedule reserves.	25
Exhibit 4-2. Roadmap for nanopore technology development.....	26
Exhibit 4-3. Detailed and high-level schedules. The Orbilander concept has ample funded schedule margin (8.5 months) over the APL-required margin (4.9 months).	27
Exhibit 5-1. Orbilander cost relative to other Flagship-class missions. Missions currently in development or study are denoted with an asterisk.	28
Exhibit 5-2. Estimated Phase A–F Enceladus Orbilander mission costs by level-3 WBS element (FY25\$K).....	29
Exhibit 5-3. Inputs to cost distributions in FY25\$K.	29
Exhibit 5-4. Cost risk analysis and S-curve summary.	30
Exhibit B-1. Complementarity of the life detection investigations.	B-3
Exhibit B-2. Power of geochemical measurements as context for interpreting the life detection search results.	B-4
Exhibit B-3. Instrument characteristics used to model the Life Detection Suite.	B-6
Exhibit B-4. Instrument characteristics used to model the Remote Sensing and Reconnaissance Suite.	B-7
Exhibit B-5. Instrument characteristics used to model the In Situ Suite.....	B-7
Exhibit B-6. Sample requirements for each measurement and instrument of the LDS derived for this study.	B-12
Exhibit B-7. Expected biomass and biopolymer concentration in the Enceladus ocean and in Earth’s ocean.	B-13
Exhibit B-8. Sample reservoirs available in the Enceladus plume.....	B-14
Exhibit B-9. Effect of lower than expected fallout rate on running the LDS. Range of fallout rates from Southworth et al. (2019). We assumed 0.1 mm/Earth year (bold) for this study, but note that the active sampling system increases robustness to lower fallout rates.....	B-16
Exhibit B-10. Planetary protection considerations add two constraints to landing site selection. In addition to the needs for landing at a site of (a) high plume fallback and (b) in view of the Sun (for imaging from orbit and once landed) and Earth (for communications), landing site selection criteria include (c) ice shell thermal conditions away from local maxima ($T_{surf} < 85$ K) and (d.) the presence of sparse boulders indicating that any snowpack is thin. Landing site candidates (1–4) were initially chosen on plume fallout alone; the numeral does not convey preference. Based on available data, landing site 4 meets the additional criteria derived from this analysis. Bottom of maps is 0° longitude. In panel c, black outlines are regions of relatively high surface temperatures identified by Howett et al. (2011). The <i>Cassini</i> CIRS-derived map of T_{surf} (cool colors) and <i>Cassini</i> radar-derived strip map of minimum Q_{endo} are reproduced from Le Gall et al. (2017). T_{surf} in the radar strip are similar to surroundings (<80 K).	B-17
Exhibit B-11. As in Exhibit B-10, but identifying regions satisfying (teal) or precluding (orange) landing site selection criteria in <i>Cassini</i> data. These preliminary identifications can be updated by analyzing <i>Cassini</i> datasets in greater depth and would be refined by Orbilander once in Enceladus orbit. Bottom of maps is 0° longitude.	B-18

Exhibit B-12. Overlap of conditions favorable to (teal) or precluding (orange) suitable landing sites. This preliminary map shows that there exist locations (e.g. near site 4 and North-East of site 3 around latitude -70°) that satisfy these conditions. Not included are considerations of slopes $<10^\circ$, which would be avoided by terrain-relative navigation. Bottom of map is 0° longitude. Landing site candidates (1–4) were initially chosen on plume fallback alone; the numeral does not convey preference. B-19

Exhibit B-13. Configuration of the nanopore system. ¹Considered equivalent to a 12-hour-to-24-hour duration, assuming a maximum 1.1-hour time to translocate 106 bases plus time for sample preparation..... B-20

Exhibit B-14. Schematic representation of a nanopore analysis where translocation events that change the electrical current across a pore are detections of single polymer features, SPF (akin to a base or set of bases of DNA). In the absence of translocation events, the electrical current along the nanopore membrane is constant noise (orange) and not recorded. Only when a translocation event is detected, current values are stored at a rate of 500 kbits/s for the event duration (blue). Since >250 SPFs are translocated per second, 500×10^3 bits/s / 8 bits / 250 SPF/s = 250 8-bit numbers (vertical grey bars) are recorded per SPF. For 106 SPF, the corresponding data stored is 2 Gb (2 kbits/SPF). The statistical time between two polymer detections increases as (analysis time)^{1/2} as the concentration of polymers that have not yet passed through the pore decreases. B-20

Exhibit B-15. Science data returned compared to capability..... B-21

Exhibit B-16. Summary of Optimal Point Solutions for Interplanetary Transfer (results from patched-conic grid search). B-22

Exhibit B-17. Interplanetary cruise broad search results demonstrate a range of options across the mass versus time-of-flight tradespace. Only optimal solutions from the broad search with TOF < 15 years are shown, where optimality is defined as those solutions that are non-dominated in minimizing launch C3, ΔV , arrival V_∞ , and/or TOF. All optimal solutions returned by the grid search are ballistic except for the ΔV -EGA. B-23

Exhibit B-18. Dual Saturn arrival date strategy for 2037 VVE maintains DSM < 50 m/s over a 21-day launch period, launch from 16 Sep 2037 – 06 Oct 2037 (patched-conic analysis)..... B-24

Exhibit B-19. Comparison of launch periods for single- versus dual-arrival 2037 VVE transfer options..... B-24

Exhibit B-20. Estimated TOF and delivered mass to Enceladus orbit, post Enceladus orbit insertion maneuver; VVE option can be accommodated with Falcon Heavy expendable launch vehicle, while 3-year ΔV -EGA and direct+JGA options require SLS Block 2..... B-24

Exhibit B-21. Twenty-four revolutions of an example period-3 L1 halo orbit converged in high-fidelity model offers natural evolution of periapsis altitudes within desired ranges for plume sampling..... B-26

Exhibit B-22. Three stationkeeping strategies are considered for science orbit maintenance. B-27

Exhibit B-23. Schematic demonstrating Stationkeeping Strategy 3 for $N_m = 2$ B-28

Exhibit B-24. Maneuver execution models assumed for stationkeeping analysis B-29

Exhibit B-25. Simulations assuming onboard dynamical model matches truth: Simulation (1) maneuver execution error model 2, Simulation (2) maneuver execution error model 1; red points indicate periapsis-targeting maneuvers, and green points represent apoapsis-targeting maneuvers..... B-29

Exhibit B-26. Limits of detection of Enceladus Flagship life-detection architectures and corresponding probabilities of a conclusive mission astrobiology result.....	B-94
Exhibit B-27. Geophysical context provided by the instrument payload. Interrogating the crust and the interior provides key context for the search for life measurements. The CML-3 version of the Orbilander did not include a TES but the CML-4 version does, increasing its science value.....	B-96
Exhibit B-28. Reservoirs accessed by different architectures.	B-96
Exhibit B-29. Survey results to quantify science value according to Equation 1. Core team responses represented on the left (solid) and collaborator responses are on the right (wavy).....	B-97
Exhibit B-30. Cost versus science value as evaluated by the team.	B-98
Exhibit C-1. Mission phases to utilize autonomous onboard optical navigation.....	C-1
Exhibit C-2. Reuse of sensors for optical navigation phases.	C-1
Exhibit C-4. “Mapped landmark matching concept” from (Johnson et al. 2007).....	C-2
Exhibit C-3. Properties of the Malin Space Science Systems ECAM-M50 imager system.	C-2
Exhibit C-6. Truth trajectory and estimated trajectory in the Enceladus-centered ecliptic J2000 frame.....	C-3
Exhibit C-5. Limb fitting technique from Christian et al. (2015)	C-3
Exhibit C-7. Parameters of the proposed Enceladus autonomous optical navigation system.	C-4
Exhibit C-8. Navigation performance in a notional scenario.	C-4
Exhibit C-9. Parameters of the proposed Enceladus autonomous optical navigation system.	C-5
Exhibit C-10. Range information used in the navigation filter.	C-5
Exhibit C-11. Navigation performance in a more conservative scenario.	C-6
Exhibit C-12. A visualization of an APLNav-type TRN algorithm, shown over the lunar surface. Each camera compares sensed images with rendered images, backing out 3D position estimates.....	C-7
Exhibit C-13. TRN results from an analysis of a simulated lunar landing, showing position error magnitude as a function of altitude and nadir GSD.	C-8
Exhibit C-14. Specifications of the OLA low-energy laser scanning system, from Daly et al. (2017).....	C-8
Exhibit C-15. Example HDA processing steps, from Johnson et al. (2008).....	C-9
Exhibit C-16. Example of the highly sloped terrain of Enceladus, centered at 52.5°E,79.2°S. A 30-m posting DEM derived from photoclinometry is shown, where each pixel is colored by its slope. Regions with slopes over 10°, comprising nearly half the region, are marked in red. Fully ¾ of the terrain has slope over 5°. While a 1-km region is apparent in the figure with entirely <10° slopes, and only a few pixels over 5°, the coarse scale of this DEM may hide local roughness including lander-scale slopes above the threshold. We use this model as a test case as it offers some of the best resolved slopes for Enceladus’ south polar terrain. In reality, Orbilander would target areas further from a tiger stripe (Damascus in this image) to meet the surface temperature and slope landing site criteria. [Image credit: Paul Schenk, LPI]	C-10

Exhibit C-17. Scenarios considered in this assessment of planetary protection compliance and corresponding thermal coupling of the NGRTG with Enceladus ice and/or snow.	C-11
Exhibit C-18. Effect of porosity ϕ on the thermal conductivity k . The solid grey curve is the relationship conservatively adopted here (see text); it yields the lowest, most insulating k at $\phi > 0.55$. However, this expression breaks down for $\phi \geq 0.7$, where several modeling and experimental efforts (other curves and data points) show that $k(\phi=0.7 \text{ to } 0.9) \approx \{10^{-1} \text{ to } 10^{-3}\}k(\phi=0)$. The orange and teal curves show relationships that were only validated in the regimes where the curves are solid. The orange curve is a thermal conductivity in $\text{W m}^{-1} \text{K}^{-1}$ (rather than a decrease factor). Data points of a given color are from the same source as the fit curve of that color.	C-12
Exhibit C-19. Quantities used in determining the fate of a NGRTG conductively coupled to Enceladus ice and/or snow.	C-15
Exhibit C-20. a. Threshold combinations of surface temperature T_{surf} and snowpack thickness D_{snow} with the most conservative insulation due to porosity in the sublimation (black curves) and melting (purple curves) descent regimes. Endogenic fluxes (orange curves) are estimated from T_{surf} at the south pole (lat. -90°) and edge of the SPT (lat. -60°); from these fluxes' depths to the ocean ($T_o = 273 \text{ K}$) are calculated (teal curves). b. Threshold combinations of D_{snow} and insulation (black curves) in the range possible for fresh snow (Exhibit C-18) and corresponding ice shell thicknesses (teal curves) for four values of T_{surf} . c. For combinations of T_{surf} and D_{snow} corresponding to the thick black curve in panel a, RTG depth into the ice shell as a function of time. d. Fraction of the vertical distance to the ocean reached by the RTG in the cases of panel c. e. RTG depth into the ice shell as a function of time for $T_{surf} = 50 \text{ K}$ and various snowpack thicknesses. f. RTG depth into the ice shell as a function of time for $T_{surf} = 80 \text{ K}$ and 70 K and various snowpack porosities (insulations). Unless indicated otherwise, all results are for latitude 90°S (south pole, average Sun elevation 5.5°), the threshold snowpack thickness, and a surface thermal conductivity decreased by a factor 2000 (surface porosity $\geq 65\%$).	C-17
Exhibit C-21. Blast zone area predicted from empirical dependence on lander mass described in Lorenz et al. (2016).	C-19
Exhibit C-22. Amount of ammonia deposited as a function of distance from the surface at which thrusters cutoff.	C-20
Exhibit C-23. Assumed values for calculating ammonia deposition.	C-20
Exhibit D-1. Electrical Power System Block Diagram.	D-3
Exhibit D-2. Risk likelihood.	D-3
Exhibit D-3. Risk consequence.	D-3
Exhibit D-4. Risk assessment.	D-4
Exhibit D-5. Project Organization Structure.	D-4

EXECUTIVE SUMMARY

Whether life exists beyond Earth remains a fundamental question driving our exploration of the Solar System. At Saturn’s moon Enceladus, plumes of oceanic material vented into space allow the investigation of the astrobiological potential of an ocean world, hinted at by *Cassini*, without the necessity of drilling through kilometers of ice crust.

The Enceladus Orbilander is a flagship (\$2.56B in fiscal year 2025 dollars) mission concept created for the 2023–2033 Planetary Science Decadal Survey. Orbilander takes full advantage of the opportunity provided by Enceladus’ plumes to search for signs of life. A single spacecraft both orbits and lands, capturing samples from four distinct reservoirs offered by the plumes. These samples, both particulate and vapor, are then analyzed by the Life Detection Suite (LDS), a set of five instruments conducting complementary and orthogonal biosignature-seeking measurements. To provide the context that specifically enhances interpretation of LDS measurements, geochemical and geophysical investigations are conducted both in orbit and on the surface. These reveal the physio-chemical state of the ocean and core as well as the processes involved in ejection of plume material and how these affect the ocean material analyzed by the LDS.

The Orbilander can be delivered to the Saturn system via several launch vehicle and trajectory options, including a direct trajectory (7-year cruise), a ΔV -EGA trajectory (9-year cruise) and several options using an inner cruise with Venus and Earth flybys (10-year cruise). Upon Saturn Orbit Insertion, a 4-year moon tour pumps down the Orbilander’s orbit to intercept Enceladus. The most optimal arrival times balance the Jupiter flyby opportunities of the late 2030s and solar illumination at the Enceladus high southern latitudes where plume material is most abundant. This mission concept therefore targets project start in 2030.

Upon Enceladus Orbit Insertion, the Orbilander begins a 1.5-year-long campaign of landing site reconnaissance, remote sensing science, and collecting sufficient plume sample to run all but one of the LDS measurements. After successful landing, the Orbilander spends 2 years on the surface conducting multiple LDS measurements with all five instruments on actively and passively collected plume material, as well as seismic investigations. The schedule laid out here is well-defined, but the mission also has operational and resource flexibility should additional reconnaissance be needed.

As part of the design study, mission and development risks were identified and mitigation strategies proposed. Technologies key to achieving the life detection science objectives include instrumentation matured under programs like COLDTech and ICEE-2, such as aspects of the sampling system and microfluidic devices, as well as well-known techniques like high-resolution and separation-capable mass spectrometers. Autonomous onboard navigation is planned to maintain a halo orbit around Enceladus to enable passive sampling from orbit as well as reconnaissance measurements for use in site selection and landing. Terrain relative navigation is included to ensure safe landing, given that targeted areas may contain landing hazards. Continued development of radioisotope thermoelectric generator (RTG) technology and long-life batteries is essential for this long duration mission.

The Enceladus Orbilander represents an optimal point in the trade space of science value versus cost, taking advantage of the extensive knowledge of Enceladus provided by *Cassini*, how well Enceladus lends itself to a search for life in material from its ocean, and the flexibility afforded by the innovative design developed by the APL team. By taking full advantage of Enceladus’ plumes both in orbit and on the surface, Orbilander represents a robust search for life with complementary and orthogonal biosignatures as well as contextual geophysical and geochemical measurements, determining not only whether Enceladus is inhabited (at levels up to 500,000× scarcer than in Earth’s oceans) but also why.

1. SCIENTIFIC OBJECTIVES AND TRACEABILITY

Enceladus, a moon of Saturn only 500 km in diameter, hosts the best-characterized extraterrestrial ocean beneath an icy crust. *Cassini*'s fortuitous investigations indicate that the key elements for habitability—liquid water, CHNOPS, and energy—are co-located at Enceladus: a global ocean (Iess et al. 2014; Patthoff & Kattenhorn 2011; McKinnon 2015; Thomas et al. 2016) mildly alkaline like Earth's (Glein & Waite 2020); organic and salt nutrients (Waite et al. 2009, 2017; Postberg et al. 2011, 2018; Khawaja et al. 2019); and hydrothermal activity providing chemical energy (Hsu et al. 2015; Waite et al. 2017). This tantalizing evidence begs the question:

Is Enceladus inhabited? A convincing answer requires searching for multiple features of life (biosignatures) with repeatable measurements (e.g. Neveu et al. 2018). Organic biosignatures detectable at trace levels with high-TRL instruments are of special interest and well-motivated by *Cassini*'s detections of numerous organic species. Beyond the search for specific biomolecules, they indicate how far organic chemistry has progressed. The Orbilander science objectives thus include three organic biosignatures.

1. Characterize the bulk organic fraction of plume materials. Life generates structurally and chemically complex organic compounds. The complexity of organic molecules can be measured on the basis of the number of chemical steps needed to generate each molecule in the pool of detected organic compounds. This "Pathway Complexity Index" can reveal whether the level of molecular complexity in the organic fraction of a sample is the result of abiotic or biochemically driven processes (Marshall et al. 2017). A survey of the plume particulate content with high-resolution ($m/\Delta m \geq 10^4$) mass spectrometry with a sensitivity range of ≥ 1000 Da and relative abundance precision of 20% would provide the data necessary to determine the Pathway Complexity Index and build a context inventory of organic species that can be compared to known biotic and abiotic distributions.

2. Characterize amino acids. The relative concentrations of amino acids derived from biotic sources reflect life's preference for specific molecules based on the functional roles they can perform, whereas abiotic amino acids exhibit patterns dominated by easily formed, low-formation-energy molecules (Dorn et al. 2011). An excess of one enantiomer¹ can also indicate biological processing, as suggested by the preference toward L-amino acids in Earth life (Glavin et al. 2019). These measurements require distinguishing the relative molar abundances of glycine and enantiomers of at least four other L/D-amino acids (including both abiotic and biotic representatives) to an accuracy of $\leq 10\%$ (Europa Lander SDT, 2017).

3. Characterize lipids. As with amino acids, the distribution abundance pattern of lipids as a function of carbon chain-length can be used to discriminate between abiotic and biotic sources (Summons et al. 2008; Georgiou & Deamer 2014). Lipids and/or their hydrocarbon derivatives can persist in the environment over geologic time, being resilient to degradation by, e.g., heat or water (Eigenbrode et al. 2008). To detect lipids and discern structural and abundance patterns, the relative molar abundance of molecules up to ≥ 500 Da must be determined with $\leq 20\%$ accuracy.

Multiple, independent measurements of molecular qualities in different organic compounds are a sound and often recommended life detection strategy (ELS DT 2017; NASEM 2019). To further reduce uncertainty on the sources of these compounds, Orbilander has two high-risk, high-reward objectives:

4. Search for a polyelectrolyte. The reliance on a polymer with repeating charge (polyelectrolyte) as a means to store and pass on genetic information could be a universal feature of life (Benner 2017). Nanopore technology has emerged as a powerful tool to detect polyelectrolytes at very low abundances and with minimal sample preparation but is currently in the early stages of space-qualified development (Carr et al. 2017; Sutton et al. 2019). The presence of a polyelectrolyte in a sample from Enceladus would be difficult to refute as evidence for life. Any contamination can be screened based on similarities to terran DNA/RNA, which are unlikely to be the exact same products of molecular evolution on Enceladus. Beyond "just" detecting life, this measurement may begin to crack the code of extraterrestrial genetic

¹ Enantiomers are chiral molecules that are mirror images of each other, such as L/D-amino acids.

sequences which, together with chemical context, could offer insight into how any life found on Enceladus operates from molecular to biosphere scales.

5. Search for any cell-like morphologies. Morphologies resembling cells can serve as a strong biosignature when collocated with chemical activity like autofluorescence (Bhartia et al. 2010; Europa Lander SDT 2017; Nadeau et al. 2016, 2018). Microscopes able to resolve non-icy particles $<0.2 \mu\text{m}$ in diameter are of relatively high technology readiness. There is risk in that the fraction of (dead or alive) cells whose morphological integrity survives plume ejection is uncertain; preliminary experiments suggest percent-level preservation (Bywaters et al. 2020).

We strongly encourage further development of these technologies but do not recommend stalling an Enceladus mission should development be slower than anticipated. A compelling search-for-life mission is possible with technology currently at or above TRL 4.

The Orbilander is designed to detect life from orbit at levels $\sim 500\times$ scarcer than in Earth's oceans from orbit, and from the surface at levels $\sim 500,000\times$ scarcer than in Earth's oceans (§B.1.3.1). Life at these detection levels can be sustained by Enceladus' supply of energy and CHNOPS determined from *Cassini* data.

To what extent is Enceladus' ocean able to sustain life and why? The objectives below provide key geochemical and geophysical context for life detection in two ways. First, they quantify the biomass that Enceladus can theoretically support. Second, they help determine how the plume samples may have changed since synthesis in the ocean through ascent and ejection, thereby allowing the inference of sub-surface conditions from plume measurements.

6. Physical and chemical environment. Quantifying the pH, temperature, salinity, and the availability of nutrients and energy sources in the ocean constrains how much biomass it can support and therefore how much biological signal one might expect in the ocean (e.g. Cable et al. 2020). Such measurements require mass spectrometers capable of measuring carbonate and oxidant species (at 20% precision) and/or ion-selective electrodes (e.g. Glein & Waite 2020).

7. Internal structure. Geochemical factors are closely associated with the structure and dynamics of the interior and crust. For example, the rate at which water-rock interactions produce chemical disequilibria depends on local pressures and temperatures (e.g. Vance et al. 2016). Seismic monitoring over several Enceladus days reveals the structure and dynamics of the core, crust, and ocean (Vance et al. 2018).

8. Vent structures. Understanding the delivery of oceanic material through the vents and into space is essential for understanding whether and how this process affects the geochemical and astrobiological investigations. The shape of the vents and geomorphology of the plume source region can be measured with altimetry and stereo imaging at sub-meter scales. Very-high-frequency radar sounding of the ice crust reveals the nature of the subsurface plumbing in the crust.

Whether or not Enceladus is found to be inhabited, Orbilander measurements will conclusively tell us why (§B.1.1.2).

Where should we land? Actively sample? A landing site is scientifically compelling if it has a high enough fallout rate of plume material to allow sufficient passive sample collection within the landed mission duration ($>0.01 \text{ mm/yr}$ for the Orbilander Life Detection Suite). A safe landing site requires rigid enough regolith to support the weight of Orbilander. This is inferred by the presence of meter-sized boulders in the vicinity (anticipated based on the observations of larger boulders in the *Cassini* data, Martens et al. 2015). To meet planetary protection requirements in off-nominal landing scenarios, landing sites must have surface temperatures $<85 \text{ K}$ (§C.3). The Orbilander's direct to Earth (DTE) communications system precludes landing in a valley. To avoid tipping, $<10^\circ$ slopes are required. *Cassini* data suggest that multiple acceptable sites (§B.1.4.2). The combination of laser altimetry, imaging, and thermal emission spectroscopy would allow validation of these areas and the search for sites in the large amount of south polar terrain not adequately covered by *Cassini*.

Science Goal	Science Objective	Measurement	Instrument Type*	Functional Requirement
Is Enceladus inhabited?	1. Characterize the bulk organic fraction of volatile and nonvolatile plume materials	1A. Molecular weight distribution of organic matter from 16 Da (CH ₄) to ≥1000 Da in plume vapor and icy particles 1B. Relative abundance and diversity of organic functional groups, including whole molecules, molecular fragments and compounds potentially indicative of life such as hopanes 1C. ¹³ C/ ¹² C abundances of CO ₂ , CO, and CH ₃ -type molecular fragments	HRMS; μCE-LIF	0.0005 (HRMS) μL vapor samples; gas inlet; plume fly-throughs at altitudes ≥ 40 km for vapor; 0.0005 (HRMS) – 15 (μCE-LIF) μL ice grain samples; ice grain collection at altitudes < 40 km and on the surface
	2. Characterize the amino-acid composition of plume materials	2A. Relative molar abundances of amino acid (a.a.) isomers, including at least Gly and four of: Ala, Asp, Glu, His, Leu, Ser, Val, Iva, beta-Ala, γ-aminobutyric acid, and AIB, with at least one abiotic and biotic representative, at accuracy ≤ 10% 2B. Relative molar abundances of L- and D-enantiomers of a.a. with molecular mass b/w D/L-Ala (71 Da) and D/L-Glu (129 Da), including ≥2 among Ala, Val, and β-amino-n-butyric acid, ≥3 proteinogenic and 1 abiotic a.a., and histidine at accuracy ≤ 10%	SMS; μCE-LIF	15 (μCE-LIF) – 400 (SMS) μL ice grain samples; ice grain collection at altitudes < 40 km and on the surface
	3. Characterize the lipid composition of plume materials	3A. Relative molar abundances, composition, and commonalities of compounds that define subsets of long-chain aliphatic hydrocarbons (e.g. carboxylic acids, fatty acids, (un)saturated hydrocarbon chains) up to 500 Da at accuracy ≤ 20%		15 (μCE-LIF) – 100 (SMS) μL ice grain samples; ice grain collection at altitudes < 40 km and on the surface
	4. Search for evidence of a genetic biopolymer in plume materials	4A. Presence of a polyelectrolyte (polymer with a repeating charge in its backbone)	Nanopore	10 mL ice grain samples; ice grain collection on the surface
	5. Search for evidence of cells in plume materials	5A. Morphology (size, shape, and aspect ratio) of non-icy particles as small as 0.2 μm in diameter. 5B. Organic content (e.g. native autofluorescence) associated with non-icy particles	Microscope	1 μL ice grain samples; ice grain collection at altitudes < 40 km and on the surface
To what extent is Enceladus ocean able to sustain life and why?	6.1. Determine the physical/chemical environment of the ocean: Ocean pH	6.1A. Hydrogen ion concentration 6.1B. Abundances of CO ₂ , and bicarbonate or carbonate; relative abundances of all organic and inorganic species (e.g. Cl-containing compounds, carbonates, sulfates, metal hydroxides, silica, and silicates)	ESA HRMS	Ice grain collection at altitudes < 40 km and on the surface 0.0005 (HRMS) μL vapor and ice grain samples (see 1A–1C)
	6.2. Determine the physical/chemical environment of the ocean: Ocean temperature	6.2A. Relative abundances of D/H of H ₂ , D/H of H ₂ O, and ethylene/ethane 6.2B. Relative abundances of bulk organic and inorganic species (e.g. Cl-containing compounds, carbonates, sulfates, metal hydroxides, silica, and silicates) with masses ≤ 500 Da	HRMS	0.0005 (HRMS) μL vapor and ice grain samples (see 1A–1C)
	6.3. Determine the physical/chemical environment of the ocean: Ocean salinity	6.3A. Conductivity of plume materials 6.3B. Abundance of Na, Cl ions	ESA; HRMS	0.0005 (HRMS) –15 (ESA) μL ice grain samples (see 1A–1C)
	6.4. Determine the physical/chemical environment of the ocean: Sources of nutrients and energy	6.4A. Presence and relative abundances of CHNOPS-bearing compounds (including H ₂) in plume materials and other micronutrients (e.g. Ca, Mg, and Fe) 6.4B. Redox potential (Eh) 6.4C. Abundances of oxidants (e.g. SO ₄ ²⁻ , CO ₂ or HCO ₃ ⁻ , NO ₃ ⁻ , O ₂) and reductants (e.g. H ₂ S, CH ₄ , NH ₃ or NH ₄ ⁺ , H ₂) 6.4D. Presence and relative abundances of products of radiolytic decomposition of surface water ice	HRMS; ESA	0.0005 (HRMS) – 75 (ESA) μL ice grain samples (see 1A–1C)
	7. Determine the physical/chemical environment of the ocean: Structure, dynamics, and evolution of the interior	7A. Body-wave arrival times 7B. Tide-induced displacement 7C. Free oscillations 7D. Abundances of noble gases (especially ⁴⁰ Ar), K, D/H, and ¹⁶ O/ ¹⁸ O	Seismometer HRMS	Surface operations over at least 5 Enceladus days 0.0005 (HRMS) μL vapor
	8.1. Characterize the structure and dynamics of the crust	8.1A. Presence of fluid reservoirs or structural heterogeneities	Seismometer; Radar sounder; Gravity science	Surface operations over at least 5 Enceladus days; Polar orbit
		8.1B. Regional thickness of the ice crust in the south polar terrain	Laser altimeter	Polar orbit
		8.1C. Regional topography of the south polar terrain	Laser altimeter, Gravity science	Polar orbit
		8.1D. Love numbers, h ₁ , h ₂ , l ₂ , and k ₂ to 0.1%		
	8.2. Infer ascent and freezing conditions	8.2A. Composition of plume grains at various altitudes and mean anomalies	HRMS; ESA	0.0005 (HRMS) μL vapor and ice grain samples acquired at different mean anomalies
		8.2B. Rate of plume deposition	Fallout collector	Surface operations
	8.3. Determine the physical structure of the jet vent openings	8.3A. Thermal emission spectra at wavelengths 10–50 μm	TES	Polar orbit; repeat ground tracks over illuminated surfaces
		8.3B. Surface topography near the vents at sub-meter horizontal, 10-cm vertical resolution	NAC; Laser altimeter	Polar orbit; repeat ground tracks over illuminated surfaces
		8.3C. Location and extent of liquid-filled pockets in the south polar terrain	Radar sounder; Seismometer	Polar orbit, at least 10-m vertical resolution, ≤40-km swaths; Surface operations over at least 5 Enceladus days
8.3D. Horizontal and vertical surface displacement at sub-meter spatial resolution, 10-cm vertical resolution		Laser altimeter	Polar orbit; repeat ground tracks over illuminated surfaces	
Where should we land? Actively sample?	Reconnaissance for safe landing and active sampling	9A. Sub-meter stereo imagery 9B. Sub-meter altimetry 9C. Temperature maps ΔK~1 K 9D. High phase images of the plumes 9E. Color, stereo imaging of the active sampling area	NAC; WAC Laser altimeter TES NAC Context imager	Polar orbit; repeat ground tracks over illuminated surfaces Polar orbit; repeat ground tracks over illuminated surfaces Polar orbit; repeat ground tracks over illuminated surfaces Science operations during moon tour At least mm resolution, stereo overlapping FOV

*HRMS, high-resolution mass spectrometer; μCE-LIF, microcapillary electrophoresis with laser-induced fluorescence; SMS, separation mass spectrometer; ESA, electrochemical sensor array; TES, thermal emission spectrometer; NAC, narrow angle camera; WAC, wide angle camera (one of the 2 navigation cameras co-boresighted with the NAC)

Exhibit 1-1. Science Traceability Matrix (STM).

A scientifically compelling site for active sample collection will be determined via context imaging following the strategy outlined for the Europa Lander (ELSDT 2017); tailoring these requirements for the Enceladus environment should be revisited in subsequent study.

Exhibit 1-1 summarizes how these science objectives trace to a notional instrument type and mission requirements, further detailed in §B.1.2.

2. HIGH-LEVEL MISSION CONCEPT

2.1. Overview

In support of the Planetary Science and Astrobiology 2023–2033 Decadal Survey, an experienced team of engineers and scientists at the Johns Hopkins University Applied Physics Laboratory (APL) evaluated alternative mission architectures to achieve the science objectives described in §1. The study team first performed a CML 3 trade study comparing and contrasting cost, risk, and performance for several mission architectures, including a suite of orbital and landed options (see §2.3 and §B.3). Metrics developed by the science team were used to assess science return per dollar for each of these options. The science team concluded that the architecture in which a spacecraft first orbits then lands on Enceladus, the Orbilander, represents the optimal solution. The enhanced science return of sampling plume ejecta in orbit (smaller particles and gas) and on the surface (larger particles) was more efficiently achieved with the Orbilander than with two elements.

This report focuses on the results of the second phase of the study, in which the team developed a CML 4 point solution for the Orbilander mission concept. This solution demonstrates a detailed mission concept that 1) is technically feasible, 2) fully addresses the science objectives, and 3) minimizes risk and cost of implementation. We therefore present Orbilander as the recommended Flagship-class mission concept for exploring Enceladus. Mission and spacecraft design features of the Orbilander mission concept include:

- Launch in Oct 2038 with backup Nov 2039, direct trajectory with launch energy C3: 106.6 km²/s²
- **Science Phase 2050–2054**
 - **Enceladus halo orbit** with autonomous stationkeeping enables low-altitude south pole passes
 - **1.5-year orbit science; passive** plume sample collection
 - **2-year surface science; active and passive** sample collection
- 6610 kg wet mass at launch, 2690 kg landed mass, 142 kg unmarginated science payload
- Powered with two Next-Generation RTGs (NGRTGs)
- **Chemical** propulsion provides $\Delta V > 2400$ m/s as well as deorbit and landing maneuvers with onboard terrain navigation and hazard avoidance
- **Ka-band** downlink provides capability of 1.1 Tbits of total mission science data return
- **Cost: \$2.56B in fiscal year 2025 dollars** (excluding the launch vehicle)

The major mission phases—cruise, Saturn orbit pump down, Enceladus orbit, and surface operations—are described in Exhibit 2-1.

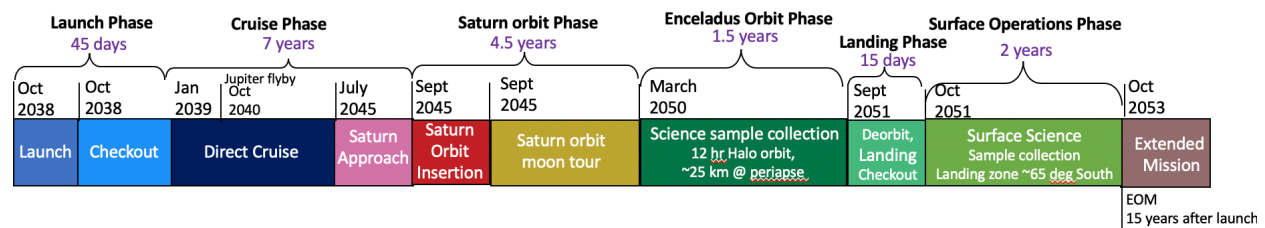


Exhibit 2-1. Mission phases from launch to end of mission (EOM).

2.2. Summary of Environments

The spacecraft is designed for the cold saturnian environment at 10 AU solar distance. The solar load at Saturn is 15 W/m². The Enceladus thermal load is 5.0 W/m² at the tiger stripes (from which the plumes emanate) and 0.3 W/m² elsewhere. The thermal design assumes that the sun elevation angle is 6° and the surface temperature of Enceladus is 100 K at the tiger stripes and 63 K elsewhere. In orbit, as a cold case, the moon's infrared temperature is taken as 63 K and its albedo as 0.75.

Radiation is not a significant design driver for the mission, given the relatively benign saturnian environment: using the SATRAD model (Garrett et al. 2005) for 4 years in Saturn's magnetosphere including an RDM of 2 leads to a TID requirement of 100 krad behind 100 mils of Al. The spacecraft will be exposed to additional moderate levels of radiation during cruise and Jupiter flyby as well as from the RTGs. Radiation dose for the mission will be assessed in detail and appropriate shielding provided for all sensitive components. Robust mass margin included in the study can be applied to increase shielding if needed.

2.2.1. Contamination Control and Planetary Protection

To meet the limits of detection of the science payload, the mission must be designed to minimize and characterize contamination by terrestrial organisms. Contamination Control thus places more stringent requirements on the mission than Planetary Protection concerns of forward contamination. The Enceladus Orbilander mission is classified as a Category IV mission because Enceladus is “of significant interest relative to the process of chemical evolution and/or the origin of life” and landing must minimize the likelihood of “contamination [of the surface] by the spacecraft that could compromise future investigations” (NPR 8020.12D²).

The project team developing this mission would demonstrate a probability $< 1 \times 10^{-4}$ contamination of liquid ocean. Provisions and mitigations for planetary protection would include use of cleanrooms and ISO class 7 protocols, monitoring and sample collection, material control plans, bakeouts, sterilization from radiation, UV and Saturn magnetosphere exposure, and use of a biobarrier during final processing through launch to eliminate as many sources of contaminants as possible from the spacecraft. A biobarrier concept is currently under development funded by a COLDTech grant (Gold et al. 2019), and implementation of this biobarrier is included in the cost estimate for this mission concept.

2.3. Architecture Assessment

In addition to the Orbilander, the team evaluated three mission architectures: (A) a large orbiter with a small lander, (B) a large lander with a small orbiter, and (C) an orbiting science laboratory. Options A and B each had a separable lander while the orbiter remained in orbit to act as a data relay to Earth. The small lander of Option A was a ballistic lander with a single instrument science payload that had a 15-day surface life (limited by battery power). LDS analysis was therefore limited to the orbiter. Option B distributed the science payload (LDS and in situ suite on lander; remote sensing and reconnaissance on orbiter), but required duplicate hardware and subsystems and a separation system. The science return of Option B could conceivably be higher than the Orbilander. However, the increased technical complexity and cost outweighed the potential benefits, especially given Orbilander's robust concept of operations (ConOps) for low downlink rates (§3.14, §B.1.4). While Option C had the least overall mission risk at the lowest estimated cost, it also had the lowest relative science return because it was the only option to not investigate the surface in situ. The Orbilander was thus chosen as the balance between maximizing science return and minimizing complexity and cost. See §B.3 for additional details of the architecture options and selection criteria.

² https://nodis3.gsfc.nasa.gov/displayDir.cfm?Internal_ID=N_PR_8020_012D_&page_name=Chapter1

2.4. Technology Maturity

The team assessed technology items currently under development that have application to the mission objectives. Several enabling technologies are included in the point design. The cost estimate (§5) includes technology development costs for items with TRL ≤ 5 , and the schedule includes maturation plans. Where possible, fallback options are included for the items at maturity levels below TRL 6. The lowest TRL items are key elements of the science payload—the nanopore sequencer and the sample receptacle and processing unit—and are thus discussed below in detail. There are several other technologies at or below TRL 5 that have a development effort funded through various grants and/or proposals (Exhibit 2-2).

Item	TRL	TRL Rationale	Example Development Efforts
Nanopore sequencer	2	Synthetic nanopores still under development; sample handling and prep still under development; several efforts underway (both for terrestrial and spaceflight use)	Carr, MIT (PICASSO 80NSSC18K1545); McKay, NASA Ames (COLDTech 80NSSC19K1028); commercial and academic efforts
Active sample collection and receptacle	3	High heritage scoops exist, but development needed to address Enceladus-specific environment; other options, e.g. rasp, drill, and/or pneumatic transfer, in development	<i>Scoops: Phoenix, Honeybee; Europa Lander scoop, JPL Raps: Badescu et al. (2019), JPL Pneumatic transfer: Zachny, Honeybee (SBIR 80NSSC20C0006; COLDTech, 80HQTR17C0006)</i>
Sample transfer and processing	5	Microfluidic systems in development, but instrument interfaces and specific implementation for Orbilander payload required	Zhong, JPL (PICASSO, 18-PICASSO18_2-0106); Short, SRI (PICASSO, 80NSSC17K0096); Malespin, NASA GSFC (ICEE2); Ricco, NASA Ames (PICASSO); COLDTech (NNX17AK36G); Bourouiba, MIT (PICASSO, 80NSSC20K1092)
Passive sample collection and receptacle	5	Specific implementation for Enceladus environment designed and developed, but flight-qualifying tests remain	Adams, APL (COLDTech 80NSSC17K0618; NNX17AF48G)
μ CE-LIF	5	Specific implementation for Enceladus environment designed and developed, but flight-qualifying tests remain	Mathies, UC Berkley (ICEE-2 80NSSC17K0600; MatISSE 80NSSC19K0616); Stockton (NNX15AM98G; NNX16AM82H); Cramer et al. (2016, 2018), JPL (PICASSO)
Microscope	5	Systems in development, but flight-qualifying tests remain	Nadeau, Portland State University (ICEE-2 80NSSC19M0122); Bedrossian et al. (2017)
Biobarrier for launch	5	Systems in development, but flight-qualifying tests remain	APL/GSFC/NASA Ames HQ funding; Gold et al. (2019)
Autonomous optical navigation	3	SMART Nav (TRL 6, although application would be different); Autonav, optical velocimetry; landmark tracking; see §C.1	<i>OSIRIS-REx; DART; Dragonfly; Mars 2020</i>
Terrain relative navigation (TRN)	6	Descent phase using TRN; hazard avoidance using LIDAR; see §C.2.	<i>ALHAT; RLL-DP; DART; Dragonfly</i>

Exhibit 2-2. Summary of lowest TRL items, the assignment rationale, and some examples of development efforts currently underway. Continued support for technological developments like these is encouraged.

The Life Detection Suite largely consists of instrument types that have previously flown and require tailoring to the Orbilander-specific requirements, including the mass spectrometers (HRMS, SMS) and the ESA. Development is currently on track to be TRL 6 for μ CE-LIF and microscope systems under programs like COLDTech, PICASSO, and MatISSE; Orbilander also carries schedule to accommodate this development.

The nanopore sequencer requires the most development. The technology exists for detecting the presence of a biopolymer and sequencing but is not yet flight-qualified for autonomous *in situ* use (TRL 2). Oxford Nanopore Technologies' MinION™ nanopore sequencer, for example, has been successfully operated on the International Space Station (Castro-Wallace et al. 2017) and during parabolic flights of varying simulated gravity (Carr et al. 2020). However, the MinION™ relies upon biological nanopores that degrade over timescales of months that are tuned to terrestrial polyelectrolytes. For long-duration *in situ* missions to environments with planetary protection concerns, an autonomous biopolymer sequencing capability would require both synthetic nanopores and a biologic-free workflow. Synthetic nanopores are currently in development (e.g. Bywaters et al. 2017) for application both in spaceflight and terrestrial investigations, but currently no synthetic nanopore sequencing systems are in commercial use.

For the purposes of the CML 4 study, the Orbilander active sample collector and receptacle are based on those of *Phoenix* at Mars. In practice, the unique surface characteristics of Enceladus require a unique solution. The collector may be a scoop (as modeled here), a rasp (as on the Europa Lander mission concept; also in development for Enceladus, Badescu et al. 2019), or a drill (as on *Dragonfly*). The receptacle may instead be a pneumatic system like on *Dragonfly* but modified for an airless body (as is being developed for the Moon). Development and test in a flight-like environment is planned in Phases A and B.

The Orbilander subsystems include typical engineering development for the mission and do not require technology development. The autonomous navigation algorithms would benefit from early simulations to perform a trade study comparing algorithm options, and to reduce risk during development. The biobarrier for the launch vehicle is assumed to be developed to TRL 6 under a COLDTech grant. The project cost and schedule estimates assume continuation of the COLDTech technology demonstrations into a full implementation of the biobarrier. The same assumption is made for the sample collection, transfer, and processing systems that are currently under development as part of existing COLDTech grants. The schedule includes additional time in Pre-Phase A to accommodate integration and tailoring of the different sampling processing systems currently in development for specific implementation on the Orbilander.

2.5. Key Trades

The study team assessed options for all major design decisions and selected the best approach for the mission concept using a combination of mission performance requirements and engineering judgement of the technical benefit, cost, schedule, and risk trade-offs. Major system and subsystem design decisions are

Trade Study	Options Considered	Selected Approach	Rationale
Spacecraft orientation	Spin stabilized 3-axis stabilized	3-axis stabilized	3-axis control required for significant portions of the orbit, science collection, telecom, and landing. Spinning is an option for cruise only.
Attitude control system	Reaction wheels Thrusters	Reaction wheels	Significant propellant savings to use reaction wheels. Reaction wheels meet required pointing performance.
Propulsion	Electric propulsion Chemical propulsion	Chemical propulsion using bi-propellants	Most mass-efficient solution and simplest approach. Provides the most science payload to Enceladus orbit.
Mechanical configuration	Landing legs Landing legs plus pallet	Landing legs	Most robust solution considering range of predicted surface characteristics.
Power source	Solar arrays RTG power source	NGRTG 16-GPHS variant	Most mass-efficient solution for providing power at Saturn distance. Enables landing without staging for simple, lowest risk solution.
High-gain antenna (HGA)	Parabolic dish Antenna array	2.1-m parabolic dish HGA	Most mass-efficient solution for data return to meet science needs.
Telecom band	X-band only vs. Dual X and Ka-band	X-band for 2-way and Ka-band for science data return	Small mass and cost increase for benefit of significant improvement in science data return.
Autonomous stationkeeping	Optical nav processing in avionics or stand-alone package	Opnav in avionics coprocessor	Most mass- and power-efficient solution; meets performance reqs. and uses common sensors for landing and stationkeeping.
Trajectory design	Inner cruise Direct with Jupiter flyby Direct without flybys	Direct with Jupiter flyby	Direct trajectory with Jupiter balances most mass-efficient solution with anticipated achievable launch vehicle C3.
Contamination control and planetary protection	Cleanliness protocols Pre-launch Sampling Biobarrier in LV	Cleanliness protocols, sampling and biobarrier	All cleanliness protocols will be used to reduce bioburden to acceptable levels; sampling during I&T and biobarrier use on the launch vehicle.
Launch vehicle	Falcon Heavy Exp SLS B2 w/CASTOR30B SLS B2 w/Star48 SLS B2 w/Centaur Atlas V551	SLS Block 2 with CASTOR30B upper stage Alternate option: Falcon Heavy Expendable	SLS with high C3 enables direct trajectory w/Jupiter flyby to shorten transit time to Saturn. FHE with C3=41 offers low-cost alternate with modified thermal design for inner cruise to use Venus flybys in place of the high C3.

Exhibit 2-3. The Enceladus team conducted a number of system-level trades during concept development.

described in Exhibit 2-3. Future trades include autonomous navigation implementation approach, interplanetary and moon tour trajectory optimization (§B.2), surface sample collection architecture (scoop vs.

drill), options for sample transfer system, propulsion system propellant management device (PMD) design, and NAC options.

3. TECHNICAL OVERVIEW

3.1. Instrument Payload Description

The candidate payload is selected to meet the requirements of the Science Traceability Matrix while also satisfying additional mission constraints such as total mass and power consumption (Exhibit 3-3). The candidate instruments are based on recently flown hardware with the needed capabilities wherever possible. However, some instruments would require some modifications to meet the environmental conditions, sensitivities, fields of view, etc. For these instruments, the listed characteristics and TRLs reflect the engineering judgements of experienced space instrument builders. Other instruments are currently being developed under various funding streams. For these instruments, the values for mass, power, and other characteristics have a larger uncertainty.

The payload consists of three instrument suites and the sampling system. The **Life Detection Suite (LDS)** includes instruments of overlapping and complementary capabilities to provide a robust search for biosignatures (§B.1). The **Remote Sensing and Reconnaissance Suite (RSRS)** surveys the surface and subsurface of Enceladus from orbit. Together these data provide insight into the physical nature of the vents and south polar terrain, necessary both for landing and understanding plume ejection mechanics. The **In Situ Suite** surveys the surface and subsurface of Enceladus while landed. §B.1.4.4 details the traceability from the science objectives to the payload and a

description of the instrument calibration procedures and data products is given in §D.1. The **Sampling System (SS)** is responsible for (1) collecting sufficient volumes of plume samples, (2) delivering the sample to the science payload, (3) processing the sample in preparation for the LDS analyses, (4) delivering the processed product to the LDS, and (5) flushing the system in between analyses to minimize cross-sample contamination. These steps are detailed in §B.1.2.4.

The science operations described here demonstrate that measurement activities, including instrument calibrations, can be scheduled such that the total instantaneous power at any given time is below 100 W and that an average science data rate of 40 kbps is adequate to return all science data in a timely manner within Phase E (see also §B.1.4).

3.1.1. Instrument Operations in Orbit

In orbit, the LDS is run in three notional modes, based on sample volume requirements and complementarity of the measurements. In LDS Mode A (LDS-A), Orbilander’s first interrogation of the plume ice

		Orbital Modes			Surface Modes	
		LDS-A	LDS-B	LDS-C	LDS Contingency	LDS Full
Sample required (µL)	HRMS				0.0005	0.0005
	SMS		100	400	500	500
	µCE-LIF	15		15	15	15
	ESA	15	76.5		91.5	91.5
	Microscope	1	1		1	1
	Nanopore					10000
	Total (µL)	31	178	415	606	10606
Sample collection	Passive in orbit (orbits)	20	111	130		
	Passive on surface (Earth days)				22.1	387.1
	Active on surface (scoops)				1	2

Exhibit 3-1. Modes of the LDS. Passive sample collection drives the cadence of analyses in both orbital and surface phases of the mission. In orbit, it takes longer to build up enough sample, so intermittently conducting a subset of the LDS measurements ensures science return at a reasonable pace. The sample required for each instrument is derived from analogies with terrestrial ocean abundances and described in detail in §B.1.3.1.

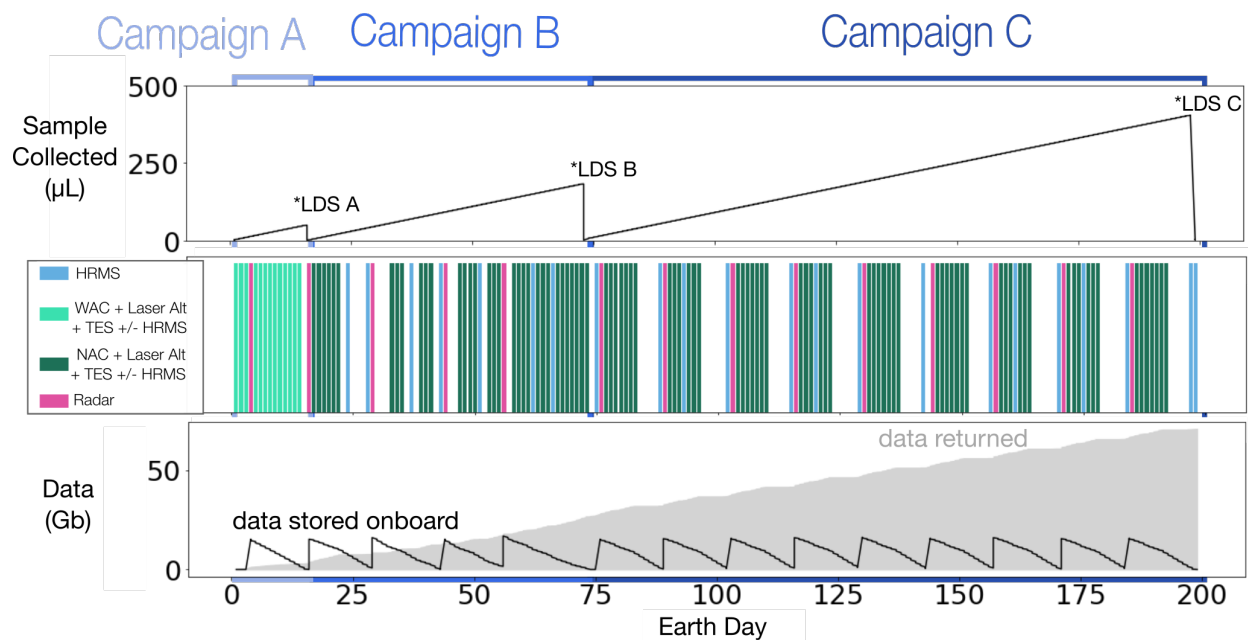


Exhibit 3-2. Concept of science operations for the first 200 days of Orbilander's orbital phase.

particles, general characteristics of the sample are acquired with the ESA (informing decisions on preparation requirements for future modes), a survey of organic material is conducted with the μ CE-LIF, and a search for cells is conducted by the microscope. The SMS searches for lipids with additional microscope and ESA measurements in LDS-B. In LDS-C, the most sample-demanding mode, both the μ CE-LIF and SMS search for amino acids and enantiomeric excess. §B.1.3 details the rationale behind the sample requirements, and Exhibit 3-1 shows the modes and associated collection times for each LDS measurement.

We assume that the 1-m² funnel accumulates ice grains at a rate of 1.6 μ L/pass through the plume (Guzman et al. 2019; see also §B.1.4). Thus, it takes many orbits to build up enough sample for each LDS mode, separating the orbital phase of the mission into three campaigns. (The ConOps described in Exhibit 3-2 includes extra orbits for sample collection margin.) Orbilander leverage this accumulation time to run the RSRS.

During Orbital Campaign A (collecting enough sample for LDS-A), RSRS data collection with the WAC (either of two navigation cameras co-boresighted with the NAC), laser altimeter, and TES for landing site reconnaissance is prioritized (“Recon Orbits”). Operating these three instruments easily fits within our power and data profiles. During this stage, WAC observations are prioritized over NAC to survey a broader area from which targets for NAC imaging will be selected by the science team. Within the first 15 days of the orbital phase, we accumulate and return at least 264 WAC images (equivalent to more than 2 \times areal coverage of the south pole), and 22 laser altimeter and TES passes are acquired and returned.

With these data, the science team selects potential landing sites to target during Campaigns B and C with the NAC, laser altimeter, and TES. Although the actual landing site is only a few square meters, candidate landing sites are defined as a 5 km \times 5 km square area to assemble the greatest body of information about the surface integrity of the potential landing region. High-resolution imaging multiple times (assuming 30–50% overlap) under various lighting conditions to determine their surface roughness and to create the stereo pairs necessary for characterizing local slopes requires on the order of 300 NAC images to characterize 1 landing site (§B.1.4.2). According to these assumptions, at the end of Campaign C, we accumulate enough NAC images to characterize 42 landing sites.

The radar sounder produces a tremendous amount of data and thus operates during dedicated orbits for 200 s during closest approach. At Orbilander's maximum orbital velocity (\sim 200 m/s), the radar sounder

Payload Elements		Mass (30% Cont)		Average Power (40% Cont)		Data	
		CBE (kg)	MEV (kg)	CBE (W)	MEV (W)	Per Measurement (Mb)	Minimum Total (Gb)
Life Detection Suite	HRMS	20	26	70	98	180	5.8
	SMS	12	16	65	91	164	1.6
	ESA	3	4	15	21	28	0.28
	μCE-LIF	4	5	6	8	0.20	0.002
	microscope	3	4	15	21	33	0.33
	nanopore	4	5	5	7	2000	6.0
Remote Sensing and Reconnaissance Suite	Radar Sounder	12	16	25	35	16000	224
	Thermal Emission Spectrometer	4	5	13	18	0.31	0.06
	Laser Altimeter	7	9	17	24	6.8	1.3
	Narrow Angle Camera	20	26	5	7	4.2	53
	Wide Angle Camera (in spacecraft MEL)	–	–	3	4	4.2	0.18
In Situ Suite	Seismometer	5	7	4	6	0.46	0.69
	Context Imager	4	5	12	17	50	1.62
Sampling System	Funnel	20	26	0	0	0	0
	Scoop	10	13	30	42	100	0.6
	SPS	14	18	10	14	50	0.5
Total		142	185	295	413	–	299

Exhibit 3-3. Payload mass, power, and data table. For a detailed description of the data derivation, see §B.1.4.4. The minimum total data shown here represents only the data collected in the first 200 days in orbit and 176 days on the surface.

interrogates a 40-km swath across the surface along track (cross-track extent depends on the orbital altitude; §3.12.3). With vents placed about every 5 km along the tiger stripes (Helfenstein et al. 2015), a 40-km swath has a >99% chance of covering a vent. With 1 vent every 40 km, the probability would decrease to 64%. Radar sounding orbits occur at least once during each campaign for a total of at least 14.

Analysis by the HRMS on the vapor collected via the gas inlet can also be run during Recon Orbits but brings the total power consumption during science operations to just under the 100 W maximum allocation. Should power prove a concern, HRMS measurements can be run on separate orbits during any campaign, especially during the relaxed cadence of B and C.

After 200 days, the minimum orbital science objectives have been met, leaving 63% of the remaining orbital phase as schedule margin. The orbital phase of the Orbilander mission is therefore robust to a low abundance of landing sites and to lower-than-anticipated targeted species in the plume. After an appropriate landing site has been selected, secondary mission objectives can be executed (e.g. gravity science and reflectometry) but were not further detailed as part of this study.

3.1.2. Instrument Operations on the Surface

On the surface, the availability of larger sample volumes means that the LDS can be run concurrently. The first LDS is run in “contingency mode” (all instruments except the nanopore, which requires an order of magnitude more sample than the other instruments combined) as soon as enough sample is collected via the passive collector. The full complement of LDS instruments (“full mode”) is subsequently run at about a monthly cadence, alternating between samples collected with the funnel and with the scoop for a total of three full mode runs on passively collected sample, three full mode runs on actively collected sample, and one contingency mode on passively collected sample. This relaxed timeline still provides ample time for downlink of data as well as characterization and decision of where to actively collect by the science team within the first 176 Earth days (§B.1.4.4), leaving 76% of the landed phase as margin against, for example, uncertainties in biomass (§B.1.3.3, §B.3.3.1).

The context imager's fields of view cover the area accessible to the scoop with overlap for stereo. Illuminating the surface with full-spectrum LEDs allows night imaging. Images are taken to identify scooping sites and to characterize and monitor the scoop mechanism.

The seismometer is a short period seismic probe notionally placed on the surface by the scoop-bearing arm during checkout post-landing. Placement on the surface, rather than on the spacecraft, should enable higher performance between 0.1 and 1 Hz and significantly higher at frequencies > 1 Hz where the spacecraft serves as a noise source (e.g. Panning & Kedar 2019). However, a body-mounted instrument should be capable of operating with a factor of a few of the instrument's noise floor during mechanically quiescent periods. Thus, non-deployed options with acceptable sensitivity are also feasible.

3.2. Flight System

The Orbilander flight system utilizes a single spacecraft to bring the three payload suites first into orbit and then to the surface of Enceladus. Exhibit 3-4 shows the flight system in its landed configuration. The spacecraft is nuclear powered, using two Next Generation Radioisotope Thermoelectric Generators (NGRTGs) and a lithium-ion battery. The all-chemical propulsion system features two HiPAT bipropellant engines for higher ΔV maneuvers; such as Saturn Orbit Insertion (SOI), satellite flybys, Enceladus Orbit Insertion (EOI), and landing maneuvers; and monopropellant thrusters for lower ΔV maneuvers (i.e. stationkeeping and attitude control). The flight system is three-axis stabilized and has a fully redundant guidance and control subsystem.

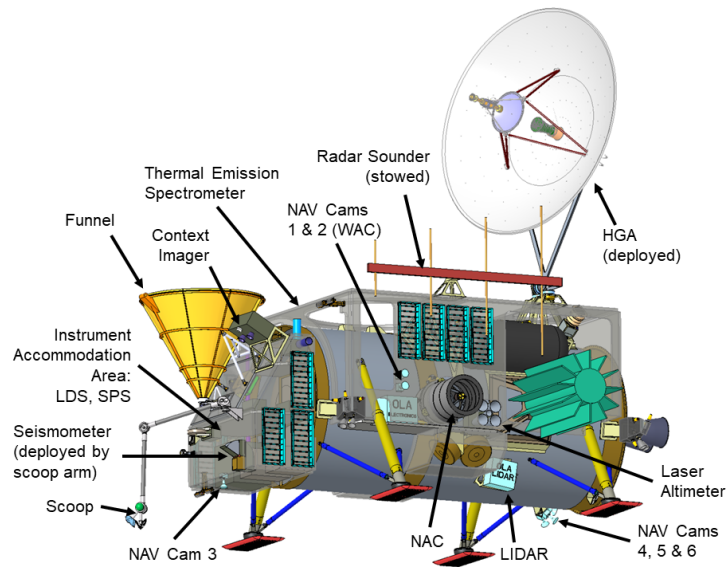


Exhibit 3-4. Orbilander configuration, with deployed antenna after landing on Enceladus.

The spacecraft has eight total antennas: one Ka-band high-gain antenna (HGA), used for science data downlinks, one X-band medium-gain antenna (MGA), three X-band low-gain antennas (LGAs), and three fan beam antennas (FBAs). The HGA and MGA are co-boresighted on a body-mounted, deployable, gimbaled mechanism that allows for pointing toward Earth while on the surface. The spacecraft block diagram is shown in Exhibit 3-5.

The Orbilander mass budget (Exhibit 3-6) shows that the flight system wet mass includes the 30% margin, as required in the study guidelines. Consumables are calculated using Maximum Possible Value (MPV) mass.

The Orbilander is powered primarily by the two NGRTGs. The power system design includes a 46 Ah battery (beginning of life, BOL) which is available for use during periods of peak power usage such as maneuvers, orbit insertion, and landing. The systems team estimated a power budget for 18 different modes of operation. The driving power modes are shown in Exhibit 3-7. The budgets assume a 30% reserve of the power available from the NGRTGs and battery, degraded for mission life. For each mode, the available power varies according to mission life at the time of the event. The landing mode is the driving case for the battery capacity when considering degradation of the battery and RTGs at SOI (L+7 yr) and Landing (L+14 yr). The power load profile was used to size the battery assuming a maximum depth of discharge of 50% and a 30% power load margin. The battery is not needed for surface operations. Spacecraft hardware will be exercised as needed to ensure mission life is met. The flight system characteristics are shown in Exhibit 3-8.

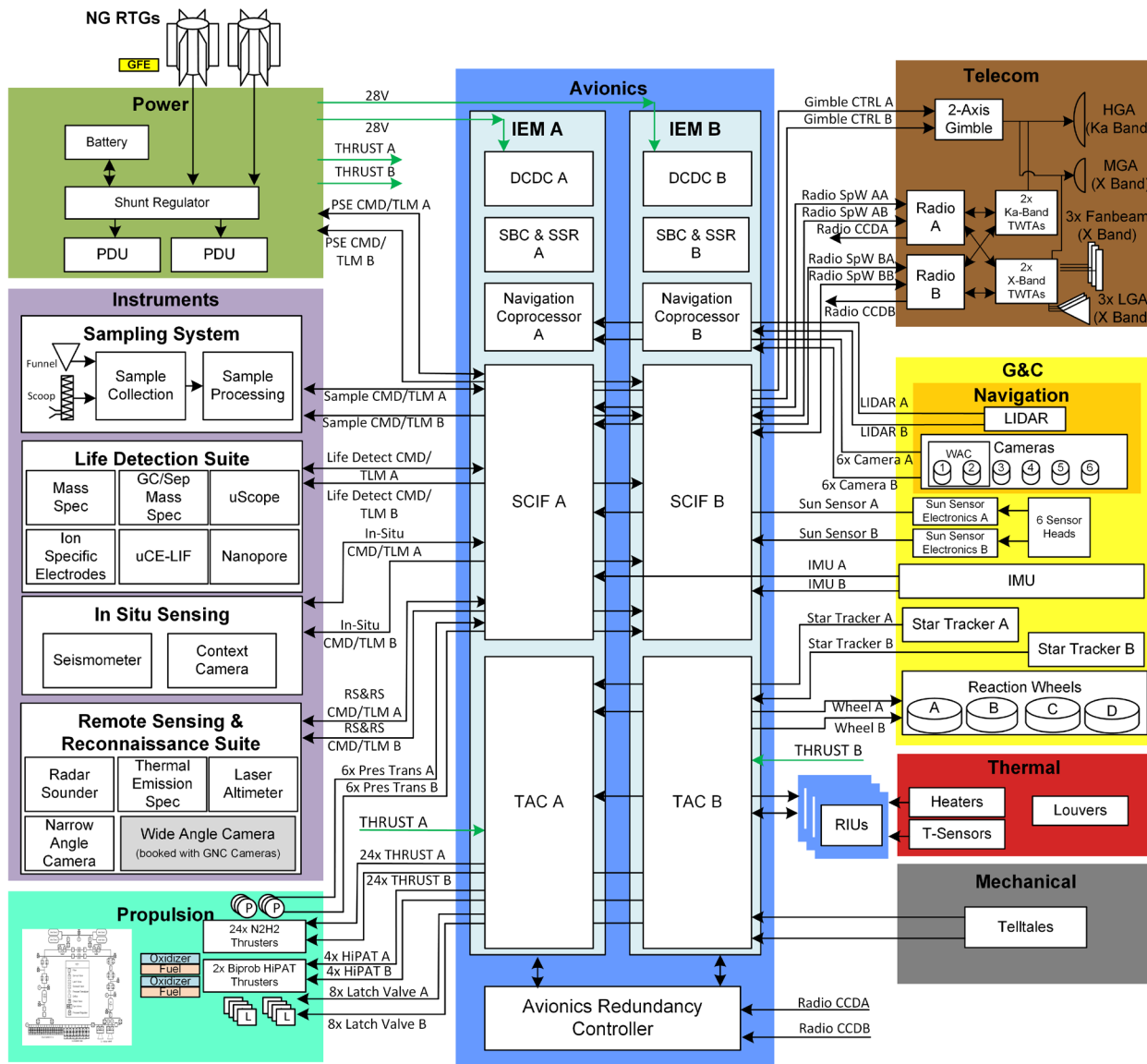


Exhibit 3-5. Enceladus Orbilander block diagram.

3.3. Mechanical

The Orbilander is structurally designed to survive launch and landing environments. The mechanical design, shown in Exhibit 3-9, consists of a primary, secondary, and landing system structures. The Orbilander design fits a 5-m fairing, providing launch vehicle (LV) flexibility.

The core of the primary structure is a cylinder surrounding and supporting the propulsion tank through flexures and interfaces with the LV through a marmon ring for launch. There are localized stiffeners on the core structure at interfaces with the propulsion tank, outer primary structure, secondary structure and lander system structure. The outer primary structure is honeycomb with radial support to the core structure. Most instruments are attached to the outer honeycomb panels in strategic locations to support launch packaging, thermal management, sample collecting during Enceladus orbit and after landing, sensor placement for mapping Enceladus, autonomous landing, and communication line of sight.

The secondary structure consists of RTG brackets, bi-axial gimbal brackets, and thruster stanchion/brackets which interface directly with the core primary structure. Brackets anchor the RTGs to the core primary and elevate the RTG beyond the plane of surrounding hardware allowing visibility to deep space with minimal obstructions. The wideband communication antenna biaxial gimbal attaches directly to the core primary structure via a bracket that elevates it clear of the secondary structure with a boom between the biaxial gimbal and the antenna; achieving an obstruction-free communication path to Earth. During launch, the wideband communication antenna is anchored to the primary structure using flexures and a release mechanism. The launch locks release during post-launch checkouts to exercise the gimbal periodically, maintaining bearing lubrication and preventing cold-welding during the long cruise to Enceladus.

The landing structure attaches directly to the core primary structure and consists of four landing legs. Each landing leg consists of a tripod of two fixed struts and one collapsible strut united at a pivot that secures the landing foot. The collapsible strut uses embedded honeycomb as the energy-absorbing material. The design allows landing survival of up to 2 m/s vertical and 0.5 m/s horizontal velocity.

3.4. Electrical Power

The Electrical Power Subsystem (EPS) provides power generation, regulation, distribution, and energy storage for the vehicle through all mission phases. The subsystem is designed to provide 30% margin in all load cases (Exhibit 3-7). The EPS subsystem block diagram is shown in Exhibit D-2. Two NGRTGs of the 16-GPHS variant provide power to the vehicle. Together, the RTGs provide 800 W when initially

Mission Mass Summary	
Subsystem	CBE (kg)
Instruments (Payload)	142
Mechanical	630
Landing Structure	150
Avionics	15
Propulsion, including residuals	357
Power	174
Guidance, Navigation, and Control (GNC)	66
Thermal	110
RF (Telecom)	109
Harness	124
Flight System CBE Dry Mass	1877
Margin (kg) (30% of MPV dry mass)	813
Dry Mass (Max possible value)	2690
Usable N ₂ H ₄ (MPV)	2416
Usable Oxidizer (NTO-MON3) (MPV)	1489
Pressurant	15
TOTAL Spacecraft Consumable Mass	3920
Total Wet Mass MPV	6610

Exhibit 3-6. Orbilander mass budget by subsystem.

Subsystem/Component	Orbit Ka-band Data Downlink	Orbital Science	Surface Science	Surface Telecom	SOI Prep	SOI	Landing Prep	Landing
	CBE (W)	CBE (W)	CBE (W)	CBE (W)	CBE (W)	CBE (W)	CBE (W)	CBE (W)
Instruments	30	100	100	30	30	30	30	30
Avionics	25	25	25	25	40	40	40	40
Propulsion	5	5	0	0	330	371	270	322
Power	23	23	23	23	23	23	23	23
GNC	113	116	3	3	111	45	175	109
Thermal	40	40	40	40	40	40	40	40
RF (Telecom)	152	7	7	172	127	127	127	127
Harness	12	9	6	9	21	20	21	21
Total CBE Power Loads	400	325	204	302	721	695	725	711
Margin (30% of MPV)	177	177	170	170	309	298	311	305
Total Power with Margin	577	502	374	472	1031	994	1037	1017
RTG Power (Max possible value)	589	589	566	566	660	660	589	589
Year since launch (degradation)	13 years	13 years	15 years	15 years	7 years	7 years	14 years	14 years
Battery Capacity Required (Ah)	–	–	–	–	17.5		15.6	
Discharge Duration	–	–	–	–	1.4 hours		1 hour	
Battery Depth of Discharge	–	–	–	–	44%		43%	

Exhibit 3-7. Orbilander has sufficient power margins with two NGRTGs.

Flight System Element Parameters	Value/Summary, units
Design life	204 months (mission life + 2 years)
Structure	
Structures material (aluminum, exotic, composite, etc.)	aluminum and composite
Number of deployed/articulated structures	Three (HGA/MGA, active sampling scoop and arm, radar sounder)
Thermal Control	
Type of thermal control used	Passive, with louvers and heater control
Propulsion	
Estimated ΔV budget	2402 m/s
Propulsion type(s) and associated propellant(s)/oxidizer(s)	Biprop ($N_2H_4/NTO-MON_3$)
Number of thrusters (specific impulse, Isp)	2x – HiPAT (326 s); 8x – 22N (220 s); 16x – 4.4 N (215 s)
Custom propellant and pressurant tanks	1x – 2576L hydrazine; 1x – 1230L NTO; 2x – 172L He pressurant
Attitude Control	
Control method (3-axis, spinner, grav-gradient, etc.)	3-axis stabilized
Control reference (solar, inertial, Earth-nadir, Earth-limb, etc.)	Varied – e.g. Earth and Enceladus targeting
Attitude control capability	0.05°
Attitude knowledge limit	0.025°
Articulation/#-axes (solar arrays, antennas, gimbals, etc.)	1 articulation, 2-axis HGA gimbal
Sensor and actuator information (precision/errors, torque, momentum storage capabilities, etc.)	Sun sensors (radial accuracy < $\pm 0.5^\circ$) Star trackers (pitch/yaw accuracy within ± 10 arcsec) IMU (bias stability < 0.0015°/hr, 1 σ) Reaction wheels (25 Nms momentum storage capability, 0.075 Nm torque capability)
Command & Data Handling	
Flight element housekeeping data rate	4 kbps
Data storage capacity	128 Gb
Maximum storage record rate, playback rate	3000 kbps, 3000 kbps
Power	
Power source	2 NGRTGs, 16-GPHS
Expected power generation at BOL and end of life (EOL)	741 W (launch), 589 W (landing), 566 W (EOL)
Power consumption (science, data transmission)	Orbit: 400 W, 325 W CBE; Surface: 203 W, 301 W CBE
Battery type, storage capacity	Li-ion, 46 Ah BOL

Exhibit 3-8. Flight system element characteristics table.

loaded with fuel and are estimated to provide 741 W at launch and 566 W at EOM, assuming the RTGs are loaded 3 years before launch. The RTGs are provided by NASA and installed at launch base. Spacecraft testing is achieved using RTG simulators.

RTG output power is regulated by a linear sequential shunt system with design heritage to the *Van Allen Probes (VAP)* and *New Horizons (NH)* missions. The shunt regulator also provides battery charge control using a fault-tolerant, three-stage majority voted control loop to ensure charge voltage control is maintained under all conditions. The shunt regulator implements a linear sequential topology that can operate with the failure of any single stage and includes redundant communications interfaces to the spacecraft avionics. In addition, the regulator includes redundant cell-balancing circuits, in development for the *Dragonfly* mission, to manage the differences in cell self-discharge rates through the mission. This topology is an improvement on the cell shunt balancing topology used on the *VAP* mission.

Excess RTG power is dissipated in two sets of shunt resistors. These are located internal and external to the thermal zones described in the §3.11. The external shunts are sized to provide constant dissipation to internal thermal zones for full range of power throughout the mission.

Power distribution is provided by block redundant Power Switching Units (PSUs) similar in concept and topology to many previous missions, including *VAP*, *Europa Clipper*, *Parker Solar Probe (PSP)*. The switching services are divided into safety and non-safety services; multiple inhibits prevent the former from inadvertent activation. The safety services can also be de-energized when not in use to conserve power.

Energy storage is provided by 8 series-connected 42 Ah large-format lithium-ion cells that provide 46 Ah at BOL. The battery supplements the RTG power during high-power modes such as SOI and landing. The battery capacity is estimated to decline by 13% at SOI and 22% at landing. The battery design includes a bypass switch connected in parallel with each cell in the stack, as implemented on *VAP*. This feature allows a failing cell to be removed from the stack, providing single fault tolerance within a single battery.

3.5. Propulsion

The propulsion subsystem is a dual-mode pressure-regulated system that provides ΔV capability and attitude control for the spacecraft. The propellants are hydrazine, N_2H_4 , and nitrogen tetroxide (NTO), N_2O_4 . The baseline propellant load is 3905 kg of usable propellants to deliver 2402 m/s of ΔV plus 175 kg for all GNC needs during the mission (including landing) with 5.6% contingency.

The system consists of two main bipropellant (N_2H_4/NTO) apogee engines in the 445-645 N class (100–150 lbf), eight 22 N (5 lbf) monopropellant (N_2H_4) steering thrusters, sixteen 4.4 N (1.0 lbf) monopropellant (N_2H_4) attitude control system thrusters, and components required to control the flow of propellants and monitor system health and performance. Several flight-proven options exist for each component of the propulsion system, though delta-qualification testing of some components may be required.

For the purposes of this study, performance data for the Aerojet Rocketdyne HiPAT Dual Mode 445 N engine, Aerojet Rocketdyne MR-106E 22 N thrusters, and Aerojet Rocketdyne MR-111C/G 4.4 N thrusters were used, but alternate options exist, such as NAMMO's Leros-1B and Moog-Isp's MONARC-22-6 and -22-12 engines. The MR-106E has heritage on the *MESSENGER* spacecraft and the MR-111C/G has heritage on multiple spacecraft, including *MESSENGER*, *NH*, and *PSP*.

Propellants are stored in two custom cylindrical titanium tanks with spherical caps, one for hydrazine and one for NTO. Both tanks contain custom PMDs to ensure positioning of gas-free propellant for all maneuvers at the tank outlets. The PMD development is driven by the landing maneuver described in §3.7, when most of the bipropellant will be depleted, and begins in Phase A with an industry partner to reduce risk. The maximum expected operating pressure (MEOP) for the mission is 250 psi. Helium pressurant is stored at a MEOP of 4500 psi in two custom composite-overwrapped titanium pressure vessels. The design uses separate routings of check valves, latch valves, and series-redundant pressure regulators to limit fuel and oxidizer migration to the shared pressurant tanks. *MESSENGER* used a similar isolation design in flight.

The PMD supplier is put on contract in Phase A in order to evaluate the propellant tank designs, specifically to assess the risk of propellant availability at the tank outlets during the landing maneuver. The remaining components used to monitor and control the flow of propellant and pressurant—latch valves, filters, orifices, check valves, pyro valves, pressure regulators, service valves, and pressure and temperature transducers—are selected in Phase A from a large catalogue of components with substantial flight heritage. During Phase A, a trade study evaluates alternate pressure regulation schemes.

3.6. Guidance, Navigation, and Control

The Guidance, Navigation, and Control (GNC) subsystem provides three-axis stabilization within a fully redundant system. Attitude and rate knowledge are obtained from two box-redundant star trackers (ST) and one internally redundant Inertial Measurement Unit (IMU). Control is maintained via three reaction wheels, with

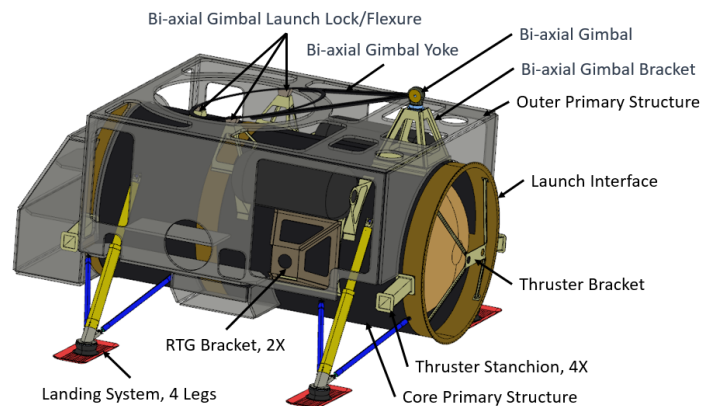


Exhibit 3-9. Orbilander mechanical system.

a fourth available as a spare. Multiple Sun sensors heads provide safemode attitude knowledge through an internally redundant electronics box. Adjustments in translational velocity (ΔV) are implemented by the bipropellant thrusters or 5-lbf monopropellant thrusters, described in §3.5, depending on the magnitude of the desired change; 1-lbf monopropellant thrusters implement the momentum management of the reaction wheels. Autonomous onboard navigation enables the pump down timeline to Enceladus orbit and supports orbit maintenance, detailed in §3.12.2, §3.12.3, and §B.2. Orbilander carries a total complement of six wide angle navigation cameras. Four cameras provide coverage and redundancy for station keeping operations; two navigation cameras are co-boresighted with the NAC for TRN and hazard avoidance during descent as well as serving as redundant science WACs. During descent and landing, control is handed over to the thrusters with a Scanning LIDAR and downward-facing cameras provide position and velocity knowledge, augmenting the standard flight hardware.

Driving requirements on the GNC design include the time of flight for the moon tour and science orbits at Enceladus, both of which require frequent changes in the vehicle's attitude. Propellant mass required to accomplish these turns, coupled with the pointing requirements of the science cameras for reconnaissance ($<0.02^\circ$) and orienting the HGA to Earth ($<0.05^\circ$), led to the selection of reaction wheels over a thruster-only design. The long mission duration also led to the selection of hemispherical resonator gyros for the IMU for reliability. The GNC design draws heavily on flight heritage from *PSP*, *MESSENGER*, *Cassini*, and *OSIRIS-REx* for both in hardware selection and flight algorithms.

3.7. Descent and Landing

A safe landing ellipse (5 km \times 5 km) will be identified during the science orbit phase (§B.1.4.1). The landing sequence begins with a Descent Orbit Insertion (DOI) maneuver at apoapsis to target a 5-km altitude near periapsis. As the vehicle descends and nears periapsis, in addition to standard IMU and ST measurements, the navigation camera imagery is used for Terrain Relative Navigation (TRN) image-to-Digital-Elevation-Model (DEM) correlation. Images collected by the Orbilander during orbital operations are transmitted to the ground for DEM creation and the relevant DEMs are uploaded to the Orbilander prior to initiating the landing phase. This allows a targeting correction to be incorporated in the second maneuver, Powered Descent Initiation (PDI), which is executed near periapsis, dependent on the selected landing site. After this burn, a terminal guidance procedure is initiated to safely navigate the spacecraft to the landing site. A ΔV of 258 m/s is allocated for descent plus an additional 100 kg of propellants for TRN, hazard avoidance, and final rotation to land.

During terminal guidance from 5 km to 10 m, TRN allows the Orbilander to horizontally navigate to within 0.5 km of the desired landing site. Image-to-DEM correlation is used down to ~ 500 m, depending on the resolution of the DEMs. The TRN then switches to image-to-image correlation. Hazard avoidance—the identification of a safe landing site within the targeted ellipse where the Orbilander will not tip over due to rocks or terrain slope—is accomplished through the use of LIDAR throughout the terminal descent. The 250 m altitude serves as a decision gate to the acceptance of a landing target. TRN and hazard avoidance techniques are detailed in §C.2.

Once the final landing site is determined by the spacecraft, the vehicle descends from 250 m to 10 m and moves to a 25 m standoff distance from the landing site. With the bipropellant engine facing perpendicular to the surface, byproducts of the combustion may contaminate the surface and negatively influence the science observations (§C.4). To avoid the potentially contaminated area, at 10 m the main engine throttles up for ~ 5 s before cutting off permanently. At the same time, monoprop thrusters will initiate a pitch over maneuver. The combination of these firings will propel the lander up to a 20 m height, translate 25 m downtrack, and rotate the lander to a legs-down position, thus moving the vehicle clear of the blast zone area (§C.4). Once the rotational and translational rates have been arrested by the monoprop thrusters, the vehicle descends safely to the surface with a vertical velocity < 2 m/s and horizontal velocity < 0.5 m/s. Safely landed, attitude measurements from the STs are used to align the HGA to Earth for communications. Exhibit 3-10 summarizes the landing procedure.

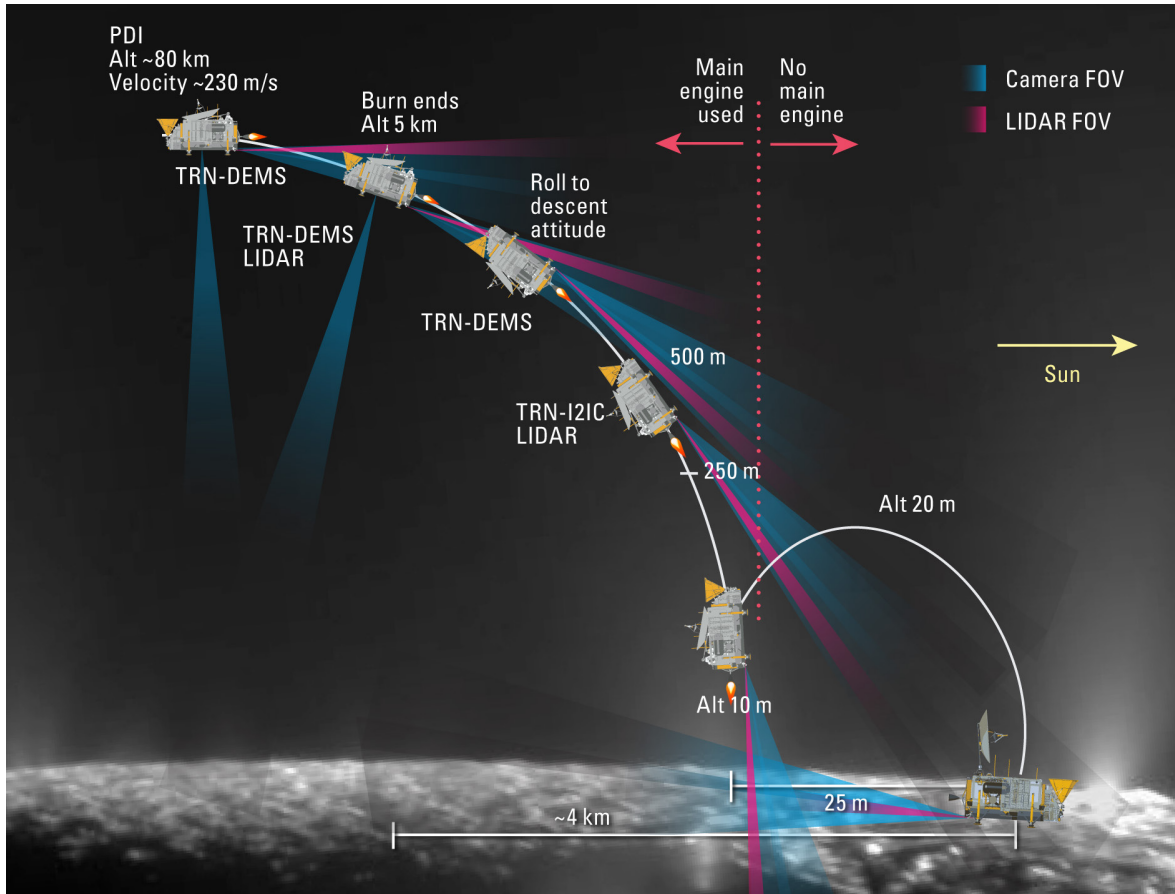


Exhibit 3-10. Orbilander descent and landing strategy. By translating 25 m vertically, Orbilander lands clear of thruster-contaminated surface (§C.4).

3.8. Avionics

The avionics subsystem design for the Orbilander provides the necessary interface and computer electronics to support the bus and instrument payload, flight software, spacecraft autonomy, and autonomous spacecraft navigation during the Enceladus orbit and landing phases of the mission. The avionics are fully block redundant with cross-strapped interfaces to the instrument and spacecraft components (e.g. GNC, telecom, power, propulsion) where applicable. To support the limited continuous power output of the spacecraft, multiple power modes of operation are provided, not to exceed 40 W. Storage of the mission data products is supported by 128 Gbits of nonvolatile memory that the avionics are capable of forwarding to the radio at sustained data rate of at least 100 kbps for a given 6-hour downlink period.

Baseline design of the subsystem heavily leverages heritage APL avionics design elements. The majority of the avionics subsystem are contained within redundant card stacks based on the heritage Integrated Electronics Module (IEM) approach implemented since *NH*. A combined single-board computer (SBC) and solid-state recorder design would leverage heritage design elements from *PSP*, *IMAP*, and *DART* SBC designs. Spacecraft Interface and Thruster Actuator cards of *PSP* heritage are candidates for build-to-print use. The redundancy controller design leverages *PSP*'s Avionics Redundancy Controller and the *Dragonfly* Redundancy Controller Card design elements. The Navigation Coprocessor Card meets the processing throughput requirements of the autonomous navigation elements and is based on *Dragonfly*'s IEM Navigation Coprocessor currently in development.

3.9. Flight Software

The Orbilander flight software has no unusual or stressing requirements. A typical software implementation that meets the needs of the mission is implemented in C code running on a Vx Works real-time operating system. The software manages the telecommunications uplink and downlink using CCSDS protocols for data handling. Commands are received in CCSDS telecommand packets that are either processed by the flight software or dispatched to subsystems or instruments as indicated by the packet header. The flight software supports storage of command sequences (macros) which can be executed by a time-tagged command stored in flight processor memory. The flight software collects engineering and science data from the instruments and manages the storage on the solid state recorder. The software includes an autonomy engine that supports fault detection and correction. The autonomous navigation will likely be implemented on a separate navigation coprocessor from the main avionics flight computer.

3.10. Telecommunications

The Enceladus Orbilander telecommunications system has heritage from *PSP* and *NH* with elements that will fly on *DART* and *Dragonfly*. It features redundant, cross-strapped Frontier Radios. Uplinks operate at X-band and primary science downlinks at Ka-band. Spacecraft downlink at X-band is also provided, primarily for early operations, cruise, and landing phases. The two Frontier Radios interface via SpaceWire to the avionics. Both Ka-band and X-band downlinks provide the modulated exciter output from each radio a passive hybrid coupler, feeding input signals to redundant traveling-wave tube amplifiers (TWTAs). A TWTA failure would not limit the use of either radio, nor would a single radio failure limit the use of a single TWTA. The selected TWTA output is routed through a protective isolator to a diplexer and switching network to combine uplink and downlink paths to the selected antenna. The uplink signal is passed from the selected antenna through the switching network and diplexer to the selected Frontier Radio receiver. The telecom block diagram is shown in §B.3.2.

The Enceladus Orbilander uses eight antennas. A dual-band 2.2 m HGA mounts on a 2-axis gimbal for surface operations. The MGA is integrated with the HGA subreflector. Three X-band LGAs are used during launch and cruise operations. Three FBAs are used during cruise and during descent and landing.

3.11. Thermal

All electrical power produced by the RTGs, isolated from the main spacecraft structure, is assumed to be either (a) utilized by spacecraft components as electrical power or (b) shunted to components for heating or radiators for rejection. Most components are in one of two thermal zones that are internally radiatively coupled via high emissivity coatings (e.g. black paint). In addition to a 0.65 m² radiator, louvers reject heat during the hot case near Earth just after launch. The HGA, covered in a radome, will be used as a sun-shade near Earth. At Saturn, the two 0.8 m² louvers are closed and the external shunt is disabled via a variable conductance heat pipe.

Thermal switches shunt any excess electrical power internally. Heat is spread internally with constant conductance heat pipes, thermal straps, and doublers. Heaters installed on the propellant and pressurant tanks, as well as survival heaters for other components, require up to 100 W of the RTG electrical power. Survival heaters may be replaced with 1 W radioisotope heater units (RHUs) for components that have ample hot margin.

The engines are thermally isolated from the rest of the spacecraft. The tanks are covered in 20 layers of multilayer insulation (MLI) and thermally isolated from the main spacecraft structure. Additional MLI blankets enclose the entire spacecraft, excluding antennas and thrusters, totaling nearly 100 m² of MLI. This design keeps all internal components within a -30°C to +50°C range up to arrival in Enceladus orbit. Several instruments need to be kept above 0°C when powered on; these are located in the instrument assembly thermal zone near the funnel so that the whole volume can be easily heated by shunted electrical power from the RTGs. This design would be able to maintain 0°C for these components even in safe

mode at EOM, either in Enceladus orbit or on the 60 K surface. Although sensitive to the final spacecraft geometry, multiple reflecting surfaces may be used to harvest some thermal waste heat from the RTGs.

3.12. Mission Design and Navigation

The trajectory design for Orbilander has five phases: (1) launch and interplanetary cruise to Saturn, (2) Saturn system entry to capture at Saturn and Saturnian pump down (moon tour) to reduce orbital energy, (3) Enceladus Orbit Insertion, (4) science operations in orbit, (5) landing on Enceladus’ surface. A high-level overview of each phase is provided here with additional details included in §B.2.

3.12.1. Launch and Interplanetary Cruise

For the Orbilander, a launch later in the late 2030s is determined to be ideal for Enceladus both to maximize south pole lighting during the science phase and to provide additional time for NGRTG availability. A direct transfer exploiting an opportunistic Jupiter Gravity Assist (JGA) option is selected as the baseline to minimize propellant mass and to avoid an inner cruise. While shorter time-of-flight (TOF) options exist, a longer TOF was pursued for this study to allow for reduction of Saturn arrival V_∞ (capture ΔV) and to delay arrival at Enceladus for improved south pole lighting conditions. The launch open trajectory appears in Exhibit 3-11, with details of the prime and back-up launch periods given in Exhibit 3-12. The launch C3 requirements are accommodated by the SLS Block 2 with a CASTOR 30B upper stage. Other trajectories with less-capable launch vehicles are available and would require some modifications to the design presented here, such as accounting for the increased thermal loads of the inner solar system and increased capture ΔV . Details on alternative interplanetary transfer itineraries and launch vehicle options are provided in §B.2.

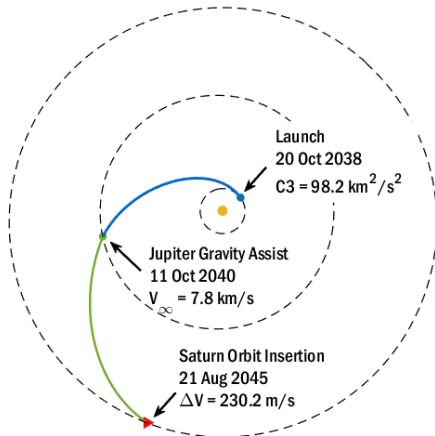


Exhibit 3-11. Interplanetary cruise, direct transfer + JGA 2038 launch open trajectory.

	Prime	Back-Up
Launch Period	20 Oct 2038 – 09 Nov 2038	15 Nov 2039 – 06 Dec 2039
Max. C3 (km ² /s ²)	106.6	105.2
Max. Launch Dec. (degrees)	40.1	22.3
Jupiter Flyby Date	11 Oct 2040	04 Aug 2041
Jupiter Flyby Altitude (km)	4.73×10^6	8.62×10^6
Time-of-Flight (years)	7.0	7.0
Arrival V_∞ (km/s)	3.3	4.0
Arrival Date	21 Aug 2045	13 Nov 2046

Exhibit 3-12. Launch periods for direct transfer with JGA, patched conic analysis. (Other viable interplanetary options exist).

3.12.2. System Capture and Pump-Down

Upon arrival to the Saturnian system, an SOI maneuver of 232 m/s is performed at a periapsis altitude of 2400 km to capture into a 158-day orbit about Saturn. A Periapsis Raise Maneuver (PRM) of 605 m/s is performed at the first apoapsis to target a subsequent Titan flyby (at sufficient distance to not contaminate the spacecraft), which begins the pump-down phase of the mission. Tour design in the Saturnian system is extremely complex, as the low mass of the moons requires many flybys of each moon to reduce orbital energy, and leveraging maneuvers are generally required between each pair of flybys to increase the flyby energy-reduction efficiency (Strange et al. 2009). The moon tour design

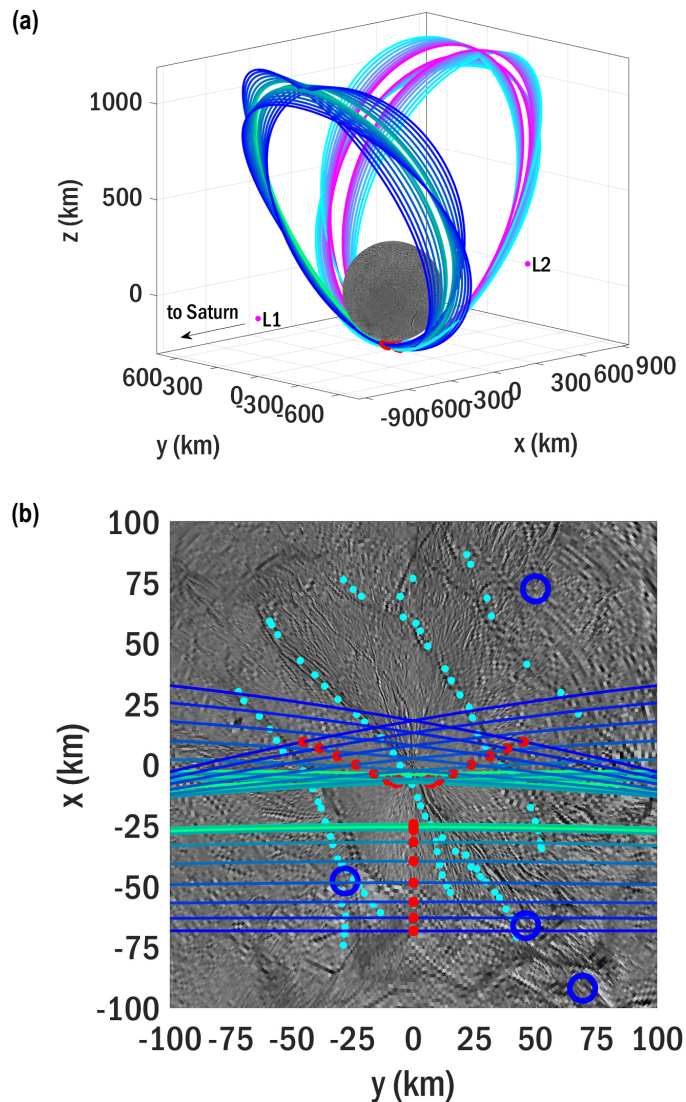


Exhibit 3-13. Period-3 halo orbits about Enceladus. (a) Sample members from L1-family (blue-green) and L2-family (cyan-magenta), where each orbit is plotted with a unique color; (b) L1-family ground-tracks near the south pole, with tiger stripes highlighted in cyan and potential landing target areas (based on high rates of plume fallout) in blue circles. The study team selected a period-3 halo L1 orbit for the Orbilander mission.

Orbilander mission design exploits halo orbits to reach the range of altitudes desired for LDS science and the span of ground tracks desired for remote sensing and reconnaissance.

The halo orbits of the Saturn-Enceladus Circular Restricted Three-Body Problem (CR3BP) are chosen because they offer altitudes within the desired range near the south pole. (Haapala 2014). Some members of the halo family are predicted to be stable in the CR3BP; however, this stability appears to break down once transitioned to a high-fidelity model. With orbital periods of ~ 12 hours, the halo orbits are amenable for stationkeeping maneuver cadences. While the period-1 halo orbits offer repeat ground-tracks over the south pole of Enceladus, the period-3 family is preferred as it provides greater ground-track diversity needed to accommodate reconnaissance science. Families associated with both the L1 and L2 libration

space is infinitely vast, with significant numerical and computational challenges in the identification of flight-quality trajectories. The NASA ROSES solicitation “Astrodynamics in Support of Icy Worlds Missions” (NNH18ZDA001N-ADYN) supports the need for development of the astrodynamics analysis tools required to address the Saturnian pump-down search problem. The results of this ROSES investment should be leveraged for the moon tour design for future Enceladus concepts.

The moon tour proceeds with leveraged pump-down sequences exploiting flybys of Titan, Rhea, Dione, and Tethys, bringing the spacecraft to the first Enceladus encounter. Next, a series of Enceladus flybys further reduce orbital energy, at which point the Enceladus Orbit Insertion (EOI) maneuver is performed to begin the science orbital operations phase. Overall, the estimated total deterministic ΔV is 660 m/s, which includes 560 m/s for the Pump-Down phase and 100 m/s for EOL. The total flight time for the pump down is ~ 4.5 years in length. Additional details on the moon tour are available in §B.2.2.

3.12.3. Science Orbit

The science orbital operations phase is nominally 1.5 years. Optimal orbital altitudes for plume sampling range 20-60 km to collect both larger particles as well as vapor (Guzman et al. 2019) at minimal relative velocity. Identification of stable orbits that reach these altitudes near the south pole is a challenging task, with only orbits requiring active control to avoid impact with Enceladus (“unstable” orbits) available at the inclinations and altitudes required (Russel & Lara 2009; Massarweh & Cappuccio 2020). Here we describe how the

points exist, with the L1 family providing best coverage for areas of high plume fallout. Sample members from both the L1 and L2 families are plotted in Exhibit 3-13a, where only the portion of each family corresponding to periapses ranging between 20-75 km altitude are retained. Exhibit 3-13b shows a close view of L1 family ground-tracks near the pole where each distinct period-3 orbit has three passages of periapsis (indicated in red), each roughly 12 hours apart. Because these orbits are unstable, a stationkeeping strategy is required and detailed in §3.13.2, §B.2.3, and §C.1.

3.13. Navigation and Orbital Maintenance

3.13.1. Navigating Interplanetary Cruise and Moon Tour

During the interplanetary transfer, a clean-up maneuver 7 days after launch adjusts the transfer to the nominal path after launch injection errors are assessed. Additional maneuvers are required to accurately target the JGA approach conditions and to correct for any errors accumulated during the flyby.

The Orbilander is primarily navigated during the moon tour using standard radiometric navigation, augmented by optical navigation images of the Saturnian satellites, with all processing being done on the ground, as was done by *Cassini* during its tour (Bellerose et al. 2019). During each orbit, 2–3 trajectory correction maneuvers (TCMs) are employed to maintain the reference trajectory. The TCMs are notionally planned 3 days prior to each moon encounter to target the correct flyby conditions and 3 days after the closest approach to clean-up errors built up during the flyby and are assumed to total 4 m/s per flyby. For most revolutions, a deterministic leveraging maneuver is executed near apoapsis as part of the reference tour design and an apoapsis-targeting maneuver is planned.

During the later portions of the tour, specifically the Rhea, Dione, and Tethys pump-down phases, the time between successive moon flybys can become relatively short (<7 days). During these portions of the tour, closing the navigation loop on the ground between successive flybys may be difficult. On *Cassini*, short flyby cadences were accommodated by applying a single targeting maneuver that ensured safe flyby altitudes for both encounters (Ballard et al. 2010). Alternatively, a “missed-flyby” strategy could be employed, where the altitude of the second flyby is enforced to be sufficiently high that the probability of impact is ensured to be within a desired tolerance.

Another approach would be to use an onboard navigation system using solely passive optical data, thus eliminating the round-trip light-time delays required by radio contact with the Earth. Analysis indicates that such an approach may be feasible in the Saturnian system due to the large number of satellites available for triangulation (Bradley et al. 2019). An onboard autonomous navigation system, called AutoNav, has been employed successfully on several deep space missions (*Deep Space 1*, *Stardust*, and *Deep Impact*), primarily to navigate interplanetary cruise and flybys and impacts of comets (Riede et al. 2007). Another onboard system, SMART Nav (Small-body Maneuvering Autonomous Real-Time Navigation), will be demonstrated on the DART mission to perform terminal guidance to impact an asteroid (Atchison et al. 2014; Chen et al. 2018). The two techniques use different algorithms. AutoNav uses multiple triangulation sightings to perform a complete orbit determination solution and computes maneuvers based on dynamically integrating the orbital motion. SMART Nav provides estimates of a linearized projection of B-plane error for a given flyby and computes maneuver recommendations based on the time remaining to encounter, the uncertainty in the error estimate, and the maneuverability of the spacecraft. The addition of AutoNav or SMART Nav algorithms to the mission could allow for automated trajectory targeting and/or clean-up maneuvers. Further study is recommended to determine the most robust and efficient method for navigation of the short-duration flyby cadence phases of the tour, either by passive, fail-safe means on the ground, or onboard orbit determination and maneuver planning (Exhibit C-1).

3.13.2. Maintaining the Science Orbit

Maintaining the nominal science orbit will require maneuvers to ensure the spacecraft will not impact with the surface nor depart from orbit with potential for re-encounter with Enceladus at a future date. With roughly 12 hours between subsequent passages of periapsis, an autonomous stationkeeping method

is thus likely necessary to maintain the science orbit. Alternatively, a biasing-maneuver strategy could be explored to enable ground-based station-keeping maneuver design that ensures the spacecraft does not impact with Enceladus within a prescribed number of revolutions but would likely lead to an increase in the ΔV required for station-keeping. Propellant margin included in the design can be applied if needed.

As described for the pump-down phase of the mission, onboard optical navigation is included in the design to enable autonomous stationkeeping (Exhibit C-1). The optical system currently includes dedicated navigation cameras, a scanning LIDAR, and the sharing of the narrow angle FOV science camera. The use of the science altimeter could aid in the accuracy of the optical navigation solution for stationkeeping. To perform onboard orbit determination, techniques such as triangulation, landmark tracking, optical velocimetry, and optical limb localization are viable candidates. Details on one possible autonomous stationkeeping implementation are provided in §C.1.

Parameter	Value	Units
Science Orbit Inclination	76.3 - 128.1	degrees
Science Orbit Periapsis Altitude	19.8 - 64.3	km
Science Orbit Apoapsis Altitude	1000 - 1110	km
Science Orbit Period	12.1	hrs
Mission Lifetime	180	mos
Maximum Eclipse Period	2.7	hrs
Launch Site	KSC	
Total Flight Element #1 Mass with contingency (includes instruments)	2690	kg
Propellant Mass without contingency	3698	kg
Propellant contingency	5.6	%
Propellant Mass with contingency	3905	kg
Launch Adapter Mass with contingency	100	kg
Total Launch Mass	6710	kg
Launch Vehicle	SLS Block 2 + CASTOR 30B	Type
Launch Vehicle Lift Capability	7468 (C3=106.6)	kg
Launch Vehicle Mass Margin	758	kg
Launch Vehicle Mass Margin (%)	10.1	%

Exhibit 3-14. Mission design table.

3.13.3. Landing

While in the science orbit, reconnaissance imaging would be employed to create DEMs and to identify candidate landing sites. During landing (§3.7), TRN would be employed for descent, while hazard avoidance techniques find a safe landing site through the use of LIDAR. These techniques are summarized in Exhibit C-1 and detailed in §C.2.

3.13.4. Mission Design Parameters and ΔV Budget

Key parameters of the mission design are outlined in Exhibit 3-14 demonstrating robust margins. ΔV margin and propellant contingency are included as shown. The ΔV budget for all phases of the mission is provided in Exhibit 3-15, including both deterministic maneuvers, and statistical correction maneuvers to account for dynamical modeling errors, maneuver and flyby execution errors.

3.14. Concept of Operations

Post launch and commissioning, the Enceladus Orbilander has five mission phases: cruise to Saturn, Saturn orbit insertion and the Saturn moon tour, Enceladus science orbit operations, landing, and surface science operations. Mission operations for each phase are summarized in Exhibit 3-16.

During the 7-year cruise, the NASA DSN 34-m antennas will be used during two 4-hour X-band communications tracks per

Event	Deterministic (m/s)	Statistical (m/s)	Notes
Launch	0.0	25.0	Launch injection clean-up
Jupiter Gravity Assist	0.0	10.0	Flyby-targeting and clean-up
Saturn Orbit Insertion	232.0	7.0	Saturn capture
Periapsis Raise Maneuver	605.0	18.5	Targets Titan-flyby
Moon Tour	560.0	176.0	Leveraging and flyby targeting and clean-up
Enceladus Orbit Insertion	100.0	3.0	Insert into science orbit
Orbit Stationkeeping	0.0	275.0	Science orbit maintenance
Landing	250.0	7.5	De-orbit and descent to landing site
Subtotals	1747.0	522.0	Totals without margin
Margin		133.0	Unallocated margin
Total		2402.0	Total ΔV

Exhibit 3-15. ΔV budget by mission event.

week to perform nominal operations, including spacecraft housekeeping data downlink, uplink of command loads, and real-time evaluation of spacecraft health and status. Increased DSN coverage for ranging and navigation data will be scheduled around the Jupiter gravity assist as required. Continuous DSN coverage will be scheduled during the Jupiter flyby. Similarly, increased coverage is required during the weeks leading up to Saturn orbit insertion maneuver and continuous coverage will be scheduled surrounding orbit insertion.

Once in Saturn Orbit, a 4.5-year Saturn moon tour consisting of flybys of several of Saturn’s moons is performed in order to reach Enceladus orbit. The final phase of the moon tour entails multiple flybys of Enceladus in increasingly smaller orbits. During the moon tour, the NASA DSN 34-m antennas are used during five 8-hour tracks per week to perform nominal operations, including navigation tracking, spacecraft housekeeping data downlink, science data downlink, uplink of command loads, and real-time evaluation of spacecraft health and status. Science operations during the moon tour were identified but not detailed at this level of study (§B.1.4.1).

The Orbilander orbits Enceladus with a period of 12 hours for 1.5 years. During each 3.5-hour closest approach, plume material is collected via the funnel and the science payload is operated (§3.1.1, §B.1.4.2). Two 8-hour tracks per day are required to downlink science data, downlink spacecraft and instrument housekeeping data, uplink command loads, and conduct real-time evaluation of spacecraft and instrument health and status. Stationkeeping maneuvers will be performed using auto navigation once every 12 hours

Communication link Information	Cruise	SOI & Saturn Moon Tour	Enceladus Orbit	Landing	Surface Operations
Number of Contacts per Week	2	5	14	1	5
Number of Weeks for Mission Phase, weeks	364	234	78	1	104
Downlink Information, includes 3 dB margin					
Downlink Frequency Band, GHz	8.4	8.4	32	8.4	32
Telemetry Data Rate(s), kbps	0.16	0.16	40.0	Tones only	40.0
Transmitting Antenna Type(s) and Gain(s), DBi	MGA 25.86	MGA 25.86	HGA 52.6	FBA 12	HGA 52.6
Downlink Receiving Antenna Gain, DBi	67.96	67.96	77.69	73.68	77.69
Transmitting Power Amplifier Output, W	65	65	60	65	60
Total Daily Data Volume, MB/day	0.288	0.576	288	N/A	81
Uplink Information, includes 6 dB margin					
Uplink Cadence	Weekly	~Daily	2x Daily	N/A	~Daily
Uplink Frequency Band, GHz	7.182	7.182	7.182	(none)	7.182
Telecommand Data Rate, kbps	0.0156	0.0156	2.0	N/A	2.0
Receiving Antenna Type(s) and Gain(s), DBi	MGA 24.5	MGA 24.5	HGA 41.2	N/A	HGA 41.2

Exhibit 3-16. Mission operations and ground data systems table. Enceladus has five major mission phases.

at apoapsis. The 12-hour elliptical orbit with stationkeeping maneuvers and spacecraft contacts at apoapsis and science data collection at periapsis is similar to the *MESSENGER* mission.

For landing, a descent orbit insertion maneuver is performed at apoapsis, followed by a 20-minute powered descent breaking maneuver at periapsis. Continuous coverage using the NASA DSN 34-m antennas will be scheduled during the landing sequence.

The Enceladus Orbilander operates on the surface for 2 years. Science data collection is performed as described in §3.1.2 and §B.1.4.3. One 6-hour communications contact per Enceladus orbit, once every 1.33 days, is required to downlink science data, downlink lander and instrument housekeeping data, uplink command loads, and real-time evaluation of lander and instrument health and status.

Risk ID	Risk	L	C	Mitigation
M1	IF autonav and onboard autonomy cannot handle the closely spaced events of the moon tour, THEN orbit pump-down will be adversely affected	2	5	(a) Pre-launch development and simulation (b) Pre-loaded backup burns
M2	IF landing event fails to be successfully completed (tipover, hazards on surface, crash, sink into snowpack), THEN science return is adversely affected	2	4	(a) Set constraints for safe landing site consistent with expectations of Enceladus surface and verify with science payload (§B.1.4.1) (b) Prioritize landing site reconnaissance in orbital phase ConOps to characterize many potential landing sites (§3.1.1) (c) Conduct pre-launch simulations of landing sequence (d) Significant science return possible from orbit alone (§B.3.3.2)
M3	IF autonomous stationkeeping is not effective, THEN orbit maintenance will require more demanding communication operations	2	3	(a) Ground in the loop to maintain orbit (b) Modify ConOps to ensure adequate data return within link budget margin (see §B.1.4.4 for current margin)
M4	IF unable to find a landing site that meets criteria, THEN science return is impacted	2	3	(a) Schedule margin accommodates extra time in orbit to identify suitable landing site (§3.1.1) (b) Stay in orbit full mission with significant science return (§B.3.3.2)
M5	IF plume density and fall rate assumptions are less than expected prior to launch, THEN sample collection will be impacted	1	3	(a) Significant collection schedule margin both in orbit and on the surface to accommodate longer accumulation times (Exhibit 3-1); (b) Use high-phase imaging to assess plume activity and update fallout model; update assumptions prior to orbit and landing; adjust orbit altitudes and landing site selection criteria (§B.1.4.1); (c) Active and passive sampling mechanisms operating on surface (§B.3.3.1)
D1	IF low-TRL instruments cannot be demonstrated at TRL-6 by PDR, THEN backup solutions must be developed to minimize impact on science return	3	3	(a) Identify backup instruments that could be used to provide lower science return. Nanopore remains highest risk; several solutions are currently being developed on existing grants and development efforts (Exhibit 2-2; §B.1.2.1). Microscope serves similar "confirmation" biosignature function (§B.1.1.1).
D2	IF mechanisms do not operate as expected in Enceladus surface environment after the long cruise, orbit, and landing, THEN science return is impacted	1	4	(a) Rigorous life testing (b) Simulated environments during pre-launch testing (c) Exercise mechanisms during cruise and orbit phase
D3	IF LV C3 capability not available in 2038, THEN backup options need to be developed	2	2	(a) Develop inner cruise backup trajectory (b) Modify thermal design for inner cruise
D4	IF NGRG power output is not at 400 W BOL and degradation not less than 1.9%/ year, THEN available power is insufficient	1	3	(a) Modify design to add 3rd RTG (if risk realized prior to PDR) and/or add additional batteries (b) Modify operations to reduce power load (c) Maintain ample power margins
D5	IF strict contamination requirements cannot be maintained during flight systems development, test, and launch, THEN science measurement will be impacted	1	3	(a) Use biobarrier (Exhibit 2-2) (b) Rigorous CC cleanliness program which supersedes PP requirements (c) Lose margin on limits of detection

Exhibit 3-17. Enceladus top risks. Risk and consequence likelihoods scale as 1 (very low), 2 (low), 3 (moderate), 4 (high), and 5 (very high). See §D.4 for more detailed definition.

3.15. Risk List

The top Enceladus Mission (M) and Development (D) Risks have been identified with likelihood (L) and consequence (C) levels along with associated mitigation strategies (Exhibit 3-17) and are summarized in a 5 × 5 risk matrix (Exhibit 3-18).

As with any surface-exploring mission, landing is a critical event that comes with inherent risks (M2, M4). Part of the mitigation is defining a safe and scientifically compelling landing site (see §B.1.4.2); the reconnaissance payload is specifically designed to meet these requirements. The other part takes advantage of the natural mitigation strategy offered by Enceladus' plumes by conducting science operations both in orbit and on the surface. If a suitable landing site is not found within the set of 42 characterized during the nominal 1.5 years of orbital operations (§B.1.4.2), Orbilander simply stays in orbit longer, continuing to search for suitable landing sites while also collecting sample to conduct repeated LDS measurements (except the nanopore). With the 4.1× schedule margin of landed operations, this extra time in orbit can be accommodated with minimal science impact. Increasingly southern latitudes become suitably sunlit as the mission continues. If no landing site is found, only the seismometer and nanopore

investigations are completely lost, though LDS investigations are limited to the smaller ice grains and vapor available in orbit (Exhibit B-8).

One of the necessary assumptions of this study is the biomass available in the plume which drives the science concept of operations (§B.1.3.1). Several mitigation strategies are employed to mitigate the risk of overly optimistic assumptions (M6). The nominal orbital phase (1.5 years) is 2.7× longer than the time estimated to collect enough sample for one contingency LDS measurement (Exhibit 3-1); the nominal schedule is therefore robust to a similar factor of low biomass. Additionally, sampling on the surface is itself a mitigation due to the access to larger volumes of material and larger plume particles. Changes to plume fallout rate are addressed three ways: including an active sampling mechanism to quickly retrieves large sample volumes; including ample schedule margin on the surface; and imaging at high phase during the moon tour. Two years of surface operations yields three contingency LDS measurements if the plume fallout at the landing site is an order magnitude lower than our assumptions (Exhibit B-9). See §B.3.3.1 for further details about the resiliency of Orbilander to biomass uncertainty.

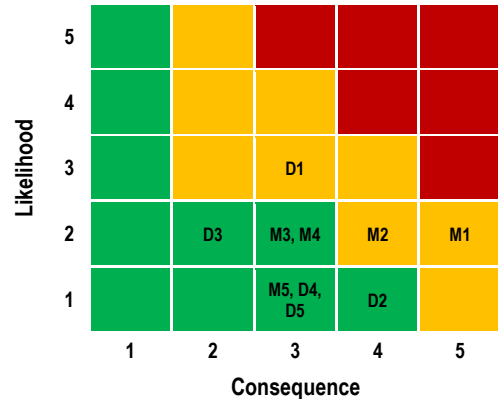


Exhibit 3-18. Enceladus risk matrix. High risks are red; medium risks are yellow; and low risks are green. Full definition of these categories is given in §D.4.

4. DEVELOPMENT SCHEDULE AND SCHEDULE CONSTRAINTS

4.1. Mission Schedule

The high-level mission schedule is based on similar APL and NASA missions and development efforts and is shown in Exhibit 4-3B while details are captured for Phases A–F of the mission in Exhibit 4-3A. This detailed schedule includes recommended pre-Phase A development activities for the LDS and the Sampling System (§2.4). The development phase critical path includes the LDS as well as design, fabrication, test, and integration and test (I&T) activities for EM and FM LDS systems and spacecraft I&T and Launch Site Processing. The schedule contains a total of 8.5 months of funded schedule reserves as illustrated in Exhibit 4-1.

4.2. Technology Development Plan

The Orbilander mission concept as defined here assumes technology development for aspects of the science payload. A TRL roadmap for the nanopore sequencer is given in Exhibit 4-2. Notably, unlike other payload elements, there are currently no flight-qualified nanopore sequencers. Cognizant of this risk, in addition to the schedule leverage, the science objectives include the search for cells as another non-chemical, “confirmation” biosignature. Thus, without the nanopore, the payload would still be capable of conducting a compelling, orthogonal search for life.

Funded Schedule Margin	Duration (Months)
Each Subsystem	3.0
KDP-C to Launch Site Readiness	4.5
Launch Site Ops Duration	1
Project Total Funded Schedule Margin	8.5

Exhibit 4-1. Orbilander schedule reserves.

The NAC also requires development to facilitate imaging in the low-light environment of Enceladus without smearing at Orbilander’s orbital velocity. This translates to enlarging the primary mirror and lengthening the optical tube (by about 40% and 20%, respectively, §B.1.2.2). Adapting the chosen instrument analog to these specifications is equivalent to a TRL 5 to 6 development. However, alternative NAC

options may be considered that do not require the same level of development. Technology development for the remaining instruments of the RSRS and In Situ Suite is in family with other flagship missions (e.g. modifications to accommodate specific implementation on Orbilander). For example, the exact radar sounder frequency and beam pattern should be specifically designed to reflect the unique environment of Enceladus (e.g. thin shell, less radiation noise than at Jupiter) and the Orbilander architecture (e.g. operating at low velocities and altitudes) as well as incorporating lessons learned and best practices from the radar sounder investigations at Europa and Ganymede with NASA’s *Europa Clipper* and ESA’s *JUICE*.

The optimum design for active sampling at Enceladus (e.g. scoop, rasp, drill) and the associated in-take mechanism (e.g. receptacle, pneumatic transfer) requires dedicated study and must be selected before or during Phase A to facilitate integration with the Sampling System and accommodation on the spacecraft.

Stage	Nanopore Technology Development	Off Ramp
TRL 3->4: <i>Proof of concept matured to breadboard and laboratory experiments show desired performance parameters for Enceladus life detection requirements.</i>	Technical requirements: system utilizes no biologics, down-selection of flight-material, multipore-conductivity measurements, signal interpretation provides a mean accuracy / pore / polymer subunit equivalent to a Phred score of 10 (i.e. 90% accuracy), technical replication (r^2) of 0.99 or greater.	Phase A
TRL 4-> 6: <i>System meets all requirements for automated operation and is demonstrated on ground.</i>	Technical requirements: performance of critical components and stability of reagents are proven in flight-like environments; interfaces to sample acquisition system developed and tested in flight-like environments.	Preliminary Design Review
TRL 6-> 8: <i>Flight qualification.</i>	Demonstration against all flight-ready parameters.	Pre-Ship Review

Exhibit 4-2. Roadmap for nanopore technology development.

5. MISSION LIFE-CYCLE COST

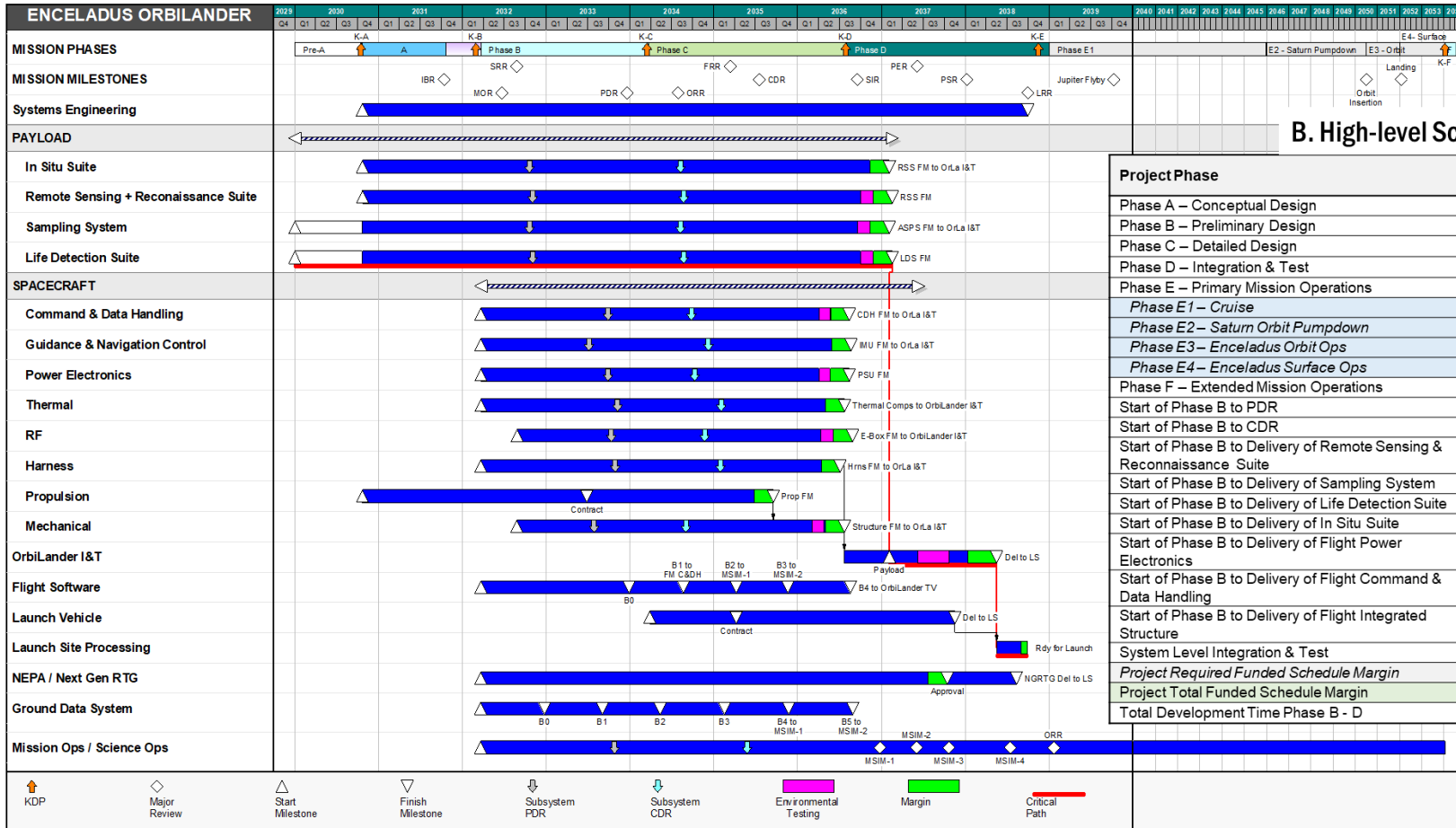
The cost estimate prepared for the Enceladus Orbilander is commensurate with a CML 4 mission concept. The payload and spacecraft estimates capture the resources required for a preferred point design and take into account subsystem-level mass, power, and risk. Our estimate also takes into account the technical and performance characteristics of components. Estimates for Science, Mission Operations, and Ground Data System elements whose costs are primarily determined by labor take into account the Phase A–D schedule and Phase E timeline.

The result is a mission estimate that is comprehensive and representative of expenditures that might be expected to execute Enceladus Orbilander as described. Including LV costs, the Phase A–F mission cost, including unencumbered reserves of 50% (A–D, excluding LV costs) and 25% (E–F, excluding DSN charges), is \$3135.6M in fiscal year 2025 dollars (FY25\$). Excluding LV costs, the Enceladus Orbilander Phase A–F mission cost is \$2557.6M FY25\$ (Exhibit 5-1).

5.1. Mission Ground Rules and Assumptions

Estimating ground rules and assumptions are derived from revision 4 of the “Decadal Mission Study Ground Rules” dated November 22, 2019. Mission costs are reported using the level-2 (and level-3 where appropriate) work breakdown structure (WBS) provided in NPR 7120.5E. Cost estimates are reported in FY25\$. The NASA New Start inflation index provided by the Planetary Mission Concept Studies Headquarters (PMCS HQ) is used to adjust historical cost, price data, and parametric results to FY25\$ if necessary. Responsibility for the mission is spread throughout the NASA community. APL is modeled as the lead facility for design, development, manufacturing, integration, and testing of the three stages and spacecraft. APL is also assumed to lead mission operations during Phase E. Design, development, and integration of instruments is assumed to include a number of organizations (for this class of mission, typically after a competed selection). Dollars to advance instruments below TRL 6 to TRL 6 are included in the development estimate. Phase A–D cost reserves are calculated as 50% of the estimated costs of all components excluding the launch vehicle. Phase E–F cost reserves are calculated as 25% of the estimated

A. Detailed A-F Schedule



B. High-level Schedule

Project Phase	Duration (Months)
Phase A – Conceptual Design	12.0
Phase B – Preliminary Design	24.0
Phase C – Detailed Design	28.3
Phase D – Integration & Test	29.0
Phase E – Primary Mission Operations	180.4
Phase E1 – Cruise	83.9
Phase E2 – Saturn Orbit Pumpdown	54.0
Phase E3 – Enceladus Orbit Ops	18.0
Phase E4 – Enceladus Surface Ops	24.5
Phase F – Extended Mission Operations	6.0
Start of Phase B to PDR	20.9
Start of Phase B to CDR	39.9
Start of Phase B to Delivery of Remote Sensing & Reconnaissance Suite	58.9
Start of Phase B to Delivery of Sampling System	58.4
Start of Phase B to Delivery of Life Detection Suite	58.9
Start of Phase B to Delivery of In Situ Suite	58.5
Start of Phase B to Delivery of Flight Power Electronics	52.8
Start of Phase B to Delivery of Flight Command & Data Handling	52.8
Start of Phase B to Delivery of Flight Integrated Structure	52.1
System Level Integration & Test	21.8
Project Required Funded Schedule Margin	4.9
Project Total Funded Schedule Margin	8.5
Total Development Time Phase B - D	81.4

Exhibit 4-3. Detailed and high-level schedules. The Orbilander concept has ample funded schedule margin (8.5 months) over the APL-required margin (4.9 months).

costs of all Phase E elements excluding DSN charges. This estimate assumes no development delays and an on-time launch in October 2038.

At present, a LV of sufficient capability to support the Enceladus Orbilander mission is in development. We assume that a LV meeting mission requirements will be available by Orbilander’s scheduled launch. LV costs are estimated based on the expected capability.

5.2. Cost Benchmarking

The cost and scope of the Enceladus Orbilander concept is well in family of a NASA flagship-class mission. The estimated cost to develop and operate the Enceladus Orbilander compares favorably to current flagship missions under development as well as past examples in Exhibit 5-1. In particular, the estimated costs for Enceladus Orbilander fall within 1.4% of the estimate at completion (EAC) for *Europa Clipper* and 13.9% of the EAC for *Europa Lander*, indicating that Enceladus Orbilander is on target in terms of science return, engineering scope, and cost for a current flagship mission.

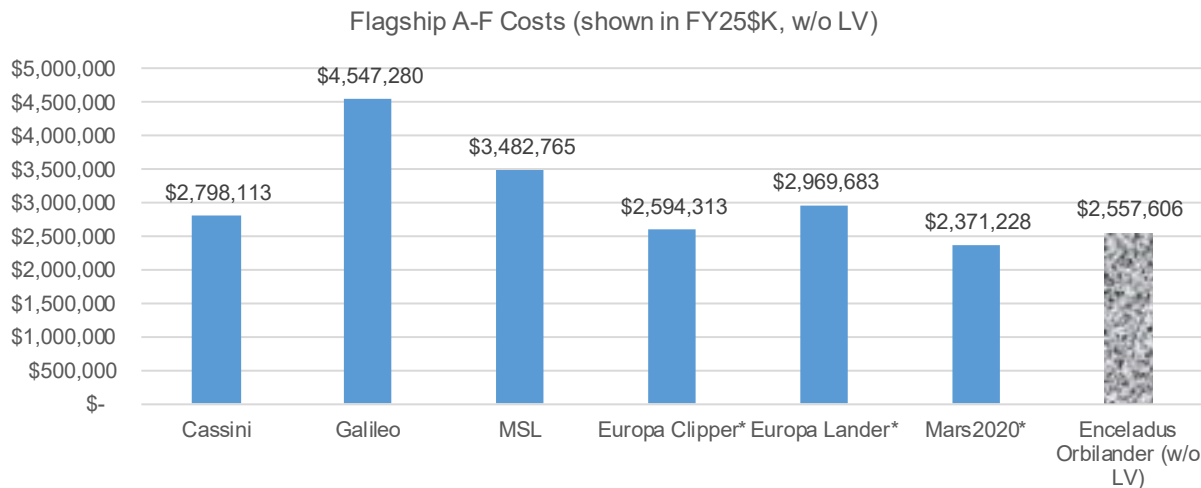


Exhibit 5-1. Orbilander cost relative to other Flagship-class missions. Missions currently in development or study are denoted with an asterisk.

5.3. Costing Methodology and Basis of Estimate

The Enceladus Orbilander CML 4 mission cost estimate is a combination of high level parametrics, bottom-up, and analog techniques and incorporates a wide range of uncertainty in the estimating process. No adjustments were made to remove the historical cost of manifested risk from the heritage data underlying the baseline estimate. Therefore, before reserves are applied, the estimated costs already include a historical average of the cost of risk. This approach is appropriate for capturing risk and uncertainty commensurate with early formulation stages of a mission. §B.4 details the basis of estimate for each element, summarized in Exhibit 5-2.

WBS	Description	Phases A–D	Phases E–F	Total	Remarks
1,2,3	PM/SE/MA	\$172,206	N/A	\$172,206	E–F contained in WBS 7
4	Science	\$50,948	\$119,446	\$170,394	
5	Payload	\$497,145	N/A	\$497,145	
	Payload Management	\$37,676		\$37,676	
	High-Resolution Mass Spectrometer	\$93,443		\$93,443	
	Separation Mass Spectrometer	\$72,751		\$72,751	
	Ion Selective Electrodes	\$17,400		\$17,400	
	Microcapillary Electrophoresis Laser-Induced Fluorescence	\$16,913		\$16,913	TRL 5
	Microscope	\$19,957		\$19,957	TRL 5
	Nanopore Sequencer	\$18,108		\$18,108	TRL 2
	Radar	\$33,100		\$33,100	
	Laser Altimeter	\$36,211		\$36,211	
	Camera	\$25,808		\$25,808	TRL 4–5
	Thermal Emission Spectrometer	\$24,968		\$24,968	
	Seismometer	\$12,066		\$12,066	
	Context Imaging	\$11,588		\$11,588	
	Sample System & Collection	\$77,157		\$77,157	TRL 5
6	Spacecraft (Orbilander)	\$463,866	N/A	\$463,866	
7	Mission Operations	\$26,816	\$285,494	\$312,311	\$29.2M DSN charges
8	Launch Vehicle & Services	\$578,000	N/A	\$578,000	\$12M RHU, \$26M RTG
9	Ground Data Systems	\$25,239	\$17,065	\$42,303	
10	System I&T	\$122,048	N/A	\$122,048	
	Subtotal w/ LV	\$1,936,268	\$422,005	\$2,358,273	
	Subtotal w/o LV	\$1,358,268	\$422,005	\$1,780,273	
	Unencumbered Reserves	\$679,134	\$98,199	\$777,333	A–D: 50%, E–F: 25%
	Total w/ LV	\$2,615,402	\$520,204	\$3,135,606	
	Total w/o LV	\$2,037,402	\$520,204	\$2,557,606	

Exhibit 5-2. Estimated Phase A–F Enceladus Orbilander mission costs by level-3 WBS element (FY25\$K).

5.4. Confidence and Cost Reserves

The cost risk ranges by major WBS element as inputs for the Orbilander probabilistic cost risk analysis to quantify total cost risk are found in Exhibit 5-3 and are described below.

PM/SE/MA. Given the use of cost-to-cost factors to estimate these functions, both the cost estimating relationship (CER) and underlying cost drivers are allowed to range so that all sources of uncertainty can be quantified.

Science, Ground Data Systems, and Mission Operations. These are low-risk cost elements but are subject to cost growth as part of the cost risk analysis.

Payload. Given that the point estimate informed by a combination of NICM and

WBS	Cost Element	Project Estimate	70th Percentile
1,2,3	Mission PM/SE/MA	\$172,206	\$243,455
4	Science	\$170,394	\$212,992
5	Payload	\$497,145	\$742,182
6	Spacecraft	\$463,866	\$616,437
7	Mission Operations	\$312,311	\$390,388
9	Ground Data Systems	\$42,303	\$52,879
10	I&T	\$122,048	\$172,545

Exhibit 5-3. Inputs to cost distributions in FY25\$K.

historical analogies for each instrument, the highest value of the historical analogy, NICM with TRL adjustments, or the SEER Space cross-check is used to inform the Enceladus payload risk model to capture the uncertainty of the CML 4 costing effort.

Spacecraft. Each subsystem is subject to a data-driven risk analysis based on historical APL cost growth. Mass input also varies in the SEER-H model consistent with early design programs to 30% over CBE.

I&T. I&T percentage used for the point estimate is the same percentage used for the risk analysis. The I&T cost risk estimate grows along with the estimated cost growth in hardware.

Per the Decadal Study Ground Rules, the estimate includes unencumbered cost reserves of 50% of the estimated costs of all Phase A–D elements except for the LV, plus 25% of the estimated costs of Phase E–F elements, excluding DSN charges. A probabilistic cost risk analysis shows 74% confidence that the Phase A–F mission is achievable within the estimated costs of this study (see Exhibit 5-4). The high confidence level is driven primarily by the robustness of the required reserves posture for this mission concept. Given a typical competitive pre-Phase A NASA environment with 25% reserves on Phase A–D elements and 10% reserves on Phase E–F elements, the probabilistic cost risk analysis shows 61% confidence that the Phase A–F mission would be achievable with the less robust reserves posture. A 50th to 70th percentile confidence level is expected and reasonable for a pre-Phase A concept with this level of reserves. A coefficient of variation (standard deviation/mean) of approximately 39% indicates appropriate levels of conservatism given the early formulation phase. The model confirms the point estimate and provides a reasonable basis for the Enceladus CML 4 study.

Description	Value (FY25\$K)	Confidence Level
Point Estimate	\$2,358,273	47%
Mean	\$2,699,757	
Standard Deviation	\$1,063,612	
Cost Reserves	\$777,333	
PIMMC	\$3,135,606	74%

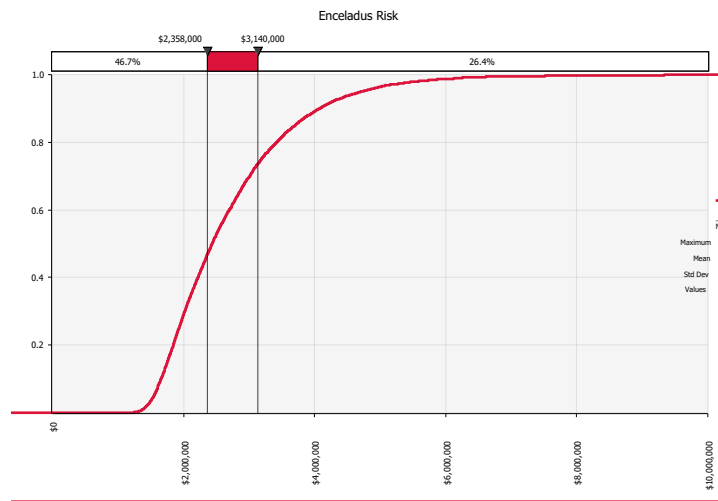


Exhibit 5-4. Cost risk analysis and S-curve summary.

APPENDIX A. ACRONYMS

AFM	Atomic Force Microscope
ALHAT	Autonomous Landing Hazard Avoidance Technology
APL	Johns Hopkins University Applied Physics Laboratory
BOE	Basis of Estimate
BOL	Beginning of Life
BOM	Beginning of Mission
BUE	Bottom-up Estimate
ΔV -EGA	Deep-space propulsive maneuver followed by Earth Gravity Assist
C&DH	Command and Data Handling
CBE	Current Best Estimate
cc	Cubic Centimeter
CCSDS	Consultative Committee for Space Data Systems
CHNOPS	Carbon, hydrogen, Nitrogen, Oxygen, Phosphorus, and Sulfur
CML 3	Concept Maturity Level 3 (trade space study)
CML 4	Concept Maturity Level 4 (point design study)
COLDTech	Concepts for Ocean worlds Life Detection Technology
ConOps	Concept of Operations
COTS	Commercial Off the Shelf
CR3BP	Circular Restricted Three-Body Problem
DART	Double Asteroid Redirect Test
DEM	Digital-Elevation Model
DNA	Deoxyribonucleic Acid
DOI	Descent Orbit Insertion
DraMS	Dragonfly Mass Spectrometer
DSN	Deep Space Network
DTE	Direct to Earth
EAC	Estimate at Completion
ELSDT	Europa Lander Science Definition Team
EM	Engineering Model
EOI	Enceladus Orbit Insertion
EOL	End of Life
EOM	End of Mission
EPS	Electrical Power Subsystem

ESA	Electrochemical Sensor Array, also European Space Agency
FBA	Fan Beam Antenna
FM	Flight Model
FOV	Field of View
GCMS	Gas Chromatograph Mass Spectrometer
GDS	Ground Data System
GNC	Guidance, Navigation, and Control
GPHS	General-Purpose Heat Source
GSE	Ground Support Equipment
GSFC	NASA Goddard Space Flight Center
HGA	High-Gain Antenna
HQ	Headquarters
HRMS	High-Resolution Mass Spectrometer
I&T	Integration and Testing
ICEE-2	Instrument Concepts for Europa Exploration 2 (NASA Program)
IEM	Integrated Electronics Module
IMAP	Interstellar Mapping and Acceleration Probe
IMU	Inertial Measurement Unit
ISO	International Standards Organization
JGA	Jupiter Gravity Assist
JPL	Jet Propulsion Laboratory
JUICE	Jupiter Icy Moons Explorer
kpbs	kilobits per second
L1, L2	LaGrange point 1, LaGrange point 2
LC-MS	Liquid Chromatography before Mass Spectrometry
LDS	Life Detection Suite
LED	Light-Emitting Diode
LGA	Low-Gain Antenna
LIDAR	Light Detection and Ranging
LV	Launch Vehicle
μCE-LIF	Microcapillary Electrophoresis with Laser-Induced Fluorescence
MatISSE	Maturation of Instruments for Solar System Exploration
MEL	Master Equipment List
MEOP	Maximum Expected Operating Pressure
MESSENGER	MErcury Surface, Space ENvironment, GEOchemistry, and Ranging

MEV	Maximum Expected Value
MGA	Medium-Gain Antenna
MICA	Microfluidic Icy-World Chemistry Analyzer
MIT	Massachusetts Institute of Technology
MPV	Maximum Possible Value
MGA	Medium-Gain Antenna
MLI	Multilayer Insulation
MOps	Mission Operations
MSL	Mars Science Laboratory
NAC	Narrow Angle Camera
NASEM	National Academies of Sciences, Engineering, and Medicine
NGRTG	Next-Generation RTGs (NGRTGs) Radioisotope Thermoelectric Generator
NH	New Horizons
NICM	NASA Instrument Cost Model
NPR	NASA Procedural Requirements
NTO	Nitrogen Tetroxide
OSIRIS-REx	Origins, Spectral Interpretation, Resource Identification, Security, Regolith Explorer
PDI	Powered Descent Initiation
PDR	Preliminary Design Review
PI	Principal Investigator
PICASSO	Planetary Instrument Concepts for the Advancement of Solar System Observations
PMCS	Planetary Mission Concept Studies
PMD	Propellant Management Device
PM/SE/MA	Project Management, Systems Engineering, Mission Assurance
PRM	Periapsis Raise Maneuver
PS	Project Scientist
PSP	Parker Solar Probe
PSU	Power Switching Unit
PRM	Periapsis Raise Maneuver
RDM	Radiation Design Margin
RF	Radio Frequency
RHU	Radioisotope Heater Unit
RNA	Ribonucleic Acid
ROM	Rough Order of Magnitude
RSRS	Remote Sensing and Reconnaissance Suite

RTG	Radioisotope Thermoelectric Generator
SAM	Sample Analysis at Mars
SBC	Single-Board Computer
SDT	Science Definition Team
SMART Nav	Small-body Maneuvering Autonomous Real-Time Navigation
SMS	Separation Mass Spectrometer
SOI	Saturn Orbit Insertion
SPS	Sample Preparation Subsystem
SPT	South Polar Terrain
SS	Sampling System
ST	Star Tracker
STM	Science Traceability Matrix
SwRI	Southwest Research Institute
TCM	Trajectory Correction Maneuver
TES	Thermal Emission Spectrometer
TID	Total Integrated Dose
TOC	Total Organic Carbon
TOF	Time of Flight
TRL	Technology Readiness Level
TRN	Terrain Relative Navigation
TWTA	Traveling-Wave Tube Amplifier
UV	Ultraviolet
V&V	Verification and Validation
VAP	Van Allen Probes
VEE	Venus-Earth-Earth
VVE	Venus-Venus-Earth
WAC	Wide Angle Camera, either of the two navigation cameras co-boresighted with the NAC
WBS	Work Breakdown Structure
WCL	Wet Chemistry Lab

APPENDIX B. DESIGN TEAM REPORT

B.1. Science Motivation and Detailed Implementation

B.1.1. Science Questions and Objectives

The primary goal of the search for life is addressed by the direct search for biosignatures and support by quantifying the habitability of the ocean and understanding the mechanics of ejection that affect the sample between its synthesis and its measurement. The latter two goals provide crucial context to the search for life. Together, these three goals represent an appropriately broad Flagship-level scientific scope, providing meaningful understanding into the extent to which, and why, Enceladus is habitable and (perhaps) inhabited. Here, we show the science traceability from goals to measurements in the STM (Exhibit 2-1).

B.1.1.1. Search for Evidence of Life Beyond Earth

There are numerous and diverse techniques for life detection (e.g. Neveu et al. 2018; Exhibit B-1), far more than can fly on any single mission. We prioritize chemical biosignatures (over structural or physiological) for several reasons. (1) The data required are broad enough to provide context amidst the search for specific biosignatures, so insight into prebiotic chemistry can be gleaned even if life is not detected. (2) *Cassini* confirmed organic compounds in the plume material, so measurements that require further analysis of organics are lower risk. (3) Several technologies are currently available (TRL 6 or higher) that can make complementary and/or repeated measurements, making the results more robust against instrumental false positives (by adding complementarity) or malfunction (by adding redundancy).

However, recognizing that a claim of life detection with chemical biosignatures alone is less convincing (e.g. Fox & Strasdeit 2017), we also include two high risk but high-reward confirmation measurements: the search for a polyelectrolyte and cell-like morphologies.

1. Pathway Complexity Index

Biochemistry on Earth facilitates and relies on the creation of a variety of complex molecules. Thus, organic molecule complexity has been put forth as a possible biosignature, though the definition of complexity remains a topic of active research. One compelling framework for quantifying this elusive biosignature is the Pathway Complexity Index put forth by Marshall et al. (2017). These authors showed that the distribution of operations and number of types of operations needed to create each molecule from an observed pool of organic compounds can distinguish abiotic from biotic processes, without assumptions about the nature of the biochemistry at work. Thus, this metric is agnostic to the kind of life that may exist on a planetary body.

A survey of the plume particulate content with a high resolution ($m/\Delta m \geq 10^3$) mass spectrometer with sensitivity range ≥ 1000 Da would provide the data necessary to determine the Pathway Complexity Index and build a context inventory of organic species that can be compared to known biotic and abiotic distributions. The broad nature of these measurements also offers the opportunity for fortuitous science return by facilitating the identification of other potential biomolecules or environmental indications such as saccharides that are not specifically targeted.

2. Amino Acid Characterization

The detection of amino acids alone is not necessarily a biosignature, given that they can be created from both abiotic and biotic processes. However, there are at least three attributes of biologically derived amino acids here on Earth that can be exploited to discern abiotic or biotic origin. (1) A pattern in the relative abundance of amino acids (the “Lego Principle”) can be a distinguishing metric (Lovelock 1965; McKay 2004; Summons et al. 2008; Shapiro 2009; Davies et al. 2009; Dorn et al. 2011). The relative

concentrations of amino acids derived from biotic sources reflect life's preference for specific molecules based on the functional roles they can bestow. In contrast, the relative concentrations of amino acids derived from abiotic sources are dictated by reaction kinetics and thermodynamics, and tend to exhibit specific patterns dominated by small, easily formed, low-formation-energy molecules. (2) Homochirality in amino acids can serve as another biosignature. Terrestrial biochemistry tends to exclusively use left-handed enantiomers, while abiotic processes are less preferential. Right-handed homochirality of amino acids would strongly suggest a biological origin from an instance of life distinct from Earth's. (3) Biological processes tend to take up light isotopes, creating an imbalance in the ratios of $^{13}\text{C}/^{12}\text{C}$, $^{15}\text{N}/^{14}\text{N}$, and D/H of the relevant compounds.

Together, these three measurements provide a more robust biosignature than any one of them, as recently discussed in detail by Glavin et al. (2019). However, given the relative difficulty of measuring the isotopic abundances of specific compounds with current high-TRL instrumentation (though technologies are advancing; see Arevalo et al. 2019), we prioritize relative molar abundances and chirality.

3. Lipid Characterization

Like amino acids, the distribution abundance pattern of lipids as a function of carbon chain-length can be used to discriminate between abiotic and biotic sources (Summons et al. 2008; Georgiou & Deamer 2014). Lipids and/or their hydrocarbon derivatives can persist in the environment over geologic time, being resilient to degradation by, e.g., heat or water (Eigenbrode et al. 2008). To detect lipids and discern structural and abundance patterns, the relative molar abundance of molecules up to ≥ 500 Da must be determined with $\leq 20\%$ accuracy. Isotopic measurements can add strength to the interpretation of a lipid distribution pattern, where biologically derived lipids would be expected to have lighter isotopes (Hortia & Berndt 1999), but are not included in this study's measurements due to a lack of high-TRL instrumentation at this time.

4. Polyelectrolyte Search

A polyelectrolyte, a polymer with repeating charge, is likely a universal feature of life indicative of biological entities capable of Darwinian evolution (Benner 2017). Depending on the detection method, this biosignature can be agnostic to the biochemistry at work (Pinheiro et al. 2012). Furthermore, the data required are broad in the sense that they could be used for characterization of the polymer (e.g. number of letters in its alphabet). The presence of a polyelectrolyte in a sample from Enceladus would be difficult to refute as evidence for life. Any contamination can be screened based on similarities to DNA/RNA on Earth, which are unlikely to be the exact same products of molecular evolution on Enceladus. Beyond "just" detecting life, this measurement may begin to crack the code of extraterrestrial genetic sequences which, together with chemical context (Objective 1), can offer insight into how any life detected on Enceladus operates from molecular to biosphere scales. The power of this measurement drove us to prioritize the search for polyelectrolytes over the characterizations of cells. The technology exists for detecting the presence of a biopolymer and sequencing but is not yet flight-qualified (Carr et al. 2017). The MinION™ nanopore sequencer, for example, has been successfully operated on the International Space Station (Castro-Wallace et al. 2017) and parabolic flights of varying simulated gravity (Carr et al. 2020), but relies upon biological pores that would degrade over long-lived missions. Synthetic nanopore systems are in development (Exhibit 2-2).

	RUNG	FEATURE	MEASUREMENT		
	Roughly, subjectively ordered by (top to bottom): 1. decreasing strength of evidence for life 2. increasing ease of measurement				
LIFE	Darwinian evolution	Changes in inheritable traits in response to selective pressures	Not practical under mission constraints		
	Growth & Reproduction	Concurrent life stages or identifiable reproductive form, motility	Cell(-like?) structures in multiple stages		
	Metabolism	Major element or isotope fractionations indicative of metabolism	Deviation from abiotic fractionation controlled by thermodynamic equilibrium and/or kinetics		
		Response to substrate addition	Waste output (compound, heat)		
		Co-located reductant and oxidant	Deviation from abiotic distribution controlled by thermodynamic equilibrium and/or kinetics		
	Molecules & Structures Conferring Function	Polymers that support information storage and transfer for terran life (DNA, RNA)	Abundance		
		Structural preferences in organic molecules (non-random and enhancing function)	Polymer with repeating charge		
		Pigments as evidence of non-random chemistries (e.g. specific pathways)	Enantiomeric excess > 20% in multiple amino acid types		
		Organics not found abiotically (e.g. hopanes, ATP, histidine)	Presence		
		Complex organics (e.g. nucleic acid oligomers, peptides, PAH)	Presence		
SUSPICIOUS BIOMATERIALS	Potential biomolecule components	Monomeric units of biopolymers (nucleobases, amino acids, lipids for compartmentalization)	Presence		
	Potential metabolic byproducts	Distribution of metals e.g. V in oil or Fe, Ni, Mo/W, Co, S, Se, P	Presence		
		Patterns of complexity (organics)	Deviation from equilibrium (P(Poisson distribution of pathway complexity) < 0.01?) or abiotic kinetic distribution		
	Biofabrics	Textures	Biologically mediated morphologies, preferably with co-located composition		
	Habitability	Liquid water, building blocks, energy source, gradier			
				microscope	
			HRMS		
			HRMS	ESA	
			nanopore		
			nanopore		
			SMS	uCE-LIF	
			microscope		
			HRMS		
			HRMS	SMS	uCE-LIF
			SMS	uCE-LIF	
			HRMS		
			HRMS	SMS	uCE-LIF
			HRMS	ESA	

Exhibit B-1. Complementarity of the life detection investigations. Left-hand side modified from Neveu et al. (2018). HRMS, high-resolution mass spectrometer; μ CE-LIF, microcapillary electrophoresis with laser-induced fluorescence; ESA, electrochemical sensor array; SMS, separation mass Spectrometer; TES, thermal emission spectrometer; NAC, narrow angle camera; WAC, wide angle camera (either of the two navigation cameras; co-boresighted with the NAC).

5. Cell Search

Identifying an intact cell can represent a strong biosignature, orthogonal to the chemical biosignatures listed above, if the identification does not rely upon morphology alone. Several additional cellular attributes are measurable with spaceflight instrumentation: motion, autofluorescence, and biomechanical properties. The motility of a cell can be readily distinguished from cell-like morphologies on random Brownian trajectories (Nadeau et al. 2016) and is thus a compelling biosignature. However, measuring motion (and biomechanical properties) requires that sampled cells remain alive after their journey from

the ocean to space (if sampled in the plume) and on the surface (if sampled there), the likelihood of which is only beginning to be constrained (Bywaters et al. 2020). To avoid the requirement of a viable cell, targeted additional attributes are restricted to autofluorescence.

B.1.1.2. Quantify the Habitability of the Enceladus Ocean

Cassini already established that Enceladus’ ocean meets the minimal requirements for habitability, thereby providing the evidentiary basis for a follow-up life detection mission. Significant improvements over *Cassini* measurements and new insight into Enceladus’ interior structure would enable major advances in quantifying the habitability of a subsurface ocean environment. This includes narrowing by orders of magnitude the current uncertainty on how much biomass Enceladus can support (see Exhibit B-26), quantifying the bioavailable energy from many metabolic reactions, and thereby providing clues about the expected spatial distribution of biomass (e.g. water-rock or water-ice interfaces and whether they extend inside the rocky core and ice shell, homogeneous distribution of metabolic substrates vs. need for concentration at patchy hydrothermal vent locations). Providing the “why”, “why not”, and “how likely” to a life detection result from an environmental perspective, the following objectives are key contextual evidence supporting the primary life-detection goal.

6. Physical/chemical environment of the ocean: hydrothermal conditions

Quantifying the habitability of the ocean (a separate question from whether it is inhabited) requires measurements of the physical and chemical state of the environment. Together, these measurements represent a rich scientific investigation that promises to provide the first detailed physiochemical picture of an extra-terrestrial ocean, with information on par in many cases with what is known about the Earth’s deep ocean. A partial list of the parameters to be determined is shown in Exhibit B-2, organized as an example flowchart for assessing the habitability of the ocean.

Determination of parameters such as hydrothermal temperatures and pH is accomplished by measuring sets of neutral and ionic species containing salts (Na, K, Mg, Ca) and the elements CHNO, all of which are geothermometers and inputs to thermodynamic models of carbon speciation (e.g. Giggenbach 1988; Glein et al. 2015; Glein & Waite 2020). The extent of hydrothermal chemistry is provided by additional such species and the measurement of ⁴⁰Ar (McKinnon 2010). Insight into the evolution of the hydrothermal system comes from comparing ⁴⁰Ar, D/H, K, and ¹⁶O/¹⁸O to baseline values and trends set by measurements of possible sources (e.g. cometary ices) and processes (e.g. volatile encapsulation in clathrate hydrates).

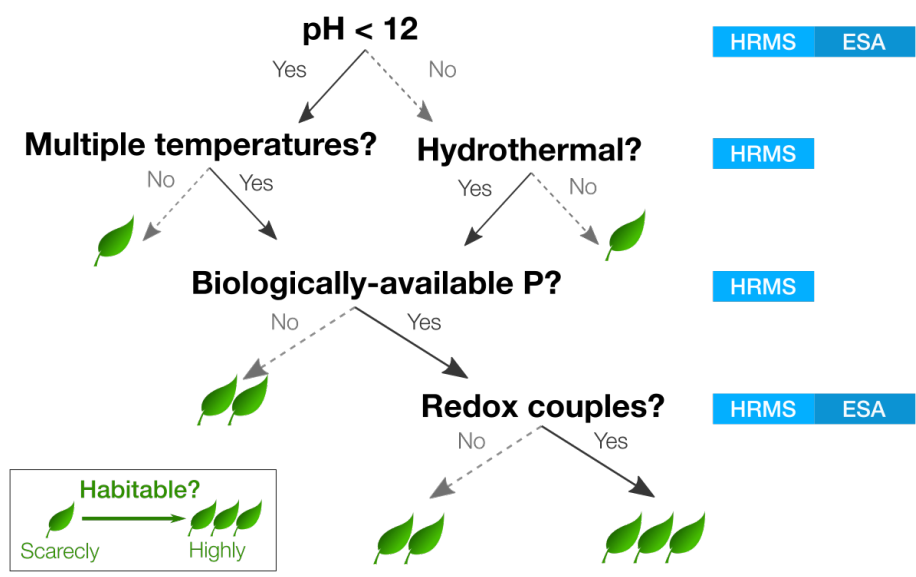


Exhibit B-2. Power of geochemical measurements as context for interpreting the life detection search results.

Assessing the bioavailability of key elements requires completing the CHNOPS inventory, especially the molecular carriers of P and S. Abundances of many pairs of reduced and oxidized species commonly found in metabolic processes on the Earth are measured to determine the redox state of the ocean relative to chemical equilibrium. This enables calculation of chemical affinities for specific metabolic reactions, which can be used to both quantify the biomass that can be supported by a given metabolism (Cable et al. 2020) and to assess the contribution of biological activity to the chemical state of the ocean (Waite et al. 2017).

7. Physical/chemical environment of the ocean: structure and dynamics of the interior Understanding the structure and dynamics of the interior via seismic and gravity-field investigations (e.g. Vance et al. 2018) provides key insight into the spatial extent and longevity of geochemical interactions. For example, a porous core provides a larger interface area for water rock interactions and has implications for internal dissipation and the conditions necessary to sustain a global ocean (e.g. Neumann & Kruse 2019). Determining the structure and dynamics of the ice shell helps quantify mechanisms and timescales of transport of oxidized species from the surface into the ocean that may act together with burial under plume fallout (million-year timescales = kilometer-scale shell thickness/millimeter-per-year fallout rates; Southworth et al. 2019). Gravity field and seismic investigations can provide observational constraints (e.g. Vance et al. 2018). Specifically, measuring the tidal Love number k_2 to better than 0.1% would help in detecting tidal lag and constraining the extent of tidal dissipation in the interior (Ermakov et al. white paper: “A Recipe for Geophysical Exploration of Enceladus”). Measurements of the relative numbers h_2 and l_2 to the same accuracy would help disambiguate the interpretation of the internal rheology. The seismic package described in this study would have a high likelihood of detecting waves generated by strike slip motions in the ice and possibly also noise generated at the ice-ocean interface by turbulent fluid flows. Detecting waves *generated* in the rocky interior may prove difficult, given the unique problem in ocean worlds that the global ocean filters out the shear components of seismic waves, but both gravity and seismic measurements would be useful in detecting and inferring porous region in the upper part of the rocky interior. Seismology might also be used to investigate stratification in the ocean. Seismic propagation in Enceladus, including waves from the deeper interior, is an active area of study (white papers by Vance et al.: “Planetary Seismology: The Solar System’s Ocean Worlds” and “Distributed Geophysical Exploration of Enceladus and Other Ocean Worlds”), but Enceladus’ seismic activity should be more observable than events on the Moon due to the icy satellite’s small size and short tidal cycle.

8. Investigate plume ejection mechanisms

The presence of water-rock interaction products in the ice grains (Postberg et al. 2011; Hsu et al. 2015; Waite et al. 2017) proves that the ultimate source of the plume material is the subsurface ocean. . Diverse compositions of plume grains coming from this single reservoir suggest that compositional enrichments or depletions are at play, e.g. due to phased changes such as vaporization at the top of the water table with possible aerosolization, sublimation from grains, and condensation of vapors (Khawaja et al. 2019).

The path between ocean and surface, however, remains ill constrained. Several hypotheses have been put forward (e.g. Schmidt et al. 2008; Kite & Rubin 2016; Spencer et al. 2018). Discerning between these hypotheses would provide another “why”, “why not”, or “how likely” behind a life detection result by constraining the possible modifications plume material might experience along the journey from the ocean to space, and using that information to infer ocean conditions and the nature and composition of ocean material from measurements of plume material. These science objectives address how representative the plume material is of the ocean, and how to account for any ejection-driven changes to ocean material.

Establishing whether fluid reservoirs or structural heterogeneities exist within the crust would indicate whether the plume plumbing includes pockets or sills where oceanic material can concentrate (e.g. due to partial freezing). Radar sounding can reveal these structures similar to interrogations of terrestrial glaciers and ice shelves (e.g. Blankenship et al. 2009) and will be used to interrogate the Jovian moons on upcoming missions *Europa Clipper* and *JUICE* (e.g. Bruzzone et al. 2013, Heggy et al. 2017). The thickness of the crust, especially at the south polar terrain, defines the minimal path length for a conduit between the

ocean and surface, and can be determined from radar sounding and seismic monitoring (e.g. Vance et al. 2018). By analogy with geysers and other subsurface fluid motions on Earth, seismic measurements would also reveal the amounts of materials, their speed, and fluid-to-gas transitions occurring during ascent from the ocean. Active and passive electromagnetic measurements would offer similar advantages. Measuring the surface expression of the vent structures – morphology, topography, and thermal properties – conveys information about the venting mechanics (e.g. Nimmo et al. 2014) and associated conditions encountered by the sample (e.g. temperatures, pressures, velocity vectors, compositional interfaces).

In addition to facilitating the search for biosignatures, Orbilander’s measurements of the composition of plume ice grains and vapor as a function of altitude and Enceladus’ mean anomaly enable, respectively, investigations of whether kinetics of freezing influence composition (Thomas et al. 2019), and of the orbital control on plume activity observed by *Cassini* (Ingersoll & Ewald 2017; Ingersoll et al. 2020).

B.1.2. Traceability to Science Payload

In Exhibit B-3, Exhibit B-4, and Exhibit B-5, we show the characteristics of the model payload. These values were derived from previously flown examples and instruments in development. Notably, especially in the Life Detection Suite, we select a suite of instruments with some overlapping capabilities. This is to ensure robustness of the science investigation at the level expected for a flagship-class mission. The model payload shown here proves that a robust search for life at Enceladus is possible in the next decade with a reasonable flagship-class budget. Other implementations, especially of the LDS, are possible and could be explored.

Item	HRMS	SMS	ESA	μCE-LIF	Microscope	Nanopore	Units
Size/dimensions	0.39 × 0.39 × 0.39	0.15 × 0.25 × 0.12	0.1 × 0.1 × 0.2	0.15 × 0.15 × 0.15	0.11 × 0.2 × 0.1	0.14 × 0.22 × 0.15	m × m × m
Instrument mass without contingency (CBE)	20	12	3	3.6	3	4	kg
Instrument mass contingency	30	30	30	30	30	30	%
Instrument mass with contingency (CBE+Reserve)	26	15.6	3.9	4.68	3.9	5.2	kg
Instrument average payload power without contingency	70	65	15	6	15	5	W
Instrument average payload power contingency	40	40	40	40	40	40	%
Instrument average payload power with contingency	98	91	21	8.4	21	7	W
Instrument mission data volume without contingency	6480	1476	252	1.8	297	12000	Mb
Instrument mission data volume contingency	30	30	30	30	30	30	%
Instrument mission data volume with contingency	8.424	1.9188	0.3276	0.00234	0.3861	15.6	Gb

Exhibit B-3. Instrument characteristics used to model the Life Detection Suite.

	Narrow-Angle Camera	Wide-Angle Camera	Thermal Emission Spectrometer	Laser Altimeter	Radar Sounder	Units
Size/dimensions	0.39 × 0.39 × 0.70	0.78 × 0.56 × 0.44	0.18 × 0.18 × 0.13	0.26 × 0.28 × 0.28	1.4 × 2.0 × 0.025	m × m × m
Instrument mass without contingency (CBE)	20	0.4	3.8	7.4	12	kg
Instrument mass contingency	30	30	30	30	30	%
Instrument mass with contingency (CBE+Reserve)	26	0.52	4.94	9.62	15.6	kg

	Narrow-Angle Camera	Wide-Angle Camera	Thermal Emission Spectrometer	Laser Altimeter	Radar Sounder	Units
Instrument average payload power without contingency	5	2.50	13.00	16.5	25.00	W
Instrument average payload power contingency	40	40	40	40	40	%
Instrument average payload power with contingency	7	3.50	18.20	23.1	35.00	W
Instrument average science data rate without contingency	4190	4190	1157	10	8000	kbps
Instrument average science data rate contingency	30	30	30	30	30	%
Instrument average science data rate with contingency	5447	5447	1505	13	10400	kbps
Instrument fields of view	0.293	44.003	1	0.02	n/a	degrees

Exhibit B-4. Instrument characteristics used to model the Remote Sensing and Reconnaissance Suite.

	Context Imager	Units		Seismometer	Units
Size/dimensions	0.38 x 0.25 x 0.15	m x m x m	Size/dimensions	0.075 x 0.075 x 0.045	m x m x m
Instrument mass without contingency (CBE*)	4	Kg	Instrument mass without contingency (CBE*)	5.00	kg
Instrument mass contingency	30	%	Instrument mass contingency	30	%
Instrument mass with contingency (CBE+Reserve)	5.2	Kg	Instrument mass with contingency (CBE+Reserve)	6.50	kg
Instrument average payload power without contingency	11.8	W	Instrument average payload power without contingency	4	W
Instrument average payload power contingency	40	%	Instrument average payload power contingency	40	%
Instrument average payload power with contingency	16.52	W	Instrument average payload power with contingency	5.6	W
Instrument mission data volume without contingency	5400	Mb	Instrument average science data rate without contingency	0.35	kbps
Instrument mission data volume contingency	30	%	Instrument average science data rate contingency	30	%
Instrument mission data volume with contingency	7.02	Gb	Instrument average science data rate with contingency	0.46	kbps
Instrument field of view	15 per lens	degrees	Instrument fields of view	n/a	degrees

Exhibit B-5. Instrument characteristics used to model the In Situ Suite.

B.1.2.1. Life Detection Suite

A **high-resolution mass spectrometer** (HRMS) conducts the volatile organic and inorganic characterization for Sci. Obj. 1, 6.1-4, 7D, and 8.2 (see Exhibit 1-1). Our modeled instrument is a time-of-flight (TOF) mass spectrometer that separates ions by their transit time through a multi-bounce ion optical system. Advantages include high mass resolution ($m/\Delta m > 20,000$), wide mass range and a small footprint. A gas inlet with a cryotrap facilitates sampling the vapor during plume fly-throughs. Interior to the spacecraft, the HRMS also receives vapor from the ice particle Sampling System. Some recently flown or in-development HRMSs include MASPEX on *Europa Clipper* (Brockwell et al. 2016) and COSAC on *Rosetta Philae* (Goesmann et al. 2007). Other HRMS instruments in development for flight include the Orbitrap (Denisov et al. 2012; Briois et al. 2016; Arevalo et al. 2018; Selliez et al. 2019, 2020) and multi-turn TOF mass spectrometers (Toyoda et al. 2003).

The **separation mass spectrometer (SMS)** is used to characterize simple and complex molecules, including amino acids (relative abundance and enantiomeric excess) and lipids for Sci. Obj. 2 & 3. We selected a gas chromatograph mass spectrometer (GCMS) as the model instrument type due to its high TRL: *Curiosity* SAM (Mahaffy et al. 2012), *ExoMars* MOMA (Goesmann et al. 2017), and *Dragonfly* DraMS (Trainer et al. 2018) all include GC capabilities. After heating a sample or applying a derivatization agent to it, volatilized gases are passed through the capillary column to separate compounds by their retention time (related to molecular mass and polarity) at high enough precision to distinguish a full range of organic compounds including enantiomers. Other approaches, such as augmenting a GCMS with capillary electrophoresis, coupled to the same MS, are in development (PI Brinckerhoff, 18-ICEE2_2-0044; Creamer et al. 2017). Separation of individual compounds by liquid chromatography before their identification by MS (LC-MS) is also under investigation (e.g. Getty et al. 2013; Southard et al. 2014), although the difficulties associated with the handling of such liquids in space environments make this technique of lower TRL.

The **electrochemical sensor array (ESA)** characterizes the physical and chemical environment of the ocean (Sci. Obj. 6) by measuring the soluble ionic species in the melted plume ice grains and also determining average and individual-species redox potentials, salinity, and pH. The Wet Chemistry Lab (WCL) on *Phoenix* was the first of this kind of spaceflight instrument; it successfully operated on the surface of Mars (Kounaves et al. 2009, 2010). Recent developments—e.g. the microfluidic WCL (mWCL) and Sample Processor for Life on Icy worlds (SPLIce) supported by NASA-COLDTech and the Microfluidic Icy-World Chemistry Analyzer (MICA) supported by the NASA ICÉE-2 program—employ microfluidic engineering to decrease the volume of both the instrument and of sample needed (Chinn *et al.* 2017; Radosevich et al. 2019; Noell et al. 2019). The fluidics system that integrates the sensor array of this science instrument maximizes the synergies with the capabilities and functions of the sample transfer and processing system; some critical measurements, e.g. pH and ionic conductivity, are purposefully redundant to increase measurement certainty and provide limited dual-string capability with minimal mass and complexity penalties.

Sci. Obj. 1,2, and 3 are also addressed with measurements by the **microcapillary electrophoresis-laser induced fluorescence** microfluidics device. Fluorescent reagents specific to functional groups are mixed with the sample solution, passed through a capillary electrophoresis system to separate compounds by charge and by size, and then analyzed via laser induced fluorescence; this yields information on the concentration (from fluorescence intensity) and compound identity (time of appearance in the system) (e.g. Stockton et al. 2008, 2009, 2010, 2011). Molecules containing amino and/or carboxylic acid groups are identified with better than nanomolar sensitivity (sub-ppb) (Mathies et al. 2018). Chirality can be measured via micellar electrokinetic chromatography (Chiesel et al. 2009). These techniques rely on concentration rather than mass to achieve high sensitivity through sample accumulation and are thus specifically complementary to the SMS and HRMS investigations. Several independent and collaborative efforts are developing these kinds of instruments (Exhibit 2-2).

A **microscope** conducts the search for evidence of cells of Sci. Obj. 5. Given the relative ambiguity of relying on morphology alone for cell identification, measuring a second cell characteristic coincident with promising morphology is key to collecting less ambiguous evidence (ELS DT, Nadeau et al. 2018). For the Orbilander, we chose autofluorescence as the second characteristic as it does not require viable cells (ELS DT, Bhartia et al. 2010). More study is needed to elucidate whether autofluorescence alone would be diagnostic given the expected organic content of the plume or if/which fluorescent tags should be employed. Alternative cell characteristics could be considered. Digital holographic microscopes are capable of distinguishing biological from Brownian motion (e.g. Nadeau et al. 2016; Serabyn et al. 2016; Bedrossian et al. 2017). Atomic force microscopes (AFM) can probe the biomechanical properties of cell candidates (Dorobantu et al. 2012) and have been flown for non-astrobiology science objectives (Barth et al. 2001). The Orbilander microscope is modeled after the requirements described by the ELS DT (without the AFM component) and is based on the *Phoenix* MECA microscope (Hect et al. 2008). Several groups are funded to develop microscopes specifically for astrobiological (rather than geochemical) investigations, microscopes that utilize multiple excitation wavelengths (including deep-UV) to excite biological

autofluorescence and fluorescent stains that target structural and functional biomarkers (membrane lipids and proteins; Quinn et al. 2019) and digital holographic imaging (Kim et al. 2020).

Polyelectrolytes are detected and characterized with a **solid state nanopore sequencer** to address Sci. Obj. 4. Liquid sample is passed through a flow cell with synthetic pores with an applied electric field across the flow cell plane. Polyelectrolytes are made up of repeating sets of polymer features, such as the nucleobases A,T,G, and C of a DNA polymer. When a polyelectrolyte is passed through the pore, different types of features induce a current change, and the magnitude and direction of that change (positive or negative) can be indicative of that feature. Thus, the successive changes in current can identify both the single polymer features, and their ordered sequence. As described in §1 and §B.1.1.1, the science return of this kind of analysis is so powerful that this instrument is a key component of the Orbilander LDS, despite currently at low TRL. Development of solid state synthetic nanopore sequencers includes NASA programs, academic groups, and commercial enterprises, which suggests the TRL will not stay low for very long with continued funding. However, as mentioned in §3.15 and §4.2, a compelling, flagship-class astrobiological investigation at Enceladus in the next decade, like the Orbilander concept described here, does not fundamentally require a solid state nanopore sequencer, should development not proceed as anticipated.

B.1.2.2. Remote Sensing and Reconnaissance Detection Suite

The **Narrow Angle Camera (NAC)** provides the sub-m resolution imaging required to characterize surface topography (Sci. Obj. 8.1) and surface expression of the vents (Sci. Obj. 8.3), and to identify a safe landing site (Sci. Obj. 9). The NAC is modeled on the LORRI camera (Cheng et al. 2009) on *New Horizons*, which has sufficient resolution in a compact athermal design. However, to avoid smearing of high-resolution images at the spacecraft's orbital speed near periapse at Enceladus short exposure times of ~1 ms are required. This led to a need to enlarge the LORRI primary mirror to ensure sufficient light gathering for high SNR at these short exposure times. Other implementations could be pursued.

The **Wide Angle Camera (WAC)** is either of the two wide angle cameras co-boresighted with the NAC carried as part of the Navigation Camera package (§3.6–3.7). (Two navigation cameras are co-boresighted with the NAC for redundancy.) It provides the broad coverage of the south polar terrain at coarser resolutions to allow the science team to identify candidate landing site targets for the NAC observations. This strategy is critical to accomplishing Sci. Obj. 9 in a timely manner. However, the most demanding WAC requirements come from navigation (§C.1, §C.2) rather than science. The Orbilander WAC is modeled after ECAM-M50 from Malin Science Subsystem, a monochrome detector with electronics and optics similar to instruments that have flown on several previous missions.

The **Thermal Emission Spectrometer (TES)** is modeled as a point spectrometer whose measurements of surface thermal emission inform the physical structure at the jet vents (Sci. Obj. 8.3) as well as ensuring the safety of the landing site (Sci. Obj. 9; §B.1.4.2). The resulting temperature maps must have temperature sensitivity of DK~1K and FOV < 2° to image the landing site candidates (5 km × 5 km) at least two pixels across. (Too fine an FOV would place greater demands on the reconnaissance campaign and data return than what is described in §3.1.1 and §B.1.4.2.) We model the Orbilander TES on MERTIS on *BepiColombo*; other examples of this kind of instrument include OTES on *OSIRIS-REx* (Christensen et al. 2018), TES on *Mars Global Surveyor* (Christensen et al. 2001), and ETHEMIS on *Europa Clipper*.

To map the surface topography for Sci. Obj. 8.1 and 8.3 and to identify a safe landing site (Sci. Obj. 9), we use a **laser altimeter** modeled after OLA, the laser altimeter on *OSIRIS-REx*. The requirements for the laser altimeter are driven both by science (10 cm vertical resolution, sub-m spatial resolution) and by hazard avoidance (§C.2). In addition to OLA at Bennu, laser altimeters have flown to Mars (Zuber et al. 1992), Mercury (Cavanaugh et al. 2007), and the Moon (Smith et al. 2010).

The **radar sounder** addresses Sci. Obj. 8.1 and 8.3 from orbit with 10 m vertical resolution, driven by the anticipated physical structures of the vent and crust. Notably, Enceladus' south polar terrain (SPT) is presumed to be thinner and potentially in a melting regime (5 km at the SPT; Thomas et al. 2016; Cadek et

al. 2016), as well as more uniform in depth when compared to Europa where complex thermal and chemical horizons are expected to be distributed through the ice shell (e.g. Soderlund et al. 2020). Because of the number of questions regarding how and where fissures and vents operate in the subsurface of Enceladus, and their structure, we selected a 60 MHz radar system, with heritage from the VHF element of *Europa Clipper* REASON, as the model payload for Orbilander. To achieve the vertical resolution requires 15 MHz bandwidth, giving 25% relative bandwidth with a 60 MHz carrier frequency. A log-periodic dipole array 2 m long and 1.42 m at the longest crossbeam can satisfy these requirements. The 2-m boom is deployed post-EOI. Further study into the specific requirements for and implementation of a sounding investigation at Enceladus is particularly warranted given the uniqueness of the crust (thinner, different thermal gradients, potentially high porosity layers, etc.) relative to that of the Galilean satellites that have been studied for *JUICE* and *Europa Clipper*.

B.1.2.3. *In Situ Suite*

Selecting the target site for the active sampler requires a **context imager** capable of resolving the 1.5 m in front of the instrument panel at 500 μm per pixel to discern the largest grains. At least 50% overlap is necessary for stereo coverage. To facilitate imaging in the low light conditions expected during the landed phase of the mission, a simple white-light LED lamp adds a circuit board of approximately 2×3 inches into the camera electronics box. The Orbilander context imager is modeled after ELSSIE, a context imager designed for the Europa Lander (PI Murchie, APL), which is also capable of conducting a spectroscopic investigation to characterize sample provenance. The latter is not a driving requirement for Orbilander as the surface materials we target are plume fallout materials, which we will already have some understanding of from the compositional analyses conducted in the orbital phase. Examples of other context imagers include the Stereo Surface Imager on *Phoenix* (Lemmon et al. 2008) and CLIFE (PI Byrne, University of Arizona).

The **seismometer** addresses Sci. Obj. 8.1 and 8.3. Notably, these are the same objectives addressed by the radar sounder, addressed in a highly complementary manner. The seismometer is sensitive to structural transitions at much greater depths than the radar sounder (especially since we have chosen a higher frequency carrier to resolve the near surface crust at higher vertical resolution) and to the dynamics of the interior in real time. Tidally driven seismic events on Enceladus should occur at least twice a month and be of the same order of magnitude as lunar seismic events (Hurford et al. 2020); other possible sources of activity include ice shell fracturing, ocean currents, and geyser activity (Stahler et al. 2018; Vance et al. 2018). Monitoring the timing and location of these events can reveal the interior structure of Enceladus.

Noise estimates for seismic activity at Europa suggest that high-frequency geophones may be sufficient seismic probes there (Panning et al. 2018), but dedicated study of the conditions at Enceladus is necessary to make the same claim at Enceladus. For example, the magnitude of tidal events at Enceladus is predicted to be 3 orders of magnitude lower than at Europa (Hurford et al. 2020), but since Enceladus' is a smaller body, each event will be subject to less geometric spreading. In the absence of such studies, we use the requirements outlined in Vance et al. (2018) for the Orbilander seismic investigation. A short period seismometer capable of monitoring frequencies 0.1–10 Hz, such as the SEIS-SP on *InSight* (Lognonné et al. 2019), serves as our model implementation. Development of seismic packages specifically for ocean world deployment is currently underway via PICASSO (PI Yee, JPL), MaTISSE (PI Chui, JPL), ICEE-2 (PI Bailey, University of Arizona; PI Panning, JPL), and COLDTech (PI Yu, Arizona State) programs.

B.1.2.4. *Sampling System*

The Sampling System requires several five key steps.

- (1) *Collection*: Orbilander has three collection mechanisms: passive particle collector, active particle collector, and a gas inlet. A 1-m² funnel passively collects ice particles during plume flythroughs and while sitting on the surface (Adams et al. 2018). The funnel opening is protected by a recloseable cover during cruise and during descent. Collecting ice particles at the low relative velocity of the orbit

and at near zero relative velocity when landed eliminates impact-induced changes to the sample: particles in the plume travel at velocities 100–200m/s (Guzman et al. 2019) while Orbilander’s translational velocity is up to 200 m/s. (The model funnel has been tested for collection at up to 2 km/s.) Active sample collection is only conducted on the surface. The collector is modeled here as a scoop capable of retrieving 5 cc of surface ice. Optimization of the active collector (e.g. scoop, rasp, drill, pneumatic transfer) for the cold, low-gravity Enceladus environment is beyond the scope of this study but should be done in the next phase of study. The funnel and scoop both collect ice particles that are then melted within a sealed environment and then transferred to the sample preparation subsystem. A gas inlet allows vapor to pass into the HRMS during plume flythroughs; a cover prevents contamination during cruise. Descent contamination of the inlet is possible but not of concern, as on the surface the HRMS is supplied vaporized ice grains by the SS.

- (2) *Delivery to interior*: The funnel and scoop each have separate cups for receiving sample. These receiving mechanisms are kept cold to minimize sample modification before analysis. When ready for analysis, the cups are sealed and brought into the interior; alternative arrangements that minimize transfer mechanisms, as is being investigated via ICEE-2 by Honeybee and NASA Ames for the Europa Lander, may be considered.
- (3–4) *Processing and delivery to instruments*: Cups are heated to melt the ice grains. The resulting liquid is then transferred through microfluidic tubes to the Sample Preparation Subsystem (SPS) which can either deliver pristine liquid directly to an instrument or conduct preparation steps—such as filtering, division, extraction, tagging, derivatization, concentration, de-salting, de-bubbling, and characterization of properties like salinity and pH—depending on the needs of the instrument (e.g. Chinn et al. 2017, 2018; Radosevich et al. 2019). Estimating the amount of sample acquired helps inform distribution to the instruments downstream and is part of the SPS. The SMS contains a hermetically sealed supply of ultra-pure water, inert gases and dry reagents (including calibrants and standards) for sample preparation. Liquids are then delivered to the ESA, μ CE-LIF, microscope, and nanopore via microfluidic capillary tubes. The SPS provides vapor to the SMS and HRMS by vaporizing the liquid sample.

Housing common preparation techniques in one unit is an advantageous minimization of mass, power, and volume resources (e.g. efficient dual-string implementation of certain key components like pumps and sensors). Successful implementation requires an early, coordinated effort between instrument teams, which would be facilitated by continued development of microfluidic preparation and delivery systems (e.g. Exhibit 2-2). Supplies are provided for more than twice the required samples.

- (5) *Flushing*. A reservoir of sterile, contaminant-free solution flushes the SS in between analyses.

B.1.3. Sample Collection Strategies

B.1.3.1. Sample Requirements

To determine how much sample must be acquired to conduct the life detection measurements described in §B-1, we modeled the potential biomass of Enceladus’ ocean. The range of possibilities is quite large (see Exhibit B-26 and related discussion), so we present our choices, shown in Exhibit B-6, and rationale in this section.

Payload Element	Target Measurement	Expected Ocean Abundance		Instrument requirements						# Independent Analyses	Total Plume Material	
				Instrument LOD		Measurement Volume		Sample Volume				
HRMS	1.A-C; 6.1B; 6.2; 6.3; 6.4; 7D; 8.2A	3E-11	mol/ μ L	5E-15	mol/ μ L	1	μ L	0.0005	μ L	5	0.0025	μ L
SMS	2.A-B	1.5E-13	mol/ μ L	2E-11	mol	1		400		5	2000	
	3.A	3E-14	mol/ μ L	1E-12	mol	1		100		500		
μ CE-LIF	2.A-B,3.A	1.5E-13	mol/ μ L	3E-16	mol/ μ L	3		15		75		
ESA	6.4 Macronutrients	1.00E-08	mol/ μ L	1.00E-10	mol/ μ L	50		1.50E+00		5	375	
	6.4 Micronutrients	2.00E-10	mol/ μ L	1.00E-10	mol/ μ L			7.50E+01				
	6.1 pH	8 to 12		2-14			n/a					
	6.3 Salinity	0.5-3	%	0.01-30	%		15					
	6.4 Eh	-1.0 to 1.0	V	-1.0 to 1.0	V		n/a					
Microscope	4	1	cells/ μ L	1	cells	1	1		5	5		
Contingency Total								0.608	mL		2.96	mL
Nanopore	5	1E-15	g/ μ L	5E-12	g	1		10		3	30	
Full Total								10.6			33.0	

Exhibit B-6. Sample requirements for each measurement and instrument of the LDS derived for this study.

We modeled the expected total organic carbon (TOC) of the Enceladus ocean as 30 μ M (1 M = 1 molal = 1 mol per kg of H₂O), a value in between that of the average and the cold polar waters of Earth's oceans and on par with the ELSDT model for Europa (41 μ M). Unlike at Europa, our model can be compared to in situ data from *Cassini* CDA. In Saturn's E-ring, 8% of the organic-rich Type II grains have an organic concentration of 1 mM (Khawaja et al. 2019). Lower in the plume, the Type II population is more abundant, >30%, suggesting an overall concentration of organic material in the plume of ~24 μ M, in line with our terrestrial model.

We then set the expected abundance of amino acids from the ratio of protein to organic content in Earth's oceans, 1:200 (25 fg protein/cell, Zubkov et al. 1999; 10⁵ cells/g water, Whitman et al. 1998; 0.5 ppm by mass TOC, Thurman 1985). This is less conservative than the ELSDT 1:400 ratio, but lower than the predictions of Steel et al. (2017) of tens of μ M of amino acids. For lipids, we again employ a terrestrial ratio of lipids to amino acids in cells, 1:5. The concentration of free DNA in Earth's oceans is 100 ng/L (Collins et al. 2018), so we assume the same concentration of biopolymer material in Enceladus' ocean. Macro- and micro-nutrient abundances, pH, salinity, and Eh were based on *Cassini* results (e.g. Postberg et al. 2008, 2009, 2011; Hsu et al. 2015; Waite et al. 2017) and geochemical models of the Enceladus ocean (Sekine et al. 2015; Glein et al. 2015; Glein & Waite 2020).

We assumed that the cell concentration in Enceladus' ocean is 10³ cells/mL based on predicted values ($\leq 5 \times 10^3$ cells/mL; Steel et al. 2017; Cable et al. 2020) derived from interpretation of *Cassini* measurements of available energy and nutrients in the plume and measurements of microbial demands. (The biomass concentration in plume material might be higher, $\leq 10^7$ cells/mL, if plume enrichment processes such as bubble scrubbing are at play; Porco et al. 2017). Our assumption is higher than that of the Europa Lander study (100 cells/mL) derived from analog Earth environments and energetic considerations rather than direct measurements, and two orders of magnitude lower than the biomass density in Earth's oceans ($\sim 5 \times 10^5$ cells/mL; Whitman et al. 1998). The concept of operations is designed to be robust to lower biomass concentrations (Exhibit B-7). On the surface, an active sampling mechanism increases collectable sample volume and thus resiliency to biomass densities (Exhibit B-26).

B.1.3.2. Instrument Requirements

In Exhibit B-6, the limit of detection (LOD) and volume necessary to run a measurement for each instrument type were taken from published values for analogous instruments that have flown or are in development. The sample volume required for detection is thus the measured volume multiplied by the instrument LOD (including a factor of 3 for signal-to-noise ratio) divided by the expected ocean abundance.

	Cell Concentration (cells/mL)	Biopolymer Concentration (pg/mL)
Earth oceans	10^5	100
Enceladus ocean	10^3	1

Exhibit B-7. Expected biomass and biopolymer concentration in the Enceladus ocean and in Earth's ocean.

Since solid-state nanopore systems are at relatively low TRL at the time of this study, we describe here in detail how the requirements for this instrument were defined. We assumed a solid-state nanopore system that can withstand long spaceflight duration with at least four wells delivering at least four synthetic nanopores (and thus the capability for four independent analyses; this number being limited by data storage and data transfer rates, see §B.1.4.2). Sample preparation steps necessary for biopolymer detection and sequencing were assumed to be part of the instrument itself, but could be levied on the sample preparation system.

State-of-the-art nanopore sequencing systems can detect 10^{-3} pg biopolymer (equivalent to 10^3 reads of average length 10^3 bases, or 10^6 bases) in a sample that contains 1 ng biopolymer per mL (Carr et al. 2017). The expected concentration of biopolymer in the Enceladus ocean, extrapolated from comparisons with Earth's oceans, is 1 pg/mL (Exhibit B-7). To obtain 1 ng biopolymer per mL, the original sample must be concentrated by a factor of 1000. Since the sample volume required to perform a nanopore analysis is 10 μ L, the minimum original sample volume for an exotic biopolymer detection at Enceladus is 10 mL (Exhibit B-6).

B.1.3.3. Sample Collection

The Enceladus plume can be considered as four different reservoirs of material (Exhibit B-8). At altitudes $>\sim 40$ km, the individual jets mix, creating a more favorable environment for vapor sampling but particle sizes are on the order of nanometers. Below 40 km, the collimated jets contain larger, micron-sized particles (Guzman et al. 2019). On the surface, fresh fallout of larger particles (too heavy to achieve escape velocity) can be intercepted with a passive collection mechanism. Finally, surface deposits are also available, offering the opportunity to rapidly collect large sample volumes with an active sample collector. These deposits may have experienced some modification from weathering (Bergantini et al. 2014) or sintering (Choukroun et al. 2020), however.

In Enceladus orbit, the spacecraft velocity peaks at ~ 200 m/s, about the escape velocity of jet particles. Plume fly-throughs at these velocities thus allow collection with little modification to the sample. We modeled the passive collector as a funnel (Adams et al. 2018) but alternative approaches such as a plate may be suitable (Mathies et al. 2017). Using the model of Guzman et al. (2019), we assume that the flux particulates in these reservoirs is $1.6 \mu\text{L}/\text{m}^2/\text{orbit}$. This is conservatively at the lower end of published flux values (Porco et al. 2017, for example, estimate up to $6 \mu\text{L}/\text{m}^2/\text{orbit}$). Each orbit, particulates are accumulated until a desired volume is reached. The sample collection system must therefore be able to determine how much sample is acquired. The Orbilander Sampling System includes this capability (§B.1.3.4). Alternative solutions include by microscopic imaging of the collector (if the geometry allows) or of a witness plate. One could envision a set-up similar to the optical and/or atomic force microscopes onboard *Phoenix* and *Rosetta*, tailored to the expected size and number density of collected particles (Bentley et al. 2016). Alternatively, one could measure the effect of a changing mass of the collection surfaces on the frequency of a quartz crystal microbalance. This technique is commonplace in monitoring chemical contamination (e.g. deposition of organic compounds outgassed from tapes or glues) during spacecraft assembly or even in flight (Dirri et al. 2019). If the collected mass is significant (e.g. landed collection), its effect on the collector or spacecraft inertia could be monitored. This was the approach

taken for the *OSIRIS-REx* asteroid sample return mission designed to collect at least 60 g (Laurretta et al. 2017).

On the surface, the rate of passive collection depends on the distance from jet vents. Predicted fallout rates vary across the surface by orders of magnitude, reaching up to 1 mm/year (Southworth et al. 2019). In this study, we assume that the spacecraft lands in an area where fallout is at least 0.1 mm/year. The same passive collection mechanism used in orbit is employed on the surface. A recloseable cover prevents contamination during landing.

For the purposes of this study, we model the active sample collector as a scoop capable of excavating 5 cc of regolith as the active sampling collector, similar to the strategy of the ELSDT. The specific mechanism for excavating and retrieving samples in the cold, low gravity environment of Enceladus' surface warrants dedicated study. Rasps or drills (Badescu et al. 2019), perhaps combined with pneumatic transfer systems (Zachny et al. 2019) may prove better suited.

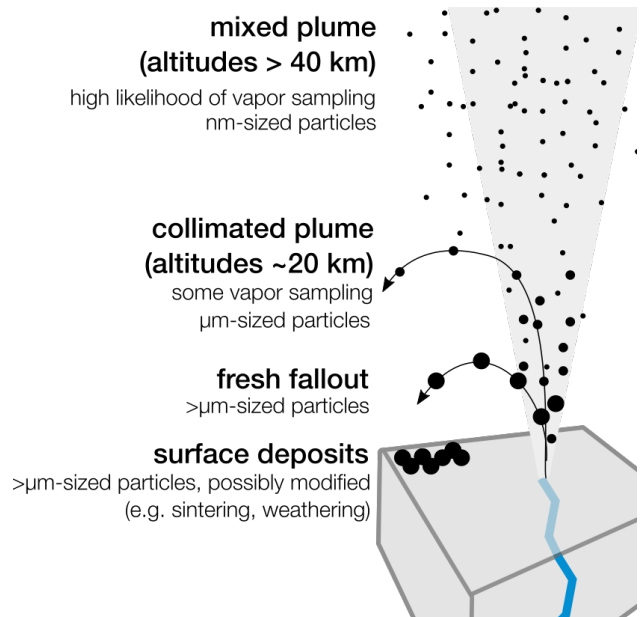


Exhibit B-8. Sample reservoirs available in the Enceladus plume.

B.1.3.4. Sample Transfer, Preparation, and Delivery

Both in orbit and on the surface, passive collection via the funnel allows sample to move down to a collection “cup” at the base of the funnel with near 100% collection efficiency (Adams et al. 2018). This cup transfers the sample to the interior of the spacecraft. Similarly, sample acquired with scoop is transferred to a collection and transfer “cup” separate from the passive cup.

Samples are kept cold for minimal modification until ready to be processed and analyzed. The cups are then sealed and heated until the ice grains melt. The resulting liquid is then transferred through fluidic tubes to the sample preparation subsystem (SPS). The SPS can then either deliver a fluid sample directly to an instrument or can first filter, divide, extract, tag, derivatize, and/or characterize aspects of the sample such as salinity and pH in order to optimize performance of the downstream analyses. The specific steps for the latter option depend on the needs of each instrument. The ESA, microscope, µCE-LIF, and nanopore instruments all receive liquid from the SPS, and the SMS and HRMS receive a vaporized sample. Compared to each instrument performing its own sample preparation, this approach of using a single SPS should significantly reduce the needed power, mass, and space. However, it requires close coordination during development between the instrument and SPS teams.

B.1.4. Concept of Operations

B.1.4.1. Saturn Moon Tour

We identified the science payload activities that could occur during the Saturn moon tour but detailed the implementation of operations is beyond the scope of this study. The flybys of other Saturnian moons presents the opportunity to exercise the remote sensing and reconnaissance suite. Photometric measurements for the cameras further inform the calibration. Using the radar sounder at other satellites will help calibrate the instrument, especially if the long tour duration can be leveraged to send back raw data. In

between moon encounters, checkouts of the LDS can occur. During the Enceladus flybys, high phase images of the plume with the NAC provides the imagery necessary to update the models of Southworth et al. (2019) of vent activity and plume fallout.

B.1.4.2. *Orbital Phase*

Orbilander's orbital period is 12 hours. During closest approach (altitudes < 100 km), the reconnaissance and remote sensing instruments operate while the passive collector accumulates sample (§3.1.1). Outside of closest approach, the spacecraft conducts stationkeeping maneuvers to maintain the unstable orbit. About 8 hours of the orbit are reserved for communications with Earth, but for planning purposes we assume only 6 hours of usable downlink for data return. At 40 kbps and accounting for housekeeping by subtracting 15%, 734 Mb of data can be returned in a 6-hour pass. Some of the LDS analyses require up to 10 hours for warm-up, sample preparation, and analysis and thus operate outside of the above timeline. These orbits dedicated to analyses are infrequent and thus easily accommodated during the 1.5-year orbital science phase.

Life Detection Science

In orbit, the timeline of Life Detection Suite (LDS) analyses is driven by the rate of sample accumulation and divided into three orbital modes (Exhibit 3-1). These are shown in Exhibit 3-1. Mode A requires 31 μL , accumulated in 20 orbits (Guzman et al. 2019), to analyze ice particles for amino acid content with the $\mu\text{CE-LIF}$, characterize the ion content with the ISE, and search for cells with the microscope. Mode B requires 178 μL , accumulated in 111 orbits, to characterize lipids with the SMS, characterize macro- and micronutrients with the ISE, and search for cells with the microscope. Mode C requires 415 μL , accumulated in 130 orbits, to characterize amino acids with both the SMS and $\mu\text{CE-LIF}$. Together, LDS A–C are equivalent to running LDS Contingency Surface Mode (Exhibit 3-1) except that the material collected represents a different reservoir of plume material (Exhibit B-8); comparing results between these modes will provide a powerful characterization of the plume.

Landing Site Characterization and Remote Sensing

Landing site reconnaissance is also prioritized during the orbital phase. We define six criteria for selecting a landing site:

1. *Must receive daylight.* Scouting with the NAC and WAC requires surface illumination by the Sun and landed DTE communications requires that Earth ($\leq 6^\circ$ from the Sun at 9.5 AU) be over the horizon for at least a few hours per Enceladus day. For Enceladus orbital insertion in 2051, this restricts landing sites locations to north of 65°S latitude. As the orbital phase unfolds, more southern latitudes and topographic highs will become sufficiently illuminated and thus provide additional scouting opportunities should no suitable landing site be identified equatorward of 65°S .
2. *Low but non-zero boulder count.* Where the surface of Enceladus has meters of fluffy snow or a thin coating of fresh fallout is not known, requiring data beyond *Cassini*. To constrain the terrain encountered by a landed element, we restrict landing sites to those with sparse meter-sized boulders whose presence indicates that the surface should be strong enough to hold the lander and the snowpack not so insulating as to facilitate penetration of RTGs into the crust if the landing is off-nominal (§C.3). Boulders are counted in NAC images and laser altimetry data.
3. *Slopes < 10°.* The landed element design is robust against tipping or sliding on slopes less than 10° . Slopes can be measured both by laser altimetry and stereo imaging with the WAC and NAC.
4. *Not in a local valley.* With the Sun and Earth so low in the sky during Southern Winter, it is important that the lander's line of sight not be blocked by local topographic features. Topographic lows can be identified both by laser altimetry and stereo imaging with the WAC and NAC.

5. *Temperatures <85 K.* Off nominal landings in areas with surface temperatures <85 K have negligible likelihoods of melting through the ice crust down to the subsurface ocean due to the heat of the RTGs, even in the most efficient melting geometries (§C.3). To identify any keep-out areas, surface temperatures are measured with the TES.
6. *Fallout rate > 0.01 mm/yr.* A 1 m² passive collector area should be able to collect enough sample to run at least 2 full runs of the LDS if fallout rates are > 0.01 mm/yr (Exhibit B-9). Below this rate, the nanopore cannot be run on passively collected sample. Thus, while the active sampling mechanism enables access to a distinct reservoir (Exhibit B-8), it is also a contingency for ensuring enough sample is collected on the surface for the nanopore. Plume fallout rate maps akin to those built from modeling plume particle trajectories based on the location, orientation, and density of plume sources determined from *Cassini* images of the plume (e.g. Southworth et al. 2019) are updated with Orbilander WAC and NAC images.

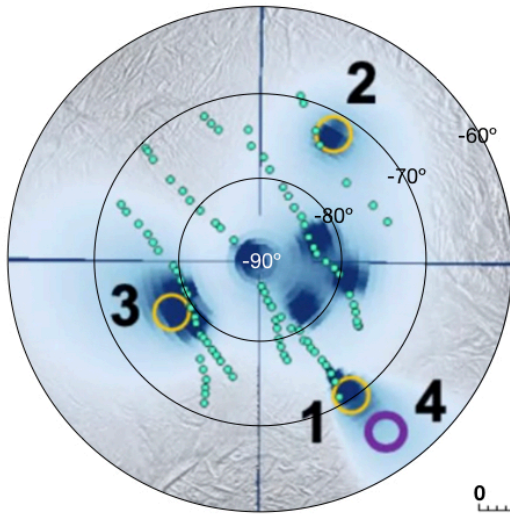
Surface Fallout Rates (mm/Earth yr)	Accumulation Rate with 1 m ² funnel (mL/Earth day)	Accumulation Time for		Measurements Possible During 2-Year Mission	
		LDS Contingency (Earth days)	LDS Full (Earth days)	LDS Contingency	LDS Full
1	2.7	0.22	3.87	3300	189
0.1	0.27	2.21	38.7	330	19
0.01	0.027	22.12	387	33	2
0.001	0.0027	221	3871	3	0

Exhibit B-9. Effect of lower than expected fallout rate on running the LDS. Range of fallout rates from Southworth et al. (2019). We assumed 0.1 mm/Earth year (bold) for this study, but note that the active sampling system increases robustness to lower fallout rates.

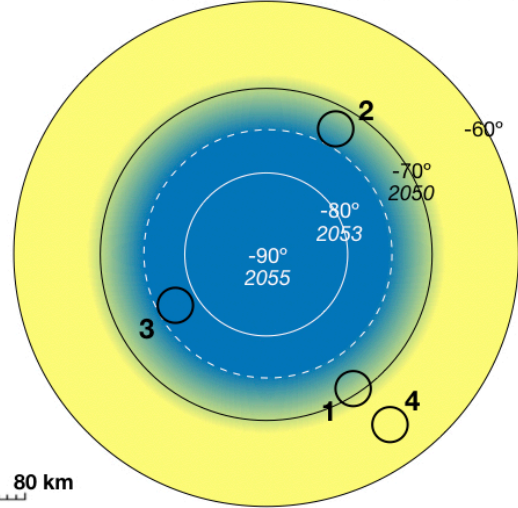
Cassini data supports the existence of landing sites that meet the above criteria, as shown in Exhibit B-10, Exhibit B-11, and Exhibit B-12. Initial landing site candidates (labeled 1–4 in Exhibit B-10, Exhibit B-11, and Exhibit B-12) were selected based on plume fallout rates from Southworth et al. (2019) and represented a few latitudes (at the time, the landing date had not been refined). Plume fallout peaks at 1 mm/year (darkest blue of upper right in Exhibit B-10 and Exhibit B-11) but the cadence of science operations is robust to plume fallout 2 orders of magnitude lower (Exhibit B-12). In the upper left of Exhibit B-10 and Exhibit B-11, we represent latitudes that experience daylight in 2051 in yellow, with blue shading indicating that more latitudes become available in time. Surface temperatures (the bottom left of Exhibit B-10 and Exhibit B-11) from CIRS measurements of the south pole show that temperatures cool off rapidly away from the tiger stripes. As Orbilander will land closer to winter solstice than these data (March 2008), the surface temperatures may be even colder than shown here. Yellow boxes from Howett et al. (2011) represent the spatial bins of the CIRS data. Martens et al. (2015) mapped the occurrence of ice blocks in the area surrounded by dashed white lines in the lower right panel of Exhibit B-10 and Exhibit B-11. *Cassini* data does not allow mapping the entire south pole in this manner, but the abundance of low ice-block count areas (darkest blue) gives confidence that the frequency of smaller size boulders useful for determining relative state of “fluffiness” are scarce but not absent (e.g. Landry et al. 2014). As described in above, Orbilander can spend more time in orbit if additional reconnaissance is required to identify a suitable landing site.

We estimate that verifying that a 5 km × 5 km area on Enceladus’ surface satisfies these criteria requires 300 images with the NAC, a rough estimate derived from representatively covering the area at least twice at different lighting conditions to allow stereo imagery. At 40 km, the NAC observes 1% of the target area and images are taken at a 1 Hz frame rate. The actual landing site is on the order of a few square meters. Thus, this strategy ensures sufficient characterization to identify a safe landing site but could be further optimized at the next level of study.

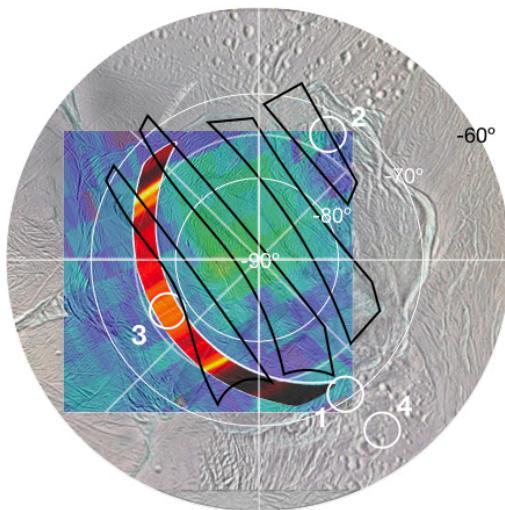
a Abundant plume fallback > 0.1 mm yr⁻¹
Southworth et al. (2019)



b Sun and Earth in view
Orbit insertion Q1 2050, Landing Q4 2051
Local slope and elevation may allow sites further south



c Ice shell not too warm: $T_{surf} < 85$ K, $Q_{endo} < 1$ W m⁻²
Howett et al. (2011); Le Gall et al. (2017)



d 10 km⁻² < 10-m boulder count < 100 km⁻²
Martens et al. (2015)

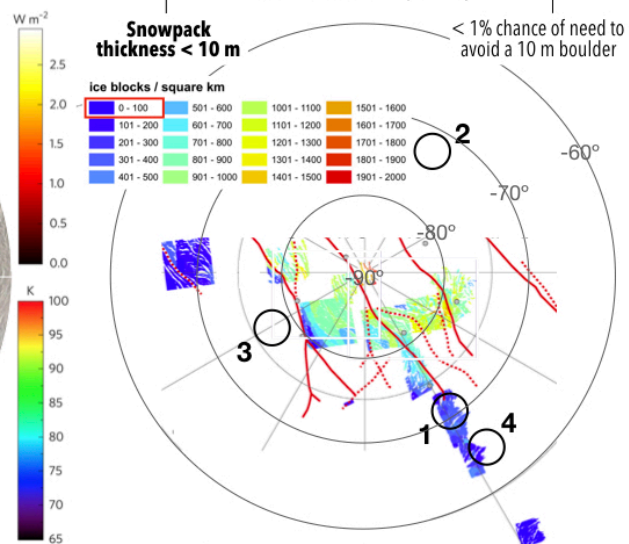
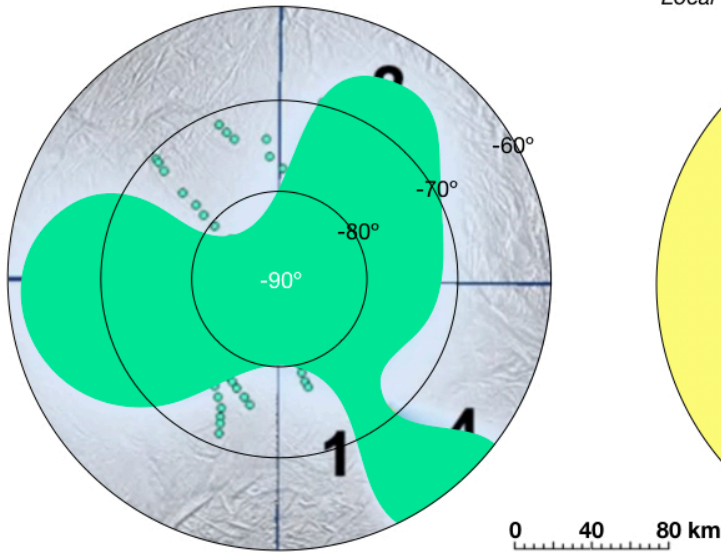
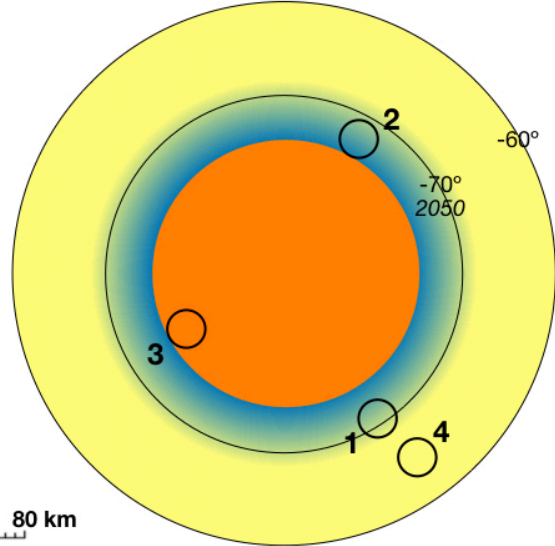


Exhibit B-10. Planetary protection considerations add two constraints to landing site selection. In addition to the needs for landing at a site of (a) high plume fallback and (b) in view of the Sun (for imaging from orbit and once landed) and Earth (for communications), landing site selection criteria include (c) ice shell thermal conditions away from local maxima ($T_{surf} < 85$ K) and (d.) the presence of sparse boulders indicating that any snowpack is thin. Landing site candidates (1–4) were initially chosen on plume fallout alone; the numeral does not convey preference. Based on available data, landing site 4 meets the additional criteria derived from this analysis. Bottom of maps is 0° longitude. In panel c, black outlines are regions of relatively high surface temperatures identified by Howett et al. (2011). The *Cassini* CIRS-derived map of T_{surf} (cool colors) and *Cassini* radar-derived strip map of minimum Q_{endo} are reproduced from Le Gall et al. (2017). T_{surf} in the radar strip are similar to surroundings (<80 K).

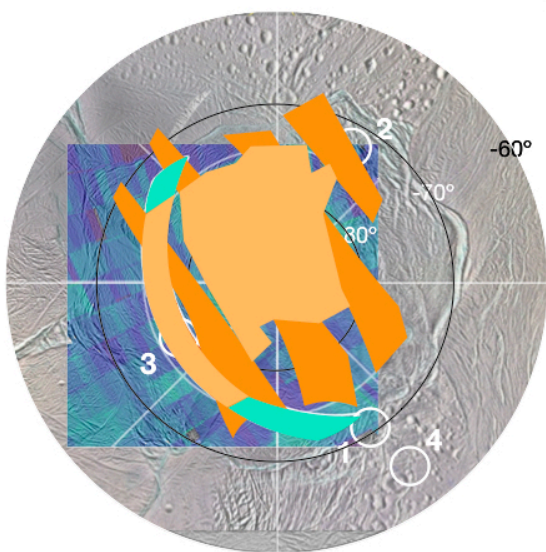
a Abundant plume fallback > 0.1 mm yr⁻¹
Southworth et al. (2019)



b Sun and Earth in view
Orbit insertion Q1 2050, Landing Q4 2051
Local slope and elevation may allow sites further south



c Ice shell not too warm: $T_{surf} < 85$ K, $Q_{endo} < 1$ W m⁻²
Howett et al. (2011); Le Gall et al. (2017)



d 10 km⁻² < 10-m boulder count < 100 km⁻²
Martens et al. (2015)

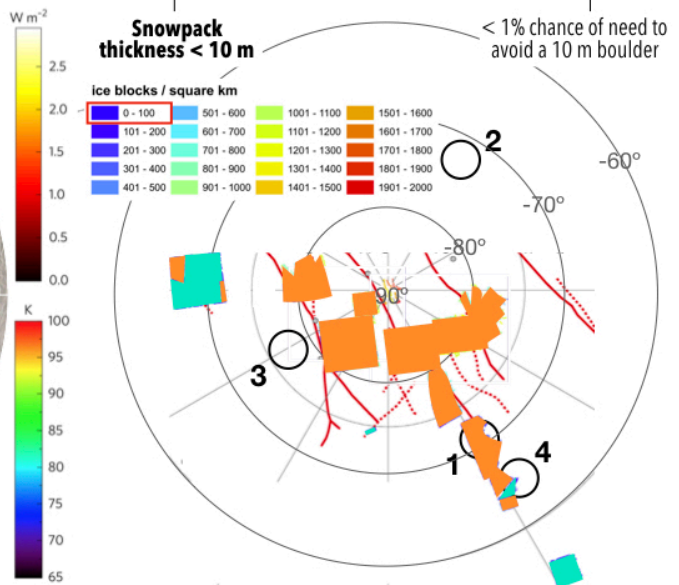


Exhibit B-11. As in Exhibit B-10, but identifying regions satisfying (teal) or precluding (orange) landing site selection criteria in *Cassini* data. These preliminary identifications can be updated by analyzing *Cassini* datasets in greater depth and would be refined by Orbilander once in Enceladus orbit. Bottom of maps is 0° longitude.

B.1.4.3. Landed Operations

Landed operations are conducted at a more relaxed cadence than the orbital campaign. The nominal 2 years on the surface is $4.1\times$ longer than required for our science objectives of 3 months of seismic monitoring, 3 full LDS runs on actively collected sample, 3 full LDS runs on passively collected sample, 1 contingency LDS run (i.e. without the nanopore) on passively collected sample, and characterization of at least 3 active collection sites. In total, this represents 24 Gb of data. At 65°S , we assume 6 hours of useable DTE communications time and use only 5 hours for science return. As above, the 40 kbps provided by GNC is decremented by 15% for housekeeping, etc., to yield 34 kbps. At this downlink rate, all data from the nominal surface mission is returned within 41 passes, where 1 pass occurs each Enceladus day ($\text{Esol} = 1.33$ Earth days). The cadence of science operations is such that there are many Esols in between activities that can be used to simply return data. Since the context camera is equipped with LEDs, all science can be done during the Enceladus night.

During a nanopore analysis, raw data are segmented into “events”, where each event represents a specific polymer feature (biopolymer sequence of k single polymer features, hereafter SPF, akin to a DNA base or set of DNA bases) detected passing through a nanopore and producing a change in signal (current level) that is then stored and transferred back, while non-events are not stored. In biological nanopores, the duration of an event is set by a motor protein that produces controlled translocations of the biopolymer strand through the pore can be >250 SPF/s. In synthetic nanopore platforms, motor proteins are not used and therefore translocation speeds are >250 SPF/s.

Impurities in the sample (e.g., soluble ions, other charged molecules) can clog the nanopores preventing translocations of the biopolymer molecule and causing signal degradation over time. An ideal configuration to mitigate signal degradation due to pore clogging is ≥ 50 pores/well. However, data handling from this many nanopores would be unmanageable (Exhibit B-13). A 4 pores/well configuration is deemed an appropriate compromise between signal degradation due to potential pore clogging and onboard data storage/transfer limitations. Sample preparation in the Sampling System can also reduce the clogging likelihood. Additional requirements for the baseline instrument are shown in Exhibit B-13.

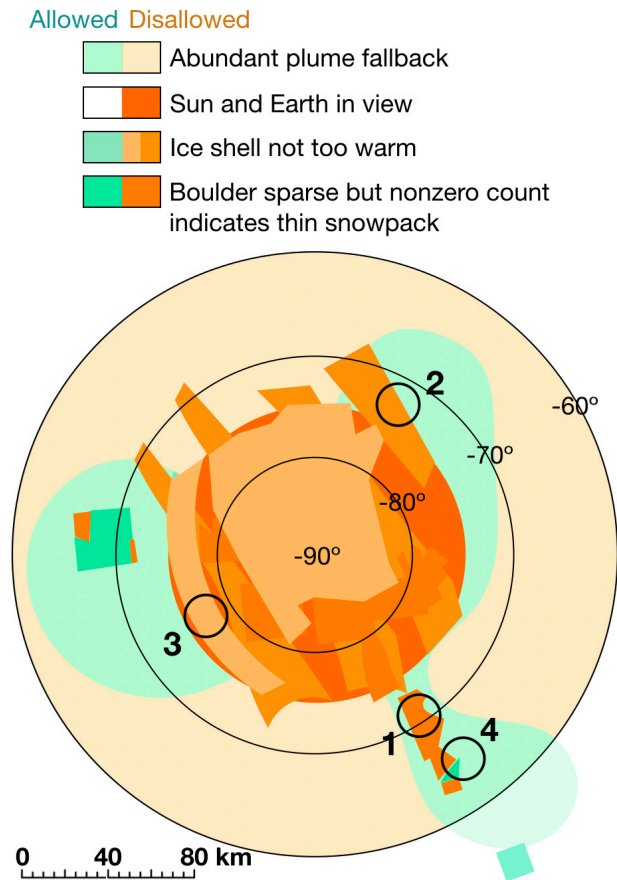


Exhibit B-12. Overlap of conditions favorable to (teal) or precluding (orange) suitable landing sites. This preliminary map shows that there exist locations (e.g. near site 4 and North-East of site 3 around latitude -70°) that satisfy these conditions. Not included are considerations of slopes $<10^\circ$, which would be avoided by terrain-relative navigation. Bottom of map is 0° longitude. Landing site candidates (1–4) were initially chosen on plume fallback alone; the numeral does not convey preference.

Quantity	Value	Units	Notes
Measurement precision	8	bits	Read out each pore (ASCII array; 4 kHz each). 16 bits is the standard precision, but 8 bits is adequate for substantial precision and/or dynamic range in current discretization while minimizing the amount of data to return.
Data sampling rate	4000	s ⁻¹	Sufficient for there to be (much) more than one data point per single polymer feature (SPF) (i.e. base or base pair) with translocations at ≥ 250 SPF per second.
Number of pores per well	4		≥ 50 ideal, but requires unmanageable data handling
Number of wells	4		Provides for 4 separate sample analyses
Data generation rate during polymer feature translocation event	500	kbits	Product of the above four numbers. Corresponds to $500 \times 10^3 / 250 = 2000$ bits/SPF, i.e. 250 8-bit readout numbers per single polymer feature. This sampling rate is robust to synthetic nanopore platforms translocating SPF much faster than biologic platforms. Data are not generated between translocation events.
Maximum data stored per 10 ⁶ -base measurement 1 (no compression)	2	Gbits	$500 \text{ kbits} \times (10^6 \text{ SPF} / >250 \text{ SPF/s})$.
	256	MBytes	

Exhibit B-13. Configuration of the nanopore system. ¹Considered equivalent to a 12-hour-to-24-hour duration, assuming a maximum 1.1-hour time to translocate 10⁶ bases plus time for sample preparation.

To minimize data storage, the nanopore software shall be capable of signal recognition. In the absence of translocation events, the electrical current along the nanopore membrane is ~ constant at 0 pA. Once a translocation event is detected, data are stored at a rate 500 kbps for the duration of the event (Exhibit B-14). Since ≥ 250 SPF are translocated per second, the minimum analysis run time for 10⁶ SPF is 1.1 h at a constant event rate, but the statistical time between polymer detection events increases as the concentration of polymers in the remaining sample decreases. Considering sample preparation steps and the expected abundance of target analytes, the duration for each nanopore analysis is baselined at 12–24 hours.

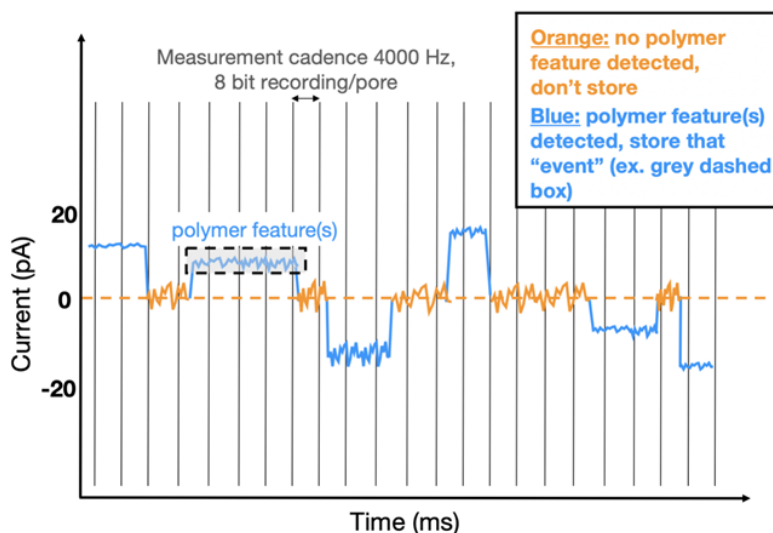


Exhibit B-14. Schematic representation of a nanopore analysis where translocation events that change the electrical current across a pore are detections of single polymer features, SPF (akin to a base or set of bases of DNA). In the absence of translocation events, the electrical current along the nanopore membrane is constant noise (orange) and not recorded. Only when a translocation event is detected, current values are stored at a rate of 500 kbits/s for the event duration (blue). Since >250 SPFs are translocated per second, $500 \times 10^3 \text{ bits/s} / 8 \text{ bits} / 250 \text{ SPF/s} = 250$ 8-bit numbers (vertical grey bars) are recorded per SPF. For 10⁶ SPF, the corresponding data stored is 2 Gb (2 kbits/SPF). The statistical time between two polymer detections increases as $(\text{analysis time})^{1/2}$ as the concentration of polymers that have not yet passed through the pore decreases.

B.1.4.4. Science Operations Data Summary

The relaxed schedule of orbital and surface operations was designed to provide resiliency to the Orbilander mission concept should biomass in the Enceladus plume be at levels lower than modeled here. Thus, while we only require the data returned from the first 200 days in orbit and the first 176 days on the surface, this translates into a 2.7× schedule margin in orbit and 4.1× on the surface. In Exhibit B-15 we show the estimated data per measurement for each instrument and the number measurements anticipated during the nominal orbital and surface operations. To estimate the data return capacity, we multiplied the number of 6-hour downlinks at 34 kbps (decrementing the full 40 kbps by 15% to account for housekeeping) during the orbital campaign (twice per Earth day) and the number of 5-hour downlinks at 34 kbps for the surface campaign (once per Enceladus day, 1.33 Earth days).

Payload Elements		Data Per Measurement (Gb)	Orbital Phase				Surface Phase					
			in 200 days		in 1.5 years		in 176 days		in 2 years			
			Measurements	(Gb)	Measurements	(Gb)	Measurements	(Gb)	Measurements	(Gb)		
Life Detection Suite	HRMS	0.1080	46	4.97	125	13.5	7	0.756	29	3.13		
	GCMS	0.1640	2	0.328	5	0.820	7	1.15	29	4.76		
	ISE	0.0280	2	0.0560	5	0.140	7	0.196	29	0.812		
	μCE-LIF	0.00020	2	0.000400	5	0.00100	7	0.00140	29	0.00580		
	Microscope	0.0330	2	0.066	5	0.165	7	0.231	29	0.957		
	Nanopore	2.0000	0	0	0	0	3	6	12	24		
Remote Sensing and Reconnaissance Suite	radar sounder	16	14	224	38	608	0	0	0	0		
	thermal emission spectrometer	0.0003	189	0.0590	516	0.161	0	0	0	0		
	laser Altimeter	0.0068	189	1.28	516	3.50	0	0	0	0		
	narrow angle camera	0.0042	12500	52.4	34187	143	0	0	0	0		
	wide angle camera	0.0042	42	0.176	114	0.478	0	0	0	0		
In Situ Suite	seismometer	0.0460	0	0	0	0	90	4.14	373	17.1		
	context imager	0.0050	0	0	0	0	324	1.62	1343	6.72		
Sampling System	funnel	-										
	scoop	0.10	0	0	0	0	6	0.6	24	2.4		
	SPS	0.05	3	0.150	8	0.400	7	0.35	29	1.45		
			Total returned in 200 days	283.5	Total returned in orbit	770.4	Total returned in 176 days	15.0	Total returned on surface	61.4		
									Total data required during mission		299	Gb
									Data return capacity for 1.5 years in orbit		804	Gb
									Data return capacity for 2 years on surface		335	Gb
									Total data return capacity		1.14	Tb

Exhibit B-15. Science data returned compared to capability.

B.2. Mission Design and Navigation Study Report

B.2.1. Interplanetary Cruise

Several options for interplanetary cruise itineraries to Saturn offer a trade in delivered mass versus time-of-flight (TOF), with variability in other parameters such as total ΔV and minimum solar distance. Four

general launch itineraries are identified for launch from 2030-2040, and are summarized in Exhibit B-16. For each itinerary, a Jupiter gravity assist (JGA) becomes in phase for a range of launch dates over the decade. Modifications to each itinerary assuming inclusion of an opportunistic JGA are also discussed in Exhibit B-16.

VEE	VVE	3-year ΔV -EGA	Direct
<ul style="list-style-type: none"> • TOF: 9.0–10.5 years • C3: 12–48 km²/s² • Arrival V_∞: 5.3–7.6 km/s • All characteristics depend on launch year 	<ul style="list-style-type: none"> • TOF: 6.3–10.2 years • C3: 23–40 km²/s² • Arrival V_∞: 6.1–9.0 km/s • All characteristics depend on launch year 	<ul style="list-style-type: none"> • TOF: 6.4–7.1 years • C3: 49–54 km²/s² • Arrival V_∞: 7.2–8.9 km/s • DSM: 660–700 m/s 	<ul style="list-style-type: none"> • TOF: 2.3–3.0 years • C3: 130–70 km²/s² • Arrival V_∞: 11.1–14.0 km/s
VEE + JGA	VVE + JGA	3-year ΔV -EJGA	Direct + JGA
<ul style="list-style-type: none"> • In phase from 2030–2033 • TOF: 9.5–10.3 years • C3: 12–24 km²/s² • Arrival V_∞: 9.0–18.5 km/s 	<ul style="list-style-type: none"> • In phase from 2031–2034 • TOF: 7.2–11.1 years • C3: 16–41 km²/s² • Arrival V_∞: 2.7–14.7 km/s 	<ul style="list-style-type: none"> • In phase from 2034–2035 • TOF: 5.9–6.2 years • C3: 49–54 km²/s² • Arrival V_∞: 12.3–16.9 km/s • DSM: 450–550 m/s 	<ul style="list-style-type: none"> • In phase from 2033–2039 • TOF: 3.4–6.8 years • C3: 86–100 km²/s² • Arrival V_∞: 2.8–14.4 km/s

Exhibit B-16. Summary of Optimal Point Solutions for Interplanetary Transfer (results from patched-conic grid search).

The Venus-Earth-Earth (VEE) transfers generally offer the lowest launch C3, while the Venus-Venus-Earth (VVE) sequences can often be employed to reduce TOF for a marginal increase in launch C3. For these inner cruise options, ballistic transfer opportunities may be available depending on the launch year. The 3-year ΔV -EGA offers intermediate values for launch C3 and TOF, but requires a large Deep Space Maneuver (DSM), while direct transfers are a ballistic option that can be exploited to minimize TOF in exchange for high launch C3 and arrival V_∞. By allowing the TOF to increase for the direct transfers, arrival V_∞ can be reduced significantly.

Optimal solutions from a patched-conic broad search for the pair of best-performing sequential launch years are presented in Exhibit B-17, assuming launch after 2035. For the direct and ΔV -EGA transfers, an opportunistic JGA comes into phase later in the decade and is useful to reduce the DSM magnitude for the ΔV -EGA, and to reduce the launch C3 for the direct transfer, thus the JGA-modified options are shown for these itineraries. The ballistic interplanetary options are considered most desirable for this concept, in order to minimize propellant mass. This eliminates the ΔV -EGA, leaving the lowest and highest launch C3 options, i.e., inner cruise and direct transfer, respectively.

The VVE is identified as the more desirable of the two inner cruise options, as it offers reduction in TOF compared with the VEE, and corresponds to launch C3 values that can be accommodated by the Falcon Heavy expendable launch vehicle. For any interplanetary transfer option, it is desirable to constrain all solutions over a 21-day launch period to arrive at Saturn at the same date and time. A single arrival date enables the design of a single pump-down sequence, which significantly reduces the technical workload for mission design and navigation due to the long and highly complex tour and tour design process. While point solutions returned by the grid search are all ballistic, construction of a 21-day launch period with a single Saturn arrival date requires DSMs with magnitudes upwards of 400 m/s near the launch period open and close.

To reduce the ΔV required for the VVE options, a dual-arrival strategy can be considered, where solutions over the 21-day launch period are allowed to arrive at Saturn at one of two arrival dates. In this case, two pump-down solutions must be constructed consistent with each arrival date. An example dual-arrival launch period is constructed for the 2037 VVE transfers, and details on the launch period parameters appear in Exhibit B-18. Solutions from the first 10 days of the launch period arrive at Saturn on Sep 20, 2046, corresponding to a ~9 year TOF. The remaining 11 days in the launch period are of roughly 10 years TOF, arriving at Saturn on 28 Sep 2047. By allowing two arrival dates, the maximum DSM magnitude over the launch period is reduced to ~50 m/s. A comparison of 21-day launch periods for

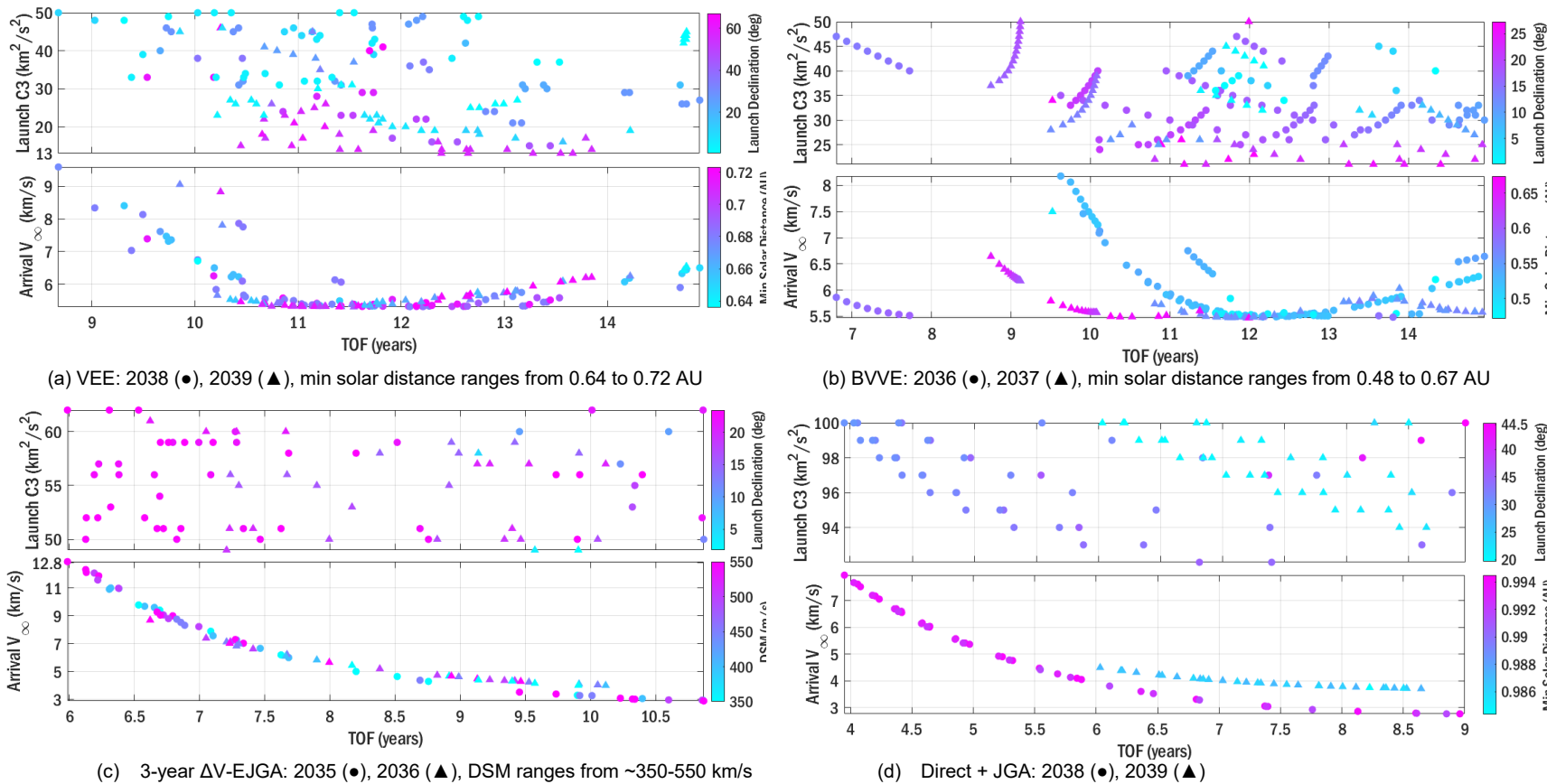


Exhibit B-17. Interplanetary cruise broad search results demonstrate a range of options across the mass versus time-of-flight tradespace. Only optimal solutions from the broad search with TOF < 15 years are shown, where optimality is defined as those solutions that are non-dominated in minimizing launch C3, ΔV , arrival V_∞ , and/or TOF. All optimal solutions returned by the grid search are ballistic except for the ΔV -EGA.

single- and dual-arrival strategies is provided in Exhibit B-19. For the launch C3 of the VVE option, the Falcon Heavy expendable launch vehicle can accommodate the mass required for the Orbilander. A stackup of estimated delivery to Enceladus' orbit is plotted in Exhibit B-20, where TOF and mass are measured at Enceladus orbit insertion.

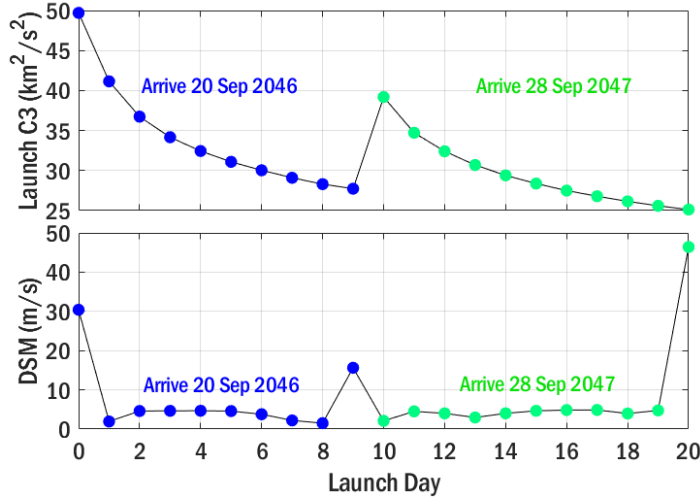


Exhibit B-18. Dual Saturn arrival date strategy for 2037 VVE maintains DSM < 50 m/s over a 21-day launch period, launch from 16 Sep 2037 - 06 Oct 2037 (patched-conic analysis)

VVE Launch Period Analysis	Single Arrival Date	Dual Arrival Date
Launch Period Dates (UTC)	13 Sep - 04 Oct 2037	16 Sep - 06 Oct 2037
Max C3 (km ² /s ²)	41.0	49.7
Max Arrival V _∞ (km/s)	6.0	6.3
Max DSM (m/s)	359.6	46.4
Min Venus Altitude (km)	400	400
Min Earth Altitude (km)	640	400
Max TOF (years)	9.3	10.0
Saturn Arrival Date (UTC)	11 Jan 2047	20 Sep 2046 or 28 Sep 2047

Exhibit B-19. Comparison of launch periods for single- versus dual-arrival 2037 VVE transfer options

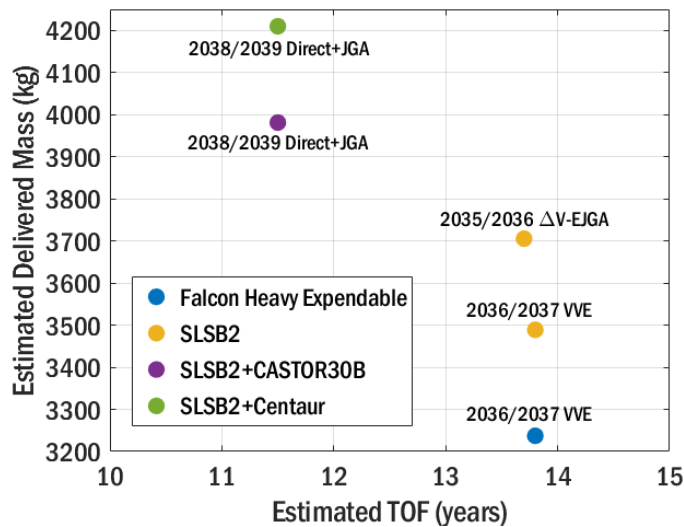


Exhibit B-20. Estimated TOF and delivered mass to Enceladus orbit, post Enceladus orbit insertion maneuver; VVE option can be accommodated with Falcon Heavy expendable launch vehicle, while 3-year ΔV-EJGA and direct+JGA options require SLS Block 2

Because ballistic or low- ΔV solutions are considered most desirable for this concept, the alternative option considered for interplanetary transfer is the direct solution. The JGA phasing provides optimal direct+JGA transfers in 2038 and 2039, thus 21-day launch periods for these two years are evaluated against the 2036-2037 VVE options for the prime and backup launch. The direct+JGA solutions are ballistic and avoid the stressing thermal conditions of inner cruise. The later launch date of the direct+JGA option is also preferable to provide additional time for NGRTG availability. Longer times-of-flight are preferable for improved lighting conditions at the south pole of Enceladus. Allowing the TOF to increase to ~ 7 years for the direct+JGA transfer enables significantly lower arrival V_∞ at Saturn, thus reducing the SOI maneuver magnitude compared with the VVE options. For these reasons, the 2028–2029 direct+JGA transfers are selected as the prime and backup launch for this concept. However, the VVE provides an alternative that can be accommodated by the Falcon Heavy expendable launch vehicle, assuming design modifications are made to accommodate inner cruise. For details on the direct+JGA launch option, see §3.12.

B.2.2. Pump-Down

A high-fidelity trajectory model, that includes all gravitational perturbations from major Solar System bodies, is used to optimize a baseline interplanetary trajectory. This high-fidelity point design converges to an earlier Earth launch date (17 Oct 2038) and later Saturn arrival date (26 Sep 2045) with a lower hyperbolic excess velocity at Saturn of 3.06 km/s. Small shifts in launch periods and differences in time of flight are common when converging lower fidelity estimates using higher-fidelity n -body models. To reduce the ΔV required to capture into Enceladus orbit, a spacecraft trajectory that relies on gravity assists from Saturn's satellites is proposed. A nominal trajectory is designed that consists of a low-altitude (2,400 km) Saturn Orbit Injection (SOI) burn of 232 m/s used to capture into elliptical orbit around Saturn with an orbital period of 158 days. Upon reaching apoapsis 82.5 days later, a Periapsis Raise Maneuver (PRM) burn of 605 m/s targets the first Titan encounter—T0—with an incoming hyperbolic excess velocity magnitude (V_∞) of 2.65 km/s.

Following T0, the trajectory performs three resonant flybys, T1 (1:3), T2 (1:2), and T3 (1:1) to decrease orbital period and Saturn periapsis altitude. A π -transfer to T4 is then used to displace the resonance location 180° and enable four more resonant flybys used for Rhea phasing and V_∞ targeting, T5 (1:1), T6 (1:2), T7 (1:2), and T8 (1:2). The Titan Pump Down phase enables an encounter with Rhea with a V_∞ of 3.09 km/sec.

The incoming hyperbolic conditions at Rhea enable subsequent resonant transfers with Rhea, Dione, and Tethys to lower orbital energy/period until Enceladus encounter. From an energy perspective, previous work (Strange et al. 2009) is used to estimate the number of flybys of each satellite and the associated deterministic ΔV required: 12 Rhea flybys followed by 9 Dione flybys followed by 12 Tethys flybys are used to target an initial Enceladus encounter with a V_∞ of 0.35 km/s. Seven additional leveraged flybys of Enceladus are used to lower V_∞ to 0.2 km/s, at which point a 100 m/s maneuver is executed for capture into Enceladus orbit. Overall, the estimated deterministic ΔV required for the entire Pump-Down sequence prior to Enceladus Orbit Insertion is 560 m/s excluding SOI and PRM. Loitering orbits are inserted as necessary to bring the overall pumpdown to 4.5 years.

The low-energy approach to Enceladus will allow access via a low-energy gateway to the science orbit detailed in the next section [Hernandez]. These transfer types have been extensively studied and will provide a time-invariant means to design the final approach leg on a near 1:1 resonance.

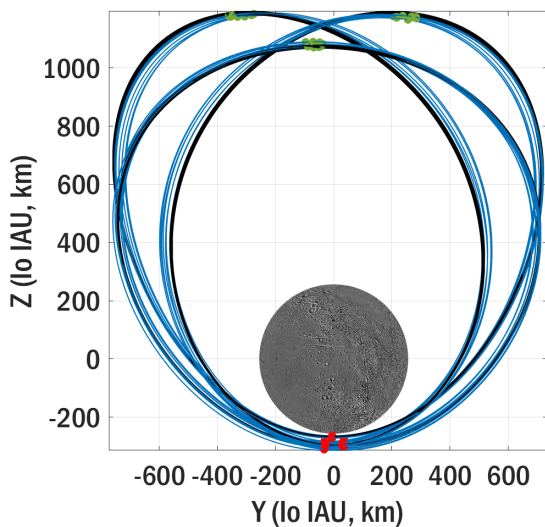
B.2.3. Science Orbit

For science orbit operations, a trajectory that offers low-altitude coverage of Enceladus' south pole is required. Diversity in altitude and groundtrack coverage over the south pole is desirable to sample the plumes at various particle densities and locations. The period-3 halo orbits predicted from the Circular

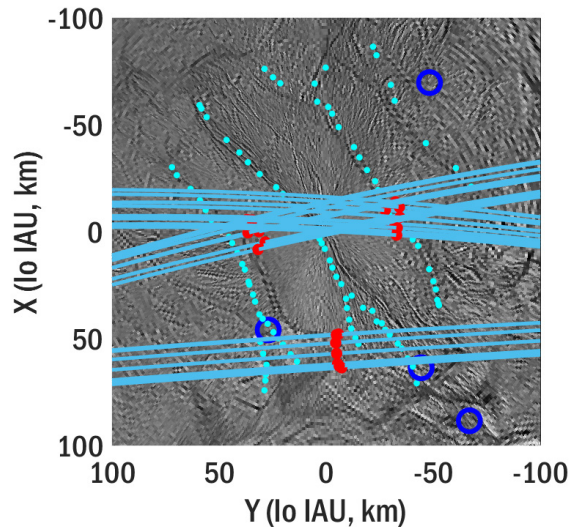
Restricted Three-Body Problem (CR3BP) offer these characteristics, with a roughly 12-hour period between subsequent passages of periapsis. Periapsis are distributed over the south pole in close proximity to the tiger stripes, and are grouped in three distinct regions.

B.2.3.1. Velocity at Periapses

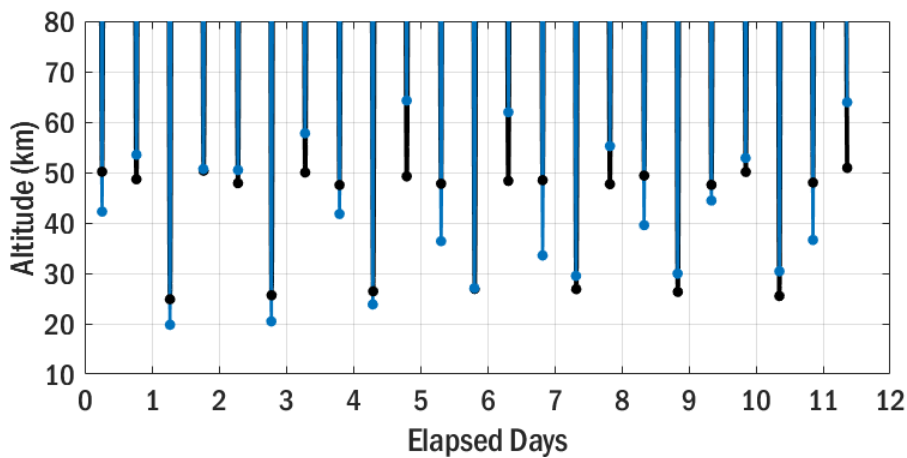
To explore the existence of the period-3 L1 halo orbits in a higher-fidelity model, an example solution is converged in a medium-fidelity dynamical model, assuming point mass gravity for the Sun and Saturn, and a spherical harmonic gravity model for Enceladus. The initial guess orbit from the CR3BP is plotted in black the Io IAU frame in Exhibit B-21 (a) in black. In the convergence process, this initial guess is discretized by defining nodes at each periapsis and apoapsis. A multiple-shooting routine is applied in which full-state continuity is enforced along the path, and all periapsis altitudes are bounded to ≥ 20 km.



(a) Initial guess from CR3BP (black); converged high-fidelity trajectory (blue) with periapses (red) and apoapsis (green) additionally plotted



(b) Groundtrack of high-fidelity solution near Enceladus' south pole, with periapses indicated in red, tiger stripes highlighted in cyan, and potential landing site target areas (based on high rates of plume fallout) indicated by blue markers



(c) Periapsis altitude evolution for CR3BP trajectory (black) and high-fidelity solution (blue)

Exhibit B-21. Twenty-four revolutions of an example period-3 L1 halo orbit converged in high-fidelity model offers natural evolution of periapsis altitudes within desired ranges for plume sampling.

The converged high-fidelity solution is composed of 24 revolutions about Enceladus, continuous in position to within # cm, and in velocity to within # mm/s, and appears in blue in Exhibit B-21 (a). Periapses and apoapses along the high-fidelity orbit are included as the red and green points, respectively.

The groundtrack near the south pole is plotted for the high-fidelity solution in Exhibit B-21 (b), with periapses in red and potential landing site targets indicated by blue circles. Whereas the groundtrack for the idealized orbit from the CR3BP roughly repeats, in the high-fidelity model there is a natural groundtrack spread that aids in covering a wider region of the south pole. There also exist families of L2 period-3 halo orbits, however the groundtrack coverage for the L1 family provides closer access to the high-density plume fallout landing sites and thus are selected as the orbits of interest for this study. The periapsis altitude evolution for both the CR3BP idealized orbit and the high-fidelity orbit are provided in Exhibit B-21 (c). While the idealized orbit maintains periapses near 25 km and 50 km altitude, the high-fidelity solution has more variation and covers 20–65 km altitudes over the 24 revolutions.

While a continuous, ballistic solution is available in the high-fidelity model, the orbit is unstable and requires stationkeeping (s/k) to remain bounded about Enceladus and to avoid impact with the moon. That is, any perturbations in the Orbilander state will cause the trajectory to depart from the vicinity of Enceladus, or will lead to impact with the moon. To maintain bounded motion in the about Enceladus, three stationkeeping strategies are explored and are described in Exhibit B-22.

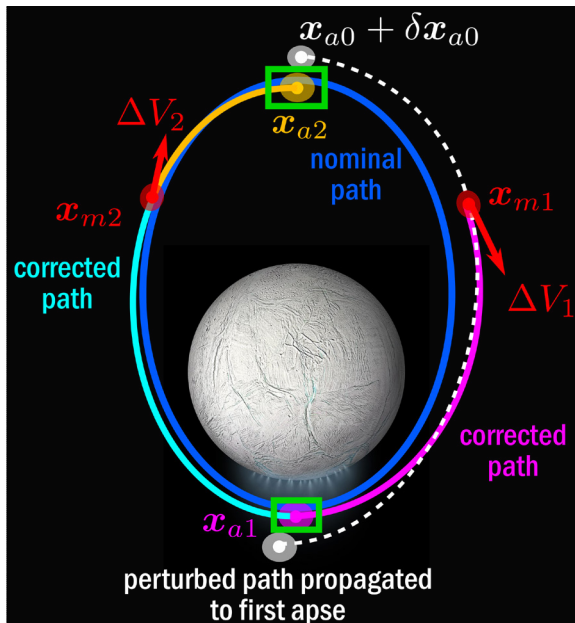
Stationkeeping Strategy	Maneuver Location(s)	Target Behavior	Performance
Strategy 1: Altitude-Bounding	Apoapsis	Periapsis altitudes ≥ 20 km	Poor: Results in gradually increasing maneuver magnitudes and uncontrolled motion
	Apoapsis + clean-up at 600-km altitude		
Strategy 2: Periapsis-Targeting	Apoapsis	Periapsis position vectors bounded within ≤ 1 km of periapses along nominal high-fidelity path depicted in Exhibit B-21	Poor: Results in gradually increasing maneuver magnitudes and uncontrolled motion
	Apoapsis + clean-up at 600-km altitude		
Strategy 3. Apse-Targeting	Each crossing of 600 km altitude	All apse position vectors bounded within ≤ 1 km of apsides along nominal high-fidelity path depicted in Exhibit B-21	Good: Maneuver magnitudes and Orbilander motion remain bounded and controlled

Exhibit B-22. Three stationkeeping strategies are considered for science orbit maintenance.

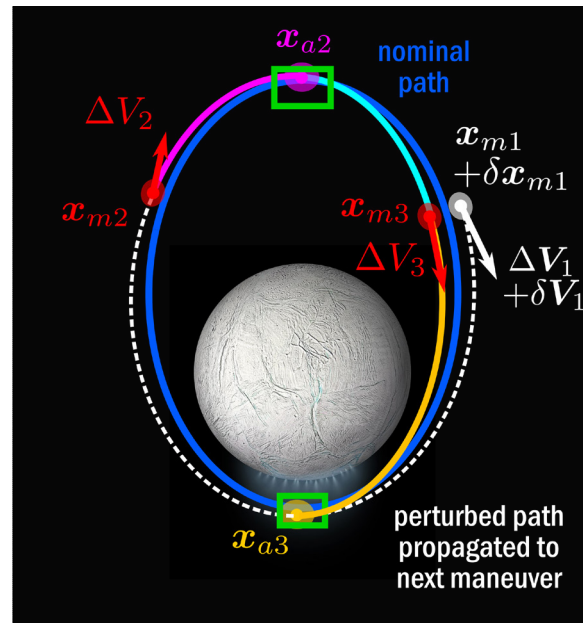
For each approach, an optimization routine is employed to minimize total ΔV while maintaining desirable motion, as defined in the “Target Behavior” descriptions. Two strategies (S/K Strategies 1 and 2) employing maneuvers at apoapsis are performed, however these approaches do not successfully control the science orbit and the simulations generally lead to gradually increasing s/k maneuver magnitudes (from <0.1 m/s to >5 – 10 m/s per maneuver) and eventual departure from or impact with Enceladus. A modification of Strategies 1–2 is also considered, in which a second clean-up maneuver is applied at the 600-km altitude crossing between apoapsis and periapsis, but does not lead to any significant improvement in performance. To maintain better long-term control of the science orbit, S/K Strategy 3 targets desirable motion at both periapsis and apoapsis of each orbit revolution. This approach leads to stable maneuver magnitudes (i.e. magnitudes that remain bounded over the duration of the simulations) and well-controlled motion over the duration of the simulations performed. In the following discussion, all results assume simulations that are governed by S/K Strategy 3.

A user-defined number of maneuvers (N_m) may be considered for each call of the optimization routine to help enforce both current and future apse behavior. For $N_m > 1$, multiple, subsequent maneuvers are simultaneously designed to enforce the desired behavior at subsequent passages of periapsis and apoapsis, and full-state continuity is enforced along the path. Although multiple maneuvers are designed in a single optimization call, only the first maneuver is executed, as uncertainties in the Cartesian 6-state and maneuver execution errors are inserted before continuing to design the next revolution. Define a maneuver state as $\mathbf{x}_{mi} = [\mathbf{r}_{mi}, \mathbf{v}_{mi}]$ and the subsequent apse state as $\mathbf{x}_{ai} = [\mathbf{r}_{ai}, \mathbf{v}_{ai}]$. Then, the stationkeeping algorithm is summarized as follows and in Exhibit B-23:

1. Begin at first apoapsis state \mathbf{x}_{a0} , inserting random state error $\delta\mathbf{x}_{a0}$ before numerically propagating to first crossing of 600-km altitude
2. Compute optimal maneuvers $\Delta\mathbf{V}_i$ for $i = i_0, \dots, i_0+N_{\text{revs}}$, subject to path continuity and apse position vector bounds
 - Bounds are defined as $|\mathbf{r}_{ai} - \mathbf{r}_{ai,\text{nom}}| < \mathbf{b}_i$, where $\mathbf{r}_{ai,\text{nom}}$ represents the apse position state along the nominal orbit, and \mathbf{b}_i is a 3-vector containing bounds applied at the i -th apse (all elements of each vector \mathbf{b}_i are equal in this study, so that $\mathbf{b}_i = b_i \cdot [1,1,1]$)
 - Numerical propagation of states within the optimization routine assumes a lower-fidelity dynamical model that is to be run on-board the spacecraft



(a) First call of optimization routine solves for first two maneuvers subject to path continuity and apse target constraints



(b) First maneuver is executed with state and maneuver execution errors, and second call of optimizer solves for maneuvers 2–3

Exhibit B-23. Schematic demonstrating Stationkeeping Strategy 3 for $N_m = 2$.

- Note that times Δt_{mai} and Δt_{ami} represent elapsed time between the current maneuver and the subsequent apse, and from that apse to the following maneuver, respectively; these times are variables in the optimization routine
3. Add random state error $\delta\mathbf{x}_{mi}$ to i_0 -th maneuver state, \mathbf{x}_{mi0}
 - State error covariances defined based on simulations described in §C.1.
 4. Add random maneuver execution error $\delta\mathbf{V}_i$ to maneuver, $\Delta\mathbf{V}_{i0}$
 5. Numerically propagate perturbed i_0 -th maneuver state $\mathbf{x}_{mi0} + \delta\mathbf{x}_{mi0} + [0,0,0, \Delta\mathbf{V}_{i0} + \delta\mathbf{V}_{i0}]$ for time $\Delta t_{\text{mai}0} + \Delta t_{\text{ami}0}$
 - Numerical propagation assumes the full high-fidelity model, and is expected to introduce modeling errors into the simulation
 6. Return to Step 2

The onboard model assumed within the optimization routine, and the full-fidelity “truth” dynamical model assumed for propagation outside of the optimizer are defined as follows:

- Onboard Model:
 - point mass gravity for the Sun, and Saturn
 - spherical harmonic gravity model for Enceladus
- Full-fidelity Model:
 - point mass gravity for the Sun, Titan, Rhea, Dione and Tethys
 - spherical harmonics gravity models for Enceladus and Saturn

Two maneuver execution models are assumed to determine the impact on the stationkeeping cost. The parameters for each model are taken from *Cassini* mission experience, and are summarized in Exhibit B-24.

Maneuver Execution Errors (1-σ)	Engine Type	Magnitude Error (%)	Direction Error (mrad)	Magnitude Cutoff (m/s)
Model 1 (Williams et al. 2009)	RCS	0.7	9	0 – 0.3
	MEA	0.02	0.6	> 0.3
Model 2 (Wagner et al. 2005)	RCS	2.0	12	0 – 0.4
	MEA	0.2	3.5	> 0.4

Exhibit B-24. Maneuver execution models assumed for stationkeeping analysis

Some preliminary simulations are performed to determine the impact of various sources of error on stationkeeping cost. Parameters varied over the simulations are the maneuver execution error model (see Exhibit B-24) and the fidelity of the onboard dynamical model. In Exhibit B-25, results of simulations assuming no dynamical modeling error are presented. In this case, it is assumed that the onboard model precisely matches truth, and the stationkeeping cost is driven by the maneuver execution error and errors due to orbit determination uncertainties. The plot depicts maneuver magnitudes throughout the simulation, and the table provides average cost over the full simulation.

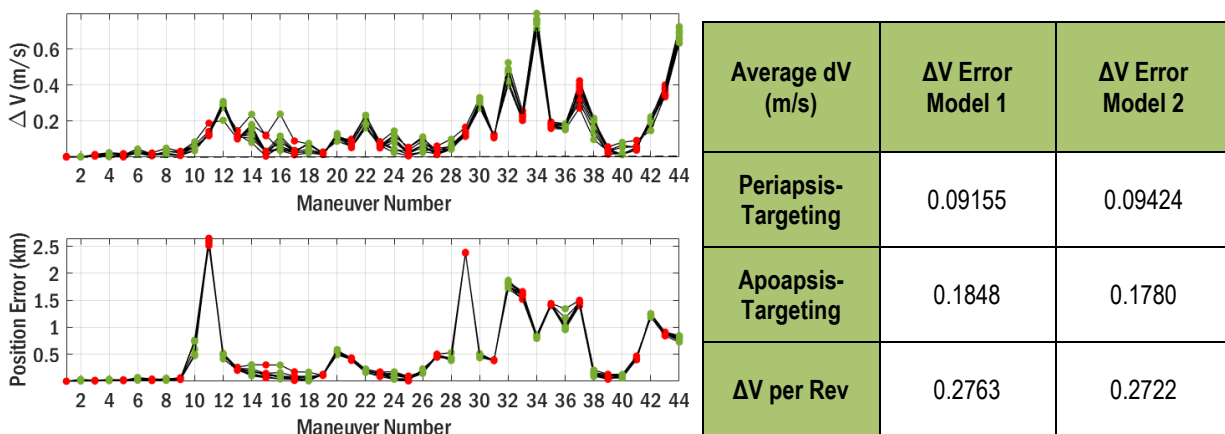


Exhibit B-25. Simulations assuming onboard dynamical model matches truth: Simulation (1) maneuver execution error model 2, Simulation (2) maneuver execution error model 1; red points indicate periapsis-targeting maneuvers, and green points represent apoapsis-targeting maneuvers

While a preliminary study of possible stationkeeping approaches was performed here, there is a rich set of trades and design options that should be further explored. Based on the work performed, the following recommendations for future study are proposed:

- **Optimal placement of maneuvers:** A single location for maneuver placement (i.e. each passage of 600-km altitude) was considered in this study. The apoapsis-targeting maneuvers were generally of larger magnitude than the periapsis-targeting maneuvers. Further study is required to determine the optimal placement of each maneuver type in order to minimize total stationkeeping ΔV .
- **Onboard dynamical model**
- **Apse-targeting bounds:** Given complete freedom (i.e. very large bounds), the apse position states for optimal ΔV appear to remain within ~ 2.5 km of the nominal solution for both periapsis and apoapsis. Constraining the position bounds to be < 2.5 km does not appear to improve the stationkeeping cost. While higher ΔV is correlated to higher position errors (see Exhibit B-25), enforcing tighter constraints on the position errors does not appear to reduce the total ΔV required.
- **Selection of N_m :** The value of $N_m = 3$ was selected to be 3 for all simulations performed in this study. Alternate values should be considered to determine the impact on the resulting cost of stationkeeping.
- **Alternative targeting approaches**

B.3. CML 3 Study

B.3.1. Architectures and Payloads

A variety of architectures are possible for returning to Enceladus. For example, the report on the Rapid Mission Architecture study (whose scientific scope was not driven by astrobiology) conducted for the 2010 Decadal Survey presented >40 possibilities. In this study, the science team considered four for CML 3 study—orbiter, Orbilander, small lander + large orbiter, and small orbiter + large lander—in order to find evaluate the relationship between science value and cost.

1. *Orbiter:* This architecture only orbits Enceladus. Operations are similar to those described for the orbital phase of Orbilander in §3.1.1, except that the priority of reconnaissance (conducted for a potential follow-on mission rather than a subsequent mission phase) is relaxed and carried out at a slower cadence. The orbiter cannot accumulate enough sample to conduct the full LDS set of measurements based on our assumptions of plume biomass. The nanopore is therefore not included in the orbiter payload (neither are the seismometer and context imager). To better map the distribution and velocities of ice particles in the plumes, an ice particle counter is included in the orbiter payload. Total science operations in orbit last 3 years. At the end of mission, the orbiter exits Enceladus orbit to be disposed of elsewhere in the Saturnian system.
2. *Orbilander:* Because of Enceladus' low gravity, once in Enceladus orbit, the ΔV required to land is trivial. The Orbilander leverages this by landing the entire spacecraft after conducting orbital science for 1.5 years. On the surface, the remote sensing and reconnaissance instruments are no longer planned for use, although one might imagine clever uses for them. (For example, science and navigation cameras mounted on different sides of the vehicle may be able to observe the surface.) This architecture was chosen for the point-design study presented in the main text. The payload of its CML-3 version did not include either a laser altimeter or a TES, but in the CML-4 study both were found to be accommodable and the TES was found to be necessary for landing site reconnaissance. These payload additions increase the science value of the CML-4 Orbilander over its CML-3 version (see §B.3.3.2).
3. *Small lander and large orbiter:* This architecture was defined to explore the end-member of simple landers combined with a highly capable orbiter. The orbiter carries the LDS and the remote sensing

suite and conducts science operations for 3 years. The small lander carries only the seismometer, whose geophysical investigation cannot be accomplished in orbit. It is designed to be robust to a ballistic landing on any side and thus requires less robust reconnaissance. Landed operations are limited to the battery lifetime to about 15 days, ensuring that the seismometer monitors multiple Enceladus' tidal cycles. Although it would be desirable for the small lander to also include the nanopore instrument, that architecture was found to not be viable. The nanopore size, mass, and power needs can be accommodated; one could envision immediate sample acquisition if surface plume fallout was squeezed through an opening in the lander at the time of ballistic landing, bypassing the need for active sampling; and the measurement could be completed in 24 hours (see §B.1.4.2); but the nanopore data (Exhibit B-13) cannot fully be relayed to the orbiter within the lander lifetime. At end of life, the lander remains on the surface and the orbiter is disposed of as in Case 1.

4. *Large lander and small orbiter*: This architecture combines a highly capable lander and a highly capable orbiter. Although termed the “small orbiter”, in the initial phase of operations, the lander and orbiter elements are attached. Much like Orbilander operations, the combined elements spend at least 1.5 years in orbit to identify a safe landing site, survey the plumes with the LDS, and conduct context measurements with the remote sensing suite. Once a safe landing site is found, the lander separates from the orbiter. On the surface, the lander operates the LDS and in situ suite for 2 years. The orbiter continues remote sensing investigations and acts as a relay for the lander. Disposal of the landed and orbital elements follows Cases 1 and 2.

The payloads for these four options are summarized in slides below.

B.3.2. Mission Design and Subsystems

In the following slides, the mission design and subsystems are described.

B.3.3. Selection of Point Design

B.3.3.1. Definition of Science Value

We defined the relative science value of the four mission architectures as a function of five factors:

$$\text{Science Value} = C_0 \mathbf{L} \times \mathbf{B} + C_1 \mathbf{P} + C_2 \mathbf{G} + C_3 \mathbf{S}$$

where C_{0-3} are weighting coefficients, \mathbf{L} is the ability to do life detection and characterization, \mathbf{B} is the resilience to biomass uncertainty, \mathbf{P} is the ability to do physical oceanography and geophysics, \mathbf{G} is the ability to do chemical oceanography and geochemistry, and \mathbf{S} is resilience to surface safety uncertainty.

Ability to do life detection and characterization

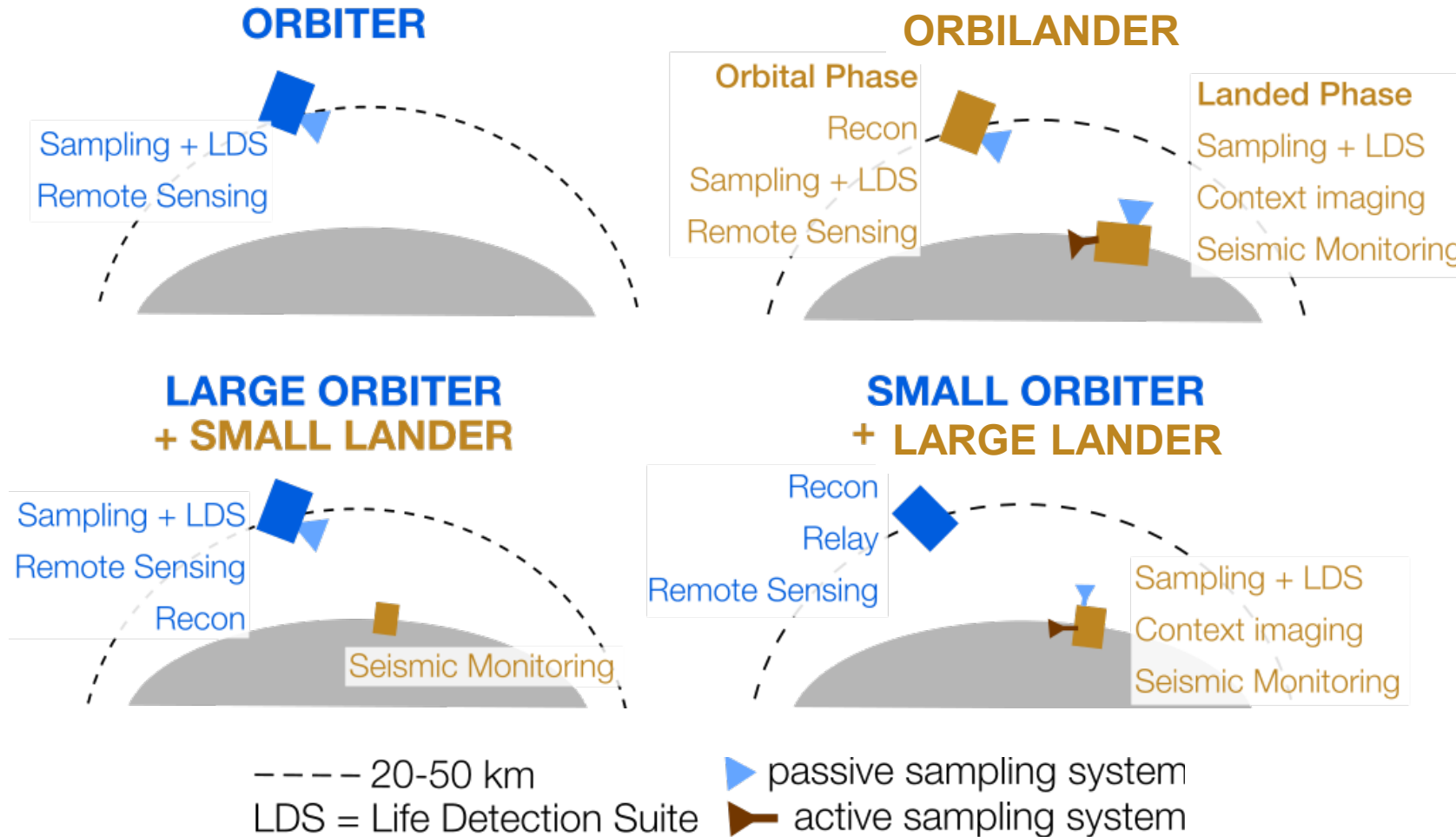
The ability to do life detection and characterization depends on the number of independent measurements of different features of life, i.e. the complementarity of the payload (Exhibit B-1). This is an important aspect as we desired a certain level of redundancy and thus robustness was desirable in the concept's ability to achieve our primary science goal. We also considered the likelihood of success with the “confirmation” component of the life detection suite, the high-risk/high-reward microscope and nanopore sequencer. The final aspect of this parameter is the ability of the payload to characterize life in the event of a positive detection. A sequenced polyelectrolyte, for example, offers insight into the exotic biochemistry but any terrestrial contaminants might also be identified and compared to known contaminant DNA sequences taken from clean rooms as part of planetary protection protocols.

Resilience to biomass uncertainty

As biomass uncertainty is perhaps the most critical unknown in designing search-for-life missions, resilience to biomass uncertainty appears as a multiplicative factor the science value equation above. The biomass density that Enceladus could support has been loosely constrained to 5×10^{-6} - 5×10^3 cells per mL

Enceladus Architecture Trade Study (CML 3)

Enceladus Architecture Options



NOTE: “Small” and “large” orbiters are actually the same size. Rather, these term signify which part of the architecture carries the Life Detection Suite, as indicated on this plot.

Mission Design

- Mission Timeline:
 - Cruise to Saturn: 7-9 years
 - Pump down: 5-7 years
 - Enceladus Science phase: 3 years
- Mission life: < 18-20 years
- Launch dates: 2031 - 2039
- Launch vehicles: SLS (w/ various upper stages) or F9-Heavy Expendable
- Launch mass range: 6000 kg – 23,000 kg
- Trajectory options: VEE (Venus and Earth flybys) or DVEGA (Earth flyby, no Venus)
- Power: Next Gen RTG (400W BOL)
- Propulsion: Chemical; with option for an EP-chemical hybrid system

Launch Vehicle and Mission Options

Itinerary	LV	Launch C3	Launch Mass (kg)	Estimated TOF (years)	Estimated Delivered Mass to Enceladus Orbit(kg)
Direct	SLSBlock1	143.6	740.0	9.9	352.8
Direct	SLSB2wCASTOR30B	143.6	4338.7	9.9	2068.6
Direct	SLSB2wCentaur	143.6	7067.8	9.9	3369.8
DVEGA3	FHeavyE	49.1	5389.5	13.9	2292.3
DVEGA3	SLSBlock1	49.1	4797.9	13.9	2040.6
DVEGA3	SLSB2	49.1	19023.8	13.9	8091.2
DVEGA3	SLSB2wCASTOR30B	49.1	19467.2	13.9	8279.8
DVEGA3	SLSB2wCentaur	49.1	23462.0	13.9	9978.8
VEE	FHeavyE	33.0	7721.7	16.4	3999.7
VEE	SLSBlock1	33.0	6270.6	16.4	3248.1
VEE	SLSB2	33.0	25858.3	16.4	13394.2
VEE	SLSB2wCASTOR30B	33.0	25274.5	16.4	13091.8
VEE	SLSB2wCentaur	33.0	29014.3	16.4	15029.0
VVE	FHeavyE	39.0	6787.3	15.9	3560.0
VVE	SLSBlock1	39.0	5666.6	15.9	2972.2
VVE	SLSB2	39.0	23132.5	15.9	12133.1
VVE	SLSB2wCASTOR30B	39.0	22968.3	15.9	12047.0
VVE	SLSB2wCentaur	39.0	26753.7	15.9	14032.5

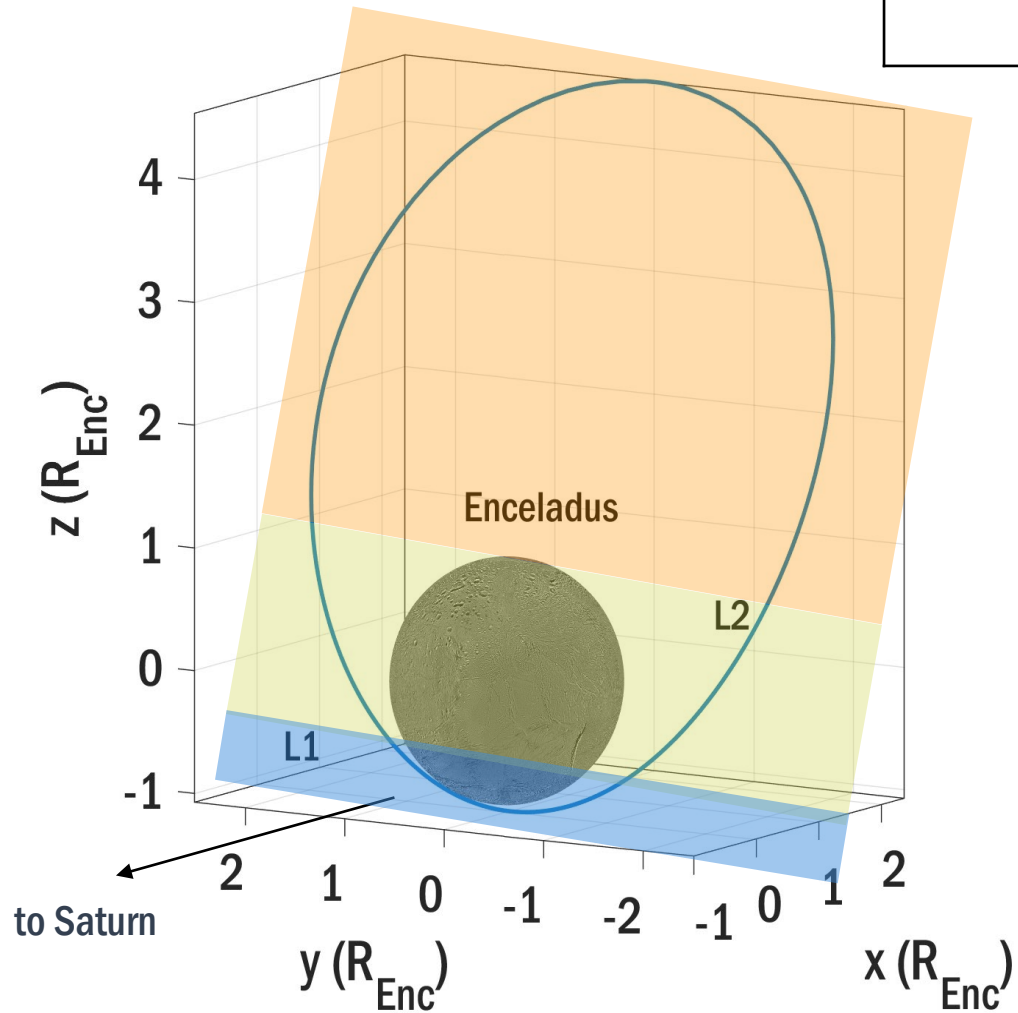
NOTE: Delivered mass estimates do not include full launch window. This was refined for the Orbilander in CML4 study (see Section 3.12-3.13).

General Orbit ConOps

- ≤ 8 hrs of communications operations assumed for each orbit
- Station keeping maneuver every 12 hours
- All architectures have some science phase in orbit
 - Orbiter
 - All science done in orbit
 - Orbilander
 - Orbiter science + recon to find a safe landing site
 - Contingency: If no safe landing site found, proceed with operations as an orbiter
 - Large Orbiter + Small Lander
 - Orbiter science + recon for small lander done in orbit
 - Small Orbiter + Large Lander
 - Orbiter science + recon to find a safe landing site
 - Once lander deployed, small orbiter does relay and remote sensing science
 - Option: may choose to also sample particles during recon

General ConOps

Altitude	400-850 km	100-400 km	<100 km
Duration	~8.7 hr	~2.5 h	~0.9 h
S/C Velocity	60 m/s	108-175 m/s	175-195 m/s
Instruments that must operate	Comm		Sample collection, remote sensing package, HRMS



- **Orbital**

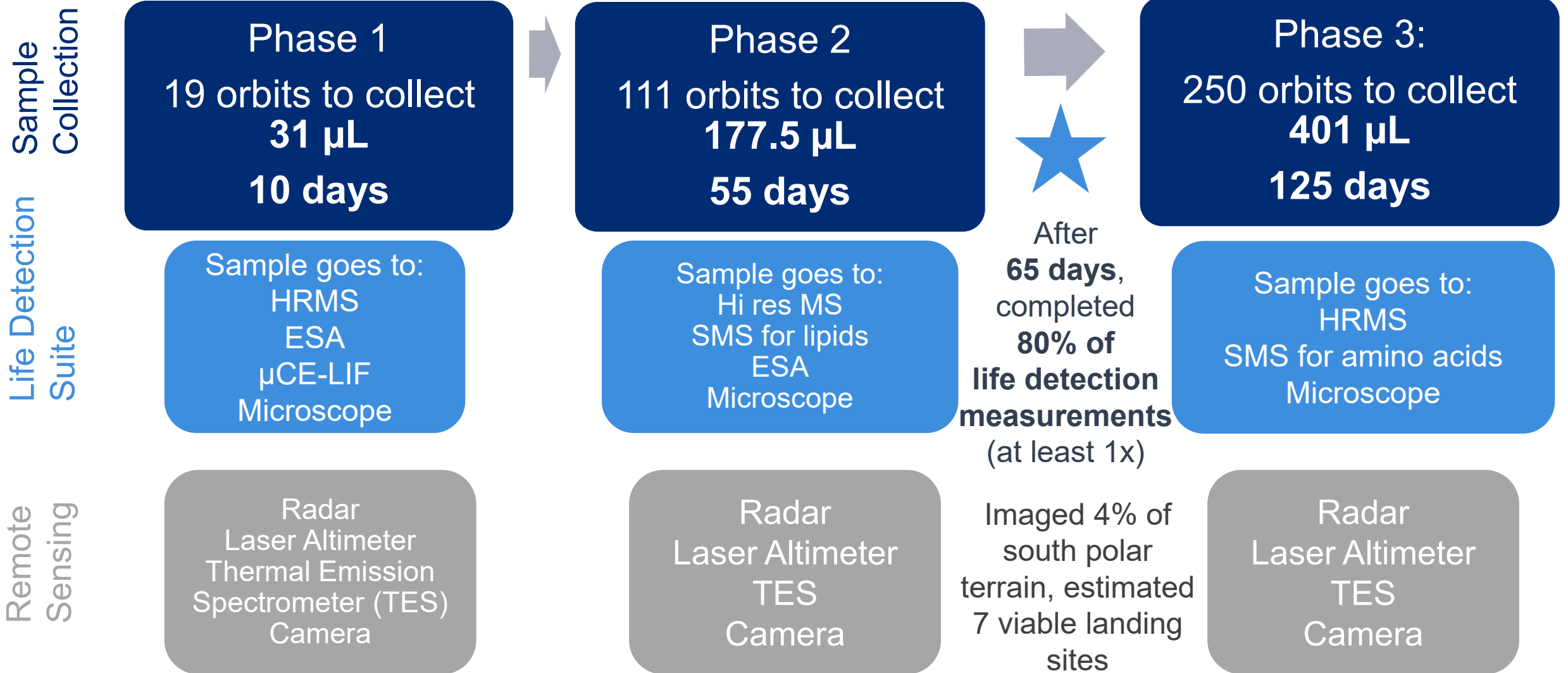
- ≤ 8 hrs of communications operations assumed for each orbit
- Station keeping maneuver every 12 hours
- Periapsis naturally varies between 20-60 km

- **Landed**

- DTE communications duration TBD (a function of landing site, season)
- All science *except* context imaging can be done during local night; strategy will need to prioritize communications whenever DTE possible

Orbital Phase ConOps Strategy

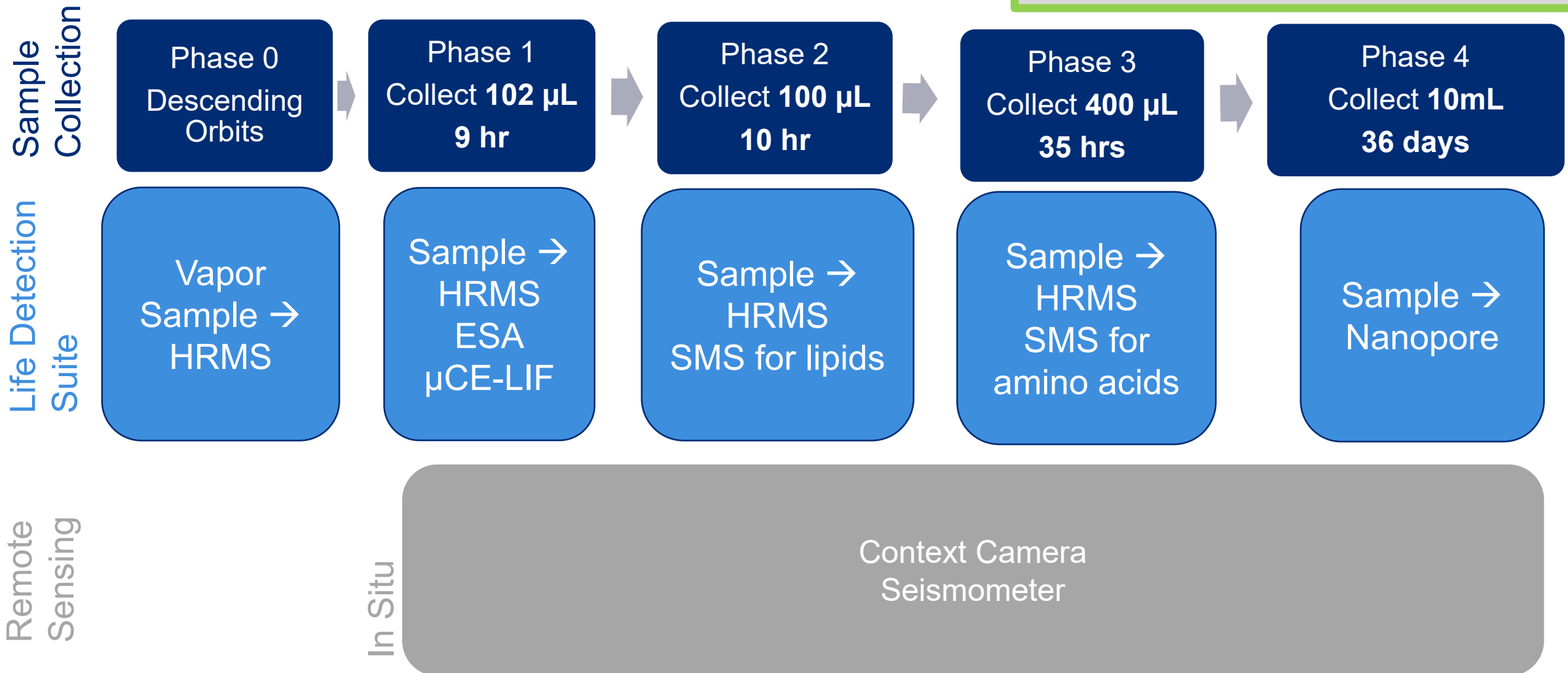
Assume: 1.6 μL per orbit (conservative); 12 hr orbital period; 1 m^2 collector



Lander ConOps **PASSIVE ONLY** Strategy

Assume: 0.1 mm/day (conservative); 1 m² detector

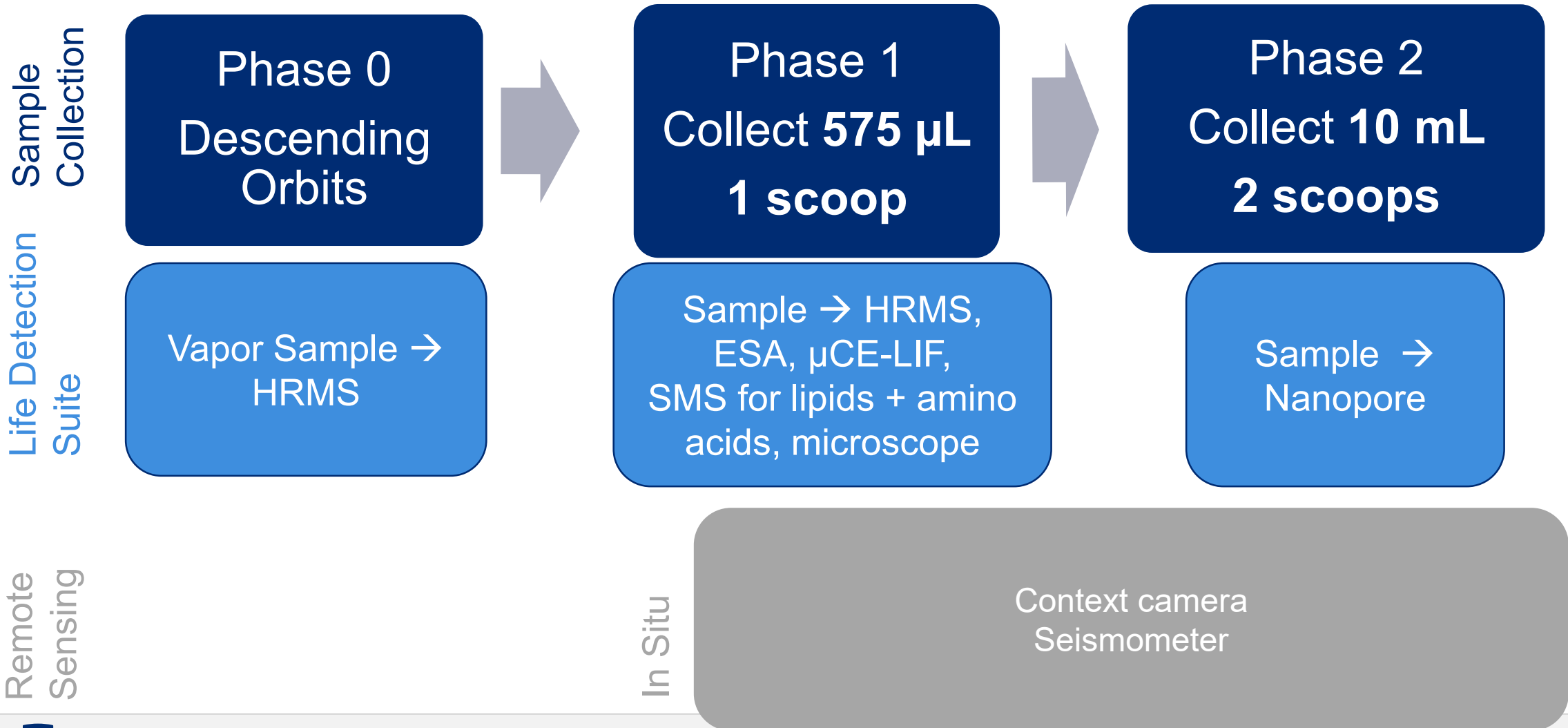
NOTE: This applies to both Orbilander and Large Lander. Orbilander's ConOps were refined at the CML4 (Section 3.1) and differ from what is shown here.



Lander ConOps ACTIVE ONLY Strategy

Assume: 5 cc/scoop (ELSDT model)

NOTE: This applies to both Orbilander and Large Lander. Orbilander's Conops were refined at the CML4 (Section 3.1) and differ from what is shown here.



Orbiter Configuration

Subsystem	Description
Propulsion	<ul style="list-style-type: none">• Bipropellant (main engine) and monoprop propulsion subsystem• 2625 m/s; 3980 kg propellants includes 100 kg for ACS prop• 2-100 lb main engines and 8 5-lb and 16 1-lb RCS engines, 1 hour SOI burn
Avionics	<ul style="list-style-type: none">• Redundant flight computers with data storage 128 Gbits
Telecom	<ul style="list-style-type: none">• X-band: Uplink & 65W Downlink• Ka-band: 60 W Downlink (40 kbps @ max range)• 2.2-m HGA, MGA, fanbeams (3), and LGAs(3)
Control	<ul style="list-style-type: none">• 3-axis: Reaction wheels(4), RCS engines• Pointing Ka 1 mrad, NAC (TBD) – need to revisit this and opnav• Star trackers(2), IMU internally redundant, sun sensors(6)
Thermal	<ul style="list-style-type: none">• Thermos bottle design, radiator, louvers, MLI
Power	<ul style="list-style-type: none">• 3 NGRTGs• 3 shunt regulators, 3 PDUs (TBD)
Mechanical Configuration	<ul style="list-style-type: none">• 130 in x 95 in x 98 in (Structure only, does not include collection funnel)
Payload	<ul style="list-style-type: none">• 115 kg CBE

Orbilander Configuration

Subsystem	Description
Propulsion	<ul style="list-style-type: none">• Bipropellant (main engine) and monoprop propulsion subsystem• 2625 m/s; 3980 kg propellants• 2-100 lb main engines and 8 and 16 RCS engines, 1 hour SOI
Avionics	<ul style="list-style-type: none">• Redundant flight computers with data storage 128 Gbits
Telecom	<ul style="list-style-type: none">• X-band: Uplink & 65W Downlink• Ka-band: 60 W Downlink (40 kbps @ max range)• 2.2-m HGA, MGA, fanbeams (3), and LGAs(3)
Control	<ul style="list-style-type: none">• 3-axis: Reaction wheels(4), RCS engines• Pointing Ka 1 mrad, NAC (TBD) – need to revisit this and opnav• Star trackers(2), IMU internally redundant, sun sensors(6)
EDL	<ul style="list-style-type: none">• Lidar, descent camera + landing thrusters, structure
Thermal	<ul style="list-style-type: none">• Thermos bottle, radiator, louvers, MLI
Power	<ul style="list-style-type: none">• 3 NGRTGs• 3 shunt regulators, 3 PDUs (TBD), TBD battery
Mechanical Configuration	<ul style="list-style-type: none">• 175 in x 95 in x 98 in (Structure only, does not include collection funnel)
Payload	<ul style="list-style-type: none">• 110 kg CBE

NOTE: During the CML4 study, the number of NGRTGs was reduced from 3 to 2 to reduce mass.

Small Orbiter with Large Lander

Subsystem	Description
Propulsion	<ul style="list-style-type: none">• Bipropellant (main engine) and monoprop propulsion subsystem• 2625 m/s; 3980 kg propellants• 2-100 lb main engines and 8 and 16 RCS engines, 1 hour SOI
Avionics	<ul style="list-style-type: none">• Redundant flight computers with data storage 128 Gbits
Telecom	<ul style="list-style-type: none">• X-band: Uplink & 65W Downlink• Ka-band: 60 W Downlink (40 kbps @ max range)• 2.2-m HGA, MGA, fanbeams (3), and LGAs(3)• UHF relay for lander comm
Control	<ul style="list-style-type: none">• 3-axis: Reaction wheels(4), RCS engines• Pointing Ka 1 mrad, NAC (TBD) – need to revisit this and opnav• Star trackers(2), IMU internally redundant, sun sensors(6)
Thermal	<ul style="list-style-type: none">• Thermos bottle, radiator, louvers, MLI
Power	<ul style="list-style-type: none">• 3 NGTRGs (1 on lander + 2 on orbiter)• 3 shunt regulators, 3 PDUs (TBD)
Mechanical Configuration	<ul style="list-style-type: none">• 200 in x 95 in x 98 in (Structure only, does not include collection funnel)
Payload	<ul style="list-style-type: none">• 138 kg (40 kg on Orbiter, 89 kg on Lander)
Lander	<ul style="list-style-type: none">• 500 kg total CBE: includes 1 NGRTG, 80 kg payload (70x95x98 in lander)• Lander includes prop system and EDL sensors

Large Orbiter with Small Lander

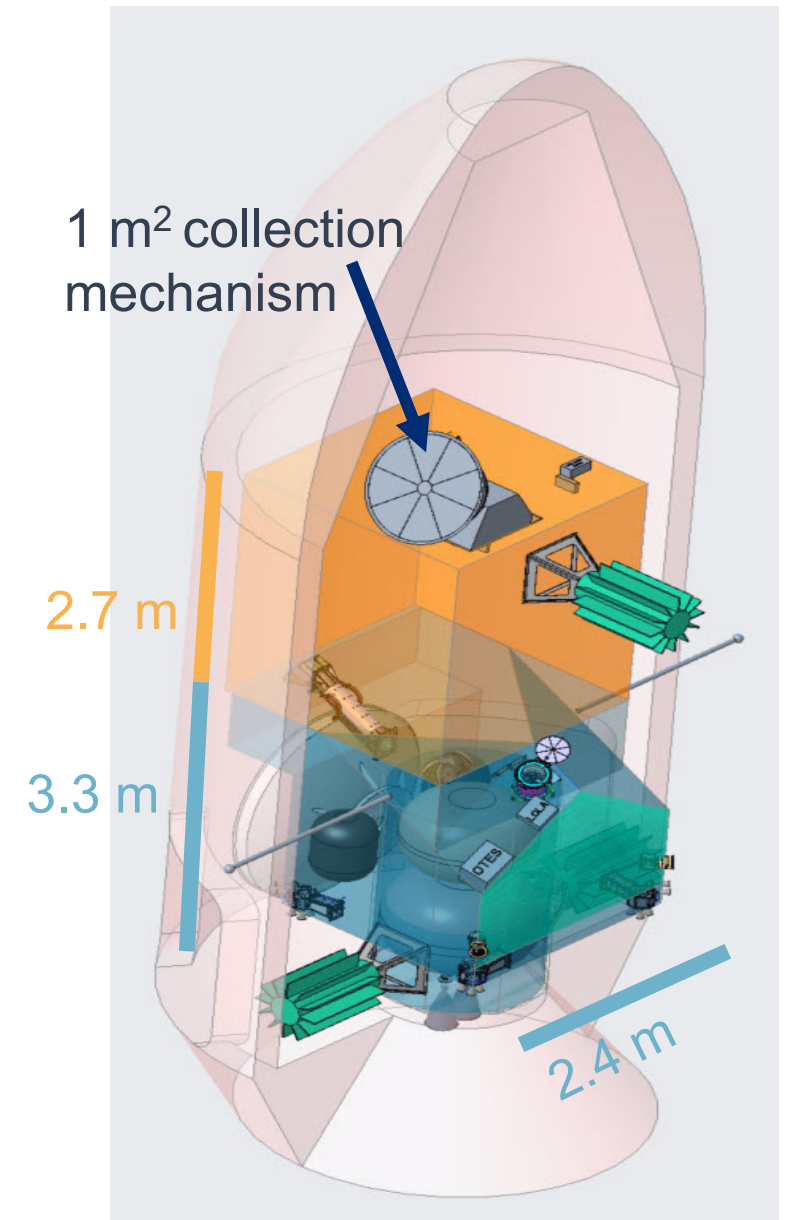
Subsystem	Description
Propulsion	<ul style="list-style-type: none">• Bipropellant (main engine) and monoprop propulsion subsystem• 2625 m/s; 3980 kg propellants• 2-100 lb main engines and 8 and 16 RCS engines, 1 hour SOI
Avionics	<ul style="list-style-type: none">• Redundant flight computers with data storage 128 Gbits
Telecom	<ul style="list-style-type: none">• X-band: Uplink & 65W Downlink• Ka-band: 60 W Downlink (40 kbps @ max range)• 2.2-m HGA, MGA, fanbeams (3), and LGAs(3)
Control	<ul style="list-style-type: none">• 3-axis: Reaction wheels(4), RCS engines• Pointing Ka 1 mrad, NAC (TBD) – need to revisit this and opnav• Star trackers(2), IMU internally redundant, sun sensors(6)
EDL	<ul style="list-style-type: none">• Lidar, descent camera + landing thrusters, structure
Thermal	<ul style="list-style-type: none">• Thermos bottle, radiator, louvers, MLI
Power	<ul style="list-style-type: none">• 3 NGRTGs (all on orbiter; small lander battery powered)• 3 shunt regulators, 3 PDUs (TBD), TBD battery
Mechanical Configuration	<ul style="list-style-type: none">• 160 in x 95 in x 98 in (Structure only, does not include collection funnel)
Payload	<ul style="list-style-type: none">• 125 kg (115 kg on Orbiter, 10 kg on Lander)

Mechanical Configuration

The [Orbiter mechanical design](#) was examined in most detail.

The [Large Lander](#) (which would separate from the orbiter in the Orbiter+Large Lander architecture) was allocated additional volume but not examined beyond ensuring (1) the passive sampling mechanism (funnel) and one RTG were attached to the lander side and (2) that the total volume fit within the launch vehicle fairing (shown left). Since the LDS fits within the Orbiter, it is safe to assume that it would fit on the Large Lander.

The small lander (not shown) was envisioned to be much smaller spacecraft than the large lander, and would easily fit within launch vehicle fairing.

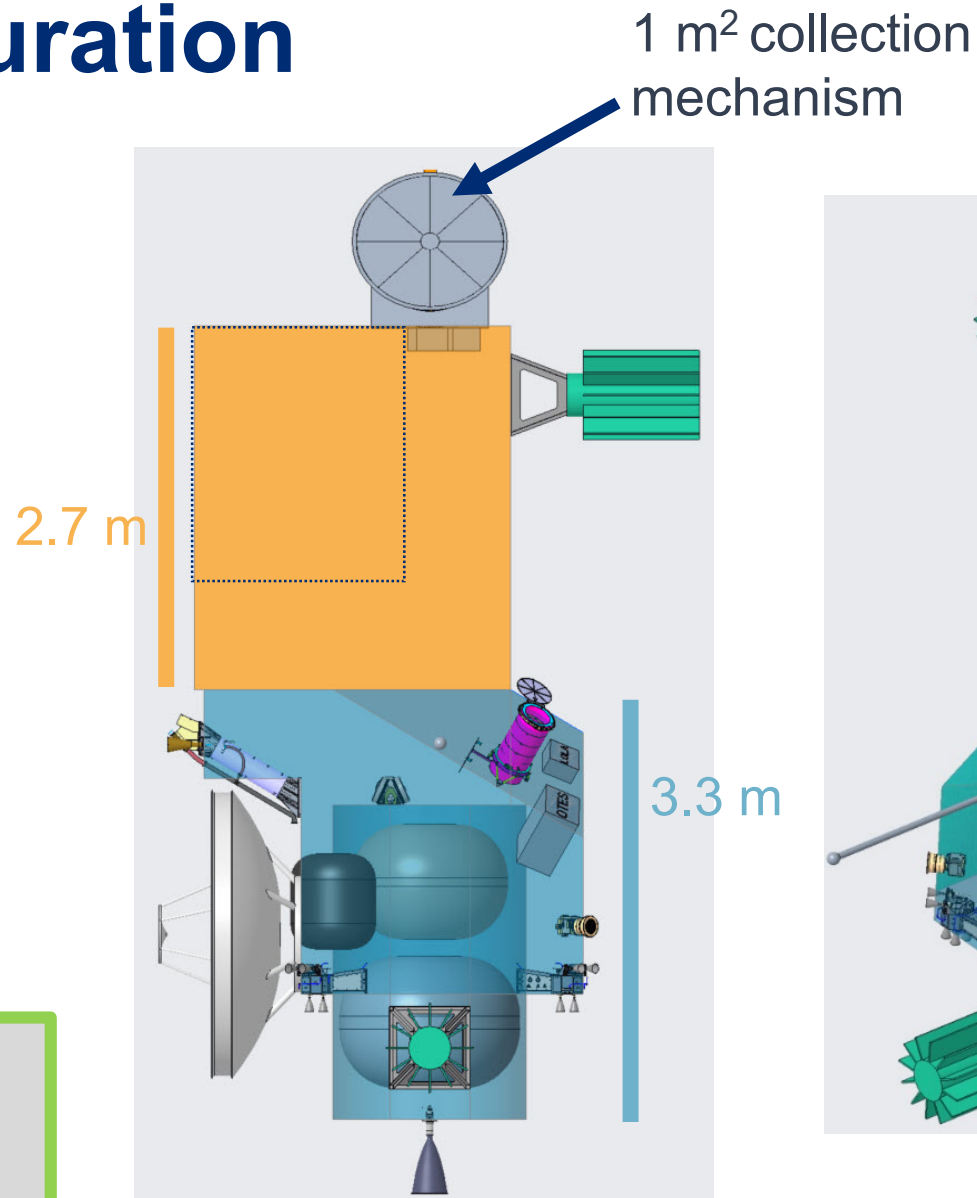


Orbiter volume in blue, with large (separable) lander in yellow box

Mechanical Configuration

- Blue = orbiter volume
- Orange = Large lander volume available
- For scale, the Europa Lander and its descent system fit in the dashed box.
- The Orbilander architecture would take the whole spacecraft down to the surface.
 - Details (legs, descent propulsion, etc.) would need to be worked during a point design

NOTE: A description of the details worked during the CML4 Orbilander study can be found in Section 3.3.



Mass Equipment List

Subsystem	Orbiter	Orbilander	Orbiter + Large Lander	Orbiter + Small Lander	
Power electronics and distribution	30	30	30	30	
Batteries	70	70	70	70	
NG-RTGs	186	186	124	186	Large Lander assumes 2x RTGs
propulsion system	370	370	370	370	Includes residuals and He
Telecom	68	68	80	80	up by 6
2 axis gimbal for HGA on surface	0	15	0	0	
Mechanical	423	423	423	423	
Big lander legs/pallet/base	0	100	0	0	
Thermal	100	100	100	100	
GNC	50	50	50	50	
EDL sensors (lidar & descent cam)	0	40	0	0	No EDL on orbiters
C&DH	12	12	12	12	
Harness	128	128	96	122	assumes 5%
Separation system for lander	0	0	20	10	
Payload Mass on Orbiter	115	110	49	115	
Total Spacecraft CBE	1552	1702	1424	1568	
Lander Vehicle Mass Target			338	100	Includes avionics
Payload mass on lander			89	10	
NG RTG on lander			62	0	
Total calculated Lander CBE			489	110	
Total Dry mass CBE	1552	1702	1913	1678	
Margin (30% of MPV Dry Mass)	667	732	823	722	
Total Dry	2219	2434	2735	2400	
Propellants	3980	3980	3980	3980	
Total Wet Mass	6199	6414	6715	6380	

Payload Mass and Power

Type	Mass (kg)	Avg. Power (W)	Data Vol. per meas. (Mb)	Total Data Vol required (Mb)	Orbiter	Orbilander	Small Lander	Large Orbiter	Small Orbiter	Large Lander
high resolution mass spec (HRMS)	20	70	108	540	X	X		X		X
separation mass spec (SMS)	12	65	164	820	X	X		X		X
electrochemical sensor array (ESA)	3	15	28	140	X	X		X		X
micro capillary electrophoresis – laser induced fluorescence (μCE-LIF)	3.6	6	0.2	1	X	X		X		X
microscope	3	15	33	990	X	X		X		X
nanopore sequencer	4	5	41,000	123000		X				X
radar	12	25	29376	499392	X	X		X	X	
ice particle counter	12	19	50	500	X			X	X	
laser altimeter	8	40	0.65	81.25	X	X		X	X	
thermal emission spectrometer	8	10.8	3.132	250.56	X			X	X	
camera	9	5	4	120000	X	X		X	X	
seismometer	5	9	40.64	609.6		X	X			X
context imager	4	11.8	50	160		X	X			X
Sampling Mechanism (collection)	Passive	20			X	X		X		X
	Active	10	30			X				X
Sample processing	4	10			X	X		X		X
Total Mass					115	110	10	115	49	89

NOTE: During the CML4, a thermal emission spectrometer was added to the Orbilander to ensure safe landing site identification (Section 3.1.1, Appendix B.1.4 and Appendix D.4.)

Power Equipment List (units in Watts)

Operating Mode	Nominal	Safe - RW	Telecom	science	Thrusting	Prop - SOI	Landing	Surface
Duration	Continuous	Continuous	8 hrs	8 hrs	10 min	2 hrs	30 min	continuous
Power electronics and distribution	20	20	25	25	25	25	25	20
Batteries								
NG-RTGs								
propulsion system - engines	20			25	110	140	110	
cat bed heaters (1 hour prior)					12			
Telecom	140	140	140	10	140	140	140	140
Gimbal for HGA (surface only)								20
Thermal	100	100	100	100	100	100	100	100
GNC	132	132	132	132	45	45	45	0
EDL sensors							50	0
C&DH	40	40	40	40	50	60	50	40
Harness loss	17	17	17	17	17	21	17	0
Payload survival power (or max op power)	50	50	50	100	50	50	50	50
Lander survival power	20	20	20		20	20		
TOTAL calculated	519	499	504	449	549	581	587	370
Margin	246	246	246	246	246	297	246	246
Total Power (Watts)	765	745	750	695	795	878	833	616
EOM available	819	819	819	819	819	990	819	819

Note: @ SOI Only 9 yrs degradation on RTG

Payload Trades

- Guiding philosophy
 - Because the primary science goal of this mission concept study is life detection, LDS is prioritized: any payload adjustments to the CML 3 architectures must first maximize the likelihood of successful science return from these measurements before considering the effect on other science objectives.
- **Sampling system**
 - Analog scoop a placeholder at CML-3
 - Optimizing for Enceladus environment
 - Low gravity
 - Fluff and hard ice possible
 - Optimizing for the lander
 - Sampling on the legs rather than a mobile arm?
 - Deposit scoop sample into funnel? Into separate receptacle?
 - Descope to either active-only or passive-only?
 - If descope to an active-only sampling system, the option for doing plume sampling in orbit is limited to the gas inlet of the HRMS, breaking the possibility of recovering science in the absence of suitable landing sites.
 - If descope to passive-only, will require more confidence in ability to get down on the surface where plume fallout is sufficient (mobility?) and increases the amount of time needed to accumulate sample.
- Other trades the science team is looking into:
 - Radar imager? Sounder? GPR? [Needs to be evaluated by the science team, in progress]
 - Laser altimeter science payload? Or can we use the laser altimeter of the TRN/EDL package? What specs for a TRN/EDL laser altimeter should we use?

NOTE: Though the science team considered possible descopes (see “Guiding Philosophy”), none were necessary to take during either the CML-3 or CML-4 studies.

During the CML-4 trade,

- The active sampling system was modeled as a scoop with its own receptacle (separate from the funnel)
- The radar sounder was re-evaluated for the Orbilander and preferred over a GPR or radar imager as the best complement to the seismic investigations.
- The laser altimeter was also revisited in the CML-4 trade and a different analog was chosen to meet both science and TRN/navigation requirements (Appendix C).

Sampling System Order of Operations

- **Passive**
 - **Orbital Phase**
 - Remove cover from funnel on the lander during orbital phase
 - Acquire particulate sample during plume fly throughs
 - Analyze with life detection suite
 - Replace cover before descent
 - **Descend** with cover closed
 - **Landed phase**
 - Remove cover once safely landed (and any potential lofted material settled)
 - Acquire particulate sample from plume fallout
 - Analyze with life detection suite
- **Active**
 - **Landed phase**
 - Recon scooping sites with context camera
 - Acquire particulate sample from surface
 - Analyze with life detection suite

Sample Systems

- Capture
 - Carrying both passive and active for Orbilander and Large Lander
 - Carrying only passive for Orbiter and Large Orbiter
 - Modeled passive as a 1 m² funnel
 - Modeled active as a scoop (could certainly revisit in point design)
- Processing
 - Modeled as a microfluidics device (e.g. SPLIce from NASA Ames).
 - Has some overlap with ESA but there is value in having separate sampling and science instruments
- Aspects we haven't thoroughly thought through yet:
 - Transfer: from capture to processing and processing to instrument
 - Storage: where does the sample go when we are building up to a desired amount?
 - Verification: how do we determine that we've collected enough sample?
 - Processing sequence: rely on instruments to do their own sample prep (easier design?) or rely on processing unit to fully processed material specific to the protocols of each instrument (mass savings?)

NOTE: Various aspects of the sampling system were revisited for the Orbilander though some were identified as beyond the scope of a CML-4 trade (Section 3.1).

ConOps for Sample Acquisition

NOTE: For updates from the CML 4 study, see Appendix B1.3-1.4

Sample mechanism type		Sample Flux		HRMS + μCE + ESA + microscope	GMCS (lipids) + HRMS + microscope + ESA	GCMS (amino acids) + HRMS	nanopore		
				31 μL	178 μL	400 μL	10 mL		
				Time to acquire sample for measurements (Earth days)			Time to acquire sample for 3x measurements (Earth days)	Time to acquire sample for measurements (Earth days)	Time to acquire sample for 3x measurements (Earth days)
Passive	1 m ² funnel in orbit	1.6	uL/m2/orbit (Guzman et al. 2019)	10	55	125	570* [2.15 Earth yr]	n/a	n/a
	1 m ² funnel on surface	0.1	mm/yr (Southworth et al. 2019)	0.11	0.65	1.46	6.7	36.5	110
Active	Scoop	5	cc scoop/day (ELSDT scoop = 7 cc)	1			3**	2	6

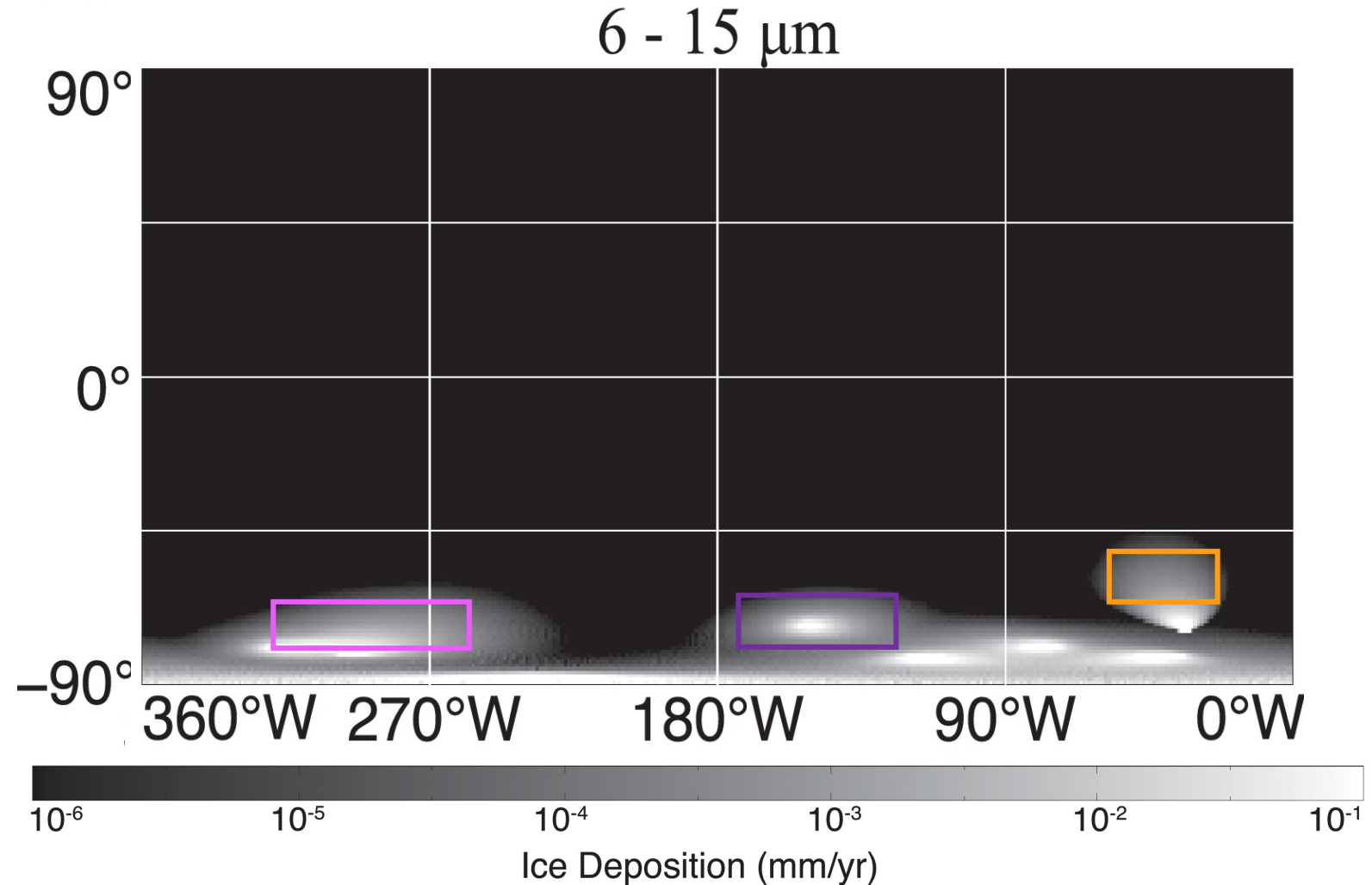
**1 scoop would get enough sample for multiple runs, but we choose 3 for independent measurements.

Landing site options

- Based on the Southworth et al. (2019) paper, there are locations north of 60°S that have plume fallout rates > 0.1 mm/yr.
- Assuming similar distribution of fallout activity in the 2040s, DTE should be feasible for a lander-only architecture, especially with launches later in the decade (next slide).

[Southworth et al. 2019](#)

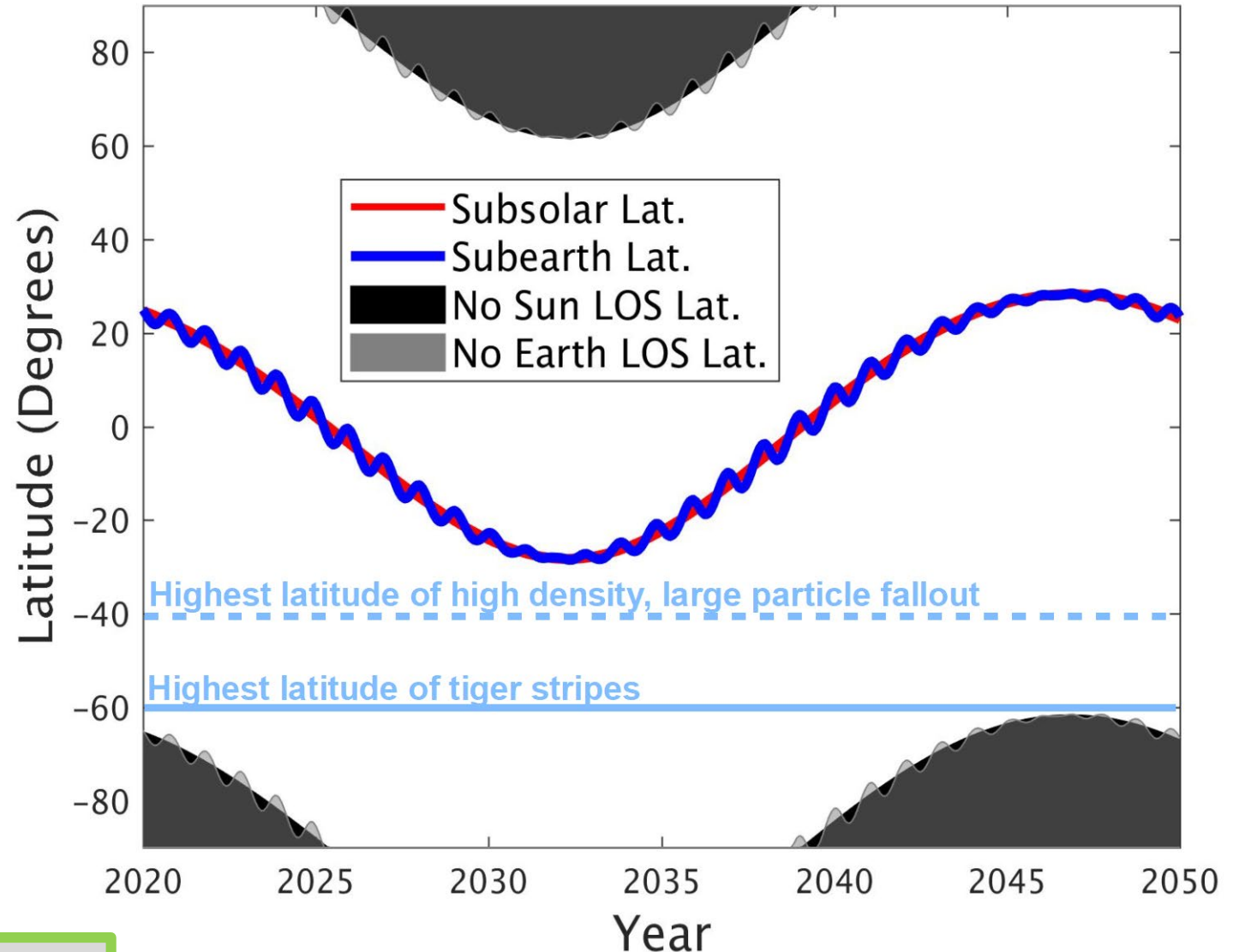
*Modeled map of **largest particles'** fallout pattern. We anticipate that a lander would get more sample than just these large grains*



Landing site options cont'd

- For launches at the beginning of the decade, we arrive at the worst possible time for a lander.
 - If we pursue a lander only architecture in the point design, we can pursue using the SLS for earlier arrival, but then we would be both fighting against the clock as winter approaches and using a more expensive launch vehicle.
 - Easier solution is to launch later in the decade (also allows for time for instrument development, etc).
- For launches >2033, mission begins after southern winter solstice.

NOTE: For the Orbilander, later launches were pursued to ensure beginning of mission with sufficient southern latitude illumination



Earliest launch 2031 Latest launch 2039
9 yr Cruise 5 yr pump down 3 yr mission

Landing Site Recon Considerations

For Orbilander, Large Lander, and Small Lander

- Camera analog: New Horizons' LORRI
- Orbiting at 30 km
 - Pixel scale on surface = 0.4-1.4m/pixel
 - Surface area per image = 0.17 -2 km²
 - ~320,000 images to cover SPT with stereo coverage
 - 1.2 Tbits of data
 - At 30 kbps with 8 hr downlink once per 12 hr orbit, ~2 Earth years to send data back
- But, we don't actually need all that data to identify a sufficient number of landing sites that are both **safe** (e.g. low slopes, low lander-scale roughness, good illumination, not too fluffy [if we can figure out a way to discern this]) and **experiencing high plume fallback**
- Assuming lander ellipse of 1 km² and that 1% of sites characterized are actually safe, we may observe **18** landing sites in **100** Earth days. It will take **70** mission days to return all this data.
- For plume recon, we may be able to take advantage of pump down phase to obtain high phase images, as Enceladus will fill the full frame with LORRI imaging during Tethys flybys

Surface Thermal Environment

- best-fit isothermal temperature 197 ± 20 K was obtained by VIMS observation of an active spot along Baghdad Sulcus (*Goguen et al.*, 2013)
- highest temperature obtained by CIRS (176.7 ± 1.3 K) at the brightest hot spot observed on Damascus Sulcus (*Spencer et al.*, 2011)
- Hodyss et al. AGU 2019
 - “Sintering of the ice caused growth of the contact regions between grains and mass redistribution, leading to the formation of agglomerate structures and some recrystallization.”
 - “Combined, these effects resulted in an increase of the penetration resistance of the bulk ice samples, with warmer samples experiencing more modification.”
 - “Results suggest plume deposits remain weak on Enceladus far from the thermal influence of the Tiger Stripes.”
- But we are targeting further away from the tiger stripes where fallout is occurring but where temperatures are probably lower (min 50 K?)
- Should we assume that the surface will be a fluffy regolith? Say 1-10m thick (*Bland et al.* 2015)?

NOTE: These questions were revisited in the CML-4 study. See Appendix B.1.3 and D.4

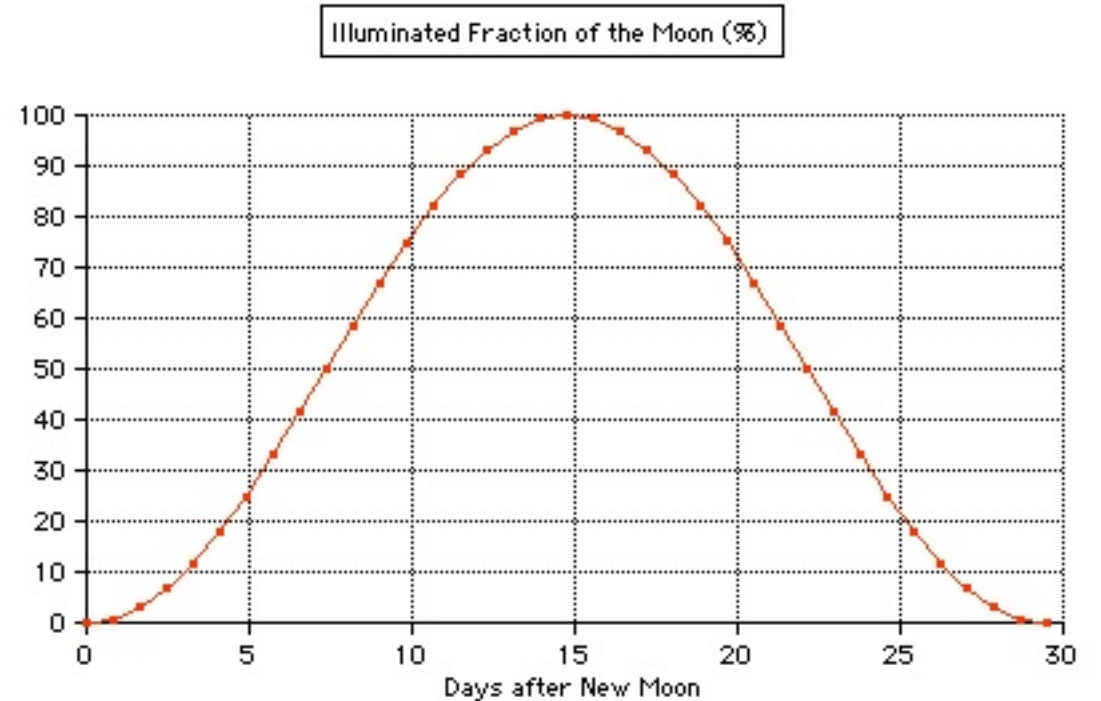
Saturnshine

- Solar flux at 9.5 AU: $1360/(9.5^2) = 15 \text{ W/m}^2$.
- Solar radiated power intercepted by Saturn with radius 58232 km: $1360/(9.5^2) * \pi * 58232000^2 = 1.6 \times 10^{17} \text{ W}$
- Saturnshine = solar power reflected off Saturn (albedo 0.34) = $5.46 \times 10^{16} \text{ W}$
- Saturnshine flux at Enceladus' orbit of semimajor axis 237948 km = $5.46 \times 10^{16} / (4 * \pi * 237948000^2) = 0.07 \text{ W/m}^2$.

Best: 0.5% of the solar flux when Enceladus is between Saturn and the Sun.

Worst: 0 when Saturn is between Enceladus and the Sun

Two thirds of the time, Saturnshine is $> 0.1\%$ of Sunshine, so we could multiply imaging exposure times by 1000 at fixed aperture and gain.



Above curve for the Moon gives an approximation of how Saturnshine varies in between these two extrema with Saturn phase. This neglects ringshine.

End of life

- Orbiters
 - Reserve enough fuel for Enceladus deorbit and crash into Saturn or other satellite
- Landers
 - Freeze in place; low likelihood of contacting ocean in nominal/off nominal landing
 - Spacecraft cleanliness requirements for Life Detection Science assumed much more demanding than Planetary Protection

NOTE: The assumptions for landing were revisited and refined during CML 4 (D.4).

Risks by Architecture

Orbiter	Orbilander	Small Orbiter + Large Lander	Large Orbiter + Small Lander
Orbit maintenance	Orbit maintenance	Orbit maintenance	Orbit maintenance
Pump down flyby cadence	Pump down flyby cadence	Pump down flyby cadence	Pump down flyby cadence
Bio cleanliness	Bio cleanliness	Bio cleanliness	Bio cleanliness
Lifetime of HW	Lifetime of hardware	Lifetime of HW	Lifetime of HW
Disposal from orbit	Disposal of RPS on surface or lift off	Dispose RPS on surface and orbit	Disposal on surface and orbit
Payload accommodation and config on SC	Payload accommodation and config on SC	Payload accommodation and config on SC	
	Land large SC, tip		
	Landing site selection and unknowns	Landing site	
	Surface contamination	Surface contamination	Surface contamination
	Mechanisms on surface	Mechanisms	Mechanisms
		Separation	

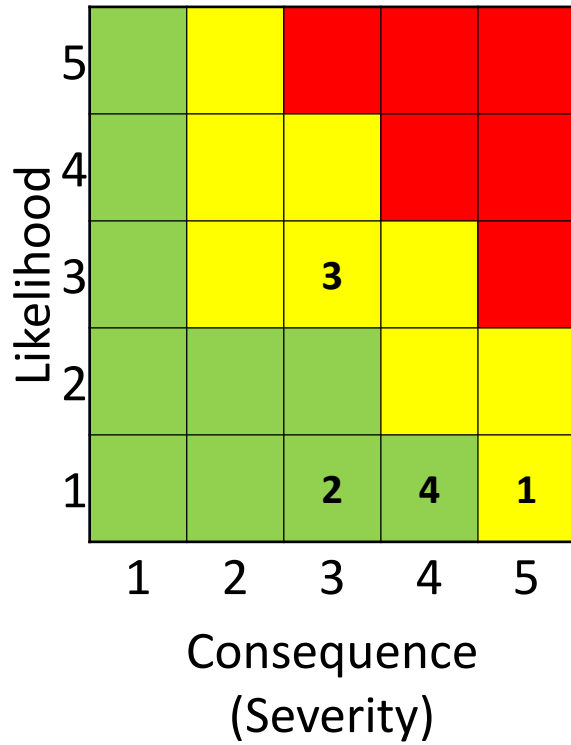
Risk Table

Risk #	Mission Type	Risk Case	Consequence	Likelihood	Consequence
1	All	Orbiter cannot maintain orbit around Enceladus	Science Objectives cannot be met	1	5
2	All	Timeline between Pumpdown maneuvers increases (extended TOF to Enceladus Orbit)	Mission Duration longer than planned (power limited)	1	3
3	All	Cleanliness Requirements levels become restrictive	Impact cost/schedule	3	3
4	All	Demonstration of hardware lifetime requirements (~20 years)	Change Mission design to shorten mission duration	1	4
5	Orbilander, Large Lander	Disposal on surface (above equator) not acceptable	Payload required would not be feasible for this mission concept	2	5
6	Orbilander, Large Lander	Underestimation of Lander complexity	Potential increases to cost/schedule, mass -> science	3	4
7	Orbilander, Large Lander	Inability to identify acceptable landing Site once in orbit	Landing not possible, reduction in science return	2	4
8	Small Lander	Inability to identify acceptable landing Site once in orbit	Landing not possible, reduction in science return	1	2
9	Orbilander, Large Lander	Lander contaminates surface/collector	Science return impacted, potential for baseline science not to be met	2	4
10	Large/Small Lander	Separation failure of Lander from Orbiter	Landing not possible, reduction in science return	1	4
11	Orbilander, Large Lander	Failure of Mechanisms on surface (Scoop, re-closing funnel cover, articulating antenna)	Reduction in Data return, inability to collect more samples -> Reduction in Science Return	1	4

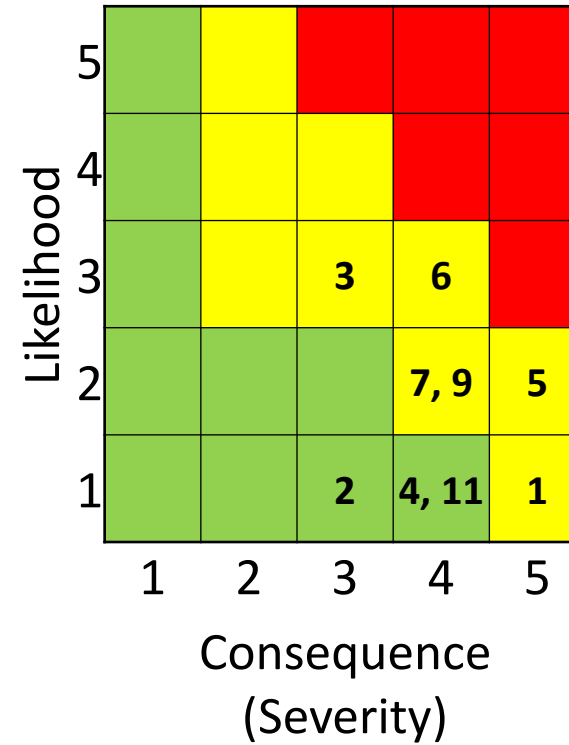
NOTE: Orbilander risks were revisited and refined during CML 4 (Section 3.15).

5 x 5 Risk Matrix

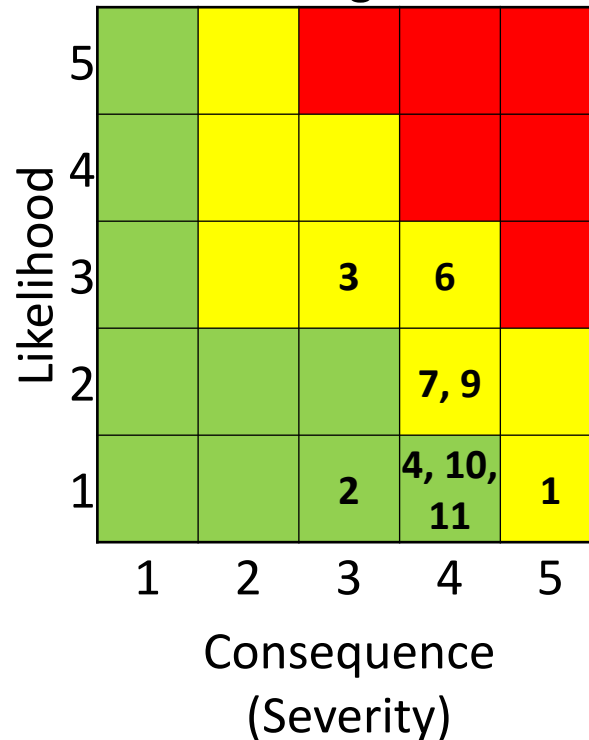
Orbiter



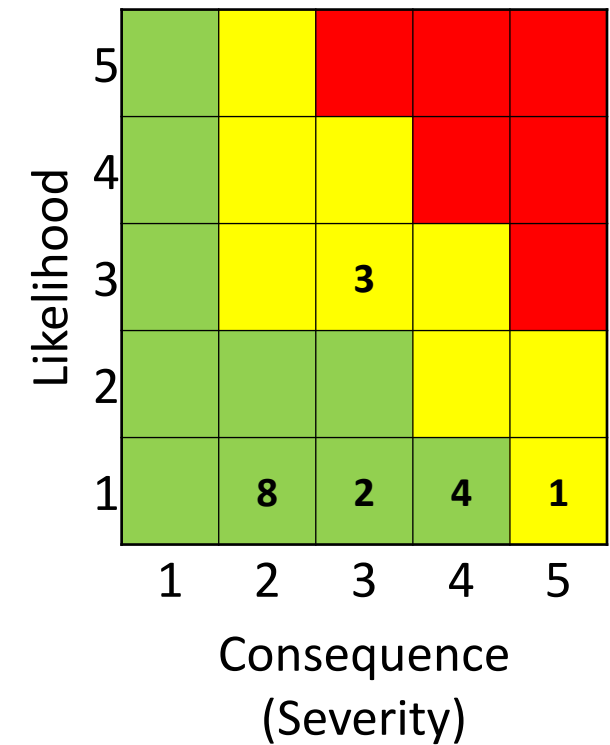
Orbilander



Orbiter + Large Lander



Orbiter + Small Lander



Enceladus Mission Concept Comparisons

	Orbiter	Orbilander	Large Orbiter + Small Lander	Small Orbiter + Large Lander
Launch mass (For mission design)	6800 kg	6800 kg	6800 kg	6800 kg
Mission life	18-20 years	18-20 years	20 years	20 years
Reserved mass & power margins	30%	30%	30%	30%
Total dry mass (MPV)	2820 kg	2820 kg	2820 kg	2820 kg
Propellants	3990 kg	3990 kg	3990 kg	3990 kg
Total Wet Mass	6199 kg	6414 kg	6715 kg	6380 kg
EOM Power Est	500W	500W	500W	500W
Data target	1 terabit	1 terabit	1 terabit	1 terabit

Top Level Comparison

Space system Configuration	Orbiter only	Orbilander	Orbiter plus lander		
Lander	NA	Med/Large Lander	Mini lander	Med lander	Orbiter
Mobility	NA	none	Possible	Possible	NA
Launch Year	2031-2039	2031-2039			2031-2039
trajectory	inner cruise	inner cruise			DVEGA, inner cruise
Launch Vehicles	SLS, FHE	SLS, FHE			SLS, FHE
Primary power source	NGRTG (3)	NGRTG (3)	Primary Battery	NGRTG(1)	NGRTG(2)
Total Power EOM	820 W	820 W	TBD	270W	270-540W
Payload Power target (peaks from battery)	150W	150 W	20 W	80W	50W
Total mass target	2800 kg Dry mass	2800 kg Dry mass			1000-2000 kg
Lander mass target			30-100 kg	475 kg	
Payload mass target	130 kg	130 kg	10-30 kg	80 kg	50-100 kg
DL Data rate estimate	30 kbps	30 kbps	Tbd – Link to Orbiter	TBD – Link to Orbiter	30 kbps
Data return target	1 Terabit	1 Terabit			1 Terabit
Pointing control	wheels and thrusters	wheels and thrusters	none	thrusters	wheels and thrusters
Propulsion	Chemical	Chemical	Chemical	Chemical	Chemical
Lifetime target at Enceladus	3 years	TBD? 3 total years split	15 days on surface	1 year	3 year
Mission duration including transit time	18-20 years	18-20 years			20 years
Launch mass	6800 kg	6800 kg			6800 kg

ΔV working assumptions

ΔV assumptions used to develop mass targets

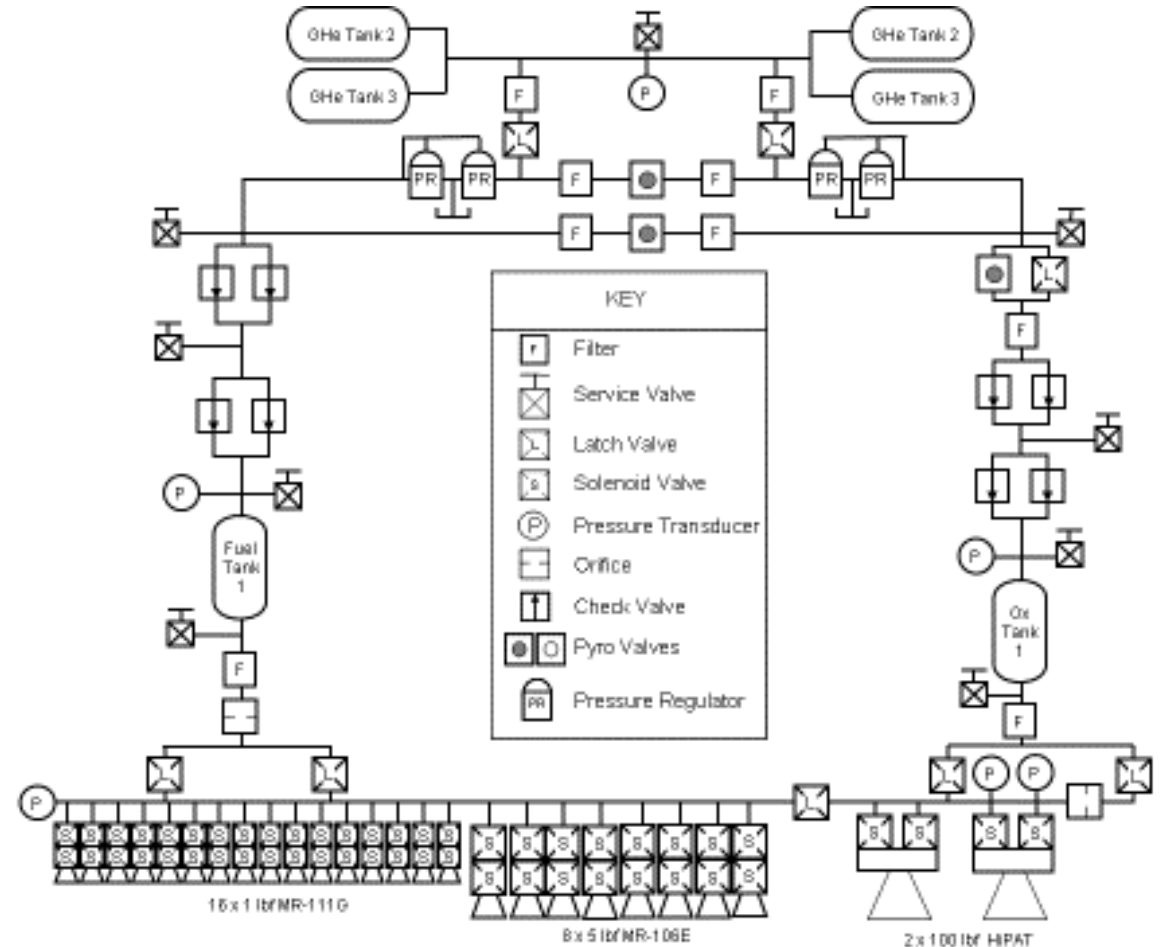
	Inner cruise	Direct	EGA -DSM
SC DV Cruise	100	0	700
SC delta v SOI (7 years)	625	1000	625
SC delta v PRM (+100 days)	500	500	500
SC DV flybys	600	600	600
SC DV to orbit	250	250	250
SC DV to land	100	100	100
Stationkeeping -monoprop	200	200	200
Disposal DV*	250	250	250
TOTAL Delta V (m/sec)	2625.00	2900.00	3225.00
Corresponding mission duration (yrs)	19.5	13.5	18.5

*Or dispose on surface – equatorial terrain

Subsystem Details

Propulsion Assumptions

- 6800 kg Wet Mass
- 2625 m/s Total Delta-V
 - 2425 m/s for biprop
 - 200 m/s for monoprop
 - 100 kg ACS propellant
- Total Propellant = 3986 kg
 - Fuel mass = 2324.4 kg
 - Oxidizer mass = 1661 kg
- Total Pressurant = 14.6 kg



Propulsion Subsystem

- Thrusters:
 - 445N (100 lbf) Dual Mode Apogee Engine (2)
 - Bipropellant (Hydrazine/NTO)
 - 22N (5.0 lbf) Hydrazine Monopropellant Thrusters (8)
 - Two sets of four for redundancy
 - Biprop maneuvers will be done with 445N and 22N steering thrusters
 - Gimbaled main engines could replace the eight 22N engines but possible issues with lifetime requirements for gimbals
 - 4.4N (1 lbf) Hydrazine Monopropellant Thrusters (16)
 - Two groups of eight for redundancy
 - ACS, Momentum Wheel Desaturation

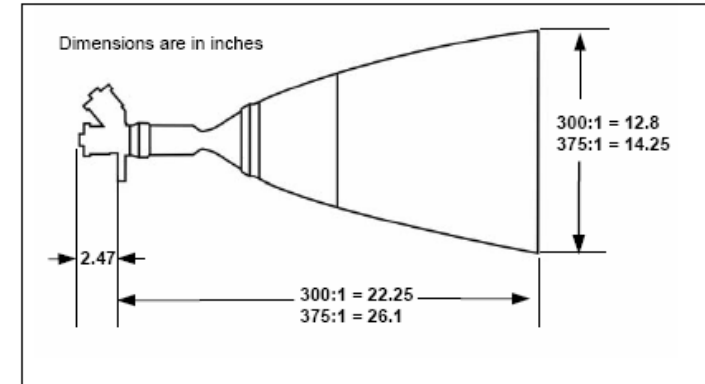
Fuel/Oxidizer/Pressurant Tanks

- Current Configuration:
 - 1 Fuel Tank, 1 Oxidizer Tank, 4 Pressurant Tanks
 - Fuel Volume = 154644 in³
 - Ox Volume = 80403 in³
 - GHe Volume = 21203 in³
 - Two big tanks better for structural reasons
- Fuel and Oxidizer tanks will require custom Propellant Management Devices (PMDs)

Dual Mode Apogee Engine

- 445N (100 lbf) 326s
Aerojet-Rocketdyne
HiPAT DM

HiPAT™ - 445N (100 lbf) DUAL MODE HIGH PERFORMANCE LIQUID APOGEE THRUSTER



Design Characteristics

- Propellant Hydrazine/NTO(MON-3)
 - Thrust/Steady State 445 N (100 lbf)
 - Inlet Pressure Range 21.4-15.2 Bar (310-220 psia)
 - Chamber Pressure* 9.4 Bar (137 psia)
 - Expansion Ratio 300:1, 375:1
 - Oxidizer/Fuel Ratio 0.73-1.18 (0.85 nominal)
 - Flowrate* 141 g./sec (0.31 lbfm/sec)
 - Valve Aerojet Solenoid, Dual Coil, Single Seat
 - Valve Power Various (46 Watts @ 28 Vdc Typical)
 - Mass 5.2 kg (11.5 lbfm)
- *at rated thrust

Performance

- Specific Impulse (lbf-sec/lbfm) 300:1 = 326
..... 375:1 = 329
- Total Impulse In Excess of 9.55×10^8 N-sec
(2.15×10^8 lbf-sec)
- Total Pulses 672
- Total Thermal Cycles 345
- Minimum Impulse Bit (lbf sec) 8
- Steady State Firing (sec) 1800

Flight Status

Program

Development Test
Europa Evaluation Test
Qualification and Flight Production

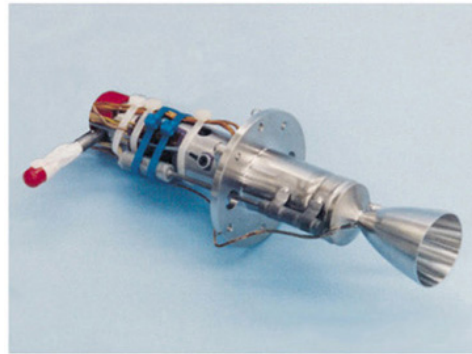
Customer/User

In-House
NASA JPL
Proprietary

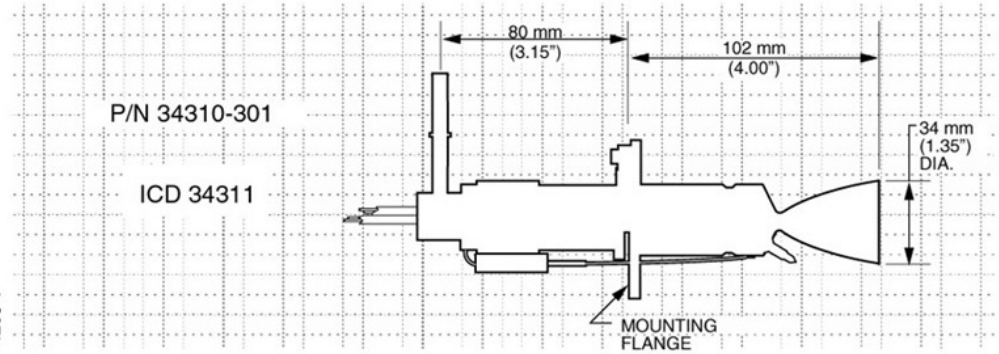
Notional 22 N (5 lbf) Steering Thruster

- Aerojet MR-106E

MR-106E 22N (5.0-lbf) ROCKET ENGINE ASSEMBLY - 28 Vdc



4266-1



Design Characteristics

- Propellant.....Hydrazine
- Catalyst.....LCH-227/202
- Thrust/Steady State..... 30.7 – 11.6 N (6.9 – 2.6 lbf)
- Feed Pressure..... 24.1 – 6.9 bar (350 – 100 psia)
- Chamber Pressure.....12.4 – 4.5 bar (180 – 65 psia)
- Expansion Ratio..... 60:1
- Flow Rate..... 13.1 – 5.0 g/sec (0.0289 – 0.011 lbfm-sec)
- Valve Dual Seat
- Cat. Bed Heater Pwr.....6.53 Watts Max @ 28 Vdc & 21° C
- Valve Heater Power 3.27 Watts @ 28 Vdc & 21° C
- Valve Power 25.3 Watts Max @ 28 Vdc & 21° C
- Mass 0.635 kg (1.4 lbfm) max

* Mars Odyssey Test Program
December, 2000

Performance

- Specific Impulse..... 235 – 229 sec (lbf-sec/lbfm)
- Total Impulse.....

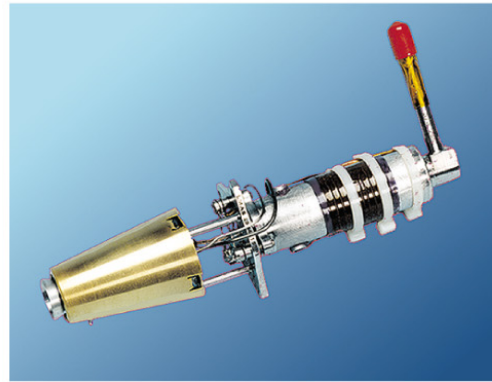
	REA 'A'	REA 'B'	Mars*
.....	120,000 N-sec (26,958 lbf-sec)	125,000 N-sec (28,044 lbf-sec)	90,587 N-sec (20,366)
- Total Pulses..... 12,405 186 66,631
- Minimum Impulse Bit 0.46 N-sec @ 12.8 bar & 16 ms ON
..... (0.103 lbf-sec @ 185 psia & 16 ms ON)
- Steady State Firing..... 2,000 sec — Single firing
..... 4,670 sec — Cumulative

- APL Heritage: MESSENGER, NEAR, and CONTOUR

Notional 4.4N (1.0 lbf) Thruster

- Aerojet MR-111C

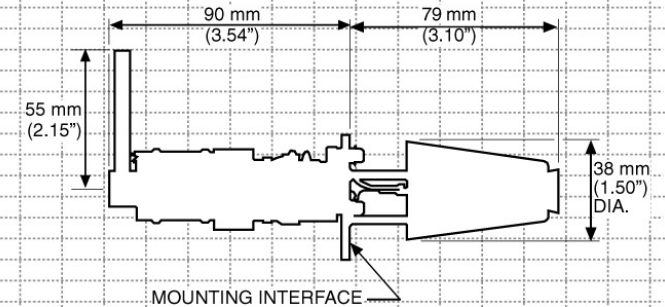
MR-111C 4 N (1.0-lbf) ROCKET ENGINE ASSEMBLY



4448-3

P/N 27720-308-11

ICD 31528



Design Characteristics

- Propellant Hydrazine
- Catalyst S405
- Thrust/Steady State 5.3 – 1.3N (1.2 – 0.3 lbf)
- Feed Pressure 27.6 – 5.5 bar (450 – 50 psia)
- Chamber Pressure 12.1 – 3.4 bar (200 – 35 psia)
- Expansion Ratio 74:1
- Flow Rate 2.4 – 0.6 g/sec (0.0053 – 0.0014 lbm-sec)
- Valve Dual Seat
- Valve Power 8.25 Watts Max @ 28 Vdc & 21°C
- Valve Heater Power 1.54 Watts Max @ 28 Vdc & 21°C
- Cat. Bed Heater Pwr 3.85 Watts Max @ 28 Vdc & 21°C
- Mass 0.33 kg (0.73 lbm)
 - Engine 0.13 kg (0.28 lbm)
 - Valve 0.20 kg (0.45 lbm)

Performance

- Specific Impulse 229 – 215 sec (lbf-sec/lbm)
- Total Impulse 260,000 N-sec (58,500 lbf-sec)
- Total Pulses 420,000
- Minimum Impulse Bit 0.08 N-sec @ 6.9 bar & 15 ms ON
 (0.0171 lbf-sec @ 100 psia & 15 ms ON)
- Steady State Firing 5,000 sec min – Single Firing

Status

- Flight Proven

Status

- AIAA-1999-2469

Propulsion Mass Summary

Item	Unit Mass [kg]	CBE/M EV	QTY	Tot. Mass [kg]
Oxidizer Tank (Custom Ox)	50.25	MEV	1	50.25
N2H4 Tank (Custom Fuel)	96.65	MEV	1	96.65
GHe Tank (Custom Pressurant)	14.46	MEV	4	57.83
HiPat	5.20	MEV	2	10.40
5 lbf Thruster (MR-106E)	0.73	MEV	8	5.84
1 lbf Thruster (MR-111G)	0.37	MEV	16	5.92
Fuel Check Valve	0.23	MEV	2	0.46
Ox Check Valve	0.25	MEV	2	0.50
Fuel/Ox Service Valve	0.15	MEV	8	1.23
Helium Service Valve	0.07	MEV	1	0.07
Pyrotechnic Valve	0.21	MEV	3	0.62
Latch Valve	0.34	MEV	6	2.04
High-Pressure Latch Valve	0.52	MEV	2	1.04
Pressure Regulators	1.20	MEV	2	2.40
Pressure Transducer	0.23	MEV	6	1.38
Filter	0.16	MEV	9	1.47
Orifice	0.03	CBE	2	0.06
Tubing / Fasteners / Tube Clamps / Etc.	20.13	WAG		20.13
Thermal Hardware (thermostats, etc.)	7.72	WAG		7.72
Cabling (Wire, Harness, Supports)	17.38	WAG		17.38
N2H4 Residuals at 50°C				38.32
Oxidizer (NTO-MON3) Residuals at 50°C				28.40
GHe Pressurant				14.56
Total Propulsion System Dry Mass				364.66
Solid Propellant				0.00
Usable GHe Cold Gas Propellant				0.00
Usable N2H4				2324.40
Usable Oxidizer (NTO-MON3)				1661.04
Total Propellant Mass				3985.44
Total Spacecraft Dry Mass				2814.56
Total Spacecraft Wet Mass				6800.00

Propulsion Subsystem - Power Summary

- SOI Peak Power: 176 W for one main engine; 282 W for two
 - Biprop injector heater power is notional and will be dependent on thermal design
- 28 VDC
- Latch Valves only powered for 100 ms
- Does not include all line/tank/component heaters.

Item	Number of Components	Power per Element (W)	CBE/MEV/WAG	Elements per Component	Power per Component (W)
HiPAT Valves	2	23	CBE	2	46
HiPAT Valve Heater	2	5	WAG	2	10
HiPAT Injector Heater	2	25	WAG	2	50
5 lbf Thruster Valve	8	12.65	CBE	2	25.30
5 lbf Thruster Valve Heater	8	3.27	WAG	1	3.27
5 lbf Thruster Cat Bed Heater	8	3.27	CBE	2	6.54
1 lbf Thruster Valve	16	4.13	CBE	2	8.26
1 lbf Thruster Valve Heater	16	1.54	WAG	1	1.54
1 lbf Thruster Cat Bed Heater	16	3.16	CBE	2	6.32
Latch Valve (1/4" Vacco)	6		CBE		18.00
High-Pressure Latch Valve	2		CBE		45.80
Pressure Transducer	6		CBE		0.90

Electric Propulsion Trade Study

- During CML-3 Architecture study, a trade was performed to evaluate an electric propulsion (EP) system using the
- Primary Thruster: Aerojet XR-5 Hall Thruster as the primary means of providing Delta-V
- Issues:
 - Large amount of power that EP systems require to achieve their excellent efficiency. For the purposes of this study, it was assumed that 1000 W of power could be delivered to the system. At just over 20% of the power it was designed for, the thruster would have an Isp of 1341 seconds and 57 mN of thrust. Additional RTGs would be required to produce enough power for the EP system.
 - Due to the low thrust of EP propulsion systems, the duration of the mission spent enroute to Enceladus orbit increases. This results in longer lifetime requirements for instruments and subsystems, as well having less power available once on Enceladus, owing to the nature of RTGs.
 - Landing approach from Orbit requires high-thrust system
- For these reasons, the engineering team proceeded with an all-chemical propulsion solution for the Orbilander.

Orbiter Hardware – Rate / Acceleration

	Weight per unit, kg	Power per unit, W	Total Weight, kg	Total Power, W	Size, m
IMU			8	30	0.3137 x 0.1829 x 0.1504
- Gyros					
- Accelerometers				1.4	

- Single IMU
 - 4 gyros / 4 accelerometers for internal redundancy
 - Redundancy internal in electronics
 - Could add additional IMU for long duration flight, power 1 at a time
- Favor hemispherical resonator gyro over fiber optic or mechanical due to potential lifetime issues
- Notional Hardware – Northrop Grumman SSIRU
 - Messenger, PSP, Cassini, etc.

Orbiter Hardware – Fine Attitude (3 axes)

	Weight per unit, kg	Power per unit, W	Total Weight, kg	Total Power, W	Size, m (each)
Star Tracker	2.6	5.6	5.2	11.2	0.164 x 0.156 x 0.348
- Optical Head					
- Electronics Unit					

- Minimum of 2 optical heads required for redundancy
 - May need third depending on science pointing requirements
 - 11.2 W assumes both trackers operated simultaneously and at 20°C (25.2 W at 60° C due to TEC)
- Options exist to reduce weight by ~1 kg per optical head (effectively remove weight of electronics unit (EU)) if perform processing on flight computer as opposed to tracker EU
- Notional Hardware – Leonardo AASTR, (Sodern Hydra similar)
 - PSP, DART

Orbiter Hardware – Coarse Attitude (2 axes)

	Weight per unit, kg	Power per unit, W	Total Weight, kg	Total Power, W	Size, m (each)
Sun Sensors			4.5	3.3	
- Sensor Head	0.25	0	1.5	0	0.0808 x 0.0808 x 0.0495
- Electronics Unit	1.5	3.3	3	3.3	0.2731 x 0.1423 x 0.0546

- Two Electronics Units for redundancy
 - Assumes only 1 electronics unit powered at a time
- Sensor head number is notional at this time, currently assuming 6
 - DART uses 5 heads for near full sky coverage prior to factoring in obstructions
 - Not redundant heads
 - Power is driven by electronics unit, not sensor heads
- Options to add spinning sun sensor if required for cruise
- Notional Hardware – Adcole DSS
 - PSP, DART, IMAP

Orbiter Hardware – Reaction Wheels

	Weight per unit, kg	Power per unit, W	Total Weight, kg	Total Power, W	Size, m (each)
Reaction Wheels	6.6	22 W / 90 W peak			0.31 x 0.31 x 0.122

- Four reaction wheels needed for redundancy
 - Frequently, all 4 are used until a failure occurs for higher performance
 - Cassini used 3 at a time and was capable of reorienting one wheel
 - Could spin all 4 at the same time
- Quoted power numbers are at maximum desired wheel speed with holding torque / peak torque
- Lubrication / bearing issues possible
 - Typically rated to “>15 years”
- Options exist to trade between mass and power for similar momentum storage
 - Heavier wheel spins at lower maximum rate, which results in a lower maintaining torque
 - Primarily effects holding power, not peak power due to higher possible max torque
 - Could limit maximum commanded torque in software / hardware modification
- Notional Hardware – Rockwell Collins RSI 25-75/60
- (similar systems) PSP, Messenger

Lander Hardware

- Star Tracker (2)
- IMU (gyros / accelerometers)
- ALHAT sensors (LIDAR)
- Propulsive system (5 lb / 1 lb thrusters)
- Hyabusa 2 LIDAR
 - 240 x 240 x 230 mm and 3.7 kg
 - Power – 18.5 W (without survival heater)
 - “DEVELOPMENT OF HAYABUSA-2 LIDAR”
 - <https://www.hou.usra.edu/meetings/lpsc2014/pdf/1922.pdf>
- NASA Navigation Doppler Lidar
 - Optical Head – 340 x 330 x 210 mm and 5 kg
 - Electronic Chassis – 280 x 220 x 200 mm and 8.7 kg
 - Power at 28 VDC – 80 W
 - <https://www.lpi.usra.edu/opag/meetings/feb2018/posters/Amzajerjian.pdf>

GNC Performance Requirements

- Sub-meter resolution for landing reconnaissance
- Position funnel to collect samples during periapsis passes
 - Consistent with camera orientation
- Point HGA to Earth
 - Potentially no gimbal
 - Not during sample collection period
- Control attitude during Deep Space Maneuver / Saturn Orbit Insertion using two 100 lb bipropellant engines

GNC Comparisons

- Cassini

- 5574 total wet launch mass
- Mono-propellant hydrazine load – 132 kg, ~100 kg used over 20 years (~20 kg in 7 year cruise, 50 kg in 4 year prime mission, 30 kg in 9 year extended mission)
- Wheels - 15 kg / angular momentum storage capacity of 36 N·m·s each
- Thrusters – Two 445 N biprop, Sixteen 0.9 N Monoprop
- “Final Cassini Propulsion System In-Flight Characterization”
<https://arc.aiaa.org/doi/pdf/10.2514/6.2018-4546>
- “In-Flight Performance of Cassini Reaction Wheel Bearing Drag in 1997–2013”
<https://arc.aiaa.org/doi/full/10.2514/1.A33047>
- “The Cassini Reaction Wheels: Drag and Spin-Rate Trends from an Aging Interplanetary Spacecraft at Saturn”

- Messenger

- Teldix (now Rockwell Collins) RSI 7-75/601 reaction wheels
 - 4.2 kg / 80 W max each
- “MESSENGER GUIDANCE AND CONTROL SYSTEM PERFORMANCE DURING INITIAL OPERATIONS”
<https://messenger.jhuapl.edu/Resources/Publications/Vaughan.et.al.2005a.pdf>
- “The MESSENGER Mission to Mercury”
https://books.google.com/books?id=U_JlwP3bXW4C&pg=PA208&lpg=PA208&dq=%22the+messenger+mission+to+mercury%22+%2280+W%22&source=bl&ots=Dw2C_OUGQz&sig=ACfU3U3P18jAFjBITzQHJVatmj4TMvo_9w&hl=en&sa=X&ved=2ahUKewj84creqYHoAhXDIHIEHf-CDW4Q6AEwAHoEAsQAQ#v=onepage&q=%22the%20messenger%20mission%20to%20mercury%22%20%2280%20W%22&f=false

Enceladus Study – Telecom Tradeoffs

Ka-Band or X-band?

NASA ground rules suggest using Ka-Band for science downlink (but can provide justification to use a different band)

Ka-band pluses and minuses

- In general, if spacecraft has an aperture-limited (i.e. dish) antenna, Ka-band can have an advantage over X-band
- Ka-Band does suffer more atmospheric losses than X-band. Data rate at low ground station elevation will be lower than data rate at higher elevations. Each pass will involve changing rates as antenna elevation changes. (This is baked into link budgets discussed here).
- HGA is generally mounted on single-axis gimbal for pointing. There may be times when you can't point the antenna to earth. When you can't use HGA, advantage goes back to X-band.
- Ka-band HGA will have narrower beam than same size X-band antenna. This will affect propellant usage and pointing loss budget.

Enceladus Study – Link Budget Intro

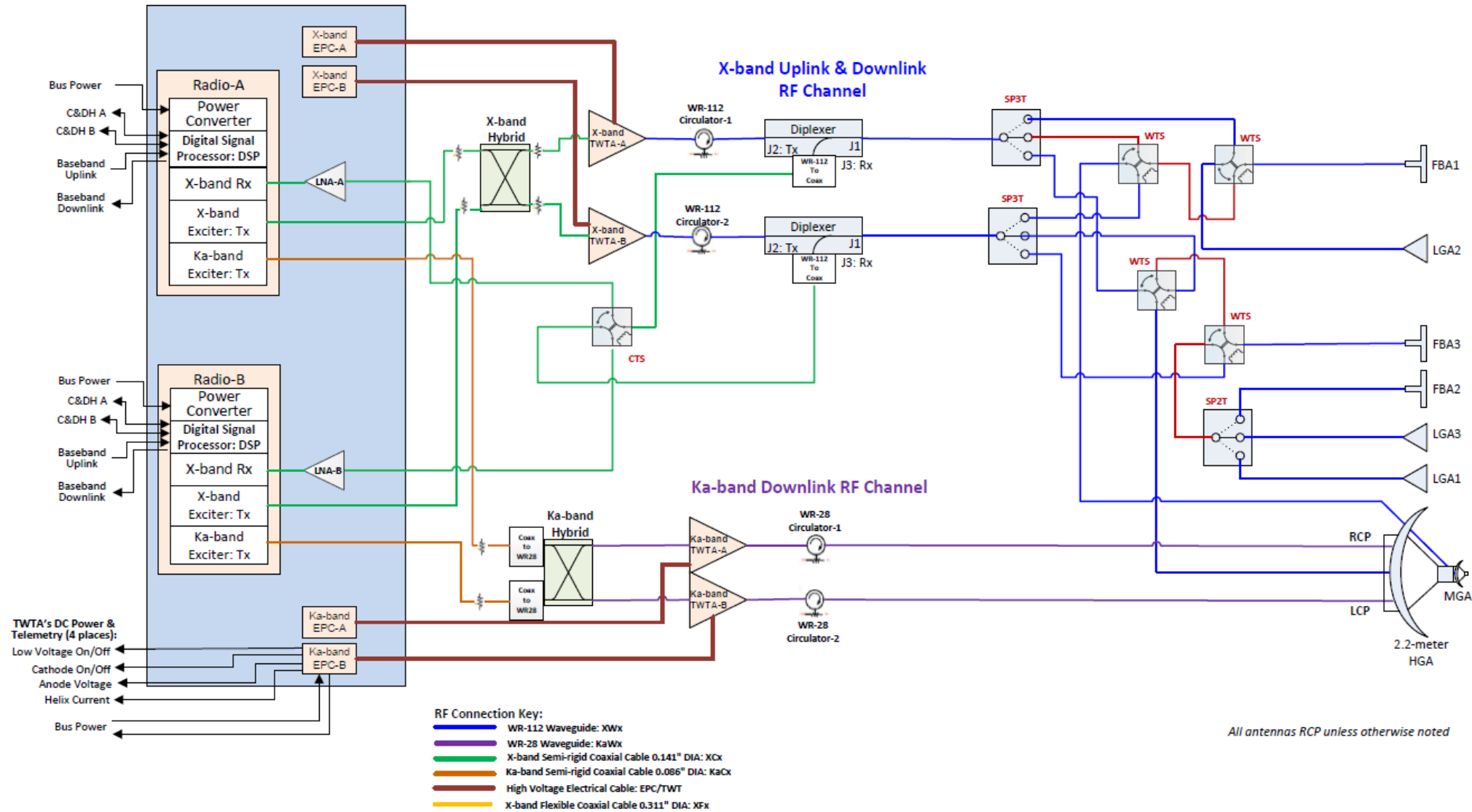
Link budget assumptions

- Baseline using DSS-54 (Madrid 34-m BWG).
- Ranging is on.
- Ka-band budgets calculated for 85% availability, 30 degrees elevation. This is a good average between lower elevation (lower data rate) and higher elevation (higher data rate) that will be used on same pass.
- X-band budgets are calculated for 90% availability, 20 degrees elevation.

Enceladus Study – Link Budget Summary

Mission Phase	S/C Antenna Used	X-Band UPL Data Rate	DNL Band	DNL Data Rate	Range	Comments
LEOPs/Cruise	LGA	30 bps	X	150 bps	0.5 AU	
Cruise	MGA	18 bps	X	190 bps	10 AU	
Thrusting	Fan Beam	(none)	X	20 bps	10 AU	
Science	Dual Band HGA (2.2 m dish)	700 bps	Ka	40 kbps	10 AU	
Relay	UHF	4 Mbps	UHF	4 Mbps	40 km	Orbiter overhead
Relay	UHF	25 kbps	UHF	50 kbps	25 kbps	Orbiter near horizon

Enceladus Telecom Block Diagram



Enceladus Study System Block Diagram

For this study, Telecom system includes the following:

- Antennas
 - Dual-band High Gain Antenna (HGA). Uses a 2.2 meter reflector. Ku-band used for downlink, X-band used for uplink.
 - X-band Medium Gain Antenna (MGA) is integrated onto the HGA assembly (behind the sub-reflector)
 - X-band Fan Beam Antenna (FBA). Assuming quantity of 3.
 - X-band Low Gain Antenna (LGA). Assuming quantity of 3.
- Traveling Wave Tube Amplifiers
 - 60 watt Ka-band TWTA (2 for redundancy)
 - 65 watt X-Band Antenna (2 for redundancy)
- Radios (2 for redundancy)

Relay for Orbiter + Lander combinations

Relay (assumes Electra/Electra-Lite)

- UHF frequency band allows use of lower gain antennas at orbiter and lander.
- 5 watt transmit output power
- Data rate adapts to variable link conditions (high data rate with orbiter close overhead, lower data rate with orbiter far away on horizon)

Enceladus Thermal Approach - Orbiter

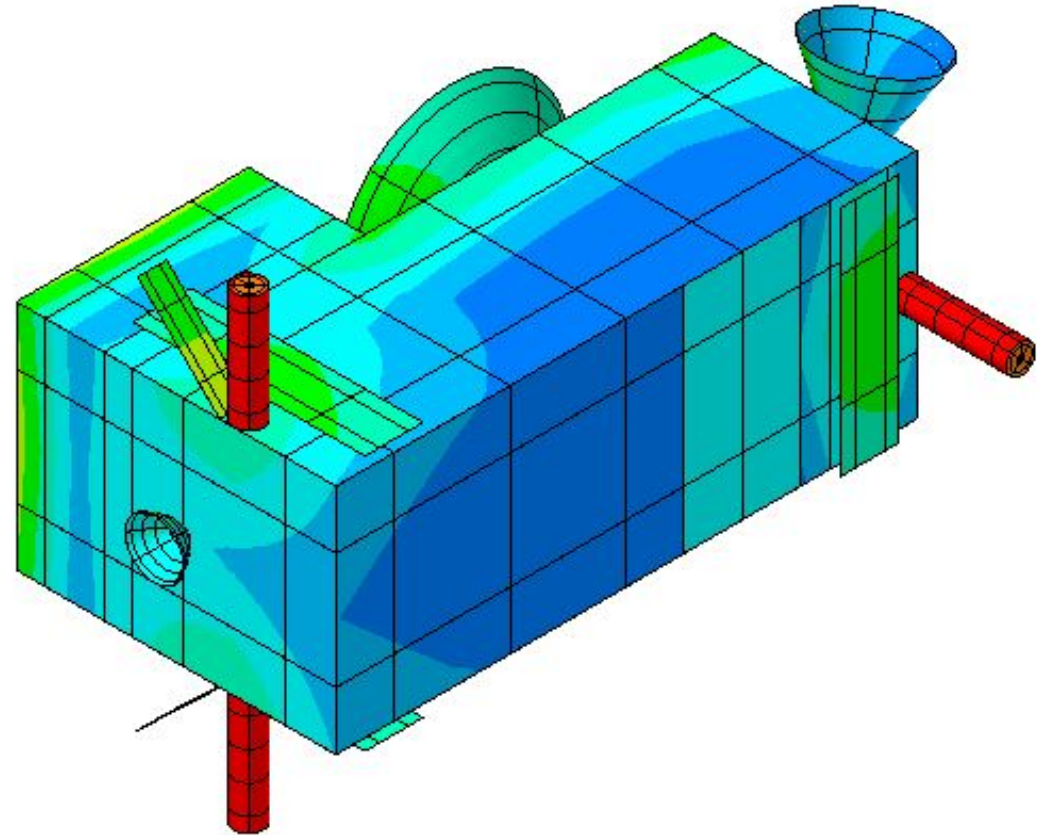
- Take “HGA thermal shield” idea from Clipper: 2m dish to shield spacecraft at Venus
- Take RTG thermal shield idea from Cassini: insulated cantilevered shields (2x 2x¼ m²) to reduce solar load on RTGs at Venus.
- Take “thermos”, shunts, and louver ideas from New Horizons:
 - use large (3x 2x0.5 m²) external shunts at Venus
 - use small internal shunts at Saturn
 - At least 100W total electrical power always available for shunting
 - louvers on anti-sun side full open at Venus, closed at Saturn
 - 0.15/0.75 emissivity for closed/open
 - 2x1 m² required size
- thermos bottle
 - everything (tanks, GNC, RF, etc) inside the “box”
 - collectively tied together in one volume
 - Heaters inside as needed (RHUs for some)
- Whole S/C wrapped in good (estar=0.1) MLI.
- Instruments all like room temperature (0 to 40 C).
- Eclipses are ok – Solar, Saturn, and Enceladus fluxes are all small.

Enceladus – Thermal Assumptions

- 3x 4kW NGRTGs at Venus, 3 x3kW at Saturn (thermal)
- Engines are thermally isolated
- Tanks all inside in thermos
- No sub-solar point assist at Venus!
- Saturn and Enceladus thermal loads ignored (tiger stripes! high albedo)
- Weak RTG conductance to S/C (required!)
- FOV limits for RTGs good enough? Similar to Cassini/New Horizons
- 2x2x4m S/C with 2m composite dish
- About half of “box” volume is tanks
- Instruments all located “near” louvers
 - Heat pipes, doublers, straps, etc used to fine tune depending on locations
- Nadir can be any of the non-HGA, non-louver, non-engine sides
 - Prefer direct view for instruments rather than being “bent”
- Up to 100W of heaters needed internally for high-power demand states
- 100W internal dissipation assumed continuously
 - If higher at Venus or lower at Saturn, bad
 - If lower at Venus or higher at Saturn, good

Enceladus Orbiter – Thermal Design

- 3 RTGs:
- External shunt radiators (3) are isolated
- Insides (instruments, RF, etc.) coupled to anti-HGA side
- Louvers on anti-HGA side (.75 to .15 effective emissivity)
- Tanks inside as part of thermos
- Instrument scoop on anti-engine side
- If any instruments need isolation, move “left” towards engines
- Fairing sizes impact possible locations of RTGs and HGA
- 6x4x4 m³ total envelope (including HGA, RTGs, engine, and scoop)



Enceladus – Thermal Summary

- Summary:
- Insides can be kept within 0 to 40C at Venus and at Saturn with above assumptions!
- Can change to “pyramid” geometry and/or bigger mounts, if RTG FOV is not adequate.
- If needed, can use Cassini radiation entrapment to ~double coupling to RTGs.
- 100kg mass for shields/radiators/louvers.
- Up to 100W of internal heaters and/or internal shunts for local control as needed.
- Heaters, doublers, straps, heat pipes, internal MLI, switchable internal shunts, and louvers can tune component set points.

Enceladus Landers - Thermal

- Orbilander:
 - Since cold is the issue and landers have a view to a warmer surface than space, lander is easier than orbiter thermally.
 - RTG FOV to space only major concern (so they don't overheat upon landing)
- Large Lander:
 - Where to put it matters due to RTG FOV.
 - Viking-style orientation (lander up front, propulsion back, HGA side) with offset RTGs works.
 - 1 (of the 3) RTG on lander:
 - This is thermally tricky due to not enough shunt heating for orbiter while too much waste heat on the lander
 - Depends on what is left on orbiter and the geometry of lander, but should be closeable
- Enceladus:
 - ~ -240C in eclipse
 - ~ -100C tiger strips
 - ~ -200C elsewhere

of ocean water, compared to $\sim 5 \times 10^5$ cells/mL in Earth's sunlit ocean (Cable et al. 2020). This wide range of uncertainty (9 orders of magnitude) reflects a compound uncertainty in Enceladus chemical energy supply (H_2 being the limiting reactant for methanogenesis, presumably the dominant metabolism at Enceladus given the relative abundances of CH_4 , CO_2 , H_2 , and H_2O in the plume; Waite et al. 2017), the biosynthesis yield for methanogenesis, and the energy needed for cellular maintenance (6 orders of magnitude; Hoehler & Jørgensen 2013). This range is depicted in green in Exhibit B-26.

According to the sample requirements (Exhibit B-6), the ensemble of life detection measurements requires 3 mL of sample, excluding sample for a nanopore biopolymer measurement. (With the nanopore, the total increases to about 30 mL.) The amount of sample required is inversely proportional to the biomass density in Enceladus' ocean: 3 mL of sample (excluding sample for the nanopore) was derived assuming a biomass density of 10^3 cells/mL, indicated in pink in Exhibit B-26. This is at the upper end of the expected biomass range in the ocean (excluding any processes that would enrich biomass in the plume, see §B.1.3.3).

The orbiter architecture can capture a few mL over its 3-year mission, achieving the ability to detect signs of a 10^3 cells/mL biosphere. A lander can both passively catch ("skyfall") and actively excavate (e.g., with a scoop) sample. With either or both sampling mechanisms, a lander can collect 2 to 3 orders of magnitude more sample in a nominal 3-year mission, respectively achieving the ability to detect 10 and 1 cells/mL. If the nanopore measurement proves essential for confirming life detection, the lander lines move to the right: the detection ability would be limited to 100 and 10 cells/mL because of a $10\times$ increase in required sample. For comparison, we also show the limit of detection requirement for the Europa lander mission concept (10^2 cells/mL; Hand et al. 2017) and the sample amount (of order 30 μ L) that can be collected in 10 to 20 Enceladus flybys by Saturn orbiters, which may be achievable with a New Frontiers mission (Cable et al. 2017; Eigenbrode et al. 2018).

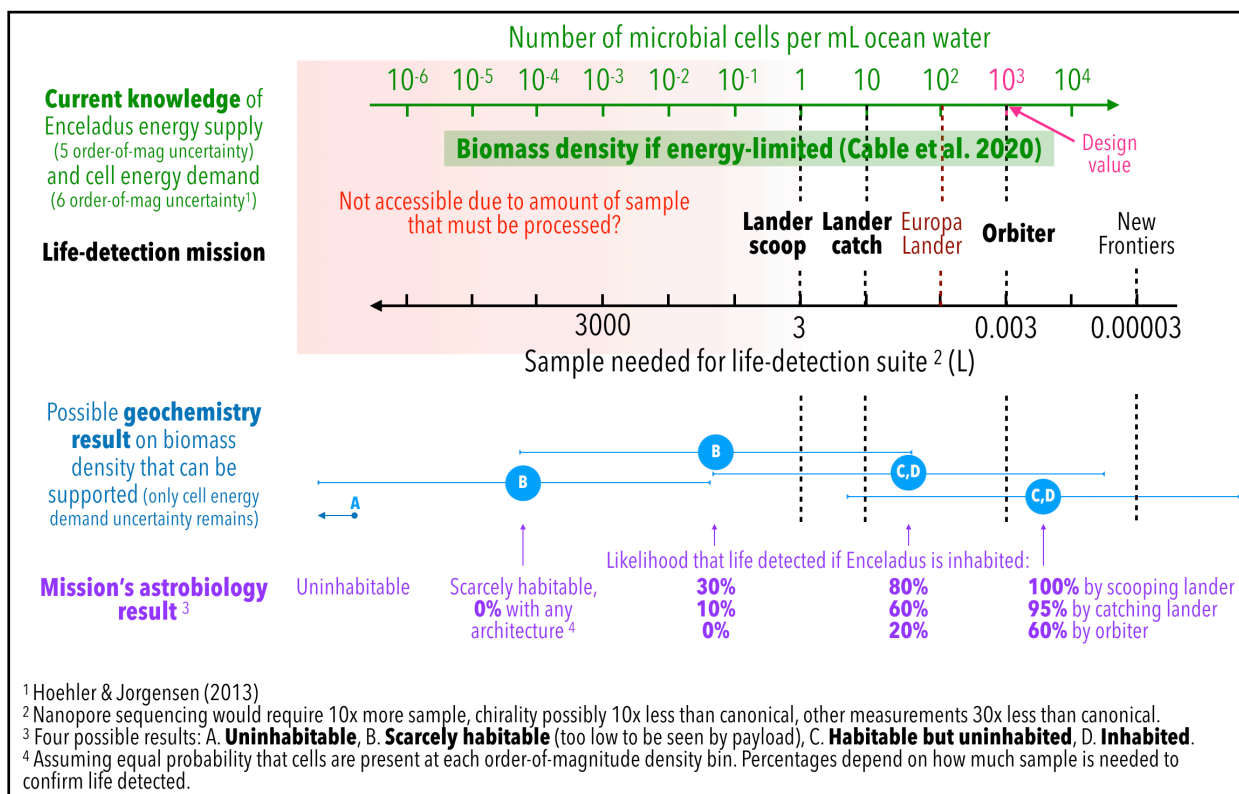


Exhibit B-26. Limits of detection of Enceladus Flagship life-detection architectures and corresponding probabilities of a conclusive mission astrobiology result.

We emphasize that the correspondence between sample needed (green scale) and lowest detectable biomass density in cells/mL (black scale) hinges on the ensemble of measurements deemed necessary and/or desirable to detect life or confirm its detection. In this case, the amino acid chirality measurement requires the most sample and is thus the primary driver of the 3 mL requirement. If one determined that amino acid chirality was not a necessary measurement to convincingly detect life, less sample would be needed to detect a given biomass density. In that case, the bottom black scale, to which the mission architectures are attached, would shift toward the left. If, on the contrary, one determined that a nanopore or microscope measurement (the requirement for which we derived to be 30 and 3 mL of sample, respectively) were necessary to convincingly detect life, the black scale and attached architectures would shift toward the right.

The above limits of biomass density detection also assume that sample collection, not sample processing, is the limiting factor on the pre-concentration volume of sample analyzed. However, processing (e.g. concentrating) sample likely becomes limiting for volumes of liters or more (red gradient box in Exhibit B-26).

Optimistically assuming that the post-mission understanding of Enceladus' geology and geochemistry collapses the current five-order-of-magnitude uncertainty on chemical energy supply flux (Cable et al. 2020) into a single value, the plausible biomass range may be reduced to perhaps the six orders of magnitude spanned by the current uncertainty in cell maintenance energy (Hoehler & Jørgensen 2013). Comparing the relative values of the limits of detection (dashed vertical bars in Exhibit B-26) and post-mission plausible biomass range estimates (horizontal blue lines) allows one to tentatively quantify the probability of mission outcomes as a function of how habitable and inhabited Enceladus may be. These are narrated as purple text in Exhibit B-26, under the assumption of equal probabilities of a biomass density in each order-of-magnitude bin. They quantify the scientific value of being able to sample more material.

Ability to do physical oceanography/geophysics and chemical oceanography/geochemistry

Habitability is often defined as requiring a solvent, bio-essential compounds, and sources of energy, but these factors must be collocated in an environment of the appropriate physicochemical conditions for a suitable amount of time (see, for example, the overview in Cockell et al. 2016 and references therein).

The science objectives include a variety of investigations for probing the physical structure of Enceladus. We therefore defined the ability to characterize Enceladus' physical oceanography and geophysics as a function of the different environments: the surface, near surface, and deep subsurface. In Exhibit B-27 we map investigations by instrument type to the environments they interrogate and show which architectures carry those instruments.

Similarly, the chemical environment of the ocean is addressed by several measurements, but the key distinction comes from the kind of sample analyzed. We considered the plume as at least four repositories, separated by the physics of ejection. The mixed plume contains a higher concentration of vapor samples and nm-sized particles and the collimated plume contains micron-sized particles; all four architecture access these reservoirs. The largest particles fallout at much lower altitudes than is safe for the spacecraft to orbit, so only landed architectures with sampling systems have access to these materials. Active sampling mechanisms are required to access surface deposits; passive sample mechanisms can access fresh fallout. Exhibit B-28 summarizes which architectures access each reservoir.

Resilience to surface safety uncertainty

Recognizing the difficulty inherent in any landing, we also included a factor for resiliency of the architectures to environmental unknowns, such as the fluffiness or thermal properties of the surface. In the evaluation, the largest landers are the least resilient as they are being compared to orbiting architectures that do not require landing. In the CML 4 study, we identified specific mitigations to improve the resiliency of the Orbilander (§3.15).

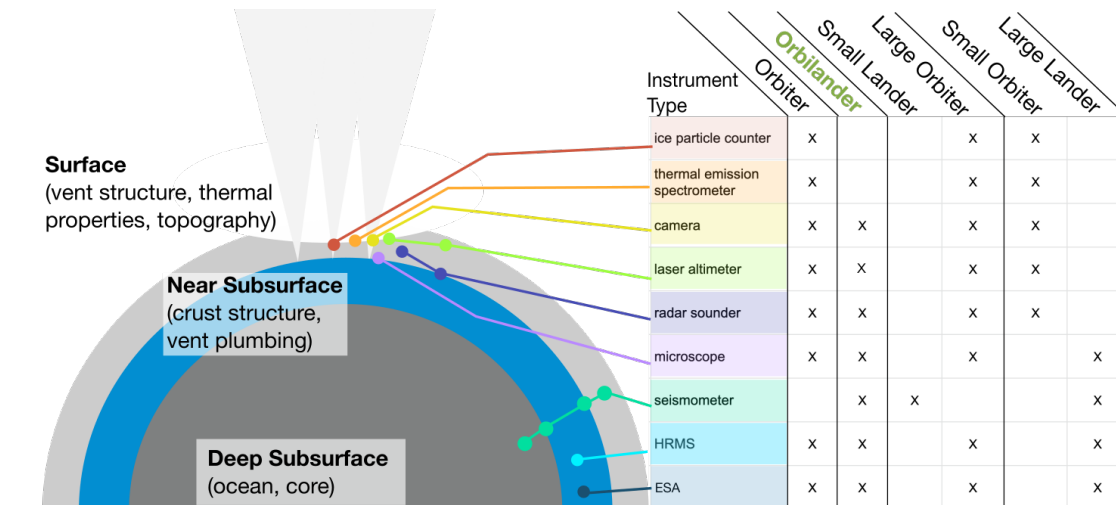


Exhibit B-27. Geophysical context provided by the instrument payload. Interrogating the crust and the interior provides key context for the search for life measurements. The CML-3 version of the Orbilander did not include a TES but the CML-4 version does, increasing its science value.

B.3.3.2. Evaluation Results

Each term of the Science Value score was evaluated independently by the science team. In Exhibit B-29 we show the responses of the core team (involved in more day-to-day decisions; $N = 12$) and the collaborators ($N = 23$) for each architecture. As part of the survey, the scientist scored how well each architecture addressed the five components of science value on a 1–10 scale. This scale was chosen based on preliminary ranking exercises. Rationales were also solicited for each component score from the collaborators; inspection of these responses did not reveal any miscommunications that would invalidate the evaluations.

Evaluating and even defining science value is an inherently subjective task, but the distribution of responses, although often wide, shows some degree of consensus. The results are largely similar between the two groups, often with greater spread in the collaborator responses. Notably, the core team responses for the life detection capability are more narrowly distributed than other categories. This seems appropriate given the emphasis placed on constructing a robust life detection suite of measurements and corresponding payload.

Based on these evaluations of science value, all four architectures make compelling science missions, but the Orbilander represents the best balance of science return versus cost (Exhibit B-30). The Large Lander + Small Orbiter demonstrates that more capability enables more “science”, but this gain is less attractive when shown against cost. In Exhibit B-30, we show the science value for the four CML-3 architectures relative to their cost estimate using a similar costing approach to that described in

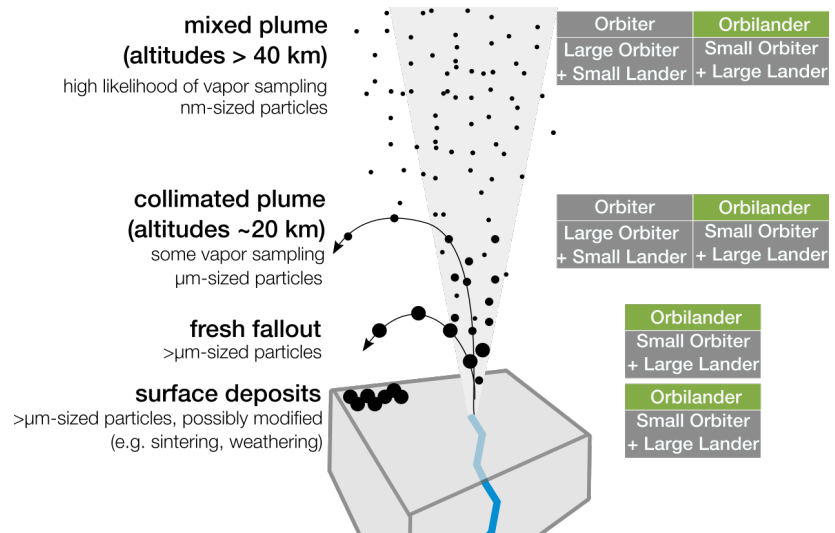


Exhibit B-28. Reservoirs accessed by different architectures.

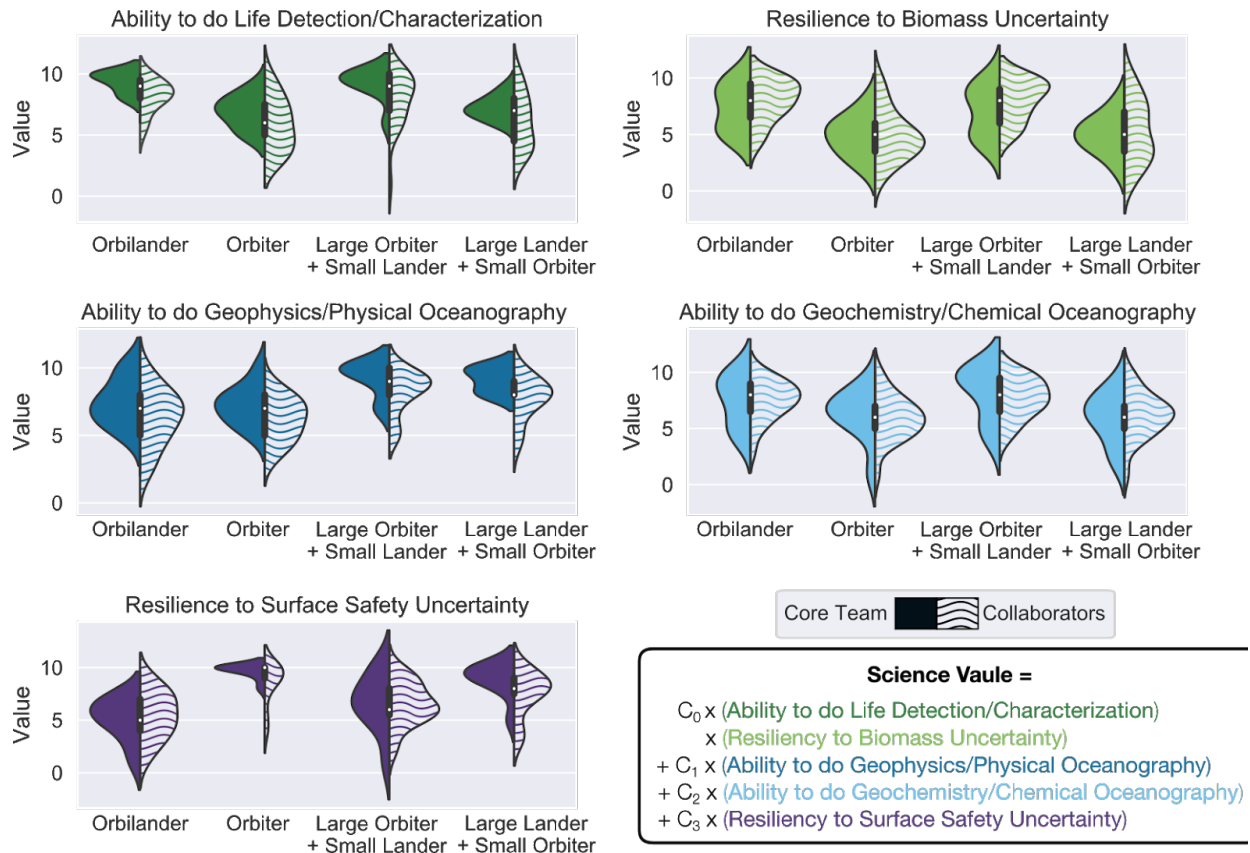


Exhibit B-29. Survey results to quantify science value according to Equation 1. Core team responses represented on the left (solid) and collaborator responses are on the right (wavy).

§5, but at a lower level of fidelity. Thus, to avoid confusion between the higher fidelity CML 4 cost derived for Orbilander, we do not show absolute cost values on the x-axis of Exhibit B-30; presumably, the CML 3 costs for other architectures would also change if evaluated at CML 4. The “knee in the curve” of science value per dollar is the Orbilander. This result does not change even using different values for the coefficients in the science value equation (C_0 – C_3).

The core team thus chose to study the Orbilander at a higher fidelity (CML 4) as described in the main text of this report. Additionally, the Orbilander represented the least-well-known option: further study would therefore yield a greater improvement on the current understanding of options for future Enceladus exploration.

B.4. Costing Methodology and Basis of Estimate

Here we provide further information on the basis of estimate for the costs presented in §5 by work breakdown structure (WBS).

B.4.1. WBS 1, 2, 3 Project Management, Systems Engineering, Mission Assurance (PM/SE/MA)

Because these functions depend on multiple mission- and organization-specific characteristics (Hahn 2014), cost analogies to analogous historical missions are preferred over cost model output, which do not take the mission into account. Existing analyses demonstrate that hardware costs are a reliable predictor of these critical mission function costs. APL has conducted thorough and rigorous analyses of PM/SE/MA costs, both for historical APL missions and for analogous missions. The BOE for Enceladus

Orbilander relies on APL’s analysis of historical PM, SE, and MA practices on *VAP*, *PSP*, and *NH*. In particular, *VAP* and *PSP* are APL’s most recent missions that were managed under the current NASA requirements (e.g. Earned Value Management System 7120.5E and 7123) and were delivered on schedule and within budget. Enceladus Orbilander will have comparable requirements. The mission PM/SE/MA cost is 15.9% of the flight system (payload + spacecraft + I&T).

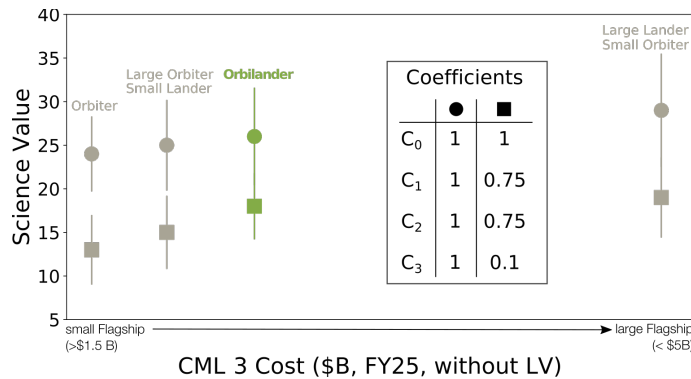


Exhibit B-30. Cost versus science value as evaluated by the team.

B.4.2. WBS 4 Science

This element covers the managing, directing, and controlling of the science investigation. It includes the costs of the PI, PS, and science team members. This element is largely level of effort. For Enceladus Orbilander, it is estimated via a rough order of magnitude (ROM) bottom-up estimate (BUE). The cost per year during Phases B–D of \$5.85M FY25\$ is comparable to *OSIRIS-REx* which expended \$6.23M FY25\$ per year. *OSIRIS-REx* has a sizeable payload suite with similar instrument types to Enceladus Orbilander. Average costs per year during operations (\$6.46M FY25\$) are also comparable to *OSIRIS-REx* (\$7.06M FY25\$).

B.4.3. WBS 5 Payload

This element includes the payload suite of instruments (Exhibit 5-2). All instrument costs underwent an iterative effort between cost, science, and engineering to ensure an estimate that adequately captures the true effort that will be required for development. This exercise involved the analysis of analogous costs where appropriate, parametric modeling, and engineering judgement. Additionally, SEER-Space was utilized as a parametric crosscheck. At the payload level, the project estimate is 2% higher than the sum of the average parametric crosscheck. The detailed BOEs by payload suite are as follows:

Payload PM/SE/MA. The payload PMSEMA costs (\$37.7M FY25\$) are estimated based on analysis of *VAP*, *NH*, *MESSENGER*, and *PSP* payload suite cost data. The Enceladus Orbilander Payload PM/SE/MA effort is estimated as 8.2% of the hardware.

Life Detection Suite. The HRMS BOE is based on *Europa Clipper* MASPEX and a NICM parametric estimate. The SMS BOE is based on *MSL* SAM, *ExoMars* MOMA and a NICM parametric estimate. It is similar to *Dragonfly* DraMS and assumes that the instrument will leverage work currently being done for DraMS. The ion selective electrodes instrument is based on NICM parametric estimate and leverages heritage from the *Phoenix* Wet Chemistry Lab. The μ CE-LIF and microscope instruments are TRL 5 instrument with estimated costs based on a NICM parametric estimate. The nanopore sequencer (TRL 2) has no flight analog; the estimated costs are thus based on a NICM parametric estimate. All instruments below TRL 6 have been applied a maturity cost correction factor (Malone et al. 2011) to account for additional development work.

Remote Sensing Suite. The radar instrument BOE is based on costs being spent on *Europa Clipper* REASON and a NICM parametric estimate. The laser altimeter BOE is based on costs from *LRO* LOLA and a NICM parametric estimate. The Enceladus Orbilander camera is TRL 4–5; it is similar to *NH* LORRI but will require modified optics. The estimated costs are based on a NICM parametric estimate. The thermal emission spectrometer BOE is based on costs from *OSIRIS-REx* OTES and a NICM parametric estimate. The WAC costs are bookkept under navigation.

In Situ Sensing Suite. The seismometer BOE is based on a NICM parametric estimate. It will leverage work performed for the *InSight* SEIS but will not be as complex as the *InSight* instrument. In particular, it will only leverage the short period probe and will not require the same vacuum vessel that caused massive launch delays for *InSight*. The context imaging instrument BOE is based on *MSL* MAHLI and a NICM parametric estimate.

Sample System. The sample system includes a collection system, processing, and sample transfer. The sample system leverages Honeybee Robotics experience on heritage sample system builds. The BOE for the Enceladus Orbilander sample system is a combination of a NICM parametric estimate and a Honeybee Robotics ROM for sample collection systems.

B.4.4. WBS 6 Spacecraft

This element includes all traditional spacecraft subsystems, as well as lander legs and optical navigation. The BOE relies primarily on a SEER-H parametric estimate. SEER-H was selected as the primary estimating methodology due to the thorough MEL available for the point design of Enceladus Orbilander. The level of detail and design captured in the MEL allows for specific tailoring of subsystem component technologies and applications. The resulting estimate includes design, fabrication, and subsystem level test of all hardware components. The exceptions are the propulsion subsystem and optical navigation which are estimated via a ROM. Additional details on these BOEs are described below. All hardware development costs include the required supporting EMs, breadboards, flight parts, ground support equipment (GSE) and flight spares identified in the MEL. This WBS does not include Spacecraft PMSEMA because it is bookkept in WBS 1, 2, 3, consistent with APL missions with in-house spacecraft builds. Additionally, SEER-Space was utilized as a parametric crosscheck: at the spacecraft level, the project estimate is 14% lower.

Optical Navigation. The Optical Navigation software of the Enceladus Orbilander has four components: self-contained, onboard navigation system; stationkeeping; TRN; and hazard avoidance. This Optical Navigation ROM estimate includes the flight software costs for the development of all four components, as well as necessary miscellaneous hardware to support the development effort. In particular, the on-board navigation system includes reuse and modification of the *DART* SMART Nav algorithm which encompasses closed-loop GNC simulation integration, analyses, verification and validation (V&V) and flight implementation. The stationkeeping algorithm has no flight heritage and requires a new development effort with all the requisite activities. TRN and hazard avoidance leverage algorithm development from *ALPHAT* and *Dragonfly*, though Enceladus Orbilander's landing and surface requirements are neither as stringent nor as complex as *Dragonfly's* as Orbilander needs only one successful landing.

Other Subsystems. The parametric estimated costs of the other spacecraft subsystems are crosschecked with historical APL builds and supplemented with current vendor quotes when applicable. In particular, vendor quotes were utilized for the material costs on the thermal subsystem (heaters, MLI) and commercial off the shelf (COTS) components in the GNC subsystem. Power subsystem costs for components such as the PSU and shunt regulators were crosschecked with cost actuals from *VAP* and *DART*. The propulsion system ROM represents an estimated cost for a dual mode prop system that will meet the Enceladus Orbilander requirements. The estimated costs include APL labor and hardware procurement costs. The hardware procurement costs are based on vendor quotes acquired for previous APL propulsion system builds of a similar nature.

B.4.5. WBS 7 and 9 Mission Operations (MOps) and Ground Data Systems (GDS)

The Enceladus Orbilander mission operations estimate includes mission operations planning and development, network security, data processing, and mission management. The pre-launch mission operations and ground data systems estimate is an analogous estimate based off of previous APL efforts on *NH*, *MESSENGER*, and *PSP*. These missions represent typical APL expenditure on pre-launch MOps and GDS for projects of comparable scope and complexity. The post-launch mission operations estimate is derived from APL historical costs per month during different operational phases. The estimate includes a

7-year cruise, 4.5-year pump down, and 3.5 years of science operations. The post-launch GDS estimate is a ROM BUE.

B.4.6. WBS 8 Launch Vehicle and Services

The mission requires a launch vehicle that will meet the launch C3 requirements. Without guidance for the cost of an SLS Block 2, based on past pricing to NASA missions of Evolved Expendable Launch Vehicles, it is assumed that it would be at least \$500M for a launch using a standard sized fairing. The price to add an upper stage would likely be no more than \$40M. This does not include NEPA and Nuclear Launch Approval costs which are covered by the cost of the RTGs in WBS 6.

B.4.7. WBS 10 Systems Integration and Testing

This element covers the efforts to assemble the cruise stage, MOI stage, descent stage and lander; integrate the four into the mission spacecraft; testbeds; and performance of spacecraft environmental testing. The costs are based on a detailed analysis of cost actuals from previous APL missions, including *MESSENGER*, *NH*, *STEREO*, *VAP*, and *PSP*. The Orbilander I&T effort is estimated as 12.7% of the hardware. Given the use of cost-to-cost factors to estimate I&T, both the CER and the underlying cost drivers are allowed to vary so that all sources of uncertainty can be quantified. As hardware cost varies, the cost-to-cost factors I&T also varies. This allows the estimate to maintain a conservative risk posture given the historical complexity of I&T.

B.4.8. Deep Space Network (DSN) Charges

This element provides for access to the DSN infrastructure needed to transmit and receive mission and scientific data. Mission charges are estimated using the Jet Propulsion Laboratory (JPL) DSN Aperture Fee tool. The DSN cost estimate covers pre- and post-contact activity for each linkage.

APPENDIX C. SPECIAL TECHNICAL ANALYSES

C.1. Autonomous Optical Navigation

Autonomous optical navigation is a key enabler for several phases of the Enceladus Astrobiology Mission: a Saturnian moon tour, the 1.5-year science operations in Enceladus orbit, and the landing on Enceladus’ surface (Exhibit C-1). These phases, due to different reasons, require onboard navigation state updates to enable safe and timely execution of spacecraft guidance, navigation, and control (GNC) maneuvers. Each phase can employ a different optical navigation strategy and may require different sensors in order to perform optimal absolute or relative state estimation.

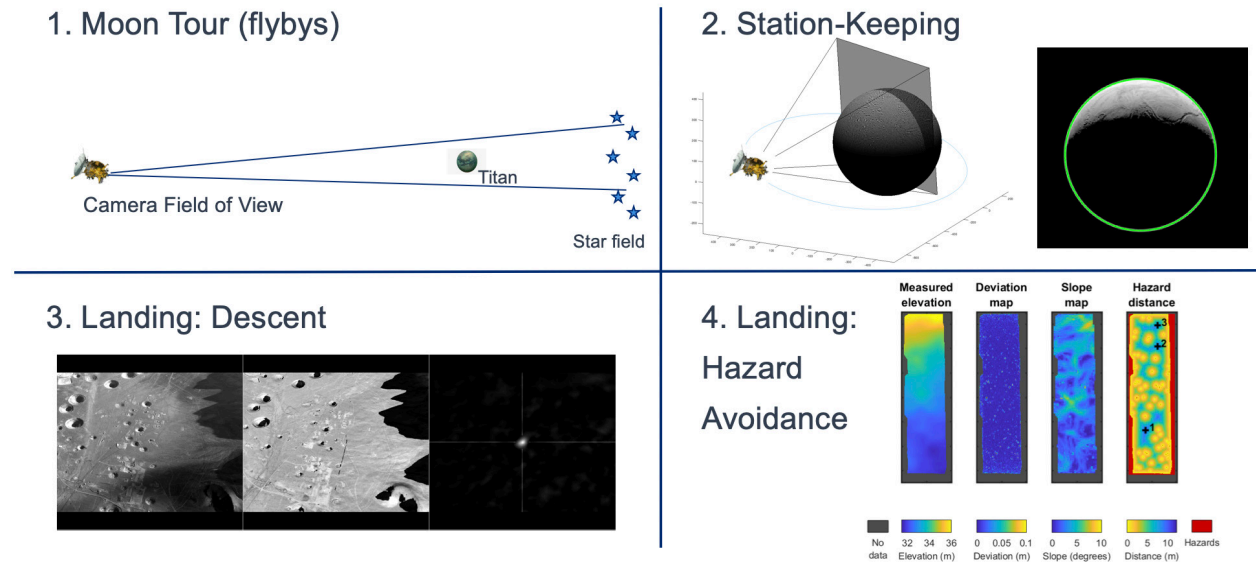


Exhibit C-1. Mission phases to utilize autonomous onboard optical navigation.

As with all space missions where SWaP is limited, the optical navigation trades evaluated high-TRL sensors, “look” opportunities and corresponding objects within the field of view (FOV), lighting conditions, and environmental conditions in order to arrive at an optimal optical system. Sensors within the optical system are used multiple times during the mission, depending on the needs of the onboard optical navigation algorithms (Exhibit C-2). The optical system currently includes dedicated navigation cameras, a scanning LIDAR, and the sharing of a narrow angle camera (NAC) science instrument.

Mission Phase	NAC Instrument	WAC Nav Cams	Scanning LIDAR	Altimeter
1. Moon tour	X	option		
2. Stationkeeping		X		option
3. Landing: Descent		X	X	
4. Landing: Hazard avoidance			X	

Exhibit C-2. Reuse of sensors for optical navigation phases.

C.1.1. Use of Autonomous Optical Navigation for Stationkeeping

Given that the selected science orbit concept is unstable with roughly 12 hours between subsequent passages of periapsis, real-time Enceladus-relative measurements must be acquired and processed on board to maintain precise orbit determination requirements necessary to maintain stationkeeping.

The primary navigational camera (Nav Cam) planned for this phase is the ECAM-M50 system developed by Malin Space Science Systems and used on the *OSIRIS-REx* mission (Getzandanner et al. 2019). The properties of this imager are shown in Exhibit C-3. The spacecraft will have two dedicated Nav Cams for the orbit determination phase and they may be reused for the landing sequence. These cameras will be distributed and oriented such that at least two Nav Cams will have Enceladus in their field of view throughout most of the orbit. One Nav Cam will provide measurements to satisfy the orbit determination requirements, with the second adding fault tolerance to the system. Blackouts in the measurement periods will be a function of planned maneuver events, science operations near periapsis, and poor illumination conditions in the field of regard on Enceladus’s surface. The second camera can be used to reduce the duration of these blackout periods.

Parameter	Value
Field of View (deg)	44 (H) x 35 (V)
Focal Length (mm)	7.1
Resolution (pixels)	2650 x 1944
Wavelength range (nm)	400 to 700

Exhibit C-3. Properties of the Malin Space Science Systems ECAM-M50 imager system.

Three optical navigation techniques were identified as promising candidates to provide navigation measurements during the science orbit for stationkeeping. The first is a landmark tracking approach that will register preselected landmarks created from *Cassini* data to onboard images to estimate the spacecraft’s relative position to Enceladus in three axes. The second is an optical limb localization method to estimate the angle from the camera’s boresight to the centroid of Enceladus by fitting an ellipse to the horizon points computed in the imaging plane. The third is an optical velocimetry method to estimate the spacecraft’s lateral velocity by comparing images taken within a short timeframe.

C.1.1.1. Landmark Tracking

Landmark tracking is an approach that has been used on several missions for ground-based and autonomous onboard navigation, with Mars 2020 being perhaps the most famous example. *OSIRIS-REx* has recently employed this approach during its Orbital-A phase to enable stationkeeping around Bennu (Leonard et al. 2019). The approach uses a database of precomputed small digital terrain maps (DTMs) that are loaded onboard the spacecraft (Exhibit C-4). For Exhibit C-4, each captured image, a set of DTMs distributed over the FOV are rendered using the estimated illumination angle and pose of the camera. These rendered patches are cross-correlated with the image to determine their location in the camera frame. Using the Enceladus-relative location of each landmark, the position of the camera is estimated. These small maps are particularly well suited for resource constrained avionics architectures.

C.1.1.2. Optical Limb Localization

Optical limb localization is a method that has been used extensively in orbit determination processes by analysts on Earth using a hybrid of manual and automated steps. However, onboard algorithms to localize the spacecraft using images of a planetary limb have been developed (Christian et al. 2015) and shown to be highly accurate with flight data from the Saturnian system (Hollenberg et al. 2019) The method is composed of the following steps and accompanying figure from Christian et al. (2015):

1. Compute coarse horizon points of the body on the image plane using limb scans along the illumination direction
2. Refine horizon points to subpixel accuracy

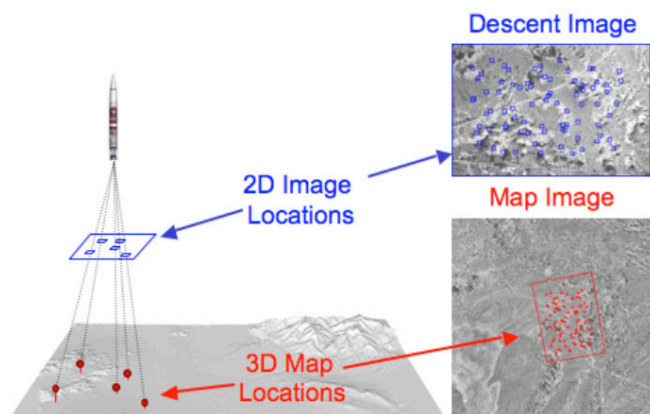


Exhibit C-4. “Mapped landmark matching concept” from (Johnson et al. 2007).

3. Fit body shape model (e.g., ellipsoid) in the image plane to horizon points
4. Localize camera to triaxial ellipsoid model of Enceladus

Limb localization performance is reduced when a planetary body's atmosphere obscures the limb or the

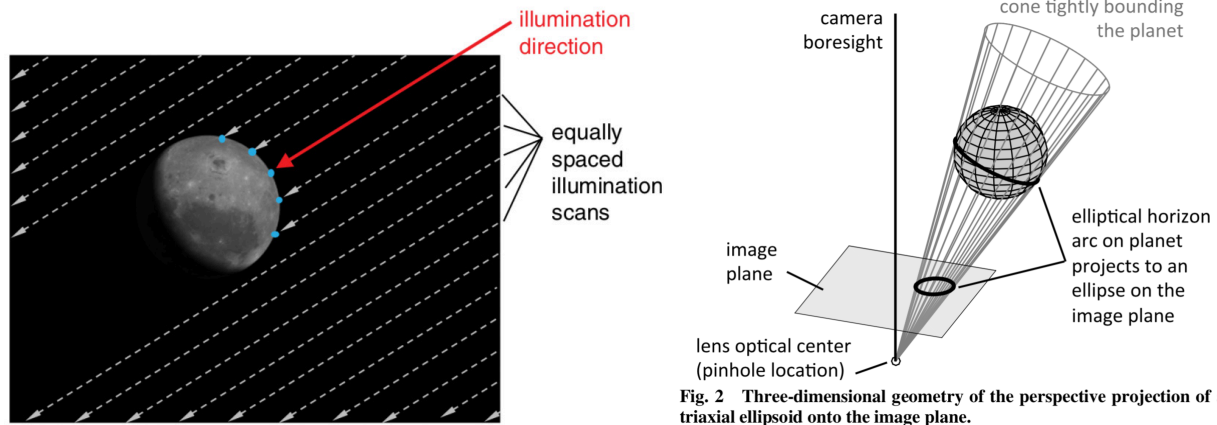


Fig. 2 Three-dimensional geometry of the perspective projection of a triaxial ellipsoid onto the image plane.

Exhibit C-5. Limb fitting technique from Christian et al. (2015)

topography is rugged enough to prevent a clean projected ellipse on the camera frame. The lack of atmosphere on Enceladus, as well as the minimal terrain relief of 2 km make Enceladus an attractive target for limb localization (Bland et al. 2019) One particular aspect of Enceladus that could be more challenging than other planetoids is the existence of surface plumes of particles. These plumes could cause the image fitting algorithms to degrade since the model which is used in the fitting algorithm will not have a prediction of the plumes. Fortunately, recent studies with *Cassini* data have shown that the performance of even standard fitting algorithms are robust to these unexpected plumes and they can be used in an onboard autonomous navigation subsystem.

The orbit determination performance of the limb localization method was assessed using a low-to-moderate fidelity simulation of the Enceladus navigation system. The dynamics of state space were defined via an N-body model with point mass gravity for the Sun, Saturnian moons Titan, Rhea, Dione and Te-thys, and including spherical harmonic gravity models for Enceladus and Saturn. The predicted orbit and the estimated orbit are overlaid in Exhibit C-6 and are viewed in the Enceladus-centered ecliptic J2000 frame. A standard Extended Kalman filter (EKF) was assumed for this study (Tapley, Schutz, and Born, 2004).

The measurement types were 1) angles to the center of Enceladus as derived from the limb-fit, and 2) a coarse range to Enceladus as derived from a scaling of the Enceladus model to the image. The measurement processing ceased when the spacecraft approached periapsis. The range threshold was set to within 100 km of the surface of Enceladus. This pause in measurements was selected so that only science operations occur during this time, thereby providing conservatism to navigation performance. The notional simulation used the following parameters:

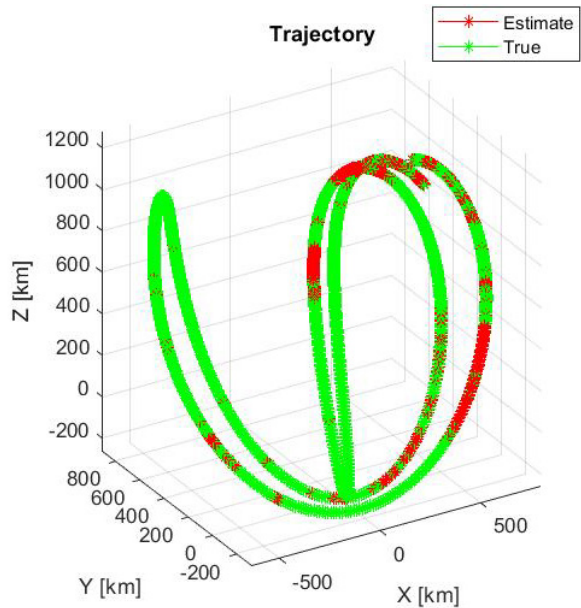


Exhibit C-6. Truth trajectory and estimated trajectory in the Enceladus-centered ecliptic J2000 frame.

These parameters were chosen based on a combination of literature references and simplicity of implementation. For example, the Nav Cam FOV is not identical to the baselined Malin ECAM-M50, but the use of a square image is a simplification and optimization for algorithm trades. The predicted navigation performance is shown in Exhibit C-8, where the steady-state 3σ error is on the order of 300 m in position and several centimeters per second in velocity. Additional unmodeled effects, such as biases in the angle measurements will degrade these results in a realized system.

Parameter	Value
Navigation Camera Field of View (deg)	40 (H) × 40 (V)
Navigation Camera Pixels	1024 × 1024
Limb Fit Accuracy-Angles (pixels)	1 (1σ)
Limb Fit Accuracy-Range (pixels)	1 (1σ)
Unmodeled Acceleration Magnitudes (km/s ²)	1e-9
Interval Between Measurements (min)	1
Close Approach Distance Mask (km)	100
Orbits	3

Exhibit C-7. Parameters of the proposed Enceladus autonomous optical navigation system.

The predictive power of these results, and thus their utility for autonomous station keeping, scales directly with the navigation errors and the model’s prediction of those errors. The results of this simulation indicate that the standard EKF approximations are largely valid for this system. The measurement and state chi-square tests also support this conclusion. In particular, the error falls within the 3σ bounds a high percentage of the time. It does not fully meet the statistical thresholds that a fully linear system with white noise would meet; in particular the velocity error exceeds the 3σ thresholds significantly around hours 6, 17, and 28. These times correspond to periapsis events and are thus times where the linearization is more sensitive to state errors. Additionally, there are no measurements available at these times due to the close-approach constraint. These deviations can likely be handled in a more rigorous manner by an alternative computation of the covariance matrix such as the sigma-points filter, or a relaxation of the close-approach constraint. The range measurements help stabilize the excursions outside of the 3σ bounds, and they should be included even if the range noise is significantly worse than that listed in the table. The range information is shown in Exhibit C-10. The top plot shows the time-history of the range to the center of Enceladus (not to the surface), the middle plot shows the 1σ range noise intensity time-history, and the bottom plot shows the solid angle subtended by Enceladus in the camera FOV. The roughly 40° FOV line was added to the bottom plot in red to show that the majority of the orbit can be completed using simple limb fitting and does not require regular feature matching on the surface of Enceladus.

The navigation accuracy is a function of many parameters. Several of these parameters are subject to modification and redesign. The previous table and figure combination represent a notional scenario and a single performance realization of a random system. If the algorithms selected do not perform as well as predicted, or the dynamical model used on-board is of significantly lower fidelity than the true system, then the performance will degrade in a corresponding manner. The following table and corresponding figure summarize a more conservative set of parameters and degraded performance. The position performance degrades by 2–3 times and the velocity performance degrades by approximately 4 times. The navigation results are more sensitive to poor performance in the angular measurement than the range measurement,

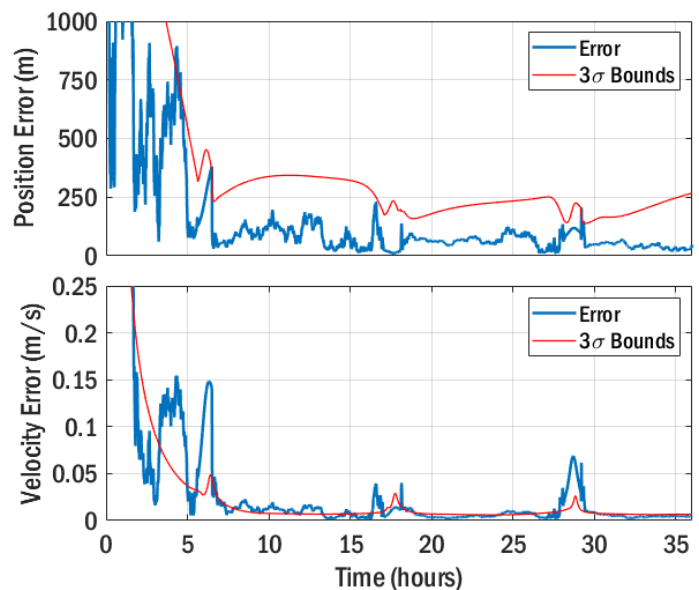


Exhibit C-8. Navigation performance in a notional scenario.

and range error magnitudes of several multiples of that used in this simulation produced only mildly degraded results. The ultimate system performance, and thus the required embedded software model fidelity, will be driven by the sensitivity of the control scheme selected to maintain the orbit.

C.1.1.3. Optical Velocimetry

Velocimetry derived from sequential optical images of the orbited body is a fairly robust technique to determine an orbit's lateral velocity. Both feature-based and featureless methods such as least squares optical flow (LSOF) have been shown to be effective in this regime. A benefit of this technique is that it does not rely on accurate DTMs to derive this information, and is therefore robust to errors in the knowledge of surface landmarks. On the other hand, a drawback to this technique is that scale cannot be directly observed in the image due to a lack of known area/feature on the surface to localize. This deficiency can be overcome through several methods: 1) a combination with the traditional radionavigation data, 2) a combination with an altimeter (e.g. LIDAR), or 3) periodic combination with another optical technique such as LSOF or limb localization. The Dragonfly mission has proposed an optical velocimetry method combined with an altimeter (Witte et al. 2019) to optically navigate near the surface of Titan.

The autonomous navigation subsystem that is capable of optical velocimetry will also be well suited for limb-based angle and range measurements. The navigation performance of this system will be better than

Parameter	Value
Field of View (deg)	40 (H) × 40 (V)
Pixels	1024 × 1024
Limb Fit Accuracy-Angles (pixels)	2
Limb Fit Accuracy-Range (pixels)	2
Unmodeled Acceleration Magnitudes (km/s ²)	1e-8
Interval Between Measurements (min)	1
Close Approach Distance Mask (km)	100
Orbits	3

Exhibit C-9. Parameters of the proposed Enceladus autonomous optical navigation system.

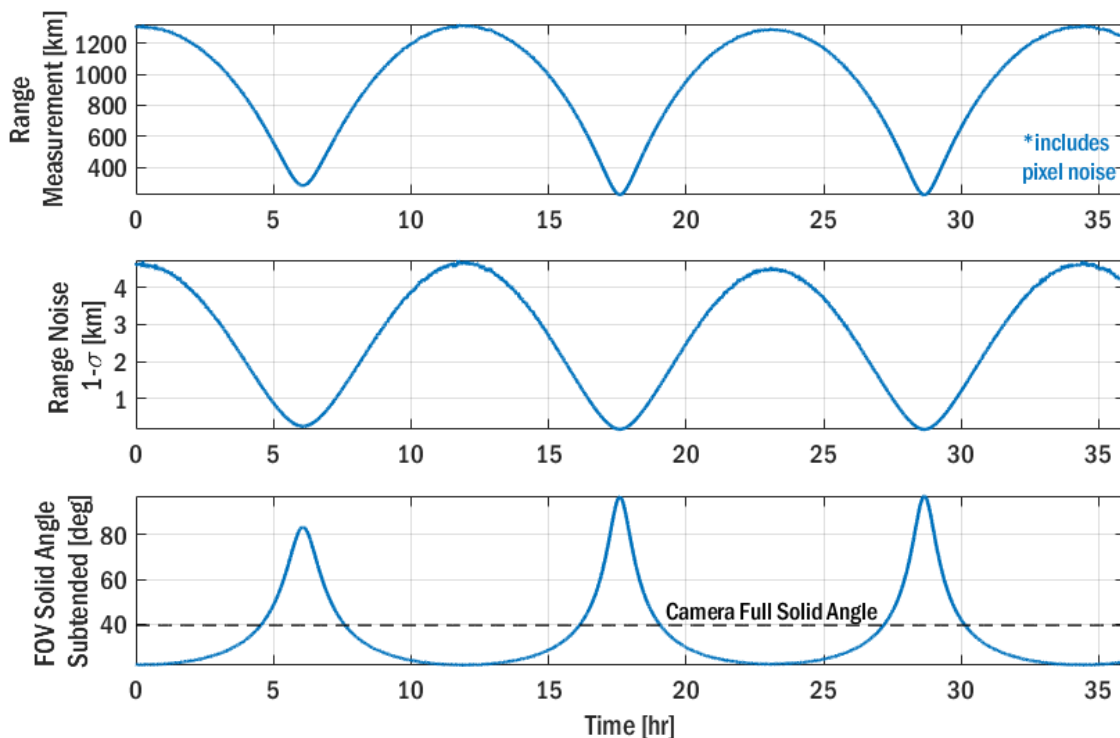


Exhibit C-10. Range information used in the navigation filter.

the limb-only system mentioned above, and so the above results are a useful benchmark. The improvement will come as a direct result of the added precise velocity measurement.

C.1.1.4. Conclusions

The autonomous optical navigation algorithms described herein span the operating regime from apoapsis to periapsis of the proposed science operations orbit. These techniques all have merit and their individual performance will be a function of the overall design. In addition, the proposed mission concept of operations allows for *in situ* calibration and evaluation of these methods before they become mission critical. During the moon tour phase, the spacecraft will execute flybys of Enceladus within 200-km altitude at closest approach. These will provide an excellent opportunity to test each optical navigation technique both onboard and with data processed on Earth, thereby providing the operations team with high confidence in the autonomous navigation capabilities of the system before handing off authority.

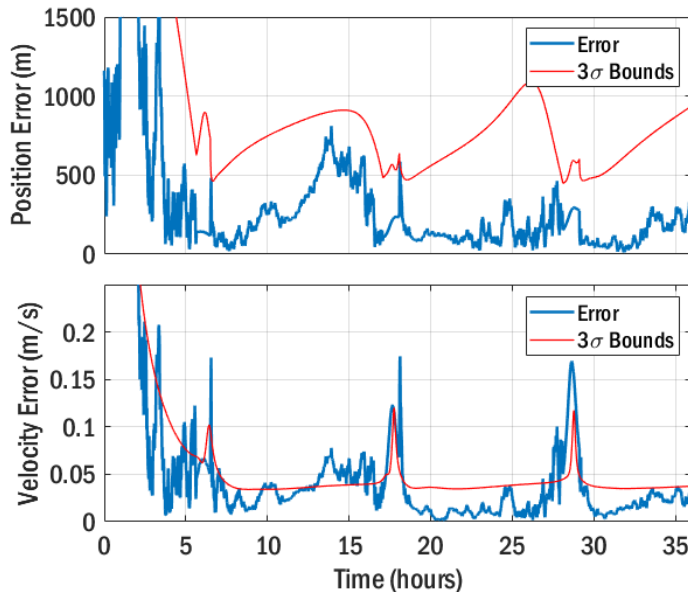


Exhibit C-11. Navigation performance in a more conservative scenario.

C.2. Descent and Landing Analysis

C.2.1. Use of Terrain Relative Navigation for Descent

Terrain Relative Navigation (TRN) is an onboard function that reports measurements of position, attitude, velocity, or a combination of the three to the GNC system. TRN measurements can be reported in the relative frame, as in velocimetry cases, or in a consistent frame, as in “absolute” navigation measurements within a reference map. TRN enables enhanced robotic exploration, allowing spacecraft to travel further distances autonomously (Witte et al. 2019) or to land with greater precision closer to sites of scientific interest (Johnson et al. 2016).

There are different techniques to achieve terrain relative navigation. A traditional approach uses digital elevation maps (DEMs) created a priori and stored onboard. These DEMs are used to render scenes during descent and then compared against images acquired by the Nav Cams to determine position and/or attitude estimates. An approach that does not use onboard DEMs is an image-to-image matching technique that compares sequential imagery in order to calculate relative pose change between image frames. The TRN algorithm evaluated in this study uses a combination of the two: using reference maps when the maps are available and at a high enough resolution compared to the ground sample distance (GSD), and switching to the image-to-image velocimetry mode when reference maps cannot be used.

During descent, imagery taken onboard is compared against either orbital reference imagery or images rendered using elevation maps, reference imagery, and estimated spacecraft state, as seen in Exhibit C-12. Due to the descent operating around an airless body, it can be assumed that spacecraft attitude can be accurately determined using star trackers, so TRN measurements can be constrained and report position measurements only. Rendered imagery can be obtained by co-registering orbital imagery with elevation maps so that each point in the map has a position and a gray value, and then using projective collinearity equations to project the map onto the focal plane array (FPA), allowing for rapid onboard rendering. By comparing onboard imagery with imagery rendered given a spacecraft’s estimated state, TRN algorithms

such as those developed during NASA’s Autonomous Precision Landing and Hazard Avoidance Technology (ALHAT) (Adams et al. 2008) and Robotic Lunar Lander Development Programs (RLLDP) (McGee et al. 2015) can determine the true spacecraft state to a high level of accuracy (Johnson et al. 2016; White et al. 2009). As the spacecraft descends, eventually the reference maps will become too coarse to be of utility to the DEM-based TRN algorithm, at which point the TRN algorithm will switch over to relative velocimetry mode, comparing sequential imagery rather than comparing to reference imagery. Without the rendering step, velocimetry mode is typically less computationally intensive, leading to the availability of faster measurements during the terminal descent and landing phase.

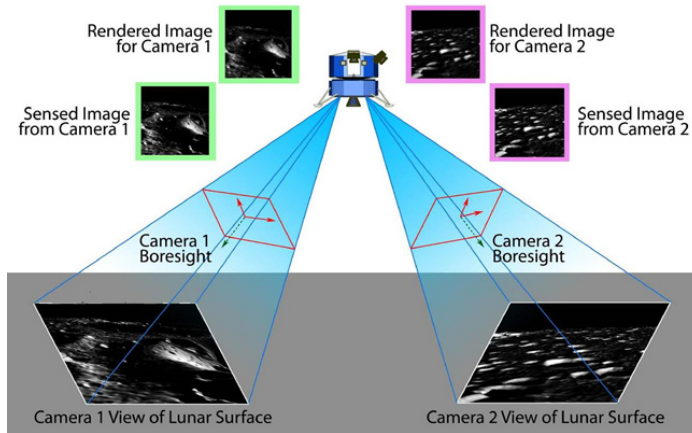


Exhibit C-12. A visualization of an APLNav-type TRN algorithm, shown over the lunar surface. Each camera compares sensed images with rendered images, backing out 3D position estimates.

The study assumes that during the portions of the descent that TRN would be employed, reference orbital imagery and elevation maps would be available to assist in position estimation. Due to the decrease of the image footprint size during descent leading to a smaller (GSD), terminal descent requires higher resolution reference maps than the initial portions of descent. This study assumes that elevation maps, along with the co-registered reference imagery, with a resolution of 5m horizontal postings are available locally around the landing site, and elevation maps with 60m postings are available throughout the descent. In addition, it is assumed that the reference imagery available is taken at the same local time as the time of descent and landing so that shadows due to terrain and lighting angles are similar between the reference imagery and imagery that will be taken during descent.

Due to the lack of Enceladus elevation maps at 60m postings broadly and 5m postings locally surrounding the landing site, a surrogate landing site and respective DEMs were obtained from the Moon. This analysis assumed the Nav Cams to be 256×256 pixels, with a field of view (FOV) of 50° . For Enceladus, the TRN imagery will be captured using the same model Malin ECAM-M50 cameras being used during autonomous station keeping, although physically located at different positions on the spacecraft and at different resolutions. While autonomous station keeping and orbit determination uses high resolution imagery, precision landing using TRN needs to be optimized for computation speed and therefore lower resolution images are preferred.

A sample descent and landing trajectory was analyzed using lunar reference maps along with high-fidelity simulated imagery using an in-house Renderer Camera Emulator (RCE) that is also being used in optical navigation simulations for the upcoming Dragonfly and Double Asteroid Redirect Test (DART) missions (Adams et al. 2019). TRN began reporting measurements at an altitude of around 30 km using the autonomous precision landing navigation (APLNav) TRN algorithm. As the spacecraft descends, the GSD decreases, which means that the same subpixel fit accuracy solutions lead to smaller 3D position estimate errors. By the time the spacecraft reaches an altitude of 5 km, 3D position error magnitudes fall below 25m, as seen in Exhibit C-13. At an altitude of around 12 km, the image footprint transitions from primarily overlapping the coarser reference maps to primarily overlapping the finer, localized reference maps around the landing site.

C.2.2. Use of LIDAR for Hazard Detection and Avoidance During Landing

LIDAR-based hazard detection and avoidance (HDA) is an enabling technology for future planetary landings. Instead of relying on ruggedized (and high-mass) structural components to survive landing on

sloped or rough surfaces, these hazards are detected during the landing sequence and the spacecraft can divert to a more benign site.

The design assumes an instrument similar to the *OSIRIS-REx* Laser Altimeter (OLA; Daly et al. 2017), which in addition to providing laser altimetry, is a highly capable scanning LIDAR. Specifications for the low-energy/high-rate laser are shown in Exhibit C-14; in addition, OLA includes a high-energy/low-rate laser which can provide altimetry from higher altitudes (>20 km at Enceladus) to support terrain relative navigation in the earlier stage of descent. During descent, the instrument will scan its field of regard with a series of laser pulses, measuring the time of flight of the return pulse to calculate the range to surface in each direction.

Onboard hazard detection algorithms ingest LIDAR scan data and process it to identify hazards and safe landing sites. Suitable algorithms were demonstrated during the Autonomous Landing Hazard Avoidance Technology (ALHAT) program (Johnson et al. 2008). First, using the instrument pose information (Allen et al. 2008), the scan angle and range data is converted to a three-dimensional point cloud and resampled to form a uniformly gridded terrain elevation map (Exhibit C-15). The elevation map is then processed for hazards: slope and roughness are calculated from the elevation, and hazards are marked where the slope or roughness exceeds a threshold value. The distance to the nearest hazard is then mapped out by applying a mathematical grassfire transform to the hazard map. The site with the greatest hazard distance may be selected, or a more complex landing site metric may be composed of a combination of the distance, the slope and roughness themselves, and auxiliary data such as the fuel needed to divert from the current trajectory to each landing site. The algorithms are also capable of producing a ranked list of sites (e.g. with a distance-only metric) for later down-select based on remaining fuel. The landing site selection data is then fed to the spacecraft GNC system. This entire process may be repeated, from scan to site selection, multiple times during the descent process.

The HDA effectiveness depends on many factors, including the characteristics of the actual terrain, the mechanical tolerance of the landing system which sets the hazard thresholds, and the performance of the LIDAR instrument (Johnson et al. 2008; Huertas et al. 2010). Because Enceladus is less thoroughly imaged than the Moon and Mars, the actual density of lander-scale hazards is not known and few constraints can be placed on the terrain. Coarse data

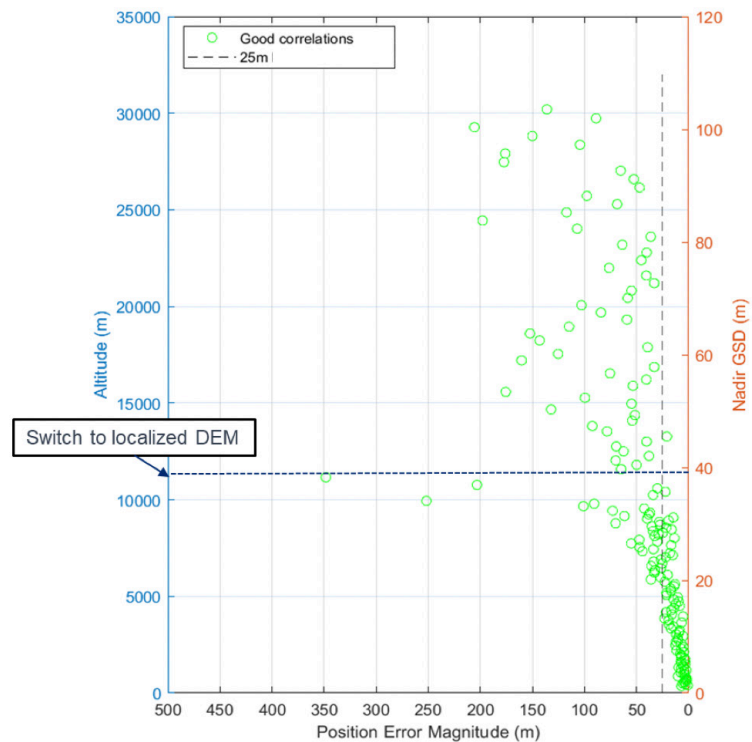


Exhibit C-13. TRN results from an analysis of a simulated lunar landing, showing position error magnitude as a function of altitude and nadir GSD.

Performance metric	Value
Maximum operational range at Bennu (4% albedo)	1.2 km
Maximum operational range scaled to Enceladus (80% albedo)	>4 km
Laser beam divergence	100 μ rad
Scanner angular precision 1σ (without ground calibration)	50 μ rad
Range measurement precision 1σ	1.1 cm
Scanner field of regard	± 6.7 by 5.9°
Pulse repetition rate	10 kHz

Exhibit C-14. Specifications of the OLA low-energy laser scanning system, from Daly et al. (2017).

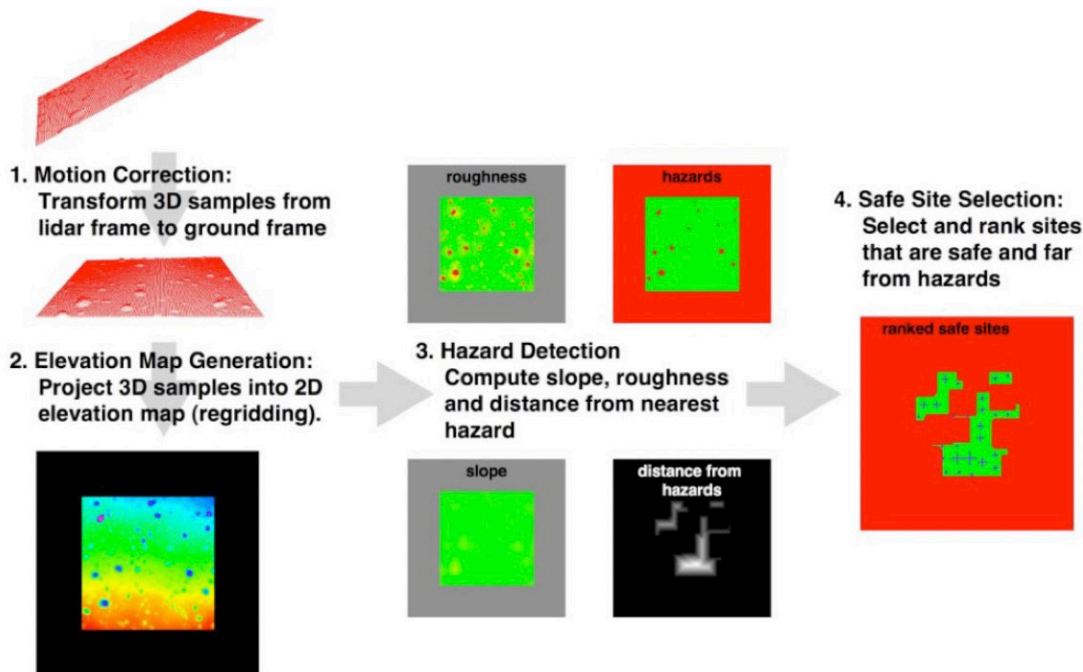


Exhibit C-15. Example HDA processing steps, from Johnson et al. (2008).

available from Cassini shows a rough surface with limited low-slope regions even at a much larger scale than the lander (Exhibit C-16). In addition, to mitigate the risk of sinking into unconsolidated terrain, the landing will not target the smoothest surface visible, but will instead aim for the vicinity of visible boulders showing that the surface can support the weight of the lander; these boulders will themselves pose potential hazards. On the other hand, the mass cost of ruggedizing the landing system drives strict (e.g. $<5-10^\circ$ slope) requirements on the landing site. These two considerations drive the selection of a highly capable instrument: from an altitude of 800 m, OLA's beam divergence and scanning system precision are capable of better than 20 cm ground sample distance (GSD). This allows reliable detection of 30 cm high obstacles, assuming roughly hemispherical shapes, and accurate measurement of surface slopes. At this same altitude, the field of regard allows mapping a 165x188 m region; this large (relative to the lander footprint) scan region improves the likelihood of finding a safe landing site on terrain that may have a high concentration of hazards. The full scan of this area at 20 cm GSD takes 78 s, fitting comfortably within the landing sequence (cf. 10 min to descend from 5-km to 200-m altitude), and near real-time onboard processing is feasible. The instrument is capable of even wider-area scans at reduced resolution from higher altitude, allowing early rejection of regions with many boulders or unacceptable slopes. Later scans, including targeted scans of small areas, are also possible to refine the site location and potentially supplement visual imagery to provide geological context for the landing site. Further study is recommended to determine the optimal scan resolution relative to descent altitude.

The study also considered a trade on the instrument needed for HDA. In particular, ASC GoldenEye, flown as the GNC LIDAR on *OSIRIS-REx*, was evaluated. However, the difficulty of the terrain drove the decision to recommend OLA. While both instruments are capable of imaging the surface from a useful altitude (more than a kilometer), and GoldenEye's 128×128 -pixel frame rate of 10 Hz provides an overall higher data rate, the driving consideration is the ratio of pixel IFOV or beam divergence to total field of view or regard. While OLA can image a >150 -m footprint at 20-cm GSD, GoldenEye's flash architecture limits the equivalent footprint to 26 m at 20 cm GSD. Generally, the GoldenEye flash architecture limits its search footprint to 128 times its GSD (the number of pixels). Safe landing requires a high probability that a safe site exists in the search footprint, or high fuel cost to divert and repeat the search in another area. Considering the challenges posed by the Enceladus surface, the latter option was considered

an unacceptable risk. LIDAR instruments are under active development for orbital rendezvous applications as well as lunar landings, so it is possible a suitable instrument at lower SWaP may become available in the next few years.

C.3. Planetary Protection and RTGs

A classic planetary protection concern for landing upon icy bodies is ensuring that the likelihood of the landed element reaching the subsurface ocean is negligible. Upon a nominal landing, Orbilander radiates about half its power or ~ 3.5 kW into the ground, most of which is due to the two RTGs which are each mounted ~ 1 m above the tips of the lander legs. Of these 3.5 kW, approximately 1 kW is RTG electrical power delivered to the spacecraft (and to a lesser extent RTG radiative power absorbed by the spacecraft) re-radiated through the MLI blankets. To ensure that the waste heat of the RTGs does not pose a planetary protection risk, we investigated four scenarios: (1) nominal landing; (2) off-nominal landing with the intact lander tilted; (3) off-nominal landing where an RTG drops off the lander; and (4) pre-landing breakup in Enceladus orbit that embeds an RTG into the surface. A fifth scenario of a hypervelocity impact into Enceladus during Saturn orbital insertion or pump-down mission phases is not investigated here, as it is assumed to have previously deemed improbable enough (e.g., through trajectory biasing) for compliance with planetary protection policy for other missions such as *Cassini-Huygens* and *Dragonfly*.

In all four cases, it is critical to consider how the RTG is in contact with the ground as conductive coupling is much more efficient at transferring heat into the surface—and thus facilitating downward transport of the RTG through the ice crust—than radiative coupling. Which thermal regime dominates is a function of both the orientation of the RTG fins and the properties of the ground. We consider two endmembers that bracket expected possibilities for the surface of Enceladus: thick, firm ice and thick, fluffy snowpack (where “thick” is relative to the meter-scale of the lander).

In scenario (1), the RTG is only radiatively coupled to Enceladus’ surface regardless of ground type. In scenario (2), though there may be a point or even a line contact between the RTG and the ground, radiative coupling still dominates. This assumption is also valid in off-nominal scenario (3) where the RTG drops off from the spacecraft after landing and the fins of the fallen RTG contact firm ground. However, if the ground is thick snowpack, then both the fins and the cylinder of the RTG contact the snow and the RTG is conductively coupled to the snow. In off-nominal scenario (4) where the RTG decouples from the

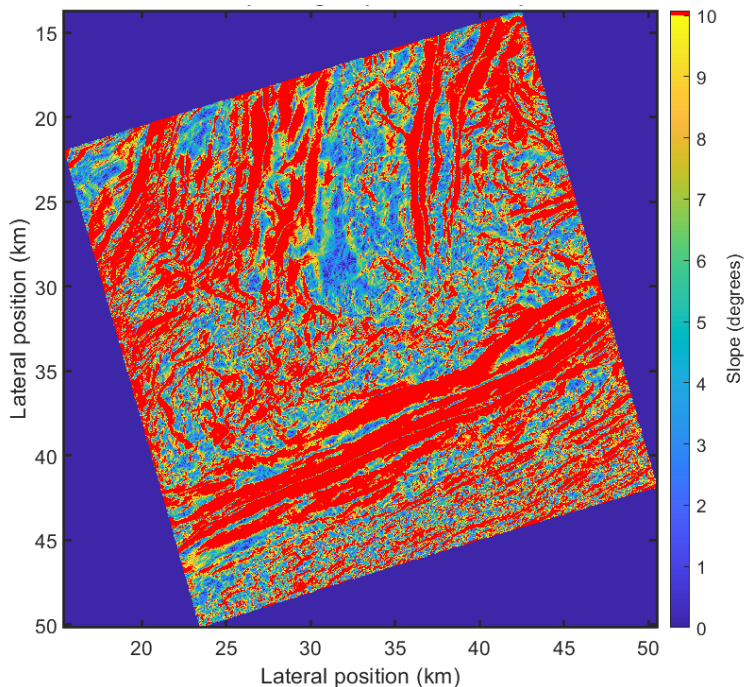


Exhibit C-16. Example of the highly sloped terrain of Enceladus, centered at $52.5^\circ\text{E}, 79.2^\circ\text{S}$. A 30-m posting DEM derived from photoclinometry is shown, where each pixel is colored by its slope. Regions with slopes over 10° , comprising nearly half the region, are marked in red. Fully $\frac{3}{4}$ of the terrain has slope over 5° . While a 1-km region is apparent in the figure with entirely $<10^\circ$ slopes, and only a few pixels over 5° , the coarse scale of this DEM may hide local roughness including lander-scale slopes above the threshold. We use this model as a test case as it offers some of the best resolved slopes for Enceladus’ south polar terrain. In reality, Orbilander would target areas further from a tiger stripe (Damascus in this image) to meet the surface temperature and slope landing site criteria. [Image credit: Paul Schenk, LPI]

spacecraft in orbit and impales the surface, we conservatively assume that the RTG is fully embedded in ice or snowpack such that the radiator fins are fully submerged. These scenarios and conditions are listed in Exhibit C-17. Note that in scenarios (1) and (2), each RTG, which has a much smaller surface area than the whole lander, would have to sublimate ice in a large enough volume for the whole lander to penetrate into the ice.

Scenario	Firm ground (ice)	Fluffy ground (snowpack)
(1) Nominal landing	Radiative coupling	Radiative coupling
(2) Intact lander tilted	Radiative coupling	Radiative coupling
(3) RTG drops off after landing	Radiative coupling	Conductive coupling
(4) RTG impaled from orbit	Conductive coupling	Conductive coupling

Exhibit C-17. Scenarios considered in this assessment of planetary protection compliance and corresponding thermal coupling of the NGRTG with Enceladus ice and/or snow.

C.3.1. Ice Sublimation Rates Due to RTG Heat in Conductive Coupling Cases

In this section, we investigate the “worst-case” scenario of conductive coupling, which maximizes heat transfer from the RTG into ice and snow. We first describe the relevant parameters and assumptions of our model, summarized in Exhibit C-19. The conditions considered here are intentionally conservative.

Temperature at RTG-ice interface. We follow the analysis of Lorenz (2012) to find the change from the local temperature T_0 (in K) of the surface or subsurface material next to the RTG due to energy input by the RTG, modified to account for the long cylindrical (rather than spherical) shape of the RTGs:

$$T(R) - T_0 = \frac{q}{2\pi\kappa L} e^{-\frac{U(R-x)}{2\kappa}} \quad [1]$$

where $T(R)$ is the temperature (in K) at distance $R = R_{RTG}$, the radius of the RTG, from the center of the RTG heat source; q is the RTG power; k is the local thermal conductivity of the surface or near-surface material (here, water ice); $\kappa = k/(\rho C_p)$ is its thermal diffusivity (with ρ its density and C_p its heat capacity); U is the RTG’s downward velocity; $L = L_{RTG}$ is the length of a cylindrical RTG; and x is the RTG depth below the surface. Cylindrical end effects are ignored and it is conservatively assumed that L_{RTG} (1 m for the NGRTG) is much greater than R_{RTG} (0.25 m for the NGRTG). For all scenarios in Exhibit C-17, $U = 0$ and Equation [1] is reduced to:

$$T(R) = T_0 + \frac{q}{2\pi\kappa L}. \quad [2]$$

For scenario (4), the impact velocity (< 250 m/s, the vector sum of the periapsis and freefall velocities) is assumed to be instantaneously dissipated in the act of fully burying the RTG in the solid ice. If $T(R) > T_{\text{melt}} = 273.15$ K, melting occurs and the RTG or lander continues to move downward. (If $T(R) > T_{\text{melt}}$, the presence of liquid water induces a local, temporary environment around the RTG that would be considered a “special region” in the terminology of the planetary protection policy for Mars (Kminek et al. 2017); however, this environment need not contact the subsurface ocean (Shotwell et al. 2019), as shown in Exhibit C-20.)

The RTG power decreases exponentially with time as

$$q(t) = q_{BOL} e^{-t \ln(2)/t_{1/2}}, \quad [3]$$

with $q_{BOL} = 4$ kW (the generated heat and power at the beginning of RTG life) and $t_{1/2} = 87.74$ years the half-life of ^{238}Pu . Landing nominally takes place ≈ 17 years after beginning of RTG life (14 years after launch), at which point $q(t) \approx 3.50$ kW for each RTG. To further ensure a conservative approach, we use 16 years after RTG beginning of life as the age to account for an earlier (off-nominal) landing.

Thermal conductivity of ice and snow. On Enceladus, some areas of the surface will be solid ice, some may be porous ice, while yet others may be blanketed by a highly porous layer of plume fallout. Closer to the tiger stripes, the “snowpack” may be deeper but have a higher strength (at least at the very top surface) due to sintering (Choukroun et al. 2020). In nonporous ice, the thermal conductivity is given by $k = 567/T_0 \text{ W m}^{-1} \text{ K}^{-1}$ (Klinger 1980). Porosity ϕ (0 for solid ice, 1 for vacuum) decreases the thermal conductivity (i.e. it is insulating); its effect can be captured by multiplying k by a factor $(1-\phi/0.7)^{4.1\phi+0.22}$ (Shoshany et al. 2002), applicable for $\phi < 0.7$. We vary a snowpack thickness, D_{snow} , between 0 and 100 m, setting $\phi = 0.65$ as a maximum starting point at the surface, decreasing linearly across the snowpack thickness to 0 at D_{snow} . Given the above expression, setting $\phi = 0.65$ at the surface likely captures the most insulating possible behavior of Enceladus surface material. Even though the porosity of freshly fallen snow on Earth can be as high as 85% and as low as 60% (Albert & Perron 2000, Proksch et al. 2016), and this porosity is likely to be even higher in the low-gravity environment of Enceladus, both modeling by Shoshany et al. (2002) and Arakawa et al. (2017) as well as experiments with porous aggregates of μm -sized SiO_2 grains (Krause et al. 2011) show that k is no more than a factor of $\sim 10^1$ to 10^3 lower than its zero-porosity value up to $\phi \approx 90\%$ (Exhibit C-18). Within this diversity of parameterizations, the above factor from Shoshany et al. (2002) is the most conservative as it produces the lowest k and, thus, warmest subsurface (Exhibit C-18). Since a k decrease factor of 10^3 is obtained with this conservative expression for $\phi \approx 0.6$, the assumption of a 65% surface porosity yields similar k as those obtained with porosities of 80-90% with other proposed k - ϕ relationships (Exhibit C-18). We are therefore confident that the assumptions adopted here adequately capture the lowest possible thermal conductivities of Enceladus surface material: they yield $k = 0.003\text{--}0.005 \text{ W m}^{-1} \text{ K}^{-1}$ in the surface temperature range 50–90 K.

Absorbed solar heat flux. The absorbed solar heat flux on a local patch of Enceladus’ surface, neglecting any topography, is given by

$$Q_{\text{solar}} = F_{\odot}(1 - Alb)\sin(SEA_{\text{avg}}). \quad [4]$$

We assume an albedo $Alb = 0.8$ and a solar flux at 9.5 AU of $F_{\odot} = 15.1 \text{ W m}^{-2}$. At high latitudes, the maximum sun elevation angle is $SEA_{\text{max}} = (obl + 90^\circ - lat)$ at noon on the southern summer solstice. Since Enceladus’ and Saturn’s equators are essentially coplanar (Baland et al. 2016), obl is assumed to be Saturn’s obliquity of $\approx 27^\circ$ (i.e. Enceladus and Saturn experience the same seasons). Because we are interested in the long-term behavior of a ^{238}Pu buried below the diurnal and seasonal thermal skin depths of the ground, it is relevant to average the SEA over a Saturn year (29.5 Earth years), which is shorter than the half-life of ^{238}Pu decay. South of the polar circle at $90^\circ - obl \approx -63^\circ$ latitude, which essentially

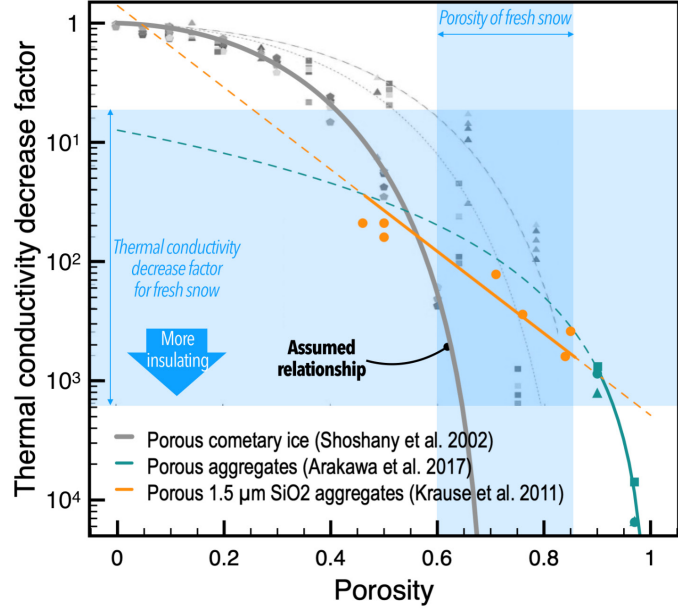


Exhibit C-18. Effect of porosity ϕ on the thermal conductivity k . The solid grey curve is the relationship conservatively adopted here (see text); it yields the lowest, most insulating k at $\phi > 0.55$. However, this expression breaks down for $\phi \geq 0.7$, where several modeling and experimental efforts (other curves and data points) show that $k(\phi=0.7 \text{ to } 0.9) \approx \{10^{-1} \text{ to } 10^{-3}\}k(\phi=0)$. The orange and teal curves show relationships that were only validated in the regimes where the curves are solid. The orange curve is a thermal conductivity in $\text{W m}^{-1} \text{ K}^{-1}$ (rather than a decrease factor). Data points of a given color are from the same source as the fit curve of that color.

encircles the SPT and targeted landing locations, the average SEA at noon (for days when it rises above the horizon) over a Saturn year is $SEA_{max} \times 2/\pi$, and the average SEA at any time of day between sunrise and sunset is $SEA_{max} \times (2/\pi)^2$. Also accounting for nighttime when effectively $SEA = 0$ yields:

$$SEA_{avg} = SEA_{max} \frac{2}{\pi^2} = (obl + 90^\circ - lat) \frac{2}{\pi^2} \quad [5]$$

Thus, SEA_{avg} is about 5.5° at the south pole and 7.5° , 9.5° , and 11.5° at -80° , -70° , and -60° latitude, respectively. This corresponds to average absorbed solar fluxes Q_{solar} of 0.29, 0.39, 0.50, and 0.60 W m^{-2} at these respective latitudes.

Endogenic heat flux. Given uncertainties regarding the structure of the ice shell below the SPT, we estimate the endogenic heat flux from the energy balance needed to obtain a given surface temperature T_{surf} . In the SPT, surface temperatures range with latitude from about 50–70 K but can be up to about 90 K in areas immediately surrounding the tiger stripe fractures (Howett et al. 2011; Le Gall et al. 2017), with very local maxima around 130 K within meters of plume source vents (Abramov & Spencer 2009). The endogenic heat flux is given as:

$$Q_{endo} = \epsilon \sigma_{SB} T_{surf}^4 - Q_{solar}, \quad [6]$$

with $\epsilon = 0.98$ the infrared emissivity of surface ice and snow and $\sigma_{SB} \approx 5.67 \times 10^{-8} \text{ SI}$ the Stefan-Boltzmann constant. For a given latitude, we only consider T_{surf} such that $Q_{endo} > 0$. With the above assumptions for Q_{solar} , the minimum temperature for $Q_{endo} > 0$ is 48 K at the south pole and 58 K at latitude -60° . Assuming $SEA = obl = 27^\circ$, that temperature becomes 71 K. For $T_{surf} = 85 \text{ K}$, $Q_{endo} = 3.04 \text{ Wm}^{-2}$ assuming -60° latitude average solar illumination and 3.36 W m^{-2} at the pole. The latter flux corresponds to the 15.8 GW of SPT endogenic power measured by Howett et al. (2011) from *Cassini* CIRS measurements being emitted through an area of 4700 km^2 , equivalent to the area within 7° of the pole or the area within 4 km of four tiger stripes each 150 km long. (In practice, the SPT emitted power also includes a component of lower heat flux over a broader area.) These fluxes also exceed the maximum values of $3.0_{-1.0}^{+0.2} \text{ Wm}^{-2}$ determined by Le Gall et al. (2017) from microwave radiometry using *Cassini* radar data of what seem to be recently active fractures distinct from the tiger stripes.

Temperatures across the ice shell. Given Q_{endo} , T_{surf} , snowpack porosity $\phi(d)$, and a snowpack thickness D_{snow} , $T_0(d)$ is propagated from T_{surf} (varied between 50 and 90 K) in depth increments Δd as:

$$T_0(d + \Delta d) = T_0(d) + \frac{\Delta d}{k(T_0(d))} Q_{endo}. \quad [7]$$

We set $\Delta d = 1 \text{ cm}$ in the uppermost 2 m and $\Delta d = 1 \text{ m}$ at higher depths since the above quantities of interest tend to vary more at shallower depth; test calculations with lower and higher Δd show that this achieves numerical convergence. From Equation [2], temperatures at the surface of the RTG cylinder (the interface between the RTG and the ice or snow of Enceladus), i.e. at the base of the fins, are computed as a function of depth in the ice shell. These temperatures initially decrease with depth in the porous layer given the decreasing porosity (and thus increasing thermal conductivity) in that layer. Temperatures then increase with depth as the ambient temperature T_0 increases from the surface temperature toward the 273 K of the subsurface ocean and the thermal conductivity decreases accordingly. We do not carry out calculations at combinations of T_{surf} and D_{snow} for which temperatures increase so fast with depth as to reach 273 K within 100 m of the surface, given that 100 m is too conservative a lower bound on ice shell thickness (Hemingway & Mittal 2019).

Process of downward transport. If the RTG is below the H_2O triple point pressure of 611 Pa, downward transport is due to ice sublimation. Otherwise, it is due to melting.

The sublimation regime is applicable in the top few meters and if the conduit bored by a descending RTG remains open to space (pressure ≈ 0 except for the sublimation vapor pressure). In this regime, the RTG continues to descend at a rate that decreases with decreasing $T(R)$ but is never zero. When the downward rate is small enough (e.g. < 1 mm/year) that other processes such as burial under plume fallout (Southworth et al. 2019) begin to dominate, the RTG is deemed to have stalled.

The melting regime is applicable if the RTG is fully embedded under several meters of ice or snow, such that the overburden hydrostatic pressure, $P = \rho(1-\phi)gd$, exceeds the H₂O triple-point pressure. (Here, $g \approx 0.1 \text{ ms}^{-2}$ is the surface gravity of Enceladus.) This regime is warranted if the RTG is covered by a minimum thickness of about $6.5/(1-\phi)$ meters of snow or ice. In the melting case, the RTG stalls if $T(R) < 273$ K (Lorenz 2012).

The temperatures $T(R)$ allowing for downward transport are lower in the sublimation regime. We therefore conservatively assume that regime going forward (but compare in one instance results with the melting regime, see Exhibit C-20a). However, it is likely that enough material would fall in the hole dug by the RTG to transition to the melting regime over time.

Evolution in time. The RTG power decreases significantly on a timescale of years. Whether downward transport due to sublimation is stalled and at what depth thus depends on the relative rates of sublimation and radioactive decay. Comparatively, the rate of burial under plume fallout is negligible, at most on the order of mm/yr (see Southworth et al. 2019). Both rates have a nonlinear feedback on the ice sublimation rate S_0 as follows (Andreas 2007):

$$S_0 = e_{sat}(T) \sqrt{\frac{M_w}{2\pi RT}} \quad [8a]$$

$$e_{sat}(T) = e^{9.550426 - 5723.265/T + 3.53068 \ln(T) - 0.00728332 T} \quad [8b]$$

Here, $e_{sat}(T)$ is the saturation vapor pressure (in Pa), i.e. the ice-vapor boundary in the H₂O phase diagram, and we take $T = \min(T(R), 273 \text{ K})$. Expression (8b) is adopted from Murphy & Koop (2005). The term M_w is the molecular mass of water ($0.018 \text{ kg mol}^{-1}$) and R is the ideal gas constant ($8.314 \text{ J mol}^{-1} \text{ K}^{-1}$). S_0 has units of a mass flux, $\text{kg m}^{-2} \text{ s}^{-1}$. We convert it to a mass sublimation rate:

$$\frac{dm}{dt} = (2\pi L_{RTG} R_{RTG} + \pi R_{RTG}^2) S_0 \quad [9]$$

and a corresponding downward transport rate:

$$\frac{dd}{dt} = \frac{(2\pi L_{RTG} R_{RTG} + \pi R_{RTG}^2) S_0}{\rho(1-\phi)A} \quad [10]$$

in kg/s and m/s, respectively. A is the relevant cross-section: the spacecraft in radiative scenarios (1) and (2), about 9 m^2 per RTG based on the Orbilander mechanical design (§3.3); or the RTG itself in conductive scenarios (3) and (4), which we take to be $A = \pi R_{RTG}^2$. The time Δt needed to reach depth $d + \Delta d$ is then determined as $\Delta d / (dd/dt)$. We repeat the calculation at depth $d + \Delta d$, computing $T(r)$ using $q(t+\Delta t)$, $T_0(d + \Delta d)$, and $k(T_0)$, for as many depths as needed until it can be determined whether the RTG descent stalls ($\Delta t \gg t_{1/2}$; we take $\Delta t = 1000$ years or 11 half-lives as a threshold; beyond, plume burial dominates) or reaches the ocean. Quantities used in this computation are summarized in Exhibit C-19.

Model validation. This model reproduces calculations performed as part of the Europa Tunnelbot study (Oleson et al. 2019). The goal of that study was to reach the ocean of Europa ($T_{surf} = 100 \text{ K}$, $D_{snow} = 0$) at depth 20 km within 3 years by melting. One of three designs considered was based on an RTG with heat sources ($q \approx 12.5 \text{ kW}$ at the time of landing) packed within $L_{RTG} \approx 1.1 \text{ m}$ of the tip of a Tunnelbot 5.75 m long and $R_{RTG} = 0.25 \text{ m}$ in radius. With these parameters, the present model predicts that descent by sublimation is achieved within 3 years if the heat sources are packed within $L_{RTG, max} = 3.45 \text{ m}$ of the Tunnelbot

Quantity	Symbol	Value/Unit	Notes/References
Spacecraft cross-section (per RTG)	A	9 m ²	Based on Orbilander mechanical configuration
Albedo	Alb	0.8	Howett et al. (2010)
Depth	d	m	
Depth step	Δd	0.01–1 m	
Snowpack depth	D_{snow}	0-100 m	Porosity decreases linearly with depth to 0 at bottom of snowpack
Saturation vapor pressure of H ₂ O	e_{sat}	Pa	Nonlinear dependence on temperature (Murphy & Koop, 2005)
Solar heat flux at 9.5 AU	F_{\odot}	15.1 W m ⁻²	
Thermal conductivity of H ₂ O ice	k	567/T W m ⁻¹ K ⁻¹	Klinger (1980)
Molar mass of H ₂ O	M_w	0.018 kg mol ⁻¹	
Obliquity	obl	26.73°	Obliquity of the Saturn system
Endogenic heat flux across ice shell	Q_{endo}	W m ⁻²	
Locally absorbed solar heat flux	Q_{solar}	W m ⁻²	
RTG power	q	W	
Beginning-of-life RTG power (per RTG)	q_{BOL}	4000 W	
Ideal gas constant	R	8.314 J mol ⁻¹ K ⁻¹	
Latitude	lat	-60° to -90°	Extent of Enceladus' south polar terrain
Characteristic RTG dimension	L_{RTG}	1 m	Length for a cylindrical RTG
RTG radius	R_{RTG}	0.25 m	Radius of cylindrical RTG
H ₂ O ice sublimation rate	S_0	kg m ⁻² s ⁻¹	Andreas (2007)
Solar elevation angle	SEA	°	Averaged over Saturn year in Q_{solar} calculation
Temperature with RTG heating	T	K	Lorenz (2012)
Local ice/snow temperature without RTG heating	T_0	K	
Surface temperature	T_{surf}	50–90 K	Abramov & Spencer (2009); Howett et al. (2011); Le Gall et al. (2017)
Time	t	s	
²³⁸ Pu half-life	$t_{1/2}$	87.74 years	
Time step	Δt	s	A function of the depth step and sublimation rate
Surface snow and ice emissivity	ϵ	0.98	
H ₂ O ice density	ρ	917–0.13*(T ₀ -273.15) kg m ⁻³	Melinder (2007)
Porosity	ϕ	0–0.65	Decreases linearly from surface value across snowpack thickness

Exhibit C-19. Quantities used in determining the fate of a NGRTG conductively coupled to Enceladus ice and/or snow.

tip. Although this model does not track descent time for the melting case, the maximum packing length for the probe to reach the ocean is calculated to be $L_{RTG, max} = 2.3$ m. Both values are slightly higher than the L_{RTG} adopted by the Europa Tunnelbot study team, validating the present model (and confirming the validity of this aspect of the Tunnelbot design).

Results of the conductive calculations for scenarios (3) and (4) are shown in Exhibit C-20. The RTG cannot reach the ocean for surface temperatures $T_{surf} \leq 87$ K and associated heat fluxes Q_{endo} if the area is free of snow ($D_{snow} = 0$). If the snowpack thickness is nonzero, there is a threshold snowpack thickness at

which the RTG becomes able to reach the ocean. This threshold is a function of surface temperature, porosity, and endogenic heat flux: the threshold decreases with increasing surface temperature, increases with surface insulation from porosity, and increases with endogenic heat flux (Exhibit C-20a,b). For example, the threshold snowpack thickness is about 10 m for both the south pole ($T_{surf} = 60$ K, equivalent $Q_{endo} = 0.44$ W m⁻²) and at 60°S latitude ($T_{surf} = 65$ K, equivalent $Q_{endo} = 0.71$ W m⁻²) for the highest surface insulation (thermal conductivity decreased by a factor 2000). These T_{surf} and Q_{endo} are typical of the SPT away from the vents (Howett et al. 2011; Le Gall et al. 2017) and yield SPT ice shell thicknesses (i.e. depth to the ocean; teal curves in Exhibit C-20a,b) at the thin end (1–2 km) of the several km inferred from Cassini gravity, topography, and libration measurements (Hemingway & Mittal 2019). Depths to the ocean are mainly controlled by the endogenic heat flux (Exhibit C-20a) and seldom affected by surface porosity (Exhibit C-20b). Surface conditions allowing an RTG to reach the ocean are only possible within kilometers of the tiger stripes where the heat flux and plume fallback are maximum. Even near the stripes, there likely exist locations (e.g. topographic highs) where the snowpack is thin (centimeters to meters) and/or the surface temperature is low, precluding the RTG from reaching deep into the ice shell.

Descent depths, even for threshold combinations of T_{surf} and D_{snow} , are in most cases tens of meters and no more than 300 m. This can be seen in Exhibit C-20c where the descent depth is shown as a function of time. The descent rate is high at first: descent through the first half of the insulating snowpack takes < 1 day (outside the displayed time range). The more compacted, less insulating bottom of the snowpack is reached within months, at which point descent has markedly slowed down to rates of meters per year. The descent rate keeps slowing down asymptotically to zero as the decrease in RTG power output outweighs the increasingly warmer and more insulating ice shell conditions encountered by the descending RTG (the apparent increase in slope around 1 year is due to the logarithmic scale used for the time axis).

The descent depth is higher for threshold combinations with lower surface temperature and higher snowpack thickness. Even in threshold cases, the descent depth is a few percent (near 20% in one case) of the vertical distance to the ocean ($T_0 = 273$ K) and therefore not a planetary protection concern (Exhibit C-20d). The ratio of descent depth to ice shell thickness is not correlated with threshold combinations of T_{surf} and D_{snow} . The descent depth decreases quickly for thinner, non-threshold snowpacks (Exhibit C-20e). It remains within tens of meters if the insulating effect of snow is varied (Exhibit C-20f).

Summary of conductive coupling case. While there are scenarios in which the RTG can penetrate to the ocean in the conservative approach of this analysis, they are less likely, off-nominal cases. Out of an abundance of caution to ensure safe deployment, we devised the landing site selection strategy described in §B.1.4.2.

C.3.2. Ice Sublimation Rates Due to RTG Heat, Radiative Coupling Case

If the RTG is only radiatively coupled to the ice or snow, RTG heat is not transferred nearly as efficiently and the RTG does not reach the ocean for any realistic parameter combinations. Here, we simplify the modeling approach by assuming two endmember cases with $T_{surf} = 50$ K and $T_{surf} = 85$ K.

In the cold case ($T_{surf} = 50$ K), we assume the surface temperature arises entirely from the endogenic flux through terrains in eclipse, since except very near the pole the minimum temperatures in most SPT areas in sunlight are above 50 K from solar illumination alone. Thus, the required minimum endogenic heat flux is $Q_{min} = \epsilon \sigma_{SB} T^4 = 0.35$ W m⁻². In the hot case ($T_{surf} = 85$ K), we assume that the heat that is not provided by the low-angle solar illumination (~ 1 W m⁻² for $SEA = obl = 27^\circ$) is provided by endogenic flux. This results in a maximum endogenic flux $Q_{max} = 1.53$ W m⁻².

The distance from the RTGs to the surface is sufficient to ensure that heat radiated from the RTGs does not sublimate ice at a rate such that the lander reaches a runaway depth. However, since the RTGs heat the surface by ~ 100 K upon landing, some high-porosity, high surface temperature situations ($T_{surf} = 85$ K and $D_{snow} = 25$ m with $\phi = 0.59$ or $D_{snow} = 3$ m with $\phi = 0.65$) result in the RTG reaching the ocean, but only for ice shell thicknesses much smaller than the current understanding of Enceladus' crust (a few km at thinnest; Hemingway & Mittal 2019). Thus, for expected ice shell thicknesses at Enceladus' south pole, no realistic situations for scenarios 1 and 2 result in reaching the ocean.

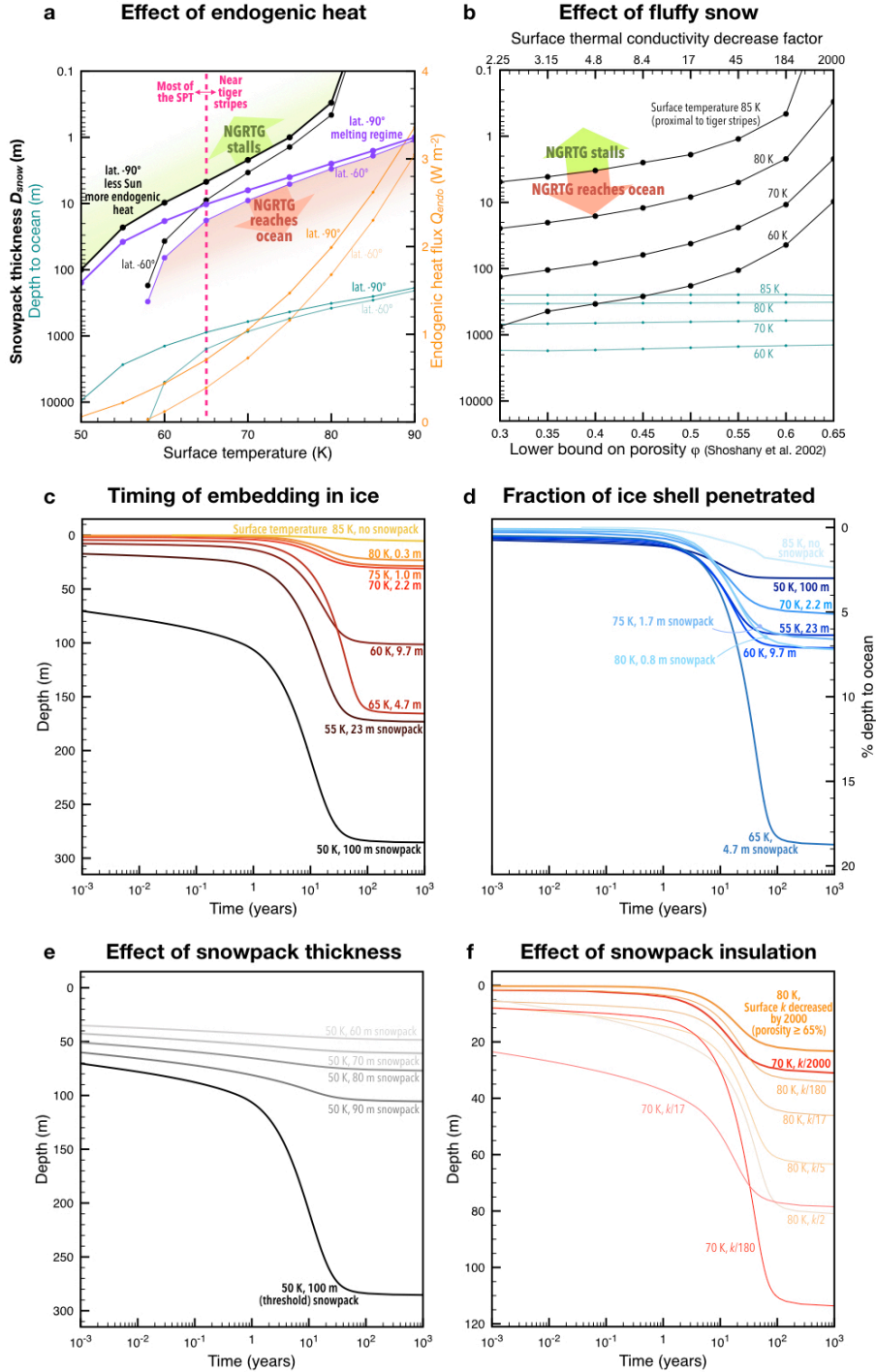


Exhibit C-20. a. Threshold combinations of surface temperature T_{surf} and snowpack thickness D_{snow} with the most conservative insulation due to porosity in the sublimation (black curves) and melting (purple curves) descent regimes. Endogenic fluxes (orange curves) are estimated from T_{surf} at the south pole (lat. -90°) and edge of the SPT (lat. -60°); from these fluxes' depths to the ocean ($T_o = 273$ K) are calculated (teal curves). b. Threshold combinations of D_{snow} and insulation (black curves) in the range possible for fresh snow (Exhibit C-18) and corresponding ice shell thicknesses (teal curves) for four values of T_{surf} . c. For combinations of T_{surf} and D_{snow} corresponding to the thick black curve in panel a, RTG depth into the ice shell as a function of time. d. Fraction of the vertical distance to the ocean reached by the RTG in the cases of panel c. e. RTG depth into the ice shell as a function of time for $T_{surf} = 50$ K and various

snowpack thicknesses. f. RTG depth into the ice shell as a function of time for $T_{surf} = 80$ K and 70 K and various snowpack porosities (insulations). Unless indicated otherwise, all results are for latitude 90° S (south pole, average Sun elevation 5.5°), the threshold snowpack thickness, and a surface thermal conductivity decreased by a factor 2000 (surface porosity $\geq 65\%$).

Assuming the conservative scenario where the spacecraft heats a ground of 50% porous water ice to 185 K, the sublimation rate is less than 0.25 m/yr (Andreas 2007). Over the course of the nominal 2-year mission, Orbilander would carve a ~ 1 m bowl. The maximum plume fallout rate predicted (1 mm/yr) is insufficient to bury Orbilander. Thus, for a nominal landing and execution of the prime mission, the lander remains on the surface at end of mission with minimal likelihood of contaminating the subsurface ocean.

This also holds for an off-nominal landing where the lander is tilted such that an RTG is in contact with the ground (scenario 2). Due to geometry (including the fins), the RTG effectively carves out the surrounding area rather than self-embedding. The spacecraft is mostly radiatively coupled to the ice such that sublimation should still be < 0.25 m/yr.

C.3.3. Ensuring planetary protection compliance

As shown in Exhibit B-10 (bottom panels), Orbilander's definition for a safe landing site includes identifying sites with surface temperatures < 85 K (with the TES) and < 10 m of snowpack (as indicated by the presence of boulders identified with the NAC). Analyses of *Cassini* data to date allow preliminary assessments of locations satisfying these criteria (Exhibit B-11), which suggests that locations meeting the criteria (and those of high plume fallback and Sun/Earth in view during Orbilander's science phase) exist (Exhibit B-12). These preliminary maps can be refined with more in-depth analysis of the *Cassini* datasets and would be updated during Orbilander's orbital reconnaissance using laser altimetry, radar, thermal emission spectrometry, and imaging. Radar measurements would help identify keep-out areas where the ice-liquid water interface is within hundreds of meters of the surface, if they exist.

In off-nominal cases where the RTG detaches, the probability of contamination is low due to three factors. First, the likelihood in scenario (4) of the RTG randomly impacting a southern hot spot with a flux > 1 W m $^{-2}$, given the 15.8 GW SPT power output measured by Howett et al. (2011), can be constrained as $(15.8 \text{ GW}/1 \text{ W m}^{-2}) / (4\pi R_{Enc}^2 (1 - \cos 30^\circ)) \approx 1/50$. Second, the mechanical fidelity of the design must be high to ensure mission success; i.e. the probability of breaking off an RTG is, by design, as low as possible. To date, no RTGs have detached on flown missions due to mechanical failure. (The Apollo 13 RTG was still carried by the lunar module upon Earth reentry; e.g. Schmidt et al. 2011.) Finally, RTGs represent less of a concern for planetary protection standards because the power output is such as to render the RTGs sterile. The typical sterilization method for laboratory equipment and surgical tools is exposure to temperature of 121°C for several hours at Earth's atmospheric pressure (1 bar). The RTG temperature can be roughly estimated (conservatively assuming perfect emissivity) as $(q(t)/[(2\pi R_{RTG}^2 + 16 L_{RTG}L_{fins})\sigma_{SB}])^{1/4} = 429$ K = 146°C at the time of landing (assuming $q(t) = 3.5$ kW 17 years past beginning of life) and 158°C around the time of launch (3 years past beginning of life). The summed terms represent the surface area of the two ends of the NGRTG cylinder and 8 fins of width $L_{fins} = 10$ cm each radiating from both sides. Detailed modeling shows that at the time of landing, the central part of the NGRTG cylinder is at 165°C with the fins at 125°C . Any microorganisms on the RTG would be exposed to such high temperatures in vacuum for 14 years, which represents a sterilizing environment superior to standard laboratory practices.

C.4. Landing Site Contamination During Descent

Following the analysis of Lorenz (2016), we consider the effect of hydrazine deposited on the surface of Enceladus during Orbilander's descent. Nitrogen-bearing compounds will be an important component of the chemical surveys, so minimizing contamination effects on these measurements is a key consideration. We devised four possible solutions:

- Scoop arm (or other active sample collection mechanisms) longer than the anticipated blast zone radius
- High enough burn cutoff heights to deposit $\text{NH}_3 < \text{the anticipated natural abundance}$
- Lander mobility
- Descent maneuver to land away from thruster-affected surface

C.4.1. Scoop Arm Length

The active sampling mechanism would be the most affected by thruster contamination. The Orbilander funnel (passive sampling) has a cover to ensure no deposit or kick up into the funnel during descent and landing. This cover opens twice and closes once: opens at Enceladus insertion to sample particles in orbit, closes in preparation for landing, and opens again once safely at the surface.

Lorenz et al. (2016) derived an empirical relationship between the blast zone area and lander dry mass. The blast zone area for the landed elements carrying the LDS considered in this study (Orbilander and the Large Lander) would $\sim 1.6\text{--}4$ m in radius (Exhibit C-21). Scoop arm reach for Mars landers include 2.35 m for *Phoenix* (the model for the Orbilander design) and 1.8 m for *InSight*. The Europa Lander Science Definition Team designed a scoop with a 1.4–2.2 m reach. Thus, an arm long enough to reach outside the blast zone area is within the family of previous designs, at the cost of reducing the candidate areas for scooping. It is unclear whether this limitation would be detrimental to the science return of the mission, given our unknowns of the Enceladus surface. It would require a modification to the context camera mounting relative to the design presented here.

	Mass (kg)	Enceladus Gravity (m/s^2)	Thrust (N)	Blast Zone Area (m^2)	Circular Radius (m)
Orbilander	1600	0.11	176	46.7	3.9
Large Lander	500	0.11	55	8.2	1.6

Exhibit C-21. Blast zone area predicted from empirical dependence on lander mass described in Lorenz et al. (2016).

C.4.2. High cutoff altitude

We calculate the ammonia deposited by a hydrazine burn as a function of cutoff distance using the mass fluence, D , (the time integral of the mass flux) for a point directly beneath the lander at a distance h_0 (Lorenz et al. 2016):

$$D = \frac{T}{\pi v h_0 g_0 I_{sp}},$$

where engine thrust T is equal to the weight of the spacecraft, v is the descent speed, g_0 is the acceleration due to gravity on Earth, and the specific impulse, I_{sp} .

The ammonia deposition rate is then the mass fluence scaled by the fraction of ammonia in the exhaust gas and the fraction that sticks to the ground. Lorenz et al. (2016) noted that the colder regolith of Europa likely makes the surface more efficient at cryotrapping the ammonia than Mars; this is even more true for Enceladus where average surface temperatures are tens of K lower than Europa. (The tiger stripes are much warmer, but we specifically target landing sites away from surfaces >85 K to avoid sublimation runaway in off-nominal landings.) Thus, the 10% fraction assumed in this calculation may be conservative for Enceladus. We echo Lorenz et al. (2016): more laboratory and/or modeling investigations into rates at which ice regoliths retain ammonia as a function of temperature and porosity are needed. Assumptions for these calculations are summarized in Exhibit C-23.

Using this model, we calculate the ammonia deposited into the surface of Enceladus for the Orbilander (green) and Large Lander (blue) and compare to the amount of NH₃ observed in the plume by *Cassini*, shown in Exhibit C-22. The molar percent of ammonia in the plume is between 0.4–1.3 (Postberg et al. 2018); taking the higher value, the naturally occurring ammonia in a 5-cc scoop is at 3.8 ppb (grey line). Thus, to emplace less than the expected amount, the Orbilander thrusters must cutoff above 35 m and the Large Lander thrusters must cutoff above 12 m. The difference lies in the factor of ~3 thrust required to slow down the heftier Orbilander (1600 kg dry mass) than the Large Lander (500 kg) which leaves the remote sensing elements in orbit.

At these heights, the free fall velocities after thruster cutoff are 2.8 and 1.6 m/s. For the Orbilander case, this was too high to be handled by the mechanical design, allowing for too much tip-over uncertainty, or requiring an unacceptable size and mass of the lander legs .

C.4.3. Mobility

Another solution is to move the spacecraft away from the blast zone after the initial landing. Given Enceladus' low gravity (0.11 m/s²), mobility can be achieved relatively simply. For example, to first order, firing thrusters to leave ground at 1 m/s at 45° to vertical allows the spacecraft to land 10 m away ballistically (a 14 s hop). This would be well outside the blast zone area.

However, implementing this movement would, in reality, be more complicated. The thermal design would need to prevent the hydrazine from freezing. The structural design would have to ensure that the legs land evenly during the initial landing to avoid a pivot point for the hop (which may be difficult a priori given the uncertainties of the Enceladus surface). The structure would also need to align the main engine such that the hopping burn does not introduce a large rotation. Furthermore, to align the main engine along the 45° to vertical on the ground would require a spinning upon descent to an altitude at which it is safe to drop; mounting the engines 90° apart is an unacceptable solution due to the reduced efficiencies throughout the mission and would introduce structural issues. Monoprop thrusters are also unacceptable due to the 200 N force required to hover. Thus, mobility was not pursued as the CML 4 solution to mitigating descent contamination for the Orbilander, in favor of a simpler solution discussed below.

If surface mobility were already considered as part of the architecture driven by the science requirements, this solution may have proved more attractive. However, for the Orbilander, the science team decided that mobility was not required. One argument for mobility is to mitigate the risk of landing in an area where plume fallout is lower than expected. We chose to mitigate this risk by including an active sampling mechanism to ensure access to large sample volumes, albeit potentially modified (Exhibit B-8). Another benefit of mobility is being able to sample different jets, which *Cassini* data suggests may be different in composition (Hedman et al. 2018). However, we could not devise a CML 4 solution that would allow

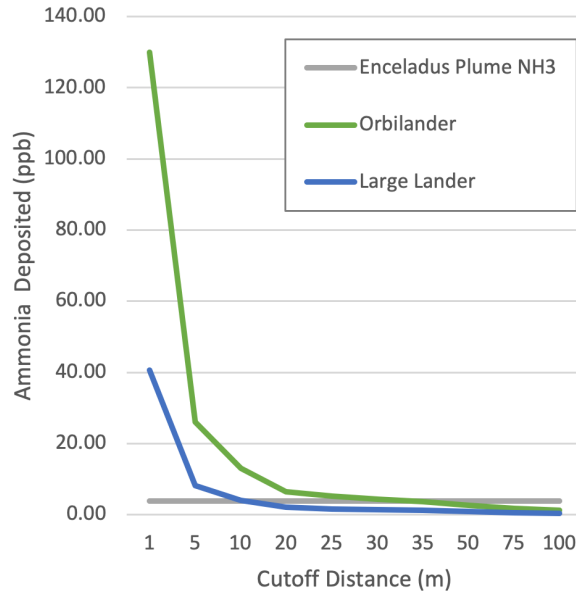


Exhibit C-22. Amount of ammonia deposited as a function of distance from the surface at which thrusters cutoff

Penetration depth (m)	0.1
Cone of expansion (°)	45
Descent speed (m/s)	200
Specific impulse (s)	220
Ammonia fraction that sticks	0.1
Surface volume penetrated (L)	100

Exhibit C-23. Assumed values for calculating ammonia deposition

sufficient cleaning of the sample capture device to ensure that results would be representative of individual jets and not the aggregate.

C.4.4. Descent Maneuver to Land Away from Thruster-Affected Surface

The preferred solution for the Orbilander is the “belly flop” maneuver described in §3.7. By firing the main engine for 5 s at 10 m above the surface while firing the monoprop thrusters, the spacecraft pitches over and is propelled up to 20 m above the surface. The resulting horizontal translation is about 25 m downtrack, well within the scouted safe area but well away from the blast zone radius. The spacecraft then executes a final rotation such that the legs are in the downward orientation before all rotational and translational motion is arrested by the monoprop thrusters. Final vertical velocity is < 2 m/s and horizontal velocity < 0.5 m/s. The higher vertical to horizontal ratio helps reduce the likelihood of tip over.

APPENDIX D. ADDITIONAL INFORMATION ON TECHNOLOGIES AND TECHNIQUES

D.1. Instrument Calibration and Data Products

In this section we describe the general calibration procedures the science payload requires on the ground and preflight as well as anticipated data products.

D.1.1. Life Detection Suite

HRMS: Calibration is performed preflight using a mix of volatile hydrocarbon gases including cross calibration with a dedicated flight spare that will be maintained for comparison purposes throughout the mission. The flight model will also be calibrated during flight (before and after each experiment) using an FC43 calibrant that produces known mass peaks across the detectable mass range. Derived products include: 1) molecular identifications and relative abundances of target molecules and 2) identification of other (non-targeted) compounds including CHNOPS redox pairs that allow determination of ocean properties such as temperature, pH, and available free energy of the system.

SMS: Calibration is performed preflight (using a mix of volatile hydrocarbon gases) and during flight (testbed operations with analytes selected based on detected mass spectra) activities. Mass calibration will occur after every experiment using a small cylinder of calibrant that produces known mass peaks across the detectable mass range, supporting analysis of trending instrument health and background signals during development and flight. Calibrated data products for a GCMS are: 1) GC temperature and retention-time calibrated gas chromatograms, 2) mass-calibrated mass spectra (MS and MS/MS), and 3) bulk evolved gas temperature and mass calibrated profiles. Derived products include: 1) molecular identifications and relative abundances of target molecules: amino acids, amino acid enantiomers, and lipid hydrocarbons (directly or in derivatized form); and 2) identification of other (non-targeted) compounds and ions including CHNOPS-bearing and some redox active species.

ESA: Flight calibration includes blanks to establish a subtractable baseline signal and water spiked with specific standards or salts at different dilutions for sensor calibration, acidification, or titration. Calibration and sensor conditioning can be done up to several days before sample analysis. Derived data products include the identity and relative concentrations of major soluble ions, molecules and redox active species in sampled materials as well as pH and conductivity of sampled materials. These data can be used as inputs for models of water activity, ionic strength, salinity, density and other geochemical and physicochemical properties.

μCE-LIF: The analysis suite includes a blank, sample, and standard runs for background subtraction and normalization as in-flight calibration. CE column mobilities are characterized before flight and confirmed in-flight with onboard amine, amino acid and carboxylic acid standards stored on the chip. Derived data include peak positions (revealing charge and size of amines, amino acids and carboxylic acids), peak intensity relative to the standard (providing quantitation), relative peak positions of chiral species (revealing the chirality ratios), integrated separation profiles (revealing the total primary organic amine and primary carboxylic acid concentrations in the sample).

Microscope: Geometric and photometric (bias, dark current levels, flat fields) calibration would be conducted preflight for the detector and illumination sources. In-flight calibration includes determining any change to dark current due to cruise. (See, for example, Thomas et al. (2004)) Derived data products include color or fluorescence images of sampled materials (in the liquid phase or after sample drying) or of particulate materials captured on sub-micron filters.

Nanopore: Flight calibration includes blanks to establish a subtractable baseline signal and might also include water spiked with a specific standard (e.g. RNA) as a positive control. Calibration will likely need to be done hours prior to sample analysis. Derived data products include values of current (pA) from each

nanopore as a function of time. For a flight instrument, and given the large amount of data generated, there will likely be limited storage of raw signals. Instead various levels of signals will be generated in situ, such as event (e.g. translocation signal) timing and characteristics, blocking current histograms and other derived products.

D.1.2. Reconnaissance and Remote Sensing Suite

NAC and WAC: The NAC and WAC cameras will undergo full calibrations in an optical calibration facility prior to delivery to the spacecraft. The cameras will be fully characterized for photometric and spectral sensitivity across the field of view, background and pattern noise, geometric distortions, and off-axis stray light sensitivity. After launch, the cameras will use stellar observations to determine their pointing relative to the spacecraft primary axes as well as to check for any photometric changes during cruise and orbital operations. For the trajectory described in the main text, which employs Jupiter Gravity Assist, the Galilean satellites can also be used to check the photometric behavior of the detectors. Calibrated data products include calibrated images of the surface used to identify boulders and other surface features and to create stereo pairs, which will be used to derive local slopes.

Radar sounder: On ground calibrations include characterizing transmitter, receiver, and antenna power and gain (e.g. Croci et al. 2007). In flight, decluttering can be facilitated by data from the instruments, such as topography from the laser altimeter and cameras as is planned for *Europa Clipper* REASON. Deploying the boom during the Saturn moon tour would allow the use of other satellites as calibration targets; though the details of this strategy were not explored during the CML 4 study. Derived data products include focused SAR radargrams. Reflectometry products require a longer baseline (and therefore larger data accumulation and return time) than was prioritized in the orbital ConOps but may be possible if the orbital phase schedule margin remains unused.

Laser altimeter: Pointing and timing references, range biases, and laser and receiver characteristics (such as responsivity, sensitivity, gain, bandwidth) will be determined during pre-flight calibration (Sun et al. 2015). Calibrated data products include laser pulse time-of-flight and spacecraft orbit position; derived data products include maps of local topography.

TES: Ground calibration activities include defining field of view, spectral line shape and sample position, spectral response, and radiometric calibration (e.g. Christensen et al. 2001). Internal calibration targets will be used in-flight. Calibrated products include raw and calibrated radiance data and associated raw and derived positional and geometric data.

D.1.3. In Situ Suite

Seismometer: Preflight calibration includes mapping ground motion to instrument response and identifying the noise sources specifically anticipated for Enceladus. Absolute calibration might be possible on the surface depending on probe deployment and housing (e.g. Pou et al. 2019). Calibrated and derived data products include spectrograms which are used to calculate key statistical descriptors like event rate, moment rate, and completeness threshold (e.g. Kagan et al. 2002; Clinton et al. 2018).

Context camera: Calibration follows similar procedures to the NAC and WAC with additional calibration for illumination sources similar to the microscope. Calibrated and derived data products include calibrated images and spectra which are used to identify scooping sites based on regolith properties.

D.2. Power

The electrical power system block diagram is shown in Exhibit D-1. An alternative EPS configuration considered replaced the lithium ion battery with a third NG-RTG. The impact to the remaining subsystem was minimal. It required additional sequent shunt stages to be added to the shunt system, which would regulate using RTG bus voltage rather than battery charge voltage. However, the estimated mass and cost were higher than the system presented above. The three RTG system also requires the commitment of 50% more plutonium to the mission, which is a national resource we believe should be conserved.

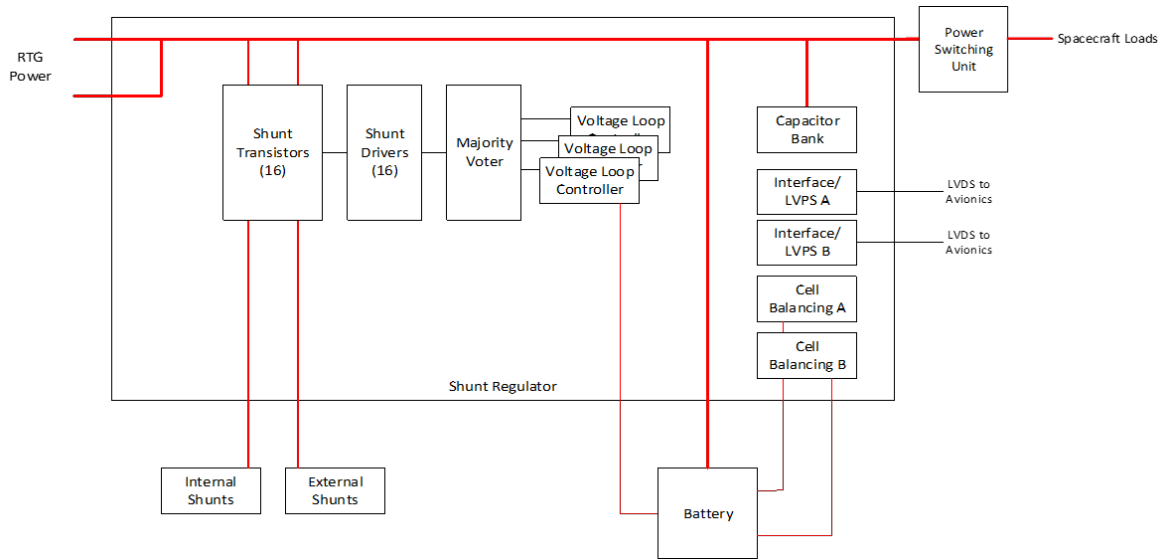


Exhibit D-1. Electrical Power System Block Diagram

D.3. Thermal Alternatives

A fluid loop may be alternative solution to the thermal design discussed in the main text. However, only MSL has demonstrated the use of fluid loop for heat supply and pick-up with RTGs. Specialized variably-entrained fluid loops, as is being considered for *Dragonfly*, could be considered. Especially if considering an alternative trajectory that includes an inner solar system tours, the potential thermal savings of using fluid loops with Orbilander's 2 RTGs was deemed insufficient to justify the additional mass, power, complexity, and possible failure introduced. Further study may be warranted.

D.4. Risk evaluation definitions

The risks and consequences identified in §3.15 were evaluated using the standard rankings defined in Exhibit D-2 and Exhibit D-3. Risk assessment categories are defined in Exhibit D-4.

Likelihood of Risk	
1 Very Low	Tech: $0.1\% < P < 2\%$; Cost/Sched: $P < 10\%$
2 Low	Tech: $2\% < P < 15\%$; Cost/Sched: $10\% < P < 25\%$
3 Moderate	Tech: $15\% < P < 25\%$; Cost/Sched: $25\% < P < 50\%$
4 High	Tech: $25\% < P < 50\%$; Cost/Sched: $50\% < P < 75\%$
5 Very High	Tech: $P > 50\%$; Cost/Sched: $P > 75\%$

Exhibit D-2. Risk likelihood.

Consequence of Risk	
1 Very Low	Minimal impact to schedule, cost, performance, or design margin
2 Low	Potential overrun $< 3\%$; non-critical path schedule slip; decrease in spacecraft or payload capability/margin but mission requirements met
3 Moderate	Potential overrun 3–10%; schedule slip affecting critical path, but not delivery; major loss of capability
4 High	Potential overrun $> 10\%$; schedule slip 1-3 months; failure to meet $> one$ L1 requirement, loss of functionality
5 Very High	Potential overrun $> 20\%$; 3-month schedule slip; loss of spacecraft or payload

Exhibit D-3. Risk consequence.




Risk Assessment	
	HIGH – Unacceptable major disruption likely. Different approach needed.
	MEDIUM – Some disruption. Different approach may be required. Management attention needed.
	LOW – Minimum impact. Minimum oversight needed.

Exhibit D-4. Risk assessment

D.5. Organizational chart

Exhibit D-5 shows how key organizations would work together to implement the mission.

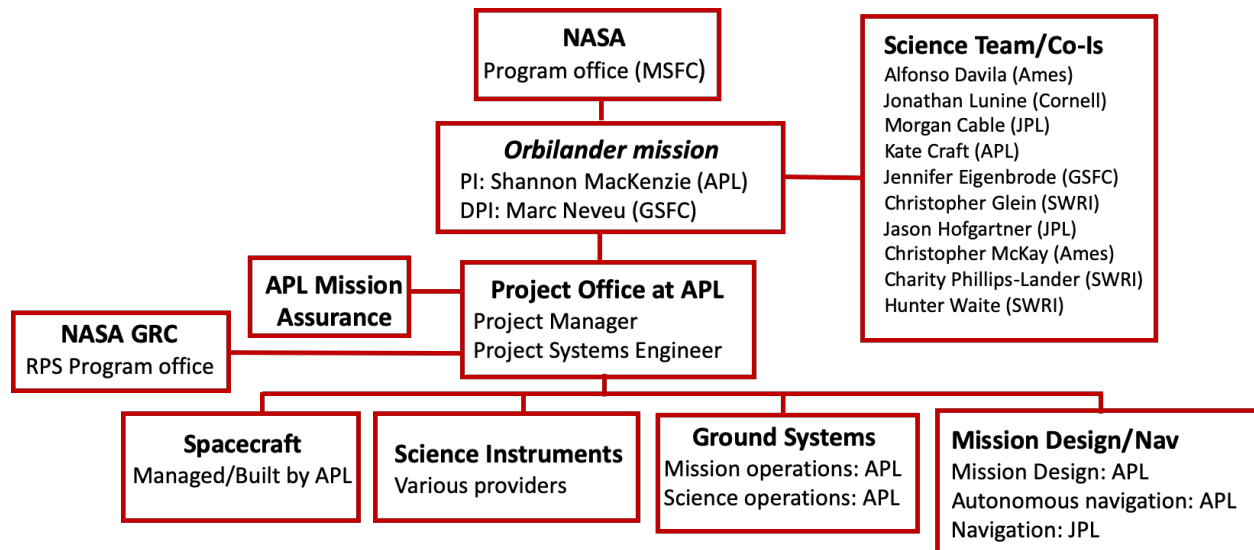


Exhibit D-5. Project Organization Structure.

APPENDIX E. REFERENCES

- Abramov, O., and J. R. Spencer (2009) “Endogenic heat from Enceladus’ south polar fractures: New observations, and models of conductive surface heating.” *Icarus* 199: 189–196.
<https://doi.org/10.1016/j.icarus.2008.07.016>.
- Açıkmeşe, B., J. M. Carson III, and L. Blackmore (2013) “Lossless convexification of nonconvex control bound and pointing constraints of the soft landing optimal control problem,” *IEEE Transactions on Control Systems Technology* 21(6): 2104–2113. doi:10.1109/TCST.2012.2237346.
- Adams, D., T. B. Criss, and U. J. Shankar (2008) “Passive Optical Terrain Relative Navigation Using APLNav,” 2008 IEEE Aerospace Conference, Big Sky, MT, pp. 1–9, March. doi:10.1109/AERO.2008.4526303.
- Adams, E., C. McKay, A. Ricco, R. E. Gold, R. Bonaccorsi, D. W., T. Boone, J. Ma, E. Hoffer, and J. Greenberg (2018) “EFun: The Plume Sampling System for Enceladus,” 42nd COSPAR Scientific Assembly, July 14–22, Pasadena, CA, B5-3.
- Adams, E., D. O’Shaughnessy, M. Reinhart, J. John, E. Congdon, D. Gallagher, E. Abel, et al. (2019) “Double Asteroid Redirection Test: The Earth Strikes Back,” 2019 IEEE Aerospace Conference, Big Sky, MT, pp. 1–11, March. doi:10.1109/AERO.2019.8742007.
- Allen, A.C., C. Langley, R. Mukherji, M. Nimelman, J. de Lafontaine, , D. Neveu, and J. W. Tripp (2008) “Full-scale testing and platform stabilization of a scanning LIDAR system for planetary landing,” *Proceedings of SPIE* 6960, Space Exploration Technologies, 696004, May.
- Andreas, E. L. (2007) “New estimates for the sublimation rate for ice on the Moon,” *Icarus* 186: 24–30.
<https://doi.org/10.1016/j.icarus.2006.08.024>.
- Arakawa, S., H. Tanaka, A. Kataoka, and T. Nakamoto (2017) “Thermal conductivity of porous aggregates,” *Astronomy & Astrophysics* 608: L7. <https://doi.org/10.1051/0004-6361/201732182>.
- Arevalo Jr., R., L. Selliez, C. Briois, N. Carrasco, L. Thirkell, B. Cherville, F. Colin, et al. (2018) “An Orbitrap-based laser desorption/ablation mass spectrometer designed for spaceflight,” *Rapid Communications in Mass Spectrometry* 32(21): 1875–1886.
- Arevalo Jr., R., Z. Ni, and R. M. Danell (2020) “Mass spectrometry and planetary exploration: A brief review and future projection,” *Journal of Mass Spectrometry* 55(1), e4454.
- Atchison, J. A., et al. (2014) “Double Asteroid Redirection Test - Mission Design and Navigation,” 24th International Symposium on Space Flight Dynamics, May 5–9, Laurel, MD.
- Atwell, W., B. Reddell, and P. Boeder (2007) “A comparison of the radiation environments in deep space,” *SAE Transactions*, 133–139.
- Baland, R. M., M. Yseboodt, and T. Van Hoolst (2016) “The obliquity of Enceladus,” *Icarus* 268: 12–31.
<https://doi.org/10.1016/j.icarus.2015.11.039>.

- Ballard, C. G., J. Arrieta, Y. Hahn, et al. (2010) “Cassini Maneuver Experience: Ending the Equinox Mission,” AIAA/AAS Astrodynamics Specialist Conference, Toronto, Canada, August. doi:10.2514/6.2010-8257.
- Barth, W., T. Debski, N. Abedinov, Tz Ivanov, H. Heerlein, B. Volland, T. Gotszalk, et al. (2001) “Evaluation and fabrication of AFM array for ESA-Midas/Rosetta space mission,” *Microelectronic Engineering* 57: 825–831.
- Bedrossian, M., C. Lindensmith, and J. L. Nadeau (2017) “Digital holographic microscopy, a method for detection of microorganisms in plume samples from Enceladus and other icy worlds,” *Astrobiology* 17(9): 913–925.
- Bhartia, R., E. C. Salas, W. F. Hug, R. D. Reid, A. L. Lane, K. J. Edwards, and K. H. Nealson (2010) “Label-free bacterial imaging with deep-UV-laser-induced native fluorescence,” *Applied and Environmental Microbiology* 76(21): 7231–7237.
- Briois, C., R. Thissen, L. Thirkell, K. Aradj, A. Bouabdellah, A. Boukrara, N. Carrasco, et al. (2016) “Orbitrap mass analyser for in situ characterisation of planetary environments: Performance evaluation of a laboratory prototype,” *Planetary and Space Science* 131: 33–45.
- Brockwell, T. G., K.J. Meech, K. Pickens, J. Hunter Waite, G. Miller, J. Roberts, J. Lunine et al. (2016) “The Mass Spectrometer for Planetary Exploration (MASPEX),” 2016 IEEE Aerospace Conference, Big Sky, MT, pp. 1–17. doi:10.1109/AERO.2016.7500777.
- Badescu, M., D. Riccobono, S. Ubellacker, P. Backes, M. Dotson, J. Molaro, S. Moreland, et al. (2019) “Sampling Tool Concepts for Enceladus Lander In-Situ Analysis,” 2019 IEEE Aerospace Conference, pp. 1–12, March.
- Bedrossian, M., C. Lindensmith, and J. L. Nadeau (2017) “Digital holographic microscopy, a method for detection of microorganisms in plume samples from Enceladus and other icy worlds,” *Astrobiology* 17(9): 913–925. <https://doi.org/10.1089/ast.2016.1616>.
- Bellerose, J., D. Roth, and S. Wagner (2019) “The Cassini Mission: Reconstructing Thirteen Years of the Most Complex Gravity-Assist Trajectory Flown to Date,” in *Space Operations: Inspiring Humankind’s Future*, 978-3-030-11535-7, Springer Nature.
- Benner, S. A. (2017) “Detecting Darwinism from molecules in the Enceladus plumes, Jupiter’s moons, and other planetary water lagoons,” *Astrobiology* 17: 840–851. <https://doi.org/10.1089/ast.2016.1611>.
- Bergantini, A., S. Pilling, B. G., Nair, N. J., Mason, and H. J. Fraser (2014) “Processing of analogues of plume fallout in cold regions of Enceladus by energetic electrons,” *Astronomy & Astrophysics* 570: A120.
- Bhartia, R., E. C. Salas, W. F. Hug, R. D. Reid, A. L. Lane, K. J. Edwards, and K. H. Nealson (2010) “Label-free bacterial imaging with deep-UV-laser-induced native fluorescence,” *Applied and Environmental Microbiology* 76: 7231–7237. <https://doi.org/10.1128/AEM.00943-10>.
- Bland, M. T., L. A. Weller, D. P. Mayer, K. L. Edmundson, and B. A. Archinal (2019) “The Shape of Enceladus from a Dense Photogrammetric Control Network,” 4th Planetary Data Workshop, Flagstaff, Arizona, LPI Contrib. no. 2151, 7048.

- Bradley, N., S. Bhaskaran, Z. Olikara, and S. Broschart (2019) “Navigation Accuracy at Jupiter and Saturn Using Optical Observations of Planetary Satellites,” Paper AAS 19-231, AAS/AIAA Astrodynamics Specialist Conference, Maui, HI, January.
- Bywaters, K., C. R. Stoker, N. Batista Do Nascimento, and L. Lemke (2020) “Towards determining bi-osignature retention in icy world plumes,” *Life* 10: 40. <https://doi.org/10.3390/life10040040>.
- Bywaters, K. B., H. Schmidt, W. Vercoutere, D. Deamer, A. R. Hawkins, R. C. Quinn, A. S. Burton, and C. P. McKay (2017) “Development of Solid-State Nanopore Technology for Life Detection,” 2017 Astrobiology Science Conference, Mesa, Arizona.
- Cable, M. L., L. J. Spilker, F. Postberg, J. H. Waite, S. Kempf, K. Clark, K. Reh, B. Sherwood, and J. I. Lunine (2017) “Enceladus Life Finder (ELF): A Proposed Mission to Assess the Habitability of a Plume-Bearing World,” *Habitable Worlds 2017: A System Science Workshop*, Laramie, Wyoming, LPI Contrib. no. 2042, id. 4124.
- Cable, M. L., M. Neveu, H.-W. Hsu, and T. M. Hoehler (2020) “Enceladus,” in *Planetary Astrobiology*, eds. V. S. Meadows, et al. (Tucson, AZ: University of Arizona Press), accepted for publication. doi:10.2458/azu_uapress_9780816540068-ch009.
- Čadek O., G. Tobie, T. Van Hoolst, M. Massé, G. Choblet, A. Lefèvre, G. Mitri, R.-M. Baland, M. Běhounková, O. Bourgeois, and A. Trinh (2016) “Enceladus’s internal ocean and ice shell constrained from Cassini gravity, shape, and libration data,” *Geophysical Research Letters* 43: 5633–5660. doi:10.1002/2016GL068634.
- Čadek O., O. Souček, M. Běhounková, G. Choblet, G. Tobie, and J. Hron (2019) “Long-term stability of Enceladus’ uneven ice shell,” *Icarus* 319: 476–484.
- Carr, C. E., A. Mojarro, J. Hachey, K. Saboda, J. Tani, S. A. Bhattachar, A. Smith, A. Pontefract, M. T. Zuber, R. Doebler, and M. Brown (2017) “Towards In Situ Sequencing for Life Detection,” 2017 IEEE Aerospace Conference, 18 pp. <https://doi.org/10.1109/AERO.2017.7943896>.
- Castro-Wallace, S. L., C. Y. Chiu, K. K. John, S. E. Stahl, K. H. Rubins, A. B. McIntyre, J. P. Dworkin, M. L. Lupisella, D. J. Smith, D. J. Botkin, and T. A. Stephenson (2017) “Nanopore DNA sequencing and genome assembly on the International Space Station,” *Scientific Reports* 7(1): 1–12.
- Cavanaugh, J. F., J. C. Smith, X. Sun, A. E. Bartels, L. Ramos-Izquierdo, D. J. Krebs, J. F. McGarry, et al. (2007) “The Mercury Laser Altimeter instrument for the MESSENGER mission,” *Space Science Reviews* 131(1–4): 451–479.
- Chen, M. H., et al. (2018) “Small-body Maneuvering Autonomous Real-time Navigation (SMART Nav): Guiding a spacecraft to Didymos for NASA’s Double Asteroid Redirection Test (DART),” 41st Annual American Astronautical Society Guidance and Control Conference, Breckenridge, CO, 2–7 Feb 2018.
- Cheng, Andrew F., H. A. Weaver, S. J. Conard, M. F. Morgan, O. Barnouin-Jha, J. D. Boldt, K. A. Cooper et al. “Long-range reconnaissance imager on New Horizons.” In *New Horizons*, pp. 189–215. Springer, New York, NY, 2009.
- Chinn, T.N., et al., “Sample Processor for Life on Icy Worlds (SPLIce): Design and Test Results”, Proc. μ TAS 2017 (21st International Conference on Miniaturized Systems for Chemistry and Life Sciences), Chemical and Biological Microsystems Society: San Diego, 2017; pp. 1479–1480

Chin, M., et al., “SPLIce: A Microfluidic Sample Processor to Enable the Search for Life on Icy Worlds”, 42nd COSPAR Scientific Assembly, Pasadena, July 14–20, 2018, Abstract ID F3.6-8-18.

Chiesl T.N., Chu W.K., Stockton A.M., Amashukeli X., Grunthaler F., and Mathies R.A. (2009) Enhanced amine and amino acid analysis using Pacific Blue and the Mars Organic Analyzer microchip capillary electrophoresis system. *Anal Chem* 81:2537–2544

Choukroun, M. et al. “Strength evolution of ice plume deposit analogs of Enceladus and Europa”. *Geophysical Research Letters* (2020)

Christensen, P.R., Bandfield, J.L., Hamilton, V.E., Ruff, S.W., Kieffer, H.H., Titus, T.N., Malin, M.C., Morris, R.V., Lane, M.D., Clark, R.L. and Jakosky, B.M., 2001. Mars Global Surveyor Thermal Emission Spectrometer experiment: investigation description and surface science results. *Journal of Geophysical Research: Planets*, 106(E10), pp.23823–23871.

Christensen, Philip R., et al. “The OSIRIS-REx thermal emission spectrometer (OTES) instrument.” *Space Science Reviews* 214.5 (2018): 87.

Christian, J.A., 2015. Optical navigation using planet’s centroid and apparent diameter in image. *Journal of guidance, control, and dynamics*, 38(2), pp.192–204.

Clinton, J., Giardini, D., Böse, M., Ceylan, S., Van Driel, M., Euchner, F., Garcia, R.F., Kedar, S., Khan, A., Stähler, S.C. and Banerdt, B., 2018. The Marsquake service: Securing daily analysis of SEIS data and building the Martian seismicity catalogue for InSight. *Space Science Reviews*, 214(8), p.133.

Cockell, C.S., Bush, T., Bryce, C., Direito, S., Fox-Powell, M., Harrison, J.P., Lammer, H., Landenmark, H., Martin-Torres, J., Nicholson, N. and Noack, L., 2016. Habitability: a review. *Astrobiology*, 16(1), pp.89–117.

Collins, R. A., Wangenstein, O. S., O’Gorman, E. J., et al. (2018). Persistence of environmental DNA in marine systems. *Communications Biology* 1, 185. doi:10.1038/s42003-018-0192-6.

Cooper, J.F., Cooper, P.D., Sittler, E.C., Sturmer, S.J. and Rymer, A.M., 2009. Old Faithful model for radiolytic gas-driven cryovolcanism at Enceladus. *Planetary and Space Science*, 57(13), pp.1607–1620.

Creamer, J.S., Mora, M.F. and Willis, P.A., 2017. Enhanced resolution of chiral amino acids with capillary electrophoresis for biosignature detection in extraterrestrial samples. *Analytical chemistry*, 89(2), pp.1329–1337.

Creamer, J.S., Mora, M.F. and Willis, P.A., 2018. Stability of reagents used for chiral amino acid analysis during spaceflight missions in high-radiation environments. *Electrophoresis*, 39(22), pp.2864–2871.

Croci, R., Fois, F., Guelfi, M., Noschese, P., Mecozzi, R. and Seu, R., 2007, July. Calibration of the SHARAD Instrument. In 2007 IEEE International Geoscience and Remote Sensing Symposium (pp. 5218–5223). IEEE.

Daly, M.G., Barnouin, O.S., Dickinson, C., Seabrook, J., Johnson, C.L., Cunningham, G., Haltigin, T., Gaudreau, D., Brunet, C., Aslam, I. and Taylor, A., 2017. The OSIRIS-REx laser altimeter (OLA) investigation and instrument. *Space Science Reviews*, 212(1–2), pp.899–924.

- Denisov, Eduard, Eugen Damoc, Oliver Lange, and Alexander Makarov. “Orbitrap mass spectrometry with resolving powers above 1,000,000.” *International Journal of Mass Spectrometry* 325 (2012): 80–85.
- Dorn, E. D., Nealson, K. H. and Adami, C. (2011). Monomer abundance distribution patterns as a universal biosignature: examples from terrestrial and digital life. *Journal of Molecular Evolution* 72: 283–295. <https://doi.org/10.1007/s00239-011-9429-4>.
- Eigenbrode, J.L., (2008). Fossil lipids for life-detection: a case study from the early Earth record. In *Strategies of Life Detection* (pp. 161–185). Springer, Boston, MA.
- Eigenbrode, J., Gold, R. E., McKay, C. P., Hurford, T., & Davila, A. (2018). Searching for Life in an Ocean World: The Enceladus Life Signatures and Habitability (ELSAH) mission concept. *cosp*, 42, F3-6.
- Europa Lander SDT (Hand, K. P., Murray, A. E., Garvin, J. B. et al.) (2017). Report of the Europa Lander Science Definition Team. <https://europa.nasa.gov/resources/58/europa-lander-study-2016-report/>
- Garrett, Henry B., James M. Ratliff, and R. W. Evans. Saturn radiation (SATRAD) model. Pasadena, CA: Jet Propulsion Laboratory, National Aeronautics and Space Administration, 2005.
- Georgiou, C. D. and Deamer, D. W. (2014). Lipids as universal biomarkers of extraterrestrial life. *Astrobiology* 14: 541–549. <https://doi.org/10.1089/ast.2013.1134>.
- Getty, Stephanie A., Jason P. Dworkin, Daniel P. Glavin, Mildred Martin, Yun Zheng, Manuel Balvin, Adrian E. Southard et al. “Organics Analyzer for Sampling Icy Surfaces: A liquid chromatograph-mass spectrometer for future in situ small body missions.” In 2013 IEEE Aerospace Conference, pp. 1–8. IEEE, 2013.
- Getzandanner, K., Rowlands, D., Mazarico, E., Antreasian, P., Jackman, C. and Moreau, M., 2016. An independent orbit determination simulation for the OSIRIS-REx asteroid sample return mission.
- Glavin, D. P., Burton, A. S., Elsila, J. E., Aponte, J. C. and Dworkin, J. P. (2019). The Search for Chiral Asymmetry as a Potential Biosignature in our Solar System. *Chemical Reviews*. <https://doi.org/10.1021/acs.chemrev.9b00474>.
- Glein, C. R. and Waite, J. H. (2020). The Carbonate Geochemistry of Enceladus’ Ocean. *Geophysical Research Letters* 47: p.e2019GL085885. <https://doi.org/10.1029/2019GL085885>.
- Goesmann, Fred, Helmut Rosenbauer, Reinhard Roll, Cyril Szopa, Francois Raulin, Robert Sternberg, Guy Israel, Uwe Meierhenrich, Wolfram Thiemann, and Guillermo Munoz-Caro. “COSAC, the cometary sampling and composition experiment on Philae.” *Space Science Reviews* 128, no. 1–4 (2007): 257–280.
- Gold, R., Eigenbrode, J., Davila, A., McKay, C., Lorentson, C., Therese, E., Canham, J., Kujawa, F., Kusnierkiewicz, D., Ottens, B. & Martin, N. (2018) Contamination Mitigations for ELSAH and Future Life Detection Missions. AbSciCon 2019 Poster 118-012
- Haapala, A. Howell, K., and Folta, D. “Incorporating the Evolution of Multi-Body Orbits into the Trajectory Trade Space and Design Process,” *Acta Astronautica*, 112, 2015. DOI 10.1016/j.actaastro.2015.02.024.

Hecht, M. H., J. Marshall, W. T. Pike, U. Staufer, D. Blaney, D. Braendlin, S. Gautsch et al. “Microscopy capabilities of the microscopy, electrochemistry, and conductivity analyzer.” *Journal of Geophysical Research: Planets* 113, no. E3 (2008).

Hedman, M. M., Dhingra, D., Nicholson, P. D., Hansen, C. J., Portyankina, G., Ye, S. and Dong, Y. (2018). Spatial Variations in the Dust-to-Gas Ratio of Enceladus’ Plume. *Icarus* 305: 123–138. <https://doi.org/10.1016/j.icarus.2018.01.006>.

Hemingway, D.J. and Mittal, T. (2019) Enceladus’s ice shell structure as a window on internal heat production. *Icarus* 332: 111–131. <https://doi.org/10.1016/j.icarus.2019.03.011>.

Hernandez, S., Restrepo, R., and Anderson, A., CONNECTING RESONANT TRAJECTORIES TO A EUROPA CAPTURE THROUGH LISSAJOUS STAGING ORBITS, AAS 19-455.

Hollenberg, C. L. , Christian, J. A., Bhaskaran, S. and Owen, W. M. “Centroiding Performance for Horizon-Based Optical Navigation with Cassini Images of Dione and Rhea,” in AAS Space Flight Mechanics Meeting, 2019, pp. 19–494

Horita, J. and Berndt, M. E. ”Abiogenic methane formation and isotopic fractionation under hydrothermal conditions,” *Science*, vol. 285, pp. 1055–1057, 1999.

Howett, C.J.A., Spencer, J.R., Pearl, J. and Segura, M. (2010). Thermal inertia and bolometric Bond albedo values for Mimas, Enceladus, Tethys, Dione, Rhea and Iapetus as derived from Cassini/CIRS measurements. *Icarus* 206: 573–593. <https://doi.org/10.1016/j.icarus.2009.07.016>.

Howett, C.J.A., Spencer, J.R., Pearl, J. and Segura, M., 2011. High heat flow from Enceladus’ south polar region measured using 10–600 cm⁻¹ Cassini/CIRS data. *Journal of Geophysical Research: Planets*, 116(E3).

Hsu, H.-W., Postberg, F., Sekine, Y., Shibuya, T., Kempf, S., Horányi, M., Juhász, A., et al. (2015). Ongoing Hydrothermal Activities within Enceladus. *Nature* 519: 207–210. <https://doi.org/10.1038/nature14262>.

Huertas, A., Johnson, A.E., Werner, R.A. and Maddock, R.A., 2010, March. Performance evaluation of hazard detection and avoidance algorithms for safe Lunar landings. In 2010 IEEE Aerospace Conference (pp. 1–20). IEEE.

Hurford, T. A., W. G. Henning, R. Maguire, V. Lekic, N. Schmerr, M. Panning, V. J. Bray et al. “Seismicity on tidally active solid-surface worlds.” *Icarus* 338 (2020): 113466.

Iess, L., Stevenson, D. J., Parisi, M., D Hemingway, RA Jacobson, JI Lunine, F Nimmo, et al. 2014. “The Gravity Field and Interior Structure of Enceladus.” *Science* 344 (6179): 78–80.

Johnson, A.E., Cheng, Y., Montgomery, J., Trawny, N., Tweddle, B.E. and Zheng, J., 2016. Design and analysis of map relative localization for access to hazardous landing sites on mars. In AIAA Guidance, Navigation, and Control Conference (p. 0379).

Johnson, A.E., Huertas, A., Werner, R.A. and Montgomery, J.F., 2008, March. Analysis of on-board hazard detection and avoidance for safe lunar landing. In 2008 IEEE Aerospace Conference (pp. 1–9). IEEE.

- Kagan, Y.Y., 2002. Seismic moment distribution revisited: I. Statistical results. *Geophysical Journal International*, 148(3), pp.520–541.
- Kim, Taewoo, Eugene Serabyn, Maximilian Schadeegg, Kurt Liewer, Nathan Oborny, J. Kent Wallace, Stephanie Rider, Manuel Bedrossian, Christian Lindensmith, and Jay Nadeau. “ELVIS: A Correlated Light-Field and Digital Holographic Microscope for Field and Laboratory Investigations.” *Microscopy Today* 28, no. 3 (2020): 18–25.
- Klinger, J. (1980) Influence of a phase transition of ice on the heat and mass balance of comets. *Science* **209**: 271. <https://doi.org/10.1126/science.209.4453.271>.
- Kim, Taewoo, Eugene Serabyn, Maximilian Schadeegg, Kurt Liewer, Nathan Oborny, J. Kent Wallace, Stephanie Rider, Manuel Bedrossian, Christian Lindensmith, and Jay Nadeau. “ELVIS: A Correlated Light-Field and Digital Holographic Microscope for Field and Laboratory Investigations.” *Microscopy Today* 28, no. 3 (2020): 18–25.
- Kounaves, Samuel P., Michael H. Hecht, Steven J. West, John-Michael Morookian, Suzanne MM Young, Richard Quinn, Paula Grunthner et al. “The MECA wet chemistry laboratory on the 2007 Phoenix Mars Scout lander.” *Journal of Geophysical Research: Planets* 114, no. E3 (2009).
- Kounaves, Samuel P., M. H. Hecht, J. Kapit, K. Gospodinova, L. DeFlores, R. C. Quinn, William V. Boynton et al. “Wet Chemistry experiments on the 2007 Phoenix Mars Scout Lander mission: Data analysis and results.” *Journal of Geophysical Research: Planets* 115, no. E1 (2010).
- Krause, M., Blum, J., Skorov, Y.V. and Trierloff, M. (2011). Thermal conductivity measurements of porous dust aggregates: I. Technique, model and first results. *Icarus* **214**: 286–296. <https://doi.org/10.1016/j.icarus.2011.04.024>.
- Le Gall, A., Leyrat, C., Janssen, M.A., Choblet, G., Tobie, G., Bourgeois, O., Lucas, A., Sotin, C., Howett, C., Kirk, R., Lorenz, R.D., West, R.D., Stolzenbach, A., Massé, M., Hayes, A.H., Bonnefoy, L., Veyssi re, G. and Paganelli, F. (2017). Thermally anomalous features in the subsurface of Enceladus’s south polar terrain. *Nature Astronomy* **1**: 0063. <https://doi.org/10.1038/s41550-017-0063>.
- Lemmon, M. T., P. H. Smith, C. Shinohara, R. Tanner, P. Woida, A. Shaw, J. Hughes et al. “The Phoenix surface stereo imager (SSI) investigation.” *LPI* 1391 (2008): 2156.
- Leonard, J.M., Geeraert, J.L., Page, B.R., French, A.S., Antreasian, P.G., Adam, C.D., Wibben, D.R., Moreau, M.C. and Lauretta, D.S., 2019. OSIRIS-REx Orbit Determination Performance During the Navigation Campaign.
- Lognonn , Philippe, W. Bruce Banerdt, D. Giardini, W. T. Pike, U. Christensen, P. Laudet, S. De Raucourt et al. “SEIS: Insight’s seismic experiment for internal structure of Mars.” *Space science reviews* 215, no. 1 (2019).
- Lorenz, Ralph D. “Thermal drilling in planetary ices: an analytic solution with application to planetary protection problems of radioisotope power sources.” *Astrobiology* 12, no. 8 (2012): 799–802.
- Lorenz, R. D. (2016). Lander rocket exhaust effects on Europa regolith nitrogen assays. *Planetary and Space Science*, 127, 91–94.

- Malone, Patrick, Roy Smoker, Henry Apgar, and Lawrence Wolfarth. “The application of TRL metrics to existing cost prediction models.” In 2011 Aerospace Conference, pp. 1–12. IEEE, 2011.
- Marshall, S.M., Murray, A.R. and Cronin, L., (2017). A probabilistic framework for identifying biosignatures using Pathway Complexity. *Philosophical Transactions of the Royal Society A: Mathematical, Physical and Engineering Sciences*, 375(2109), p.20160342.
- Martens, H.R., Ingersoll, A.P., Ewald, S.P., Helfenstein, P. and Giese, B. (2015) Spatial distribution of ice blocks on Enceladus and implications for their origin and emplacement. *Icarus* **245**: 162–176. <https://doi.org/10.1016/j.icarus.2014.09.035>.
- Massarweh, L., P. Cappuccio. “On the Restricted 3-Body Problem for the Saturn Enceladus System: Mission Geometry and Orbit Design for Plume Sampling Missions,” AIAA SciTech Forum, 6–10 January 2020, Orlando, FL. Doi:10.2514/6.2020-0467
- Mathies, Richard A., Md Enayet Razu, Jungkyu Kim, Amanda M. Stockton, Paul Turin, and Anna Butterworth. “Feasibility of detecting bioorganic compounds in Enceladus plumes with the Enceladus Organic Analyzer.” *Astrobiology* 17, no. 9 (2017): 902–912.
- McGee, T.G., Rosendall, P.E., Hill, A., Shyong, W.J., Criss, T.B., Reed, C., Chavers, G., Hannan, M., Epp, C. and Nishant, M., 2015. APLNav: Development status of an onboard passive optical terrain relative navigation system. In AIAA Guidance, Navigation, and Control Conference (p. 0853).
- McKinnon, William B. 2015. “Effect of Enceladus’s Rapid Synchronous Spin on Interpretation of Cassini Gravity: Enceladus: Global Ocean, Thick Ice Shell.” *Geophysical Research Letters* 42 (7): 2137–2143. <https://doi.org/10.1002/2015GL063384>.
- Melinder, Å. (2007). *Thermophysical properties of aqueous solutions used as secondary working fluids* (Doctoral dissertation, KTH). <https://www.diva-portal.org/smash/get/diva2:12169/FULLTEXT01.pdf>
- Murphy, D.M. and Koop, T. (2005) Review of the vapour pressures of ice and supercooled water for atmospheric applications. *Quarterly Journal of the Royal Meteorological Society* **131**: 1539–1565. <https://doi.org/10.1256/qj.04.94>.
- National Academies of Sciences Engineering and Medicine. (2019). *An Astrobiology Strategy for the Search for Life in the Universe*. Washington, D.C.: National Academies Press. <https://doi.org/10.17226/25252>
- Nadeau, Jay L., Manuel Bedrossian, and Christian A. Lindensmith. 2018. “Imaging Technologies and Strategies for Detection of Extant Extraterrestrial Microorganisms.” *Advances in Physics: X* 3 (1): 1424032. <https://doi.org/10.1080/23746149.2018.1424032>.
- Nadeau, Jay, Chris Lindensmith, Jody W. Deming, Vicente I. Fernandez, and Roman Stocker. 2016. “Microbial Morphology and Motility as Biosignatures for Outer Planet Missions.” *Astrobiology* 16 (10): 755–774. <https://doi.org/10.1089/ast.2015.1376>.
- Neveu, Marc, Lindsay E. Hays, Mary A. Voytek, Michael H. New, and Mitchell D. Schulte. 2018. “The Ladder of Life Detection.” *Astrobiology* 18 (11): 1375–1402. <https://doi.org/10.1089/ast.2017.1773>.

Noell, Aaron Craig, Elizabeth Jaramillo, Samuel P. Kounaves, Michael H. Hecht, Daniel Jed Harrison, Richard C. Quinn, Jessica E. Koehne, Joshua Forgione, and Antonio J. Ricco. “MICA: Microfluidic Icy-World Chemistry Analyzer.” In 2019 Astrobiology Science Conference. AGU, 2019.

Oleson, S., Newman, J.M., Dombard, A., Meyer-Dombard, D., Craft, K., Sterbentz, J., Colozza, A., Faller, B., Fittje, J., Gyekenyesi, J., Jones, R., Landis, G., Lantz, N., Mason, L., McCarty, S., McKay, T., Packard, T., Schmitz, P., Turnbull, E. and Zakrajsek, J. (2019). Compass Final Report: Europa Tunnelbot. NASA/TP—2019-220054. <https://ntrs.nasa.gov/archive/nasa/casi.ntrs.nasa.gov/20190026714.pdf>.

Panning, Mark P., and Sharon Kedar. “Seismic response of the Mars Curiosity Rover: Implications for future planetary seismology.” *Icarus* 317 (2019): 373–378.

Patthoff, D Alex, and Simon A Kattenhorn. 2011. “A Fracture History on Enceladus Provides Evidence for a Global Ocean.” *Geophysical Research Letters* 38 (18). –

Porco, C., DiNino, D. and Nimmo, F., 2014. How the geysers, tidal stresses, and thermal emission across the south polar terrain of Enceladus are related. *The Astronomical Journal*, 148(3), p.45.

Porco, C. C., L. Dones, and C. Mitchell. 2017. “Could It Be Snowing Microbes on Enceladus? Assessing Conditions in Its Plume and Implications for Future Missions.” *Astrobiology* 17 (September): 876–901. <https://doi.org/10.1089/ast.2017.1665>.

Postberg F., Clark R. N., Hansen C. J., Coates A. J., Dalle Ore C. M., Scipioni F., Hedman M. M., Waite J. H. (2018) Plume and surface composition of Enceladus. In *Enceladus and the Icy Moons of Saturn* (P. M. Schenk et al., eds.), pp. 129–162. Univ. of Arizona, Tucson, doi:10.2458/azu_uapress_9780816537075-ch007.

Postberg, F., N. Khawaja, B. Abel, G. Choblet, C. R. Glein, M. S. Gudipati, B. L. Henderson, et al. 2018. “Macromolecular Organic Compounds from the Depths of Enceladus” *Icarus* 378 (June): 564–568. <https://doi.org/10.1038/s41586-018-0246-4>.

Postberg, F., J. Schmidt, J. Hillier, S. Kempf, and R. Srama. 2011. “A Salt-Water Reservoir as the Source of a Compositionally Stratified Plume on Enceladus.” *Nature* 474 (7353): 620–622. <https://doi.org/10.1038/nature10175>.

Postberg, F., S. Kempf, J. K. Hillier, R. Srama, S. F. Green, N. McBride, and E. Grün. “The E-ring in the vicinity of Enceladus: II. Probing the moon’s interior—the composition of E-ring particles.” *Icarus* 193, no. 2 (2008): 438–454.

Pou, L., David Mimoun, Philippe Lognonné, Raphaël F. Garcia, O. Karatekin, M. Nonon-Latapie, and R. Llorca-Cejudo. “High precision SEIS calibration for the InSight mission and its applications.” *Space Science Reviews* 215, no. 1 (2019): 6.

Pratt, L. “Designing Spacecraft Power Systems to Solve Planetary Protection Challenges”; Report HQ-E-DAA-TN61914; <https://ntrs.nasa.gov/search.jsp?R=20180007290>

Quinn, R.C., A.J. Ricco, N. Bramall, J. Forgione, L. Timucin, T. Boone, K.F. Bywaters, M. Chin, T. Chinn, A. Escajeda, T. Hoac, D. Kemp, A. Lee, M.N. Parenteau, A. Rademacher, L.A. Radosevich, J. Shimada, M. Tan, H. Tran, and J.L. Wang Europa Luminescence Microscope, , Astrobiology Science Conference (AbSciCon) 2019, Seattle, 6/24-28/19; Paper 408-8.

Radosevich, L. A. et al., “SPLIce: A Microfluidic Sample Processor to Enable the Search for Life on Icy Worlds,” Astrobiology Science Conference (AbSciCon) 2019, Seattle, 6/24-28/19; Paper 107-4.

Riede, J. E. et al. (2007) “AutoNav Mark3: Engineering the Next Generation of Autonomous Onboard Navigation and Guidance”, AIAA Guidance, Navigation, and Control Conference and Exhibit, 21–24 Aug 2007, Keystone, CO

Russell, R., M. Lara, “On the Design of an Enceladus Science Orbit,” *Acta Astronautica*, Vol. 65, 2009. doi:10.1016/j.actaastro.2009.01.021

Schmidt, G., Dudzinski, L. and Sutliff, T. (2011). Radioisotope power: A key technology for deep space exploration. In *6th International Energy Conversion Engineering Conference (IECEC)*, 5640. <https://doi.org/10.2514/6.2008-5640>.

Shoshany, Y., Prialnik, D. and Podolak, M. (2002) Monte Carlo modeling of the thermal conductivity of porous cometary ice. *Icarus* **157**: 219–227. <https://doi.org/10.1006/icar.2002.6815>.

Shotwell, R.F., Hays, L.E., Beaty, D.W., Goreva, Y., Kieft, T.L., Mellon, M.T., Moridis, G., Peterson, L.D. and Spycher, N. (2019). Can an off-nominal landing by an MMRTG-powered spacecraft induce a special region on Mars when no ice is present? *Astrobiology* **19**, 1315–1338 <https://doi.org/10.1089/ast.2017.1688>.

Sekine, Yasuhito, Takazo Shibuya, Frank Postberg, Hsiang-Wen Hsu, Katsuhiko Suzuki, Yuka Masaki, Tatsu Kuwatani et al. “High-temperature water–rock interactions and hydrothermal environments in the chondrite-like core of Enceladus.” *Nature Communications* **6**, no. 1 (2015): 1–8.

Selliez, L., C. Briois, N. Carrasco, L. Thirkell, R. Thissen, M. Ito, F.-R. Orthous-Daunay et al., “Identification of organic molecules with a laboratory prototype based on the Laser Ablation-CosmOrbitrap” 2019, *Planetary and Space Science*, **170**, 42–51. <https://doi.org/10.1016/j.pss.2019.03.003>

Selliez, Laura, Julien Maillard, Barnabe Cherville, Thomas Gautier, Laurent Thirkell, Bertrand Gaubicher, Isabelle Schmitz-Afonso, Carlos Afonso, Christelle Briois, and Nathalie Carrasco. “High-resolution mass spectrometry for future space missions: Comparative analysis of complex organic matter with LAb-CosmOrbitrap and laser desorption/ionization Fourier transform ion cyclotron resonance.” *Rapid Communications in Mass Spectrometry* **34**, no. 10 (2020): e8645.

Serabyn, Eugene, Kurt Liewer, Chris Lindensmith, Kent Wallace, and Jay Nadeau. “Compact, lensless digital holographic microscope for remote microbiology.” *Optics express* **24**, no. 25 (2016): 28540–28548.

Smith, David E., Maria T. Zuber, Glenn B. Jackson, John F. Cavanaugh, Gregory A. Neumann, Haris Riris, Xiaoli Sun et al. “The lunar orbiter laser altimeter investigation on the lunar reconnaissance orbiter mission.” *Space science reviews* **150**, no. 1–4 (2010): 209–241

Soderlund, Krista M., Klára Kalousová, Jacob J. Buffo, Christopher R. Glein, Jason C. Goodman, Giuseppe Mitri, G. Wesley Patterson et al. “Ice-Ocean Exchange Processes in the Jovian and Saturnian Satellites.” *Space Science Reviews* **216**, no. 5 (2020): 1–57.

Southard, Adrian E., Stephanie A. Getty, Manuel Balvin, Jamie E. Elsila, Ana Espiritu Melina, Carl Koc-tecki, Deborah W. Towner et al. “Liquid chromatography-mass spectrometry interface for detection of extraterrestrial organics.” In *2014 IEEE Aerospace Conference*, pp. 1–7. IEEE, 2014.

- Southworth, B. S., S. Kempf, and J. Spitale. 2019. "Surface Deposition of the Enceladus Plume and the Zenith Angle of Emissions" 319 (February): 33–42. <https://doi.org/10.1016/j.icarus.2018.08.024>.
- Spencer, John R., and Francis Nimmo. 2013. "Enceladus: An Active Ice World in the Saturn System." *Annual Review of Earth and Planetary Sciences* 41 (1): 693–717. <https://doi.org/10.1146/annurev-earth-050212-124025>.
- Spitale, J. N., and C. C. Porco. 2007. "Association of the Jets of Enceladus with the Warmest Regions on Its South-Polar Fractures" 449 (October): 695–697. <https://doi.org/10.1038/nature06217>.
- Spitale, J. N., T. A. Hurford, A. R. Rhoden, E. E. Berkson, and S. S. Platts. 2015. "Curtain Eruptions from Enceladus' South-Polar Terrain" 521: 57–60. <https://doi.org/10.1038/nature14368>.
- Strange, N., S. Campagnola, and R. Russel, "Leveraging Flybys of Low Mass Moons to Enable an Enceladus Orbiter," AAS/AIAA Astrodynamics Specialist Conference and Exhibit, Pittsburgh, PA, 2009. Paper AAS 09-435.
- Stähler, Simon C., Mark P. Panning, Steven D. Vance, Ralph D. Lorenz, Martin van Driel, Tarje Nissen-Meyer, and Sharon Kedar. "Seismic wave propagation in icy ocean worlds." *Journal of Geophysical Research: Planets* 123, no. 1 (2018): 206–232.
- Stockton A.M., Chiesl T.N., Scherer J.R., and Mathies R.A. (2008) Polycyclic aromatic hydrocarbon analysis with the Mars Organic Analyzer microchip capillary electrophoresis system. *Anal Chem* 81:790–796.
- Stockton A.M., Chiesl T.N., Lowenstein T.K., Amashekuli X., Grunthaler F.G., and Mathies R.A. (2009) Capillary electrophoresis analysis of organic amines and amino acids in saline and acidic samples using the Mars Organic Analyzer. *Astrobiology* 9:823–830.
- Stockton A.M., Tjin C.C., Chiesl T.N., and Mathies R.A. (2011) Analysis of carbonaceous biomarkers with the Mars Organic Analyzer microchip capillary electrophoresis system: carboxylic acids. *Astrobiology* 11:519–528.
- Stockton A.M., Tjin C.C., Huang G.L., Benhabib M., Chiesl T.N., and Mathies R.A. (2010) Analysis of carbonaceous biomarkers with the Mars Organic Analyzer microchip capillary electrophoresis system: aldehydes and ketones. *Electrophoresis* 31:3642–3649.
- Summons, R.E., Albrecht, P., McDonald, G. and Moldowan, J.M., 2008. Molecular biosignatures. In *Strategies of Life Detection* (pp. 133–159). Springer, Boston, MA.
- Sun, X. and Neumann, G.A., 2014. Calibration of the Mercury Laser Altimeter on the MESSENGER spacecraft. *IEEE transactions on geoscience and remote sensing*, 53(5), pp.2860–2874.
- Sutton, M. A., Burton, A. S., Zaikova, E., Sutton, R. E., Brinckerhoff, W. B., Bevilacqua, J. G., Weng, M. M., Mumma, M. J. and Johnson, S. S., 2019. Radiation tolerance of Nanopore sequencing technology for Life Detection on Mars and Europa. *Scientific Reports*, 9(1): 1–10. <https://doi.org/10.1038/s41598-019-41488-4>.
- Tapley, B.D.; Schutz, B.E.; and Born, G.H.; 2008. *Statistical Orbit Determination*. Academic Press, Burlington, MA. ISBN: 0-12-683630-2

- Teolis, B. D., M. E. Perry, C. J. Hansen, J. H. Waite, C. C. Porco, J. R. Spencer, and C. J. A. Howett. 2017. “Enceladus Plume Structure and Time Variability: Comparison of Cassini Observations.” *Astrobiology* 17 (September): 926–940. <https://doi.org/10.1089/ast.2017.1647>.
- Thomas, P. C., R. Tajeddine, M. S. Tiscareno, J. A. Burns, J. Joseph, T. J. Lored, P. Helfenstein, and C. Porco. 2016. “Enceladus’s Measured Physical Libration Requires a Global Subsurface Ocean” 264 (January): 37–47. <https://doi.org/10.1016/j.icarus.2015.08.037>.
- Thomas, N., Lüthi, B.S., Hviid, S.F., Keller, H.U., Markiewicz, W.J., Blümchen, T., Basilevsky, A.T., Smith, P.H., Tanner, R., Oquest, C. and Reynolds, R., 2004. The microscope for Beagle 2. *Planetary and Space Science*, 52(9), pp.853–866.
- Toyoda, Michisato, Daisuke Okumura, Morio Ishihara, and Itsuo Katakuse. “Multi-turn time-of-flight mass spectrometers with electrostatic sectors.” *Journal of mass spectrometry* 38, no. 11 (2003): 1125–1142.
- Trainer, M. G., W. B. Brinckerhoff, C. Freissinet, D. J. Lawrence, P. N. Peplowski, A. M. Parsons, K. Zacny et al. “Dragonfly: Investigating the Surface Composition of Titan.” LPSC 2083 (2018): 2586.
- Vance, S.D., Hand, K.P. and Pappalardo, R.T., 2016. Geophysical controls of chemical disequilibria in Europa. *Geophysical Research Letters*, 43(10), 4871–4879.
- Vance, S.D., Kedar, S., Panning, M.P., Stähler, S.C., Bills, B.G., Lorenz, R.D., Huang, H.H., Pike, W.T., Castillo, J.C., Lognonné, P. and Tsai, V.C., 2018. Vital signs: seismology of icy ocean worlds. *Astrobiology*, 18: 37–53.
- Wagner, S.; Buffington, B., Goodson, T.; Hahn, Y.; Strange, N.; and Wong, M., 2005 “Cassini-Huygens Maneuver Experience: First Year of Saturn Tour,” AAS/AIAA Astrodynamics Specialists Conference, Paper No. AAS 05-287, Lake Tahoe, CA, August.
- Waite, J. H. 2006. “Cassini Ion and Neutral Mass Spectrometer: Enceladus Plume Composition and Structure.” *Science* 311 (5766): 1419–1422. <https://doi.org/10.1126/science.1121290>.
- Waite, J. H., C. R. Glein, R. S. Perryman, B. D. Teolis, B. A. Magee, G. Miller, J. Grimes, et al. 2017. “Cassini Finds Molecular Hydrogen in the Enceladus Plume: Evidence for Hydrothermal Processes.” *Science* 356 (April): 155–159. <https://doi.org/10.1126/science.aai8703>.
- Waite, J. H., W. S. Lewis, B. A. Magee, J. I. Lunine, W. B. McKinnon, C. R. Glein, O. Mousis, et al. 2009. “Liquid Water on Enceladus from Observations of Ammonia and 40Ar in the Plume.” *Nature* 460 (7254): 487–490. <https://doi.org/10.1038/nature08153>.
- White, J., Criss, T. and Adams, D., 2009, August. APLNav terrain relative navigation helicopter field testing. In *AIAA Guidance, Navigation, and Control Conference* (p. 5807).
- Whitman W. B., Coleman D. C., and Wiebe W. J. (1998) Prokaryotes: The unseen majority. *Proc. Natl. Acad. Sci. USA*, 95, 6578–6583.
- Williams, P.; Ballard, C.; Gist, E.; Goodson, T.; Hahn, Y.; Stumpf, P.; and Wagner, S., 2009. “Flight Path Control Design for the Cassini Equinox Mission,” AAS/AIAA Space Flight Mechanics Meeting, Paper No. 09-223, Savannah, GA, February.

Witte, I.R., Bekker, D.L., Chen, M.H., Criss, T.B., Jenkins, S.N., Mehta, N.L., Sawyer, C.A., Stipes, J.A. and Thomas, J.R., 2019. No GPS? No Problem! Exploring the Dunes of Titan with Dragonfly Using Visual Odometry. In AIAA Scitech 2019 Forum (p. 1177).

Zuber, Maria T., D_E Smith, S. C. Solomon, D. O. Muhleman, J. W. Head, J. B. Garvin, J. B. Abshire, and J. L. Bufton. "The Mars Observer laser altimeter investigation." *Journal of Geophysical Research: Planets* 97, no. E5 (1992): 7781–7797